Squeeze-film Flows, with Application to the Human Knee Joint.

Darren J. Knox

Department of Mathematics and Statistics

University of Strathclyde

Glasgow, UK

May 2014

This thesis is submitted to the University of Strathclyde for the degree of Doctor of Philosophy in the Faculty of Science.

This thesis is the result of the author's original research. It has been composed by the author and has not been previously submitted for examination which has led to the award of a degree.

The copyright of this thesis belongs to the author under the terms of the United Kingdom Copyright Acts as qualified by University of Strathclyde Regulation 3.50. Due acknowledgement must always be made of the use of any material in, or derived from, this thesis.

Signed:

Date:

Acknowledgements

I would like to take this opportunity to thank my supervisors, namely Professor Stephen K. Wilson, Dr Brian R. Duffy and Professor Sean McKee, for the guidance they have provided me throughout my time as a Ph.D. student. I would also like to acknowledge the financial support of the University of Strathclyde via a University Postgraduate Research Scholarship. Finally, I would like to thank Dr Richard Black, Dr Philip Riches and Mr Anthony Herbert, from the Department of Biomedical Engineering (formerly the Bioengineering Unit) at the University of Strathclyde, for the useful discussions that we had on the biomechanics of the human knee joint. Furthermore, I would like to thank them for providing me with the (unpublished) data shown in Figure 1.5 which they obtained experimentally.

Abstract

The squeeze-film flow of a thin layer of Newtonian fluid filling the gap between either a flat or a curved rigid impermeable solid coated with a thin rigid or elastic layer and moving under a prescribed constant load towards a thin rigid porous bed of uniform thickness coating a stationary flat impermeable solid is considered. Three related problems are considered separately, namely the case of a flat surface coated with a rigid layer, the case of a curved surface coated with a rigid layer and the general case of a curved surface coated with an elastic layer. Unlike the case of an impermeable bed, in which an infinite time is required for the two surfaces to come into contact, for a porous bed contact occurs in a finite time. Lubrication approximations are used and numerical and (where possible) analytical solutions for the fluid layer thickness, the fluid pressure and the contact time are obtained and analysed. Furthermore, in the rigid cases the fluid particle paths are calculated, and the penetration depths of fluid particles into the porous bed are determined. In particular, the behaviour in the asymptotic limit of small permeability, in which the contact time is large but finite, is investigated. Finally, the results are interpreted in the context of lubrication in the human knee joint, and some conclusions are drawn about the contact time of the cartilage-coated femoral condyles and tibial plateau and the penetration of nutrients into the cartilage.

Contents

Chapter 1

Introduction

In this thesis the squeeze-film flow of a thin layer of Newtonian fluid filling the gap between either a flat or a curved rigid impermeable solid coated with a thin rigid or elastic layer and moving under a prescribed constant load towards a thin rigid porous bed of uniform thickness coating a stationary flat impermeable solid is considered as a model for the human knee joint. In this Chapter we put the work that appears in this thesis into context with the existing literature on squeeze-film flows and explain why a squeeze film is an appropriate model for the human knee joint. In §1.1 we give an overview of the existing literature on squeeze-film flows and then in §1.2 we describe the main anatomical features of the human knee joint, in particular the complex biomechanical properties of articular cartilage and synovial fluid, and explain why a squeeze film is an appropriate model for the human knee joint. In §1.3 an outline of the thesis is given.

1.1 Squeeze-film Flow

1.1.1 Classical Squeeze-film Flow Problems

The squeeze-film flow of a Newtonian fluid between two impermeable surfaces is a classical problem in fluid mechanics (see, for example, Acheson [1] and Szeri [67]) and it is well known that, at least in theory, an infinite time is required to squeeze the fluid out of the gap between two smooth surfaces. The review article by Moore [36] contains a useful review of the early work on squeeze-film flows. The earliest work on squeeze-film flows dates back to Stefan [63] and Reynolds [50] in the late 1800s. Stefan [63] was the first to propose a relationship for the time $t(h)$ taken for the fluid layer separating two parallel concentric cylindrical discs to reduce (or increase) from its initial thickness to some given thickness h as the upper disc approaches (or is pulled away from) the stationary lower disc under a prescribed load, and he verified this relationship by experiment. In his famous paper published in 1886 the Anglo-Irish physicist Osborne Reynolds [50] obtained an expression for the time $t(h)$ taken for the thin fluid layer separating two parallel concentric elliptical plane surfaces to reduce (or increase) from its initial thickness to some given thickness h as the upper surface approaches (or is pulled away from) the stationary lower surface under a prescribed load (see equation 29 in Reynolds [50]). Reynolds [50] showed that in all cases $h = O(t^{-1/2})$ as $t \to \infty$, i.e. an infinite time is required to squeeze the fluid out of the gap between the elliptical surfaces. In the special case when the major and minor radii are equal, i.e. in the case when the surfaces are cylindrical, Reynolds [50] recovered the relationship proposed by Stefan [63], the validity of which has been supported by the experimental work of Meeten [35].

In the 1960s the squeeze-film flow of a fluid layer separating a stationary flat surface and an approaching (or retreating) sphere was considered. Brenner [14] solved the Stokes equations for slow viscous flow in the fluid layer and calculated the force exerted on the sphere by the fluid, obtaining an expression for the force in the form of an infinite series. Though Brenner's [14] infinite series solution for the force is mathematically convergent for all ratios $h/\mathcal{R} > 0$, where $\mathcal{R}$ is the radius of the sphere, the *numerical* convergence of the series is poor for ratios $h/\mathcal{R} \ll 1$. Thus in a later paper Cox and Brenner [18] obtained an asymptotic expansion for the infinite series (force) valid when $h/\mathcal{R} \ll 1$, with the leading order term in the expansion corresponding to the lubrication solution[1].

Stone [66] considered the squeeze-film flow of a more general curved surface moving towards a flat stationary surface through a thin layer of Newtonian fluid. In particular, Stone [66] considered an axisymmetric curved surface of shape $H \propto r^{2n}$, where $n \geq 1$ is an integer, and investigated the case when the surfaces approach under a constant prescribed load. Using lubrication theory to describe the fluid flow in the thin gap between the surfaces, Stone [66] showed that, similarly to the case when both surfaces are flat treated by Stefan [63] and Reynolds [50], the surfaces do not contact in a finite time. More specifically, Stone [66] showed that the time $t(h_{\min})$ taken to reduce the minimum fluid layer thickness to a value $h_{\min}$ increases as n increases, i.e. as the curved surface becomes "flatter", and is such that $t \propto \ln(1/h_{\min})$ when $n = 1$, i.e. when the surface is parabolic, and $t \propto h_{\min}^{-2(n-1)/n}$ when $n \geq 2$.

In practice, additional physical effects not included in the classical problem (such as, for example, small-scale surface roughness) will inevitably result in contact between the two surfaces in a finite time. Even in theory, the prediction of an infinite contact time is not true for non-smooth surfaces. For example, recently

[1] Cox and Brenner [18] provided a reference to Hardy and Bircumshaw [26] who attribute the lubrication solution to G. I. Taylor.

Cawthorn and Balmforth [16] showed that a wedge falling apex-first under gravity through a fluid will make contact with an underlying surface in a finite time.

1.1.2 Non-Newtonian Lubricants

The study of squeeze-film flows has not been restricted to Newtonian fluids. Many authors have considered squeeze-film flow problems in which the lubricating fluid is modelled as a power-law fluid with viscosity

$$\mu = K|\dot{\gamma}|^{M-1}, \tag{1.1}$$

where $\dot{\gamma}$ is the shear rate, $M > 0$ is the power-law index and K, which has the units $\mathrm{Pa\,s}^M$, is referred to as the consistency (see, for example, Barnes *et al.* [9]). For shear-thinning fluids $M < 1$, $M = 1$ corresponds to the Newtonian case and $M > 1$ corresponds to a shear-thickening fluid.

Scott [54] generalised the squeeze-film flow problems considered by Stefan [63] and Reynolds [50], who we recall considered the squeeze-film flow of a thin layer of Newtonian fluid of thickness h filling the gap between two parallel concentric cylindrical discs, to the case when the lubricating fluid is a non-Newtonian power-law fluid. Scott [54] showed that the force F required to pull the upper disc away from the stationary lower disc at a constant velocity V_0 is given by the so-called Scott equation $F \propto V_0^M/h^{1+2M}$. Scott [54] did not consider the case when the upper disc approaches (or is pulled away from) the stationary lower disc under a prescribed constant load. However, writing $V_0 = -\mathrm{d}h/\mathrm{d}t$ and integrating the Scott equation shows that in this case the fluid layer thickness $h = O(t^{-M/(M+1)})$ as $t \to \infty$, from which it is deduced that

- the surfaces do not contact in a finite time, similarly to the Newtonian case

$M = 1$ treated by Stefan [63] and Reynolds [50], and

- the upper disc approaches the stationary lower disc at a slower rate when they are separated by a shear-thinning ($M < 1$) fluid than it does when they are separated by a Newtonian ($M = 1$) or shear-thickening ($M > 1$) fluid.

The latter is perhaps surprising and so it is worth noting that there is experimental evidence that raises doubts about the validity of the equivalent Scott equation for yield stress fluids. Meeten [35] conducted experiments in which yield stress fluids (in particular, Brylcreem and laponite) were squeezed between two parallel concentric cylindrical discs and found that the fluid layer thickness h obeyed the Scott equation only for sufficiently large values of h.

More recently Sherwood [56] considered the squeeze-film flow of a thin layer of power-law fluid filling the gap between two concentric cylindrical discs, the upper disc being inclined at an angle θ and moving towards the stationary lower disc at a constant velocity. Sherwood [56] considered the case $\theta \ll 1$ so that the inclination of the upper disc causes only a small perturbation to the separation between the discs (in comparison to the case when the discs are parallel, i.e. when $\theta = 0$, treated by Scott [54]). Sherwood [56] showed that if θ is fixed as the discs approach then the perturbation to the force exerted on the lower disc by the fluid, which to leading order in the limit $\theta \to 0$ is given by the Scott equation, occurs at $O(\theta^2)$ and is negligible provided that the ratio $\theta\mathcal{R}/\bar{h} \ll 1$, where $\mathcal{R}$ is the radius of the discs and $\bar{h}$ is the average separation between the discs.

The squeeze-film flow of a non-Newtonian fluid filling the gap between *non-flat* surfaces has also been considered. Rodin [51] considered the approach (along their common axis) of two spheres of, in general, unequal radii separated by a thin layer of power-law fluid. Rodin [51] calculated the force F exerted on the spheres when the upper sphere approaches the stationary lower sphere at a constant velocity V_0

and showed that

$$F \propto V_0^M \begin{cases} O(1) & \text{when} \quad 0 < M < 1/3, \\ \ln\left(\dfrac{1}{h_{\min}}\right) & \text{when} \quad M = 1/3, \\ h_{\min}^{-(3M-1)/2} & \text{when} \quad 1/3 < M. \end{cases} \tag{1.2}$$

In particular, Rodin [51] showed that when $M < 1/3$, in contrast to the Newtonian case ($M = 1$) treated by, for example, Cox and Brenner [18] and Stone [66], the force F does not becomes infinite as the spheres approach contact, from which it was deduced that when $M < 1/3$ the spheres can touch in a finite contact time when pushed together under a constant prescribed load. Rodin [51] incorrectly states that when $M > 1/3$ the spheres cannot touch in a finite contact time when pushed together under a constant prescribed load. However, writing $V_0 = -\mathrm{d}h_{\min}/\mathrm{d}t$ and integrating equation (1.2) shows that the spheres can in fact touch in a finite contact time when pushed together under a constant prescribed load provided that $M < 1$, i.e. the fluid is shear-thinning. It should be noted that the solution for the force F exerted on the spheres given by Rodin [51] diverges as $M \to 1/3^+$.

Lian *et al.* [32] considered a similar problem to Rodin [51] and investigated two distinct cases. In the first case the finite radius at which the fluid pressure was taken to be equal to the ambient value (which was taken to be zero without loss of generality) was chosen to be sufficiently large so that the fluid pressure "asymptotes" towards zero. In the second case this finite radius was chosen not to be so large that the lubrication approximation is no longer valid. In both cases the force required to push the upper sphere towards the lower sphere at a constant velocity was found to decrease as M decreases, and in the former case it was shown that when $M < 1/3$ the force decreases as the minimum fluid layer thickness separating the spheres decreases.

1.1.3 Permeable Boundaries

Another situation in which a finite contact time is possible is when fluid is squeezed between surfaces with permeable boundaries. Motivated in part by the fact that classical results were unable to describe the engagement of wet porous clutch plates, Wu [76] considered the squeeze-film flow of a thin layer of fluid between two annular discs, the upper disc being coated with a porous layer. Wu [76] used lubrication theory to describe the flow in the gap between the discs, and Darcy's law to describe the flow in the porous layer, and showed that the normal force exerted on the discs by the fluid is reduced in comparison with the case when both discs are impermeable. Prakash and Vij [47] used a similar model to describe the squeeze-film flow between circular, annular, elliptical and rectangular flat plates, the lower surface being covered with a porous layer. They also used a lubrication approximation for the flow in the porous layer and obtained results similar to those of Wu [76].

Goren [24] calculated the force exerted on a sphere during its normal approach towards a permeable membrane separating two semi-infinite reservoirs of fluid. Fluid inertia was neglected from the analysis and furthermore it was assumed that the fluid flux per unit area passing through the permeable membrane was proportional to the pressure difference across it. Goren [24] found that, unlike in the case when the membrane is impermeable, the force exerted on the sphere does not increase monotonically as the thickness of fluid layer separating the sphere and the permeable membrane decreases. In particular it was found that the force is finite when the sphere and the permeable membrane are in contact. Nir [42] considered a similar problem, calculating the finite force required to pull a sphere away from contact with a permeable membrane at a constant velocity. Nir [42] showed that, when the permeability of the membrane is small relative to the product of its thickness and the radius of the sphere, the required force is inversely proportional to the square root of the permeability.

Recently Ramon *et al.* [49] considered the normal approach of a solid particle with a more general shape towards a thin permeable membrane. Similarly to Stone [66], Ramon *et al.* [49] considered particles of shape $H \propto r^{2n}$, where $n \geq 1$ is an integer. Using lubrication theory to describe the fluid flow in the thin gap between the particle and the membrane, numerical and asymptotic results for the force F exerted on the particle as it approaches the membrane at a constant velocity were obtained. It was shown that the force $F \propto k^{-(3n-2)/(3n-1)}$ increases as the permeability k of the membrane decreases or for flatter particles (larger n). In particular, for a spherical particle ($n = 1$) the force $F \propto k^{-1/2}$, in agreement with Nir [42]. Furthermore, it was shown that the particle attains a finite non-zero velocity as it sediments towards the membrane under gravity, indicating that it will come into physical contact with the membrane in a finite time. Spherical particles ($n = 1$) were shown to approach the membrane at a larger velocity than flatter particles.

Many of the authors who have considered problems where a fluid is squeezed between surfaces with permeable boundaries have used Darcy's law to describe the flow in the porous medium (see, for example, Wu [76] and Prakash and Vij [47]). Darcy's law relates the fluid volume flux per unit area $\mathbf{u}$ (the so-called Darcy velocity) flowing through a porous medium to the permeability k of the porous medium, the viscosity μ of the interstitial fluid and the pressure gradient $-\nabla P$ driving the flow, and (neglecting gravitational effects) states that the Darcy velocity $\mathbf{u}$ is proportional to the permeability k and the pressure gradient $-\nabla P$

and inversely proportional to the viscosity μ, i.e.

$$\mathbf{u} = -\frac{k}{\mu}\nabla P. \tag{1.3}$$

Darcy's law (1.3) originated as a purely empirical relationship and was proposed by the French engineer Henry Darcy [19] in 1856 to describe the flow of water through sand. However, Darcy's law has since been derived theoretically (Whitaker [73]) and, more generally, has been shown to describe the laminar flow of a viscous fluid through a porous medium.

Darcy's law (1.3) has been used in several problems, for example, squeeze-film flows (see, for example, Wu [76, 77], Prakash and Vij [47, 48], Sherwood [55], Lin *et al.* [33] and Knox *et al.* [30]), drop spreading and imbibition (see, for example, Davis and Hocking [22], Alleborn and Raszillier [2] and Nong and Anderson [43]) and linear instability analysis of Poiseuille flows (see, for example, Chang *et al.* [17]), to describe the fluid flow in a porous region adjacent to a region of fluid.

Darcy's law (1.3) is of a lower order than the Navier–Stokes equations and, consequently, a difficulty arises when using Darcy's law (1.3) to describe the fluid flow in a porous region adjacent to a region of fluid. There is, in general, freedom to impose only three of the four "usual" boundary conditions, namely continuity of tangential and normal stresses and continuity of tangential and normal velocities, at the interface between the fluid and porous regions (see, for example, Nield and Bejan [40]). A similar difficulty arises at the interface between a porous region and an impermeable boundary, where it is not, in general, possible to satisfy both no-slip and no-penetration boundary conditions. In most studies the conditions of continuity of normal stress and normal velocity (the latter of which is required to ensure conservation of mass) are imposed at the interface between the fluid and porous regions. There is, however, less agreement about which additional bound-

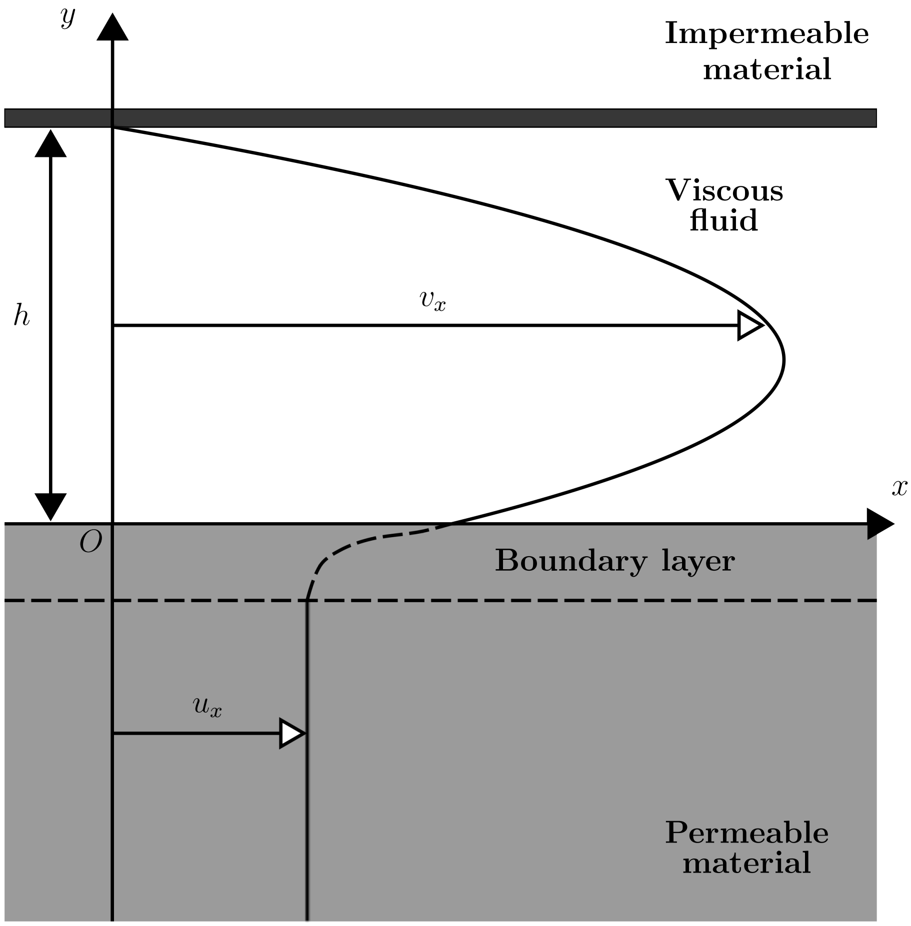

Figure 1.1: A sketch of the velocity profile proposed by Beavers and Joseph [11] for the rectilinear flow of a viscous fluid in a horizontal channel bounded from below by a permeable material at $y = 0$ and from above by an impermeable material at $y = h$

ary condition to impose at such an interface. Some authors (see, for example, Wu [76], Prakash and Vij [47], Sherwood [55], Davis and Hocking [22] and Alleborn and Raszillier [2]) have imposed a condition of no slip relative to the porous solid, so that when the porous solid is stationary the tangential fluid velocity is zero on the fluid side of the interface.

In their famous paper published in 1967, Beavers and Joseph [11] suggested that there is a boundary layer at the interface across which the tangential velocity and the shear stress adjust from their values in the fluid region to their corresponding values in the porous region. Figure 1.1 shows a sketch of the velocity profile proposed by Beavers and Joseph [11] for the rectilinear flow of a viscous fluid in a horizontal channel bounded from below by a permeable material and from above by an impermeable material. Beavers and Joseph [11] hypothesised that the effect of this boundary layer can be replaced by a slip condition at the interface, now known as the Beavers–Joseph boundary condition, and they conducted experiments which verified the validity of this hypothesis. With respect to the planar geometry illustrated in Figure 1.1, the Beavers–Joseph boundary condition states that

$$\left.\frac{\mathrm{d}v_x}{\mathrm{d}y}\right|_{y=0^+} = \frac{\alpha}{\sqrt{k}}\left(v_x|_{y=0^+} - u_x|_{y=0^-}\right), \tag{1.4}$$

where v_x is the horizontal fluid velocity, u_x is the horizontal Darcy velocity in the permeable material, k is the permeability of the permeable material and α is a dimensionless parameter that is independent of the fluid viscosity μ and depends on the "material parameters which characterize the structure of (the) permeable material within the boundary region". Note that, similarly to Darcy's law (1.3), though the Beavers–Joseph boundary condition (1.4) was originally hypothesised and then verified by experiment it has since been derived theoretically by Saffman [52] and generalised to non-planar geometries not originally considered by Beavers and Joseph [11]. The short critical note by Nield [39] provides an excellent overview of the origins and use of the Beavers–Joseph condition.

Many authors have used the Beavers–Joseph condition in problems where there is an interface between fluid and porous regions (see, for example, Wu [77], Prakash and Vij [48], Sherwood [55], Lin *et al.* [33], Chang *et al.* [17], Nong and Anderson [43] and Knox *et al.* [30]). In squeeze-film problems velocity slip has been found to reduce both the load carrying capacity and the contact time (see, for example, Prakash and Vij [48] and Lin *et al.* [33]). The difference between the results obtained using the no-slip and the Beavers–Joseph boundary conditions depends on the value of the slip length (see, for example, Prakash and Vij [48] and Sherwood [55]). Sherwood [55] considered thin-film flow in the annular gap between a solid cylinder and a cylindrical wellbore in porous rock. In particular, he calculated the force required to pull the cylinder away from the wellbore when they are initially in contact, and was able to show that velocity slip has a negligible effect on the force if the permeability is small or large.

More general models for the flow in a porous region that allow all four of the usual boundary conditions to be imposed at the interface with an adjacent fluid region have also been used. One such model is the Brinkman model. The Brinkman equation states that

$$\nabla P = -\frac{\mu}{k}\mathbf{u} + \tilde{\mu}\nabla^2\mathbf{u}, \tag{1.5}$$

where $\tilde{\mu} \not\equiv \mu$ is an effective viscosity (see Nield and Bejan [40]). The Brinkman equation (1.5) contains a second viscous term which accounts for the effects of viscous shear and is, therefore, of higher order than Darcy's law (1.3). Thus the Brinkman model gives the freedom to impose all four of the usual boundary conditions.

Lin *et al.* [33] considered an analogous problem to that treated by Wu [76], but with the flow in the porous layer described by the Brinkman model. Lin *et al.* [33] compared their results with those obtained using Darcy's law with no slip relative to the porous solid and the Beavers–Joseph condition. Reassuringly, they found no dramatic differences between the solutions obtained using the Brinkman model and Darcy's law. For example, results for the fluid layer thickness as a function of time obtained using the Brinkman model were found to lie between those obtained using Darcy's law with no slip relative to the porous solid and the Beavers–Joseph condition. Davis [20] considered the Stokes flow in the gap between two unequal concentric spheres, one porous and one solid, approaching along their common axis and used the Brinkman model to describe the flow in the larger porous sphere. Davis [20] obtained semi-analytic solutions for hydrodynamic forces exerted on the spheres as they approach at prescribed velocities and showed that the permeability of the larger sphere has the effect of reducing the force exerted on each sphere.

The use of the Brinkman model has not been restricted to squeeze-film flow problems. For example, Nield and Kuznetsov [41] considered the unidirectional pressure driven flow in the horizontal channel formed by an impermeable wall and a stratified porous layer (bonded to an impermeable wall) in which the flow was described by the Brinkman model. The stratified porous layer consisted of a homogeneous porous layer of constant permeability and a transition layer, at the interface with the fluid layer, in which the reciprocal of the permeability varied linearly across its thickness, matching with the fluid layer and the homogeneous porous layer in a continuous fashion. Nield and Kuznetsov [41] calculated the fluid volume flux through the fluid layer and the shear stress at the interface between the fluid layer and the transition layer and compared their results with the case when the "stratified" porous layer is of constant permeability, the flow through it is governed by Darcy's law and the Beavers–Joseph boundary condition is imposed at its interface with the fluid layer. They found that the models produced similar results provided that the thickness of transition layer is small relative to the thickness of the fluid layer and the thickness of the homogeneous porous layer, and that the permeability of the homogeneous porous layer is small relative to the thickness of the channel squared.

1.1.4 Compliant Boundaries

Motivated by a desire for a better understanding of, for example, the criteria under which deformable particles will stick or rebound following impact (studied by Davis *et al.* [21]), the mechanism by which inhaled particles are removed from the mucus-lined lung wall (studied by Weekley *et al.* [71]) and the elastohydrodynamics of the eyelid (studied by Jones *et al.* [29]), the effects of deformable surfaces in squeeze-film problems have also received attention.

Davis *et al.* [21] considered the approach of two deformable spheres along their centrelines through a thin layer of fluid. They used lubrication theory to describe the fluid flow in the thin gap between the spheres and Hertz contact theory of linear elasticity to determine the quasi-static surface deformation of the spheres. Though the inertia of the fluid was assumed to be negligible, they retained the inertia of the spheres in their analysis. Davis *et al.* [21] employed a semi-analytic solution method. The asymptotic solution for small deformations was obtained and this solution was used while the maximum total surface deformation of the spheres was less than five per cent of the separation between their undeformed surfaces. This solution then provided the initial conditions for the full numerical solution that was used thereafter. Davis *et al.* [21] showed that as the spheres approach a large pressure builds up in the fluid layer, deforming the surfaces of the spheres and slowing their approach. A fraction of the kinetic energy of the spheres is transformed into strain energy which is eventually released causing the spheres to “rebound”. As the spheres “rebound” a negative pressure sucks fluid into the gap between the spheres and resists their departure. The spheres, therefore, undergo a damped oscillation finally coming to rest at an equilibrium separation that depends on the Stokes number (a dimensionless measure of the inertia of the spheres relative to the viscous forces exerted on them by the fluid) and their elastic properties.

Weekley *et al.* [71] considered the approach of a parabolic surface towards a flat surface coated with a thin elastic layer through a thin layer of Newtonian fluid. As the fluid pressure increases the thin elastic layer deforms, distributing the pressure over a larger area, and hence slows the approach of the parabolic surface towards the elastic layer. Specifically, Weekley *et al.* [71] showed that the elastic layer deforms in such a way as to create a fluid layer of approximately uniform thickness, with the consequence that the approach is qualitatively the same as that of two flat rigid surfaces. Furthermore, the case when both surfaces are fixed vertically but move relative to each other with a (constant) prescribed transverse velocity was also considered. It was found that a large pressure builds up in front of the parabolic surface deforming the elastic layer whereas the low pressure behind the parabolic surface "sucks" up the elastic layer, forming a corner in its surface which is sharpened by either decreasing the separation between the surfaces or increasing their relative velocity. As time increases, the pressure driven flow through the gap between the surfaces reduces the pressure difference between the front and back of the parabolic surface, meaning that the corner becomes less sharp, and eventually a steady configuration is reached. (Note that this steady configuration has been studied by Skotheim and Mahadevan [59].)

Jones *et al.* [29] considered a similar problem to Weekley *et al.* [71] and investigated the combined effects of squeezing and relative transverse motion of the surfaces. Specifically, they considered the case when the surfaces approach under a prescribed temporally varying load, representative of the force exerted on the ocular surface by the eyelid wiper during a single blink phase, with a prescribed temporally varying relative transverse velocity, representative of the velocity of the eyelid wiper relative to the ocular surface during a single blink phase, and found results similar to those of Weekley *et al.* [71].

Recently Balmforth *et al.* [8] considered problems related to that treated by Weekley *et al.* [71], the elastic layer being modelled in three different ways, namely as an elastic half-space, as a membrane and as a beam. In each case the presence of the elastic layer was found to slow the approach of the two surfaces, as in the case treated by Weekley *et al.* [71]. Note that, unlike the case of a thin elastic layer treated by Weekley *et al.* [71], none of the models considered by Balmforth *et al.* [8] result in a fluid layer of approximately uniform thickness.

1.2 The Human Knee Joint

1.2.1 An Overview of the Main Anatomical Features of the Human Knee Joint

A squeeze film has been proposed as a model for the lubrication of the human knee joint (see, for example, Hou *et al.* [28], Stewart *et al.* [65] and the latest (40th) edition of Gray's Anatomy edited by Standring [62]). Figure 1.2 shows an MRI (magnetic resonance imaging) scan of the left knee joint in a plane parallel to the sagittal plane[2] and Figure 1.3 shows sketches of the main anatomical features of the human knee joint. The human knee joint is where the largest bones in the body, the femur and the tibia, meet. Situated at the distal (furthest from the torso) end of the femur are two rounded "knobs" which are referred to as the femoral condyles. When the knee is in flexion or extension the femoral condyles articulate with the tibial plateau which is situated at the proximal (closest to the torso) end of the tibia. Both the femoral condyles and the tibial plateau are coated

[2]The sagittal plane is the plane that passes through the centre of the body dividing it into right and left sections.

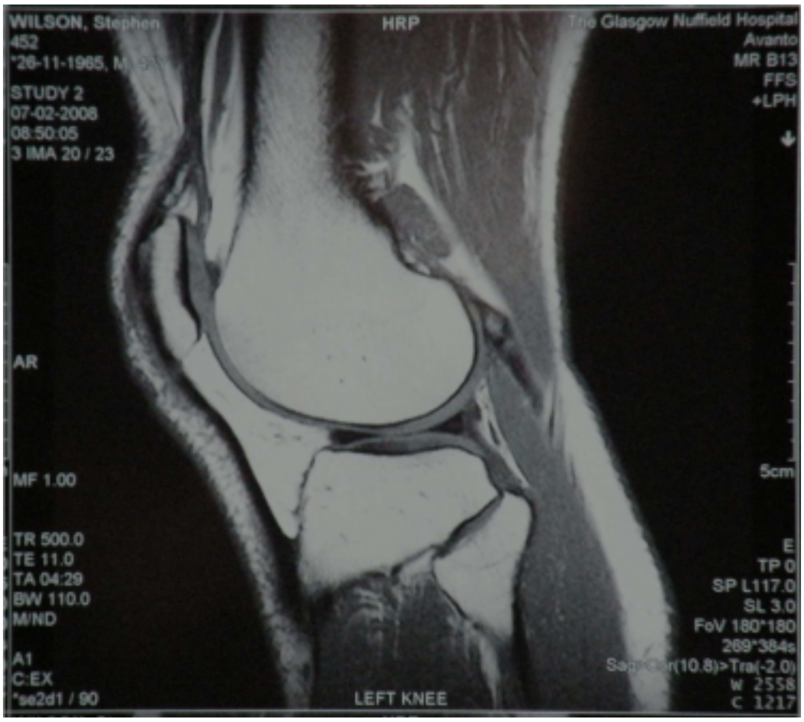

Figure 1.2: An MRI scan of Prof. Stephen K. Wilson's left knee joint

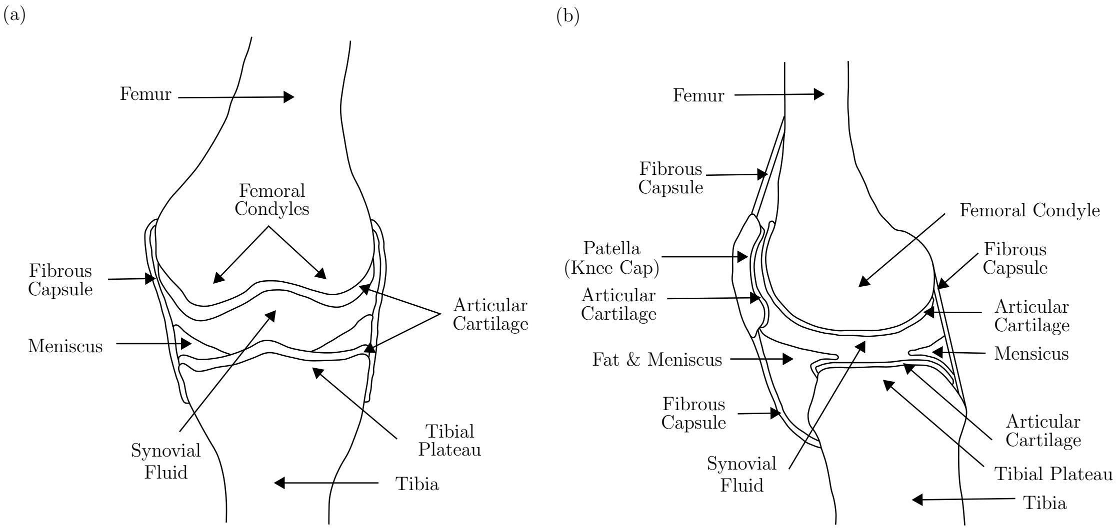

Figure 1.3: Sketches of the main anatomical features of the human knee joint. A slice through (a) the front of the knee (behind the patella) and (b) the side of the knee (through the patella)

with a thin layer of articular cartilage, which is a poroelastic material, and the gap between the femoral condyles and the tibial plateau is lubricated by a thin layer of synovial fluid. The latter is a non-Newtonian shear-thinning fluid and has an egg-white-like consistency (see, for example, Fam *et al.* [23] and Balazs [7]).

Two crescent-shaped wedges of cartilage, the lateral and medial menisci, are situated on the peripheral boundary of the tibial plateau. The menisci deepen the surface of the tibial plateau, protecting the underlying articular cartilage and stabilising the joint. The menisci are attached to the fibrous capsule which is a collection of ligaments that surround the joint, connecting the tibia with the femur and the patella (knee cap) with both the tibia and the femur. The fibrous capsule prevents the joint from undergoing any abnormal movements. Furthermore, the fibrous capsule is lined by the synovial membrane which secretes and absorbs the synovial fluid that lubricates the joint.

1.2.2 Biomechanical Properties of Articular Cartilage

Articular cartilage is a compliant connective tissue that is found in several areas throughout the human body. In particular, articular cartilage is found in the knee joint where thin layers of articular cartilage coat the femoral condyles, tibial plateau and the posterior (near the rear end) side of the patella. Articular cartilage is typically 1–6 mm thick (Ateshian and Hung [6]) and undergoes deformations of up to 15–45 per cent of its thickness in response to long-term or static loads within the physiological range (Grodzinsky *et al.* [25]). Articular cartilage is poroelastic with a porosity varying from 65 to 85 per cent for adults (see, for example, Mow and Guo [37], Carter and Wong [15], Ateshian and Hung [6], Ateshian [5] and Steward *et al.* [64]). The interstitial fluid that fills the pores is water containing sodium and chloride ions (Ateshian and Hung [6]), and when articular cartilage is loaded this fluid pressurises and can support most of the load. The fraction of the load that is supported by the fluid is known as the fluid load support and has been shown to correlate negatively with the friction coefficient (the magnitude of the ratio of the transverse and normal stresses exerted on the articular surface), i.e. the friction coefficient increases as the fluid load support decreases (Ateshian [5]).

Chondrocytes (cartilage cells) occupy 1 to 5 per cent of the tissue volume (see, for example, Ateshian and Hung [6] and Steward *et al.* [64]). The remaining tissue volume is occupied by the extracellular matrix which the chondrocytes produce and organise. The extracellular matrix consists of collagen fibres (60 per cent of the weight of the extracellular matrix), proteoglycans (25 to 35 per cent) and non-collagenous proteins (15 to 20 per cent) (Steward *et al.* [64]). The collagen fibres have a diameter of 10 to 300 nm (Ateshian and Hung [6]) and are approximately 10 times more resistant to tension than they are to compression (Carter and Wong [15]).

Articular cartilage is compositionally heterogeneous from the articular surface to the subchondral bone (the bone onto which the cartilage is attached) and can be divided into three distinct regions, namely the superficial, middle and deep zones. Figure 1.4 shows how the chondrocytes and collagen fibres are aligned throughout the thickness of the articular cartilage from the subchondral bone to the articular surface. In the superficial zone (the uppermost 10 to 20 per cent of the articular cartilage) the collagen fibres are aligned parallel to the articular surface, in the middle zone (the next 40 to 60 per cent) the collagen fibres have a random orientation, and in the deep zone the collagen fibres are aligned perpendicular to the subchondral bone (see, for example, Ateshian and Hung [6] and Steward *et al.* [64]). The collagen and interstitial fluid content is highest in the superficial

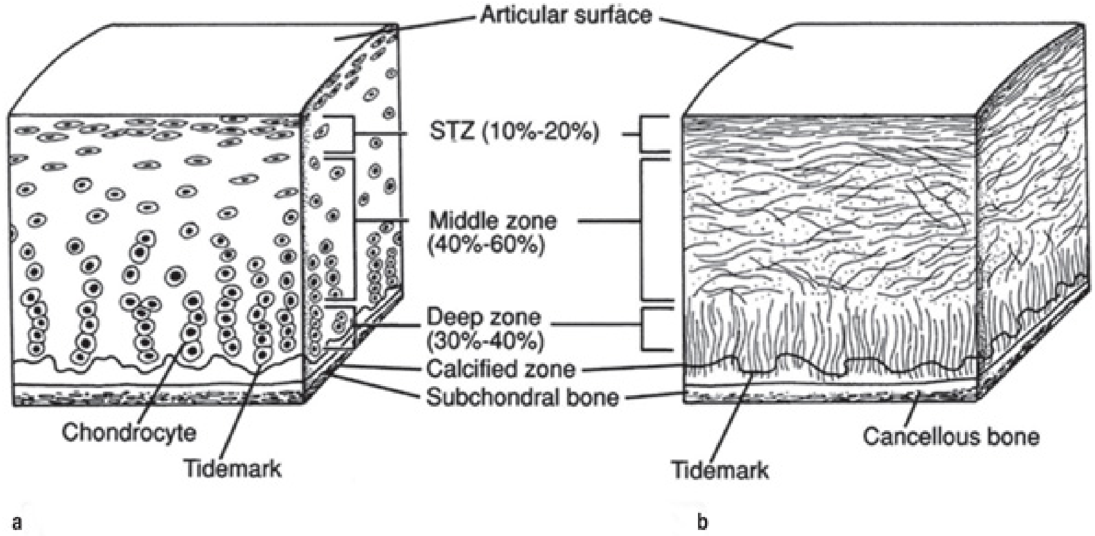

Figure 1.4: The (a) chondrocyte and (b) collagen fibre alignments in articular cartilage. Reproduced with permission from Steward *et al.* [64]

zone and decreases towards the deep zone. In contrast, the proteoglycan content is lowest in the superficial zone, increases in the middle zone and remains constant (or decreases slightly) in the deep zone (Ateshian [5]).

The proteoglycans, which are enmeshed within the extracellular matrix, are negatively charged and the total number of these charges, typically normalised by the volume of interstitial fluid, is known as the fixed charge density (Ateshian [5]) which increases as the extracellular matrix is compressed (Ateshian and Hung [6]). To maintain the electroneutrality of the tissue, more cations (atoms with a positive charge) than anions (atoms with a negative charge) are attracted into the interstitial fluid from the surrounding synovial fluid (Wilson *et al.* [74]). Therefore, a net imbalance in electrolyte concentration exists between the interstitial fluid and the surrounding synovial fluid. Consequently there is an osmotic pressure difference and the interstitial fluid exhibits a larger pressure than the surrounding synovial fluid, causing the extracellular matrix to swell. The swelling of the extracellular matrix is resisted by the tensile properties of the matrix.

As a result of its heterogeneous composition, the mechanical and electrochemical properties of articular cartilage outlined above are not uniform throughout its depth.

1.2.3 Mathematical Models for Articular Cartilage

Several mathematical models of varying degrees of sophistication have been proposed for articular cartilage and a useful review of these models has been provided by Carter and Wong [15]. One of the simplest constitutive models for articular cartilage is that of a homogeneous, linearly elastic, compressible or almost incompressible solid. This is a reasonable model during periods of short static or high frequency loading when the low permeability of articular cartilage means that it is difficult for the interstitial fluid to flow, whence the articular cartilage behaves like a single phase solid (Carter and Wong [15]). Skotheim and Mahadevan [58, 59] considered such a model for articular cartilage and were able to obtain simple expressions for the hydrodynamic lift force exerted on, when interpreting their results in the context of the knee joint, the femoral condyles by the synovial fluid as a result of relative motion between the femoral condyles and the tibial plateau. Such a model is not appropriate in the regions of articular cartilage where the interstitial fluid content is highest (namely, in the superficial zone) or when the cartilage experiences long periods of static loading (for example, when standing still) when interstitial fluid flow is likely to be significant (Carter and Wong [15]). To model such situations one must turn to either poroelasticity or biphasic mixture theory.

Poroelasticity theory was developed in the 1940s by the Belgian-American physicist Maurice Biot [12] to describe the settlement of soil samples under compressive loads. In Biot's theoretical derivation of the equations of linear poroelasticity the stress tensor for a homogeneous, linearly elastic solid is modified to include terms that account for the additional compressive stresses due to presence of the interstitial fluid. Conservation of momentum requires that the divergence of the modified stress tensor vanishes which yields three equations for the four unknowns, namely the three components of the displacement vector and the interstitial fluid pressure. Thus a fourth equation is required and this is obtained by balancing the rate of change of fluid volume fraction in a representative volume element with the volumetric flow rate per unit volume through the surface of the representative volume element. (For further details on the derivation of the equations of linear poroelasticity see Biot [12] or Skotheim and Mahadevan [57].) It is worth noting that Skotheim and Mahadevan [59] have obtained lubrication approximations to the equations of linear poroelasticity that are valid when the poroelastic layer is "long" and "thin", which is the case for articular cartilage.

Biphasic mixture theory was developed by Mow *et al.* [38] in the 1980s. Biphasic mixture theory assumes that the fluid and solid phases are mixed and exist simultaneously at each point in space. There is no modification to the stress tensors for the fluid and solid phases and the force exerted on each phase by the internal stresses is balanced with the interaction force exerted on each phase due to the relative motion of the two phases. Hou *et al.* [28] modelled articular cartilage using the biphasic mixture theory of Mow *et al.* [38]. They considered the squeeze-film flow of a thin layer of fluid in the gap between a stationary rigid impermeable flat surface coated with a thin layer of articular cartilage, in which a lubrication approximation to the biphasic mixture theory of Mow *et al.* [38] was assumed to apply, and a moving rigid impermeable parabolic surface. (It is worth noting that Barry and Holmes [10] have also derived a lubrication approximation to the biphasic mixture theory of Mow *et al.* [38].) Hou *et al.* [28] calculated the pressure in the thin fluid layer, the deformation of the articular surface and interstitial fluid flow through the articular surface.

One of the reasons that the biphasic mixture theory of Mow *et al.* [38] has proved to be a popular model for articular cartilage is that it has been shown to agree favourably with experimental work. Soltz and Ateshian [60] conducted confined compression tests on bovine articular cartilage, in which the cartilage was constrained so that it could not bulge laterally, and found that the fluid load support predicted by the biphasic mixture theory of Mow *et al.* [38] was in good agreement with their experimental results. However, unconfined compression tests have not resulted in such good agreement between theory and experiment. Unconfined compression tests on cartilage specimens have shown that at its peak the fluid load support can be as high as 99 per cent (Park *et al.* [46]), whereas the biphasic mixture theory of Mow *et al.* [38] predicts a peak fluid load support of 33 per cent in unconfined compression (Armstrong *et al.* [4]). The reason for the discrepancy between theory and experiment is that the biphasic mixture theory of Mow *et al.* [38] does not account for the tension-compression nonlinearity present in articular cartilage (recall that articular cartilage is approximately 10 times more resistant to tension than it is to compression [15]). Thus a more physically relevant model for articular cartilage should account for this tension-compression nonlinearity and Soltz and Ateshian [61] have developed a suitably modified version of the biphasic mixture theory of Mow *et al.* [38]. The findings of Armstrong *et al.* [4] and Park *et al.* [46] provide insight into the reasoning behind the structure of articular cartilage. Though articular cartilage is predominantly exposed to compressive loads, the collagen fibres are more suited to resisting tensile stresses. When the cartilage is under compression the tensile strength of the collagen fibres prevents the cartilage from bulging laterally, making it difficult for the interstitial fluid to escape. Thus this fluid becomes highly pressurised and can support the applied compressive stress, minimising friction and cartilage wear.

In addition to the models described above, models which describe the mechano-electrochemical behaviour of articular cartilage, and, in particular, the swelling behaviour of the tissue as a result of the osmotic pressure difference that exists between the interstitial fluid and the surrounding synovial fluid, have also been proposed and a useful review of these models is given by Mow and Guo [37]. However, it is worth noting that by simply adding a deformation-dependent pressure term to the biphasic mixture theory of Mow *et al.* [38], Wilson *et al.* [74] were able to account for the osmotic pressure difference and their results compared favourably with full mechano-electrochemical models.

Recently Lutianov *et al.* [34] developed a continuum model to study the repair of articular cartilage defects following treatment via autologous chondrocyte implantation (ACI) or articular stem cell implantation (ASI). Cell migration was modelled as a diffusive process and cell proliferation, cell differentiation and cell death were represented by reaction terms, resulting in a system of four reaction-diffusion-type equations for four unknowns, namely stem cell density, chondrocyte density, nutrient concentration and matrix density. For both treatments it was shown that approximately 18 months is required for full repair of the defect.

One aspect not considered by Lutianov *et al.* [34] is the interstitial fluid flow within articular cartilage. The interstitial fluid flow within articular cartilage is important for nutrient transport and unconfined compression tests of the tissue have shown that proteoglycan synthesis (the formation of proteoglycans from chondrocyte cells) has a spatial distribution that resembles the interstitial fluid velocity profile (Grodzinsky *et al.* [25]), i.e. interstitial fluid flow is an important factor in the production of proteoglycan and the maintenance of the extracellular matrix.

1.2.4 Biomechanical Properties of, and Mathematical Models for, Synovial Fluid

In the human knee joint a small amount of synovial fluid is contained within the synovial membrane (synovium). It is believed that when a person walks a thin layer of synovial fluid, reported to be up to 5×10^{-7} m thick (see, for example, Stewart *et al.* [65]), can separate the tibial plateau and the femoral condyles. However, when a person stands still for an extended period of time it is believed that the synovial fluid will eventually be squeezed out of the gap between the tibial plateau and the femoral condyles, and so the cartilage-coated surfaces will eventually come into contact (see, for example, Stewart *et al.* [65]); this is undesirable as it results in cartilage degradation and promotes the onset of osteoarthritis.

Synovial fluid is a blood plasma (the liquid component of blood that holds the blood cells in suspension) dialysate containing hyaluronic acid from which it is believed to derive its rheological properties. The hyaluronic acid content of synovial fluid is typically 0.4–4.2 mg/ml (Fam *et al.* [23]). Proteins such as albumin, γ-globulin, fibrinogen, immunoglobulin and α_2-macroglobulin are also present in synovial fluid. The protein content of synovial fluid is typically 10.4–15.8 mg/ml, and an increase of the protein content relative to the hyaluronic acid content is characteristic of the joint diseases such as osteoarthritis or rheumatoid arthritis (Fam *et al.* [23]).

Electrolytes and small molecules such as urea and glucose are also present in synovial fluid (Fam *et al.* [23]). During any physical activity, and, in particular, during walking, synovial fluid is squeezed into and sucked out of the articular cartilage. Cartilage is avascular (i.e. it does not have a blood supply) and the flow of synovial fluid into the cartilage is one of the ways that it receives nutrients such as glucose (see, for example, O'Hara *et al.* [45] and Fam *et al.* [23]).

Synovial fluid is a non-Newtonian shear-thinning fluid (see, for example, Barnes *et al.* [9] and Fam *et al.* [23]). Synovial fluid behaves like a Newtonian fluid at low and high shear rates and behaves like a power-law fluid for intermediate shear rates (Hlaváček [27]). The zero shear rate viscosity of synovial fluid is reported to be $O(1)$–$O(10)$ Pa s whereas at (high) shear rates $\dot{\gamma} = O(10^3)\,\mathrm{s}^{-1}$ its viscosity is reported to be $O(10^{-3})$–$O(10^{-2})$ Pa s (see, for example, Schurz and Ribitsch [53], Hlaváček [27] and Fam *et al.* [23]).

An appropriate model for synovial fluid that captures the behaviour described above is the Carreau model (see, for example, Barnes *et al.* [9]). However, because of its simplicity the power-law model, which we recall describes the behaviour of synovial fluid for intermediate shear rates, is an appealing alternative. In fact the synovial fluid in the human hip joint has been modelled as a piecewise power-law fluid (Hlaváček [27]).

In addition to its viscous properties described above, synovial fluid also possesses elastic properties. These elastic properties are more prominent when the fluid undergoes high frequency oscillations, characteristic of rapid joint motion, than they are when the fluid undergoes low frequency oscillations characteristic of slow joint motion. Furthermore, the elastic response of synovial fluid is positively correlated to its hyaluronic acid content and, therefore, healthy synovial fluid is more elastic than that taken from diseased knees (Fam *et al.* [23]).

1.2.5 Knee Joint Forces and Kinematics

When a person walks or stands still the vertical force $L = L(t)$ acting through the knee joint pushes the femoral condyles and the tibial plateau together creating a squeeze-film effect as the synovial fluid is squeezed out of the thin gap that separates them. (The transverse forces that act through the knee joint are typically much smaller than the vertical ones (see, for example, Taylor *et al.* [68]).) When a person stands still the vertical force $L(t)$ acting through the knee joint is approximately constant and there is little or no relative motion between the femoral condyles and the tibial plateau, and contact between the cartilage-coated surfaces of the femoral condyles and the tibial plateau can occur in a finite time (see Stewart *et al.* [65]). However, when a person walks the vertical force $L(t)$ acting through the knee joint and the relative motion between the femoral condyles and the tibial plateau vary considerably during the four stages of gait, namely “heel strike”, the “stance phase”, “toe-off” and the “swing phase”, and a thin layer of synovial fluid lubricates the femoral condyles and the tibial plateau (see Stewart *et al.* [65] and Standring [62]).

Figure 1.5 shows plots of the knee joint flexion $\theta = \theta(t)$ and the vertical force $L = L(t)$ acting through the knee joint over one step (gait cycle). The (unpublished) data shown in Figure 1.5 was obtained experimentally by Dr Richard Black, Dr Philip Riches and Mr Anthony Herbert from the Department of Biomedical Engineering (formerly the Bioengineering Unit) at the University of Strathclyde. The subject of the experiments was Mr Anthony Herbert himself and the data refers to his left knee joint. Winter’s book [75] describes how such data is obtained via experiment. The knee joint flexion θ is the angle that the tibia makes with the projection of the femur. At heel strike ($\theta = 0°$) the leg is straight and there is little relative motion between the femoral condyles and the tibial plateau. Shortly after heel strike, during the early stance phase, the vertical force L acting through the knee joint increases rapidly to its maximum value, pushing the femoral condyles and the tibial plateau together and squeezing the synovial fluid out of the thin gap

(a)

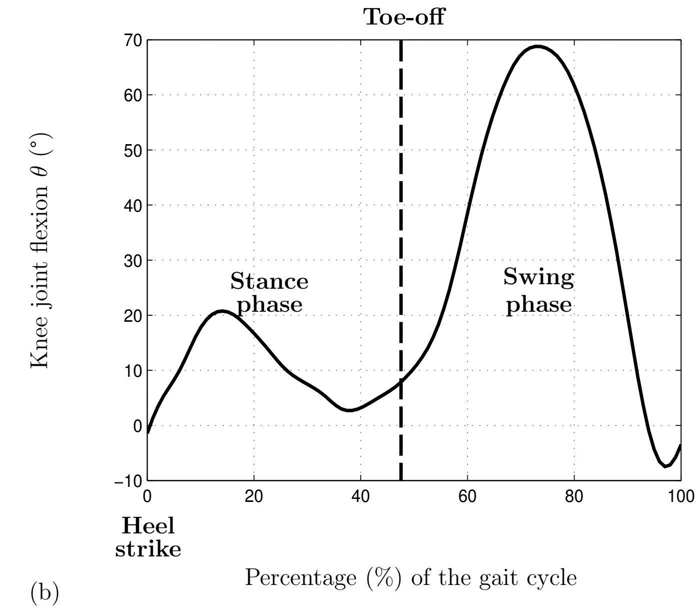

(b)

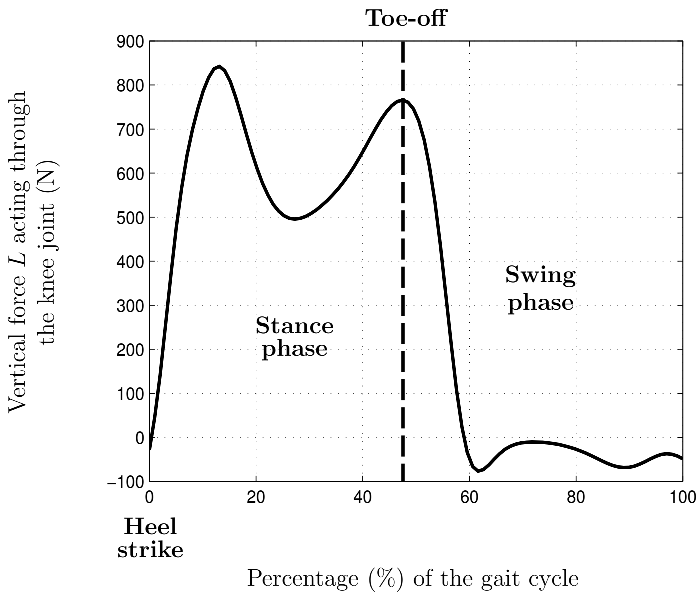

Figure 1.5: Plots of (a) the knee joint flexion and (b) the vertical force acting through the knee joint over one step (gait cycle). The (unpublished) data was obtained experimentally by Dr Richard Black, Dr Philip Riches and Mr Anthony Herbert from the Department of Biomedical Engineering (formerly the Bioengineering Unit) at the University of Strathclyde. The dashed line indicates the instant at which toe-off occurs and separates the stance and swing phases

between them. However, this period of "impulsive" loading acts for only a short time (less than 20 per cent of the gait cycle) and the synovial fluid is sufficiently viscous, and the gap that it fills sufficiently thin, that the femoral condyles and the tibial plateau remain fluid-lubricated (Standring [62]). As the foot is placed flat on the ground the vertical force L acting through the knee joint decreases and the relative motion between the femoral condyles and the tibial plateau (in preparation for the foot pushing off the ground) traps synovial fluid in the gap between them, producing a hydrodynamic lift force that opposes L and acts to separate them. As the foot pushes off the ground the vertical force L acting through the knee joint increases. There is little relative motion between the femoral condyles and the tibial plateau and, therefore, similarly to the early stance phase, the femoral condyles and the tibial plateau are pushed together and the synovial fluid is squeezed out of the thin gap between them. However, similarly to the early stance phase, the femoral condyles and the tibial plateau remain fluid-lubricated as the foot pushes off the ground.

Finally, during the "swing phase", i.e. after toe-off when the foot is off the ground, the vertical force L acting through the knee joint is smaller and the relative motion between the femoral condyles and the tibial plateau is larger than they are during the other phases of gait as the knee flexes and extends while the foot is off the ground. Thus the femoral condyles and the tibial plateau are fluid-lubricated during the swing phase.

1.3 Outline of the Present Work

As discussed earlier in §1.2.3 and §1.2.4 many authors have modelled aspects of synovial joints, and, in particular, the human knee joint, using mathematical models of varying levels of sophistication (see, for example, Mow *et al.* [38], Hou *et al.* [28], Hlaváček [27], Skotheim and Mahadevan [58, 59] and Argatov and Mishuris [3]). Even the simplest of these models result in systems of equations that must be solved numerically. This is unavoidable if one wishes to consider a model that accounts for the many complex biological features of the human knee joint; however, it is somewhat unsatisfactory. Numerical solutions to complex mathematical models can be difficult to interpret, particularly for non-mathematicians (for example, clinicians and bioengineers) who are interested in interpreting the results of such models. Thus there is a need for these numerical studies to be augmented by the study of paradigm problems which give insight into the fundamental physical and biological mechanisms. For example, it would be informative to have analytical expressions for the contact time between the cartilage-coated surfaces of the femoral condyles and the tibial plateau and the penetration depths of synovial fluid particles into the articular cartilage in terms of the geometric and material parameters associated with the human knee joint. Motivated by this, in this thesis we take a somewhat different approach to modelling the human knee joint and consider squeeze-film flow problems that account for the some of the biological features of the human knee joint, namely cartilage permeability and cartilage elasticity, in a simple manner, allowing us to make considerable analytic and numerical progress. Specifically, in this thesis we consider the axisymmetric squeeze-film flow of a thin layer of Newtonian fluid (representing the synovial fluid) separating a stationary flat impermeable surface (representing the tibial plateau), coated with a thin porous layer (representing the thin layer of articular cartilage that coats the tibial plateau), and an impermeable, and in general, curved surface of shape $H = H(r)$ (representing the femoral condyles), coated with a thin elastic layer (representing the thin layer of articular cartilage that coats the femoral condyles), as they approach under a prescribed load. Lubrication theory is used to describe the flow in the thin fluid layer and further lubrication approximations, to Darcy's law and the equations of linear elasticity, are used to describe the flow in the thin porous layer and the deformations in the thin elastic layer, respectively.

Three related but different problems are considered. In Chapter 3 we consider the inelastic case for a flat surface, i.e. $H = 0$, in Chapter 4 we, again, consider the inelastic case but for a *curved* surface of shape $H \propto r^{2n}$, where n is an integer, and finally in Chapter 5 we consider the case when this curved surface is coated with a thin elastic layer. In particular, the finite contact time, i.e. the time taken for the approaching surfaces to contact under a prescribed load, and the penetration depths of fluid particles into the thin porous layer are calculated and the results are interpreted in the context of the human knee joint. Furthermore, the simplicity of the models considered allows us to investigate limits that are of biological interest and we investigate the asymptotic limit of "small" permeability, which corresponds to the permeability of the thin porous layer being much smaller than the square of its thickness.

1.4 Presentations and Publications

I have presented various aspects of the research presented in this thesis and some material which is not included at the following conferences:

- 3^{rd} European Postgraduate Fluid Dynamics Conference, The University of Nottingham, 13^{th}–16^{th} July 2009;

- Research Student and RA Meeting on Mathematical Modelling in the Life Sciences, University of Glasgow, 2^{nd} October 2009;

- 21$^{\text{st}}$ British Applied Mathematics Colloquium Maths 2010, Edinburgh, 6$^{\text{th}}$–9$^{\text{th}}$ April 2010;

- Research Student and RA Meeting, Centre for Mathematics Applied to the Life Sciences, Ross Priory, 28$^{\text{th}}$ September 2010;

- 22$^{\text{nd}}$ British Applied Mathematics Colloquium Maths 2011, University of Birmingham, 11$^{\text{th}}$–13$^{\text{th}}$ April 2011;

- 9$^{\text{th}}$ European Coating Symposium, Turku, Finland, 8$^{\text{th}}$–10$^{\text{th}}$ June 2011.

Furthermore, the material in Chapter 3 was presented by Prof. Stephen K. Wilson at the 17$^{\text{th}}$ European Conference on Mathematics for Industry which was held in Lund, Sweden from the 23$^{\text{rd}}$–27$^{\text{th}}$ July 2012. My talk on "Mathematical Modelling of the Human Knee" at the 21$^{\text{st}}$ British Applied Mathematics Colloquium in Edinburgh in April 2010 was awarded one of the Society of Industrial and Applied Mathematics (SIAM) prizes for the best postgraduate talk.

An extended abstract for the presentation I gave at the 9$^{\text{th}}$ European Coating Symposium held in Turku in June 2011 was published in the conference proceedings [31], and the material presented in Chapter 3 has recently been published online in the IMA Journal of Applied Mathematics [30].

Chapter 2

Model Derivation

2.1 Problem Description

Consider, with reference to the cylindrical polar coordinate system (r, θ, z) shown in Figure 2.1, the time-dependent axisymmetric thin-film flow in the gap $0 \leq r < \infty$, $-H_{\mathrm{p}} \leq z \leq \tilde{h}(t) + H(r) + H_{\mathrm{p}}$ between a vertically (i.e. in the z-direction) moving rigid impermeable surface $z = \tilde{h}(t) + H(r) + H_{\mathrm{p}}$, representing the femoral condyles, and a stationary flat rigid impermeable surface at $z = -H_{\mathrm{p}}$, representing the tibial plateau, where t denotes time. The tibial plateau is coated with a thin rigid porous layer of constant permeability k, porosity ϕ $(0 < \phi < 1)$ and depth H_{p} that occupies $0 \leq r < \infty$, $-H_{\mathrm{p}} \leq z \leq 0$, representing the thin cartilage layer that coats the tibial plateau. The femoral condyles are coated with a thin, isotropic and homogeneous linearly elastic layer, with Lamé parameters λ and G such that $\lambda/G = O(1)$, of depth H_{p} (when undeformed) and density ρ_{s} that occupies $0 \leq r < \infty$, $h(r,t) \leq z \leq \tilde{h}(t) + H(r) + H_{\mathrm{p}}$, representing the thin cartilage layer that coats the femoral condyles. The thin gap between the cartilage layers is filled with, and the pores in the cartilage layer coating the tibial plateau are saturated with,

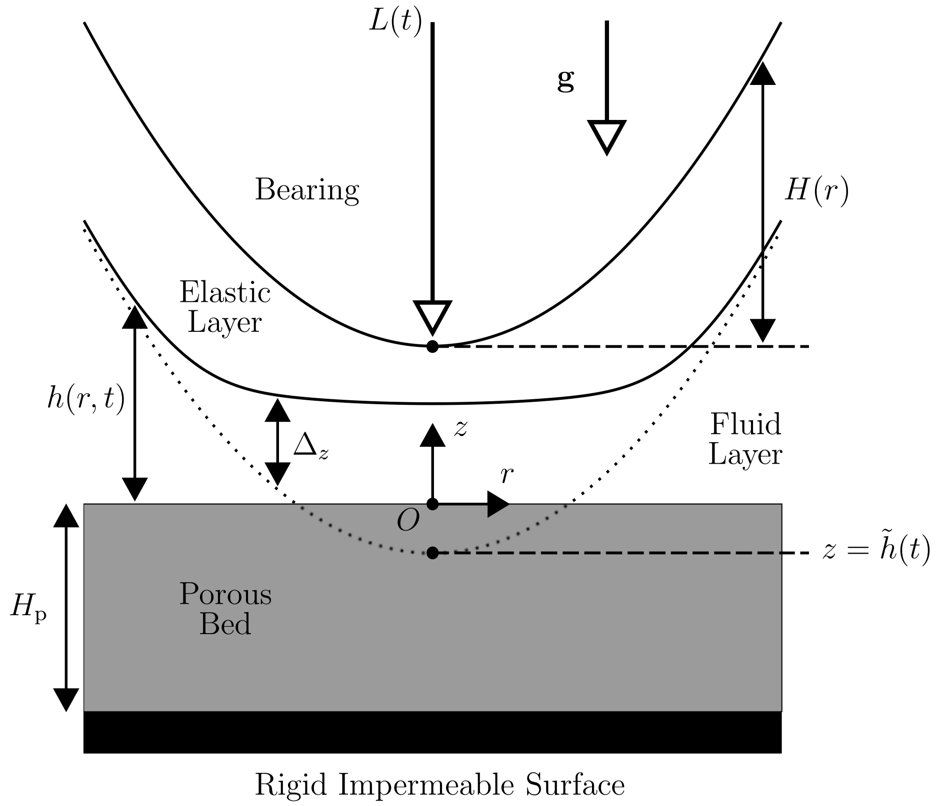

Figure 2.1: The geometry of the axisymmetric problem

synovial fluid, which is modelled as an incompressible Newtonian fluid of constant density ρ_f and viscosity μ. The thickness of the fluid layer separating the thin cartilage layers is given by

$$h(r,t) = \tilde{h}(t) + H(r) + \Delta_z(r,t), \tag{2.1}$$

where $\tilde{h} + H$ is the undeformed interface between the fluid layer and the elastic layer, i.e. the interface between the fluid layer and the elastic layer if the elastic layer had not deformed, and $\Delta_z = \Delta_z(r,t)$ is the vertical displacement of the interface between the fluid layer and the elastic layer relative to its undeformed state. The minimum of the undeformed interface between the fluid layer and the elastic layer $\tilde{h} = \tilde{h}(t)$ shall be determined as part of the solution to the problem

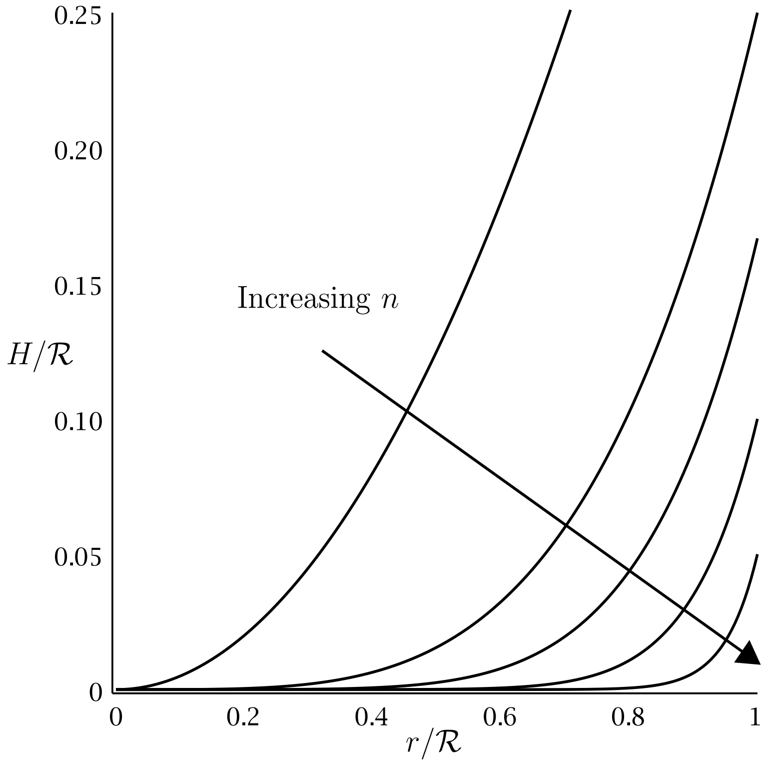

Figure 2.2: Plots of $H/\mathcal{R}$ as a function of $r/\mathcal{R}$ given by (2.2) for $n = 1, 2, 3, 5$ and 10

and $H = H(r) \geq 0$, with $H(0) = 0$, is the shape of the femoral condyles which we shall prescribe. Following Stone [66] and Skotheim and Mahadevan [59], we consider smooth axisymmetric shapes of the form

$$H(r) = \frac{\mathcal{R}}{2n}\left(\frac{r}{\mathcal{R}}\right)^{2n}, \tag{2.2}$$

where $\mathcal{R}$ is the radius of the femoral condyles and the exponent n is an integer. Figure 2.2 shows plots of $H/\mathcal{R}$ as a function of $r/\mathcal{R}$ for several values of n. Figure 2.2 shows that as n increases the femoral condyles become flatter and in the limit $n \to \infty$ the femoral condyles resemble a flat disc of radius $\mathcal{R}$, i.e. $H(r) = 0$ in $0 \leq r \leq \mathcal{R}$. We also prescribe the load $L = L(t) > 0$ that acts vertically downwards through the knee pushing the femoral condyles towards the tibial plateau.

In reality the thin layers of articular cartilage that coat the femoral condyles and the tibial plateau are poroelastic. However, in this thesis the former is modelled as elastic and impermeable and the latter is modelled as rigid and permeable. This yields a mathematical problem which is more tractable than the one that would have been obtained had both layers been modelled as poroelastic, while still including the effects of cartilage permeability and elasticity.

The present model has applications beyond the knee. To make the following presentation as general as possible, henceforth the femoral condyles, the tibial plateau, the cartilage layers, the fluid-filled gap between the bearing and the porous bed, and the synovial fluid will be referred to as "the bearing", "the rigid impermeable surface", "the porous bed", "the elastic layer", "the fluid layer", and "the fluid", respectively.

2.2 Governing Equations

2.2.1 Navier–Stokes Equations

The axiymmetric flow in the fluid layer ($0 \leq r < \infty$, $0 \leq z \leq h(r,t)$) is governed by the mass-conservation and Navier–Stokes equations

$$\nabla \cdot \mathbf{v} = 0, \quad \rho_{\mathrm{f}} \left(\frac{\partial \mathbf{v}}{\partial t} + (\mathbf{v} \cdot \nabla)\mathbf{v} \right) = -\nabla p + \mu \nabla^2 \mathbf{v} + \rho_{\mathrm{f}} \mathbf{g}, \qquad (2.3)$$

where $\mathbf{v} = (v_r, 0, v_z)$ is the fluid velocity, with radial and vertical components $v_r = v_r(r,z,t)$ and $v_z = v_z(r,z,t)$, respectively, $p = p(r,z,t)$ is the fluid pressure, and $\mathbf{g} = (0,0,-g)$ denotes (constant) acceleration due to gravity.

2.2.2 Darcy's Law

We assume that the axisymmetric flow in the porous bed ($0 \leq r < \infty$, $-H_{\mathrm{p}} \leq z \leq 0$) is governed by the mass-conservation equation and Darcy's law,

$$\nabla \cdot \mathbf{u} = 0, \quad \mathbf{u} = -\frac{k}{\mu}(\nabla P - \rho_{\mathrm{f}}\mathbf{g}), \tag{2.4}$$

where $\mathbf{u} = (u_r, 0, u_z)$ is the so-called Darcy velocity (the fluid volume flux per unit area), with radial and vertical components $u_r = u_r(r, z, t)$ and $u_z = u_z(r, z, t)$, respectively, and $P = P(r, z, t)$ is the pore pressure. Combining (2.4) shows that P is harmonic, i.e.

$$\nabla^2 P = 0. \tag{2.5}$$

The averaging process that leads to Darcy's law (see Whitaker [73]) requires that macroscopic length scales (i.e. lengths associated with the porous medium, typically $O(H_{\mathrm{p}})$) are larger than microscopic length scales (i.e. pore length scales, typically $O(k^{1/2})$). Therefore, Darcy's law (2.4b) is applicable only when $k/H_{\mathrm{p}}^2 \ll 1$. (It is shown in Chapter 6 that for articular cartilage $k/H_{\mathrm{p}}^2 = O(10^{-15})$–$O(10^{-12}) \ll 1$.)

In this thesis the physically relevant limit of small (dimensionless) permeability $k/H_{\mathrm{p}}^2 \to 0$ is investigated (see §3.2, §4.3 and §5.3), and the limit of large (dimensionless) permeability $k/H_{\mathrm{p}}^2 \to \infty$ is also investigated (see, for example, §3.3 and §4.4). As a purely mathematical exercise the analysis of the limit $k/H_{\mathrm{p}}^2 \to \infty$ is valid. However, it should be noted that it is of no physical relevance since Darcy's law is not applicable when $k/H_{\mathrm{p}}^2 \gg 1$.

2.2.3 Navier–Lamé Equations

The displacements in the elastic layer ($0 \leq r < \infty$, $h(r,t) \leq z \leq \tilde{h}(t) + H(r) + H_{\mathrm{p}}$) are governed by the Navier–Lamé equations

$$(\lambda + G)\,\nabla\left(\nabla \cdot \mathbf{U}\right) + G\nabla^2\mathbf{U} - \rho_{\mathrm{s}}\mathbf{g} = \rho_{\mathrm{s}}\frac{\partial^2\mathbf{U}}{\partial t^2}, \tag{2.6}$$

where $\mathbf{U} = (U_r, 0, U_z)$ is the displacement, with $U_r = U_r(r,z,t)$ and $U_z = U_z(r,z,t)$ being the radial and vertical displacements of the elastic layer, respectively.

Use of the Navier–Lamé equations (2.6) is justified provided that the strains in the elastic layer are small, and in this case there is no need to distinguish between deformed and undeformed configurations. In particular, boundary conditions on the surface of the elastic layer may be applied on its undeformed surface.

The vertical displacement of the interface between the fluid layer and the elastic layer relative to its undeformed state

$$\Delta_z(r,t) = U_z(r,0,t) \tag{2.7}$$

and substituting (2.7) into (2.1) we have that the fluid layer thickness h is given by

$$h(r,t) = \tilde{h}(t) + H(r) + U_z(r,0,t). \tag{2.8}$$

2.2.4 Equation of Motion of the Bearing

The net force exerted on the bearing by the elastic layer (see, for example, Bower [13]) is in the vertical direction, and is given by

$$\begin{aligned} F_z &= 2\pi \int_0^\infty \left[G \left(\frac{\partial U_r}{\partial z} + \frac{\partial U_z}{\partial r} \right) \frac{\mathrm{d}H}{\mathrm{d}r} - (2G+\lambda) \frac{\partial U_z}{\partial z} \right. \\ &\quad \left. \left. - \lambda \left(\frac{\partial U_r}{\partial r} + \frac{U_r}{r} \right) \right] \right|_{z=\tilde{h}(t)+H_\mathrm{p}+H(r)} \left(1 + \left(\frac{\mathrm{d}H}{\mathrm{d}r} \right)^2 \right)^{-1/2} r \,\mathrm{d}r. \end{aligned} \tag{2.9}$$

The equation of motion of the bearing is

$$m \frac{\mathrm{d}^2 \tilde{h}}{\mathrm{d}t^2} = F_z - L, \tag{2.10}$$

where m is the mass of the bearing. (In the context of the knee, m would be related to the mass of the person.)

2.3 Boundary and Initial Conditions

On the interface between the bearing and the elastic layer $z = \tilde{h}(t) + H_\mathrm{p} + H(r)$ the no-slip condition requires that

$$U_r = U_z = 0 \quad \text{on} \quad z = \tilde{h}(t) + H_\mathrm{p} + H(r). \tag{2.11}$$

On the interface between the elastic layer and the fluid layer at $z = h$ continuity of radial and vertical stress requires that

$$\begin{aligned} &\left. \left[\left(-p + 2\mu \frac{\partial v_r}{\partial r} \right) \frac{\partial h}{\partial r} - \mu \left(\frac{\partial v_r}{\partial z} + \frac{\partial v_z}{\partial r} \right) \right] \right|_{z=h} \\ &= \left. \left[(2G+\lambda) \frac{\partial U_r}{\partial r} \frac{\partial h}{\partial r} + \lambda \left(\frac{U_r}{r} + \frac{\partial U_z}{\partial z} \right) \frac{\partial h}{\partial r} - G \left(\frac{\partial U_r}{\partial z} + \frac{\partial U_z}{\partial r} \right) \right] \right|_{z=\tilde{h}(t)+H(r)} \end{aligned} \tag{2.12}$$

and

$$\left[\mu\left(\frac{\partial v_r}{\partial z}+\frac{\partial v_z}{\partial r}\right)\frac{\partial h}{\partial r}+p-2\mu\frac{\partial v_z}{\partial z}\right]\Bigg|_{z=h}$$
$$=\left[G\left(\frac{\partial U_r}{\partial z}+\frac{\partial U_z}{\partial r}\right)\frac{\partial h}{\partial r}-(2G+\lambda)\frac{\partial U_z}{\partial z}-\lambda\left(\frac{\partial U_r}{\partial r}+\frac{U_r}{r}\right)\right]\Bigg|_{z=\tilde{h}(t)+H(r)} \quad (2{,}13)$$

respectively. Furthermore, we impose no-slip and no-penetration boundary conditions on this interface which require that

$$v_r|_{z=h}=\frac{\partial}{\partial t}U_r|_{z=\tilde{h}(t)+H(r)} \quad \text{and} \quad v_z|_{z=h}=\frac{\partial h}{\partial t}. \quad (2.14)$$

On the interface between the fluid layer and the porous bed at $z=0$ mass conservation requires that

$$v_z=u_z \quad \text{on} \quad z=0, \quad (2.15)$$

while continuity of normal stress requires that

$$-p+2\mu\frac{\partial v_z}{\partial z}=-P \quad \text{on} \quad z=0. \quad (2.16)$$

In addition, we impose the Beavers–Joseph condition

$$\frac{k^{1/2}}{\alpha}\frac{\partial v_r}{\partial z}=v_r-u_r \quad \text{on} \quad z=0, \quad (2.17)$$

where $\alpha\,(>0)$ is the dimensionless Beavers–Joseph constant. This condition allows for velocity slip on the interface between the fluid layer and the porous bed at $z=0$ with slip length $l_\mathrm{s}=k^{1/2}/\alpha$. In the limit $\alpha\to\infty$ the slip length $l_\mathrm{s}\to 0$ and (2.17) reduces to

$$v_r=u_r \quad \text{on} \quad z=0, \quad (2.18)$$

which corresponds to no slip relative to the fluid at the interface. If we neglect the radial Darcy velocity u_r in (2.18) then the condition becomes

$$v_r = 0 \quad \text{on} \quad z = 0, \tag{2.19}$$

which corresponds to no slip relative to the stationary porous bed.

On the interface between the porous bed and the rigid impermeable surface at $z = -H_{\rm p}$ the no-penetration condition requires that

$$u_z = 0 \quad \text{on} \quad z = -H_{\rm p}. \tag{2.20}$$

As $r \to \infty$ the pressure in the fluid layer takes the ambient value, which, without loss of generality, we may take to be zero, i.e.

$$p \to 0 \quad \text{at} \quad r \to \infty, \tag{2.21}$$

and, since the fluid pressure is axisymmetric and smooth at $r = 0$, we also require that

$$\frac{\partial p}{\partial r} = 0 \quad \text{as} \quad r = 0. \tag{2.22}$$

Finally, we must also specify the initial fluid pressure, i.e.

$$p(r, 0) = \mathcal{P}_0(r), \tag{2.23}$$

and the initial minimum of the undeformed interface between the fluid layer and the elastic layer, i.e.

$$\tilde{h}(0) = H_{\rm f}\,(> 0). \tag{2.24}$$

In general, solving (2.3), (2.5), (2.6) and (2.10) would require the specification of additional boundary and initial conditions. However, as we shall show, when the fluid layer, the porous bed and the elastic layer are thin, and lubrication approximations are used to describe the flow in the fluid and porous layers and the displacements in the elastic layer, the leading order approximations to these equations may, in fact, be solved without specifying any additional conditions.

2.4 Non-dimensionalisation and Lubrication Approximation

We scale and non-dimensionalise the problem as follows:

$$\begin{gathered} r = lr', \quad z = H_\mathrm{p} z', \quad t = \frac{l}{V} t', \quad h = H_\mathrm{p} h', \quad \tilde{h} = H_\mathrm{p} \tilde{h}', \quad H = H_\mathrm{p} H', \\ v_r = V v_r', \quad v_z = \frac{H_\mathrm{p} V}{l} v_z', \quad u_r = V u_r', \quad u_z = \frac{H_\mathrm{p} V}{l} u_z', \quad U_r = H_\mathrm{p} U_r', \\ U_z = H_\mathrm{p} U_z', \quad p = \frac{\mu V l}{H_\mathrm{p}^2} p', \quad \mathcal{P}_0 = \frac{\mu V l}{H_\mathrm{p}^2} \mathcal{P}_0', \quad P = \frac{\mu V l}{H_\mathrm{p}^2} P', \quad F_z = L_0 F_z', \\ L = L_0 L', \quad k = H_\mathrm{p}^2 k', \end{gathered} \tag{2.25}$$

where a prime $'$ denotes a dimensionless variable and $l = \mathcal{R}(2nH_\mathrm{p}/\mathcal{R})^{1/2n}$, $V = L_0 H_\mathrm{p}^2/\mu l^3$, $\mu V l/H_\mathrm{p}^2 = L_0/l^2$ and L_0 are characteristic scales for radial distance, radial fluid velocity, pressure and load, respectively.

Note from (2.25) that since the characteristic scale for radial distance l depends on n, the characteristic scales for times, velocities and pressures also depend on n. This can be inconvenient as it means that it is not possible to compare the (dimensionless) solutions for these variables for different values of n. To remedy this problem we define a second set of dimensionless variables, namely

$$\bar{r} = \left(\frac{2nH_{\rm p}}{\mathcal{R}}\right)^{1/2n} r', \quad \bar{t} = \left(\frac{2nH_{\rm p}}{\mathcal{R}}\right)^{2/n} t', \quad \bar{v}_r = \left(\frac{2nH_{\rm p}}{\mathcal{R}}\right)^{-3/2n} v_r',$$
$$\bar{v}_z = \left(\frac{2nH_{\rm p}}{\mathcal{R}}\right)^{-2/n} v_z', \quad \bar{u}_r = \left(\frac{2nH_{\rm p}}{\mathcal{R}}\right)^{-3/2n} u_r', \quad \bar{u}_z = \left(\frac{2nH_{\rm p}}{\mathcal{R}}\right)^{-2/n} u_z',$$
$$\bar{p} = \left(\frac{2nH_{\rm p}}{\mathcal{R}}\right)^{-1/n} p', \quad \bar{\mathcal{P}}_0 = \left(\frac{2nH_{\rm p}}{\mathcal{R}}\right)^{-1/n} \mathcal{P}_0', \quad \bar{P} = \left(\frac{2nH_{\rm p}}{\mathcal{R}}\right)^{-1/n} P', \tag{2.26}$$

that can be used when comparing solutions for different values of n. The variables defined by (2.26) correspond to the dimensionless radial distance, time, fluid velocities, Darcy velocities and pressures, respectively, obtained having taken the radius $\mathcal{R}$ (which is independent of n) to be the characteristic scale for radial distance.

2.4.1 Navier–Stokes Equations

In dimensionless variables, with the primes omitted for the sake of clarity, the mass-conservation and Navier–Stokes equations (2.3) become

$$\frac{1}{r}\frac{\partial}{\partial r}(rv_r) + \frac{\partial v_z}{\partial z} = 0, \tag{2.27}$$
$$R^*\left(\frac{\partial v_r}{\partial t} + v_r\frac{\partial v_r}{\partial r} + v_z\frac{\partial v_r}{\partial z}\right) = -\frac{\partial p}{\partial r} + \frac{\partial^2 v_r}{\partial z^2} + O(\epsilon^2), \tag{2.28}$$
$$\epsilon^2 R^*\left(\frac{\partial v_z}{\partial t} + v_r\frac{\partial v_z}{\partial r} + v_z\frac{\partial v_z}{\partial z}\right) = -\frac{\partial p}{\partial z} - g_{\rm f} + O(\epsilon^2), \tag{2.29}$$

where the aspect ratio of both the fluid layer and the porous bed, $\epsilon = H_{\rm p}/l \ll 1$, the (reduced) Reynolds number for the flow in the fluid layer, $R^* = \epsilon^2\rho_{\rm f}Vl/\mu = \epsilon^4\rho_{\rm f}L_0/\mu^2 \ll 1$, and the non-dimensional parameter that measures the relative importance of gravitational and viscous stresses, $g_{\rm f} = \rho_{\rm f}gH_{\rm p}/(L_0/l^2) \ll 1$, are all assumed to be small. At leading order in the limit $\epsilon \to 0$ and $g_{\rm f} \to 0$ equations

(2.28) and (2.29) reduce to the classical lubrication equations

$$\frac{\partial p}{\partial r} = \frac{\partial^2 v_r}{\partial z^2}, \tag{2.30}$$

$$\frac{\partial p}{\partial z} = 0. \tag{2.31}$$

2.4.2 Darcy's Law

In dimensionless variables, at leading order in the limit $\epsilon \to 0$ (and since $g_\mathrm{f} \ll 1$ is assumed to be small) Darcy's law (2.4b) and Laplace's equation (2.5) become

$$\mathbf{u} = (u_r, 0, u_z) = -k\left(\frac{\partial P}{\partial r}, 0, \frac{1}{\epsilon^2}\frac{\partial P}{\partial z}\right), \tag{2.32}$$

$$\frac{1}{r}\frac{\partial}{\partial r}\left(r\frac{\partial P}{\partial r}\right) + \frac{1}{\epsilon^2}\frac{\partial^2 P}{\partial z^2} = 0. \tag{2.33}$$

2.4.3 Navier–Lamé Equations

In terms of the dimensionless variables (2.25) the Navier–Lamé equations (2.6) become

$$\frac{\partial^2 U_r}{\partial z^2} + O(\epsilon) = R_1^* \frac{\partial^2 U_r}{\partial t^2}, \tag{2.34}$$

$$\frac{\partial^2 U_z}{\partial z^2} - g_\mathrm{s} + O(\epsilon) = R_2^* \frac{\partial^2 U_z}{\partial t^2} \tag{2.35}$$

where $R_1^* = \epsilon^8 \rho_\mathrm{s} L_0^2 / G\mu^2 H_\mathrm{p}^2 \ll 1$, $R_2^* = \epsilon^8 \rho_\mathrm{s} L_0^2/(2G+\lambda)\mu^2 H_\mathrm{p}^2 \ll 1$ and $g_\mathrm{s} = \rho_\mathrm{s} g H_\mathrm{p}/(2G+\lambda) \ll 1$, the non-dimensional parameter that measures the relative importance of gravitational and internal stresses, are assumed to be small. At leading order in the limit $\epsilon \to 0$ and $g_{\mathrm{s}} \to 0$ equations (2.34) and (2.35) reduce to

$$\frac{\partial^2 U_r}{\partial z^2} = 0, \tag{2.36}$$

$$\frac{\partial^2 U_z}{\partial z^2} = 0. \tag{2.37}$$

2.4.4 Equation of Motion of the Bearing

In dimensionless variables, the equation of motion of the bearing (2.10) becomes

$$I\frac{\mathrm{d}^2\tilde{h}}{\mathrm{d}t^2} + \frac{2\pi}{\eta}\int_0^\infty \left.\frac{\partial U_z}{\partial z}\right|_{z=\tilde{h}(t)+1+H(r)} r\,\mathrm{d}r + L(t) = O(\epsilon), \tag{2.38}$$

where the non-dimensional parameter that measures the relative importance of the inertia of the bearing and the prescribed load L acting vertically through it, $I = mH_{\mathrm{p}}(l/V)^{-2}/L_0 = \epsilon^8 mL_0/\mu^2 H_{\mathrm{p}}^3 \ll 1$, is assumed to be small. The non-dimensional parameter

$$\eta = \frac{L_0}{(2G+\lambda)l^2} \tag{2.39}$$

measures the size of the stresses exerted on the elastic layer by the fluid relative to its elastic stiffness. When $\eta \ll 1$ is small the stresses exerted on the elastic layer by the fluid are small relative to its elastic stiffness and, consequently, only small deformations of the elastic layer occur. In the special case when $\eta = 0$ the elastic layer is rigid. When $\eta \gg 1$ is large the stresses exerted on the elastic layer by the fluid are large relative to its elastic stiffness and, consequently, the pressure in the fluid layer can readily deform the elastic layer.

At leading order in the limit $\epsilon \to 0$ equation (2.38) is simply the load condition

$$L = -\frac{2\pi}{\eta}\int_0^\infty \left.\frac{\partial U_z}{\partial z}\right|_{z=\tilde{h}(t)+1+H(r)} r\,\mathrm{d}r. \tag{2.40}$$

2.4.5 Boundary and Initial Conditions

At leading order in the limit $\epsilon \to 0$ the non-dimensionalised versions of the boundary conditions (2.11)–(2.17) and (2.20)–(2.22) are

$$U_r = U_z = 0 \quad \text{on} \quad z = \tilde{h}(t) + 1 + H(r), \tag{2.41}$$

$$\frac{\partial U_r}{\partial z} = 0, \quad \frac{\partial U_z}{\partial z} = -\eta p \quad \text{on} \quad z = \tilde{h}(t) + H(r), \tag{2.42}$$

$$v_r = 0, \quad v_z = \frac{\partial h}{\partial t} \quad \text{on} \quad z = h, \tag{2.43}$$

$$v_z = u_z \quad \text{on} \quad z = 0, \tag{2.44}$$

$$P = p \quad \text{on} \quad z = 0, \tag{2.45}$$

$$\frac{k^{1/2}}{\alpha}\frac{\partial v_r}{\partial z} = v_r - \delta u_r \quad \text{on} \quad z = 0, \tag{2.46}$$

$$u_z = 0 \quad \text{on} \quad z = -1, \tag{2.47}$$

$$p \to 0 \quad \text{as} \quad r \to \infty, \tag{2.48}$$

$$\frac{\partial p}{\partial r} = 0 \quad \text{at} \quad r = 0, \tag{2.49}$$

respectively. A new dimensionless parameter δ has been introduced on the right-hand side of (2.46) so that it can be reduced to the non-dimensionalised version of (2.19), i.e. $v_r = 0$ on $z = 0$, by letting $\alpha \to \infty$ and setting $\delta = 0$; otherwise $\delta = 1$. In dimensionless form the initial conditions (2.23) and (2.24) are

$$p(r, 0) = \mathcal{P}_0(r) \tag{2.50}$$

and

$$\tilde{h}(0) = d, \tag{2.51}$$

respectively, where we have defined $d = H_{\mathrm{f}}/H_{\mathrm{p}}$.

2.5 Unsteady Reynolds Equation

2.5.1 Solution for the Pore Pressure P and Darcy Velocities $\mathbf{u} = (u_r, 0, u_z)$

Equation (2.31) shows immediately that, since the fluid layer is thin, the leading order fluid pressure is independent of z, i.e. $p = p(r,t)$. Solving the leading order version of (2.33), namely $\partial^2 P/\partial z^2 = 0$, subject to the boundary conditions (2.45) and (2.47) using (2.32) shows that the leading order pore pressure is also independent of z, i.e. $P = P(r,t)$, and hence that at leading order (but not at higher order) the two pressures are the same, i.e. $P(r,t) \equiv p(r,t)$. The variation of P with z appears at first order in ϵ^2, and so seeking a solution to (2.33) in the form

$$P = p(r,t) + \epsilon^2 P_1(r,z,t) + O(\epsilon^4) \tag{2.52}$$

and applying the no-penetration condition (2.47) yields

$$\frac{\partial P_1}{\partial z} = -\frac{(1+z)}{r}\frac{\partial}{\partial r}\left(r\frac{\partial p}{\partial r}\right). \tag{2.53}$$

Substituting (2.52) and (2.53) into (2.32) yields

$$\mathbf{u} = (u_r, 0, u_z) = k\left(-\frac{\partial p}{\partial r}, 0, \frac{(1+z)}{r}\frac{\partial}{\partial r}\left(r\frac{\partial p}{\partial r}\right)\right). \tag{2.54}$$

2.5.2 Solution for the Displacement $\mathbf{U} = (U_r, 0, U_z)$

Solving (2.36) and (2.37) for U_r and U_z subject to the boundary conditions (2.41) and (2.42) yields

$$U_r = 0, \tag{2.55}$$

$$U_z = \eta\left(\tilde{h}(t) + 1 + H(r) - z\right)p. \tag{2.56}$$

Since the elastic layer is thin it is deformed only vertically, the vertical displacements being proportional to the fluid pressure p and decreasing linearly from a maximum value of

$$U_z|_{z=\tilde{h}(t)+H(r)} = \eta p, \tag{2.57}$$

on the interface between the fluid layer and the elastic layer at $z = h$ to a minimum value of $U_z|_{z=\tilde{h}(t)+1+H(r)} = 0$ on the interface between the elastic layer and the bearing. Substituting (2.57) into (2.8) we have that in terms of the fluid pressure p the fluid layer thickness h is given by

$$h(r,t) = \tilde{h}(t) + H(r) + \eta p(r,t). \tag{2.58}$$

Furthermore, substituting (2.56) into (2.40) we have that, in terms of the fluid pressure p, the load condition is

$$L(t) = 2\pi \int_0^\infty p(r,t) r \, dr. \tag{2.59}$$

2.5.3 Solution for the Fluid Velocity $\mathbf{v} = (v_r, 0, v_z)$

Solving (2.27) and (2.30) for v_r and v_z subject to the boundary conditions (2.43a), (2.44) and (2.46) using (2.54) yields

$$v_r = -\frac{(h-z)\left[(\alpha h + k^{1/2})z + k^{1/2}(h + 2\delta\alpha k^{1/2})\right]}{2(\alpha h + k^{1/2})}\frac{\partial p}{\partial r}, \tag{2.60}$$

$$v_z = \frac{\mathcal{F}(h,z)}{12r(\alpha h + k^{1/2})}\frac{\partial}{\partial r}\left(r\frac{\partial p}{\partial r}\right), \tag{2.61}$$

where

$$\mathcal{F}(h,z) = 2(\alpha h + k^{1/2})(6k - z^3) + 3\alpha(h^2 - 2\delta k)z^2 + 6k^{1/2}h(h + 2\delta\alpha k^{1/2})z. \tag{2.62}$$

Substituting (2.61) into (2.43b) we obtain the unsteady Reynolds equation

$$\frac{\partial h}{\partial t} = \frac{1}{12r}\frac{\partial}{\partial r}\left(\frac{r\left[h^2(\alpha h^2 + 4k^{1/2}h + 6\delta\alpha k) + 12k(\alpha h + k^{1/2})\right]}{\alpha h + k^{1/2}}\frac{\partial p}{\partial r}\right), \tag{2.63}$$

where the fluid layer thickness h is given by (2.58), which, subject to the load condition (2.59), the pressure boundary conditions (2.48) and (2.49), and the initial conditions (2.50) and (2.51), determines the pressure $p = p(r,t)$ and the minimum of the undeformed interface between the fluid layer and the elastic layer $\tilde{h} = \tilde{h}(t)$.

2.6 Streamfunction

The streamfunction $\psi = \psi(r,z,t)$ (non-dimensionalised with $VlH_{\mathrm{p}} = L_0H_{\mathrm{p}}^3/\mu l^2$) satisfies

$$v_r = -\frac{1}{r}\frac{\partial \psi}{\partial z}, \quad v_z = \frac{1}{r}\frac{\partial \psi}{\partial r} \tag{2.64}$$

in the fluid layer $0 \leq z \leq h$, and

$$u_r = -\frac{1}{r}\frac{\partial \psi}{\partial z}, \quad u_z = \frac{1}{r}\frac{\partial \psi}{\partial r} \tag{2.65}$$

in the porous bed $-1 \leq z \leq 0$, and the boundary conditions

$$\psi = 0 \quad \text{on} \quad z = -1, \quad \lim_{z \to 0^+} \psi = \lim_{z \to 0^-} \psi. \tag{2.66}$$

Solving (2.64) and (2.65) for ψ subject to the boundary conditions (2.66) yields

$$\psi = \frac{r\mathcal{F}(h,z)}{12(\alpha h + k^{1/2})}\frac{\partial p}{\partial r} \tag{2.67}$$

in the fluid layer $0 \leq z \leq h$, where $\mathcal{F}(h,z)$ is given by (2.62), and

$$\psi = kr(1+z)\frac{\partial p}{\partial r} \tag{2.68}$$

in the porous bed $-1 \leq z \leq 0$.

2.7 Fluid Particle Paths

The path $(r,z) = (r(t), z(t))$ taken by a fluid particle, initially situated at the point (r_0, z_0) (where $r_0 \geq 0$ and $-1 \leq z_0 \leq h(r_0, 0)$) is governed by the ordinary differential equations

$$\frac{\mathrm{d}r}{\mathrm{d}t} = v_r, \quad \frac{\mathrm{d}z}{\mathrm{d}t} = v_z \tag{2.69}$$

in the fluid layer $0 \leq z \leq h$, and

$$\frac{\mathrm{d}r}{\mathrm{d}t} = \frac{u_r}{\phi}, \quad \frac{\mathrm{d}z}{\mathrm{d}t} = \frac{u_z}{\phi} \tag{2.70}$$

in the porous bed $-1 \leq z \leq 0$.

Chapter 3

Squeeze-film Flow between a Flat Bearing and a Porous Bed

In this Chapter we consider the axisymmetric squeeze-film flow of a thin layer of Newtonian fluid filling the cylindrical gap between a flat bearing (i.e. the special case when the bearing shape $H(r) \equiv 0$) of radius $\mathcal{R}$ moving under a prescribed load $L = L(t)$ and a thin stationary porous bed of uniform thickness H_{p} bonded to an impermeable surface (see Figure 3.1). The equations governing the fluid pressure $p = p(r,t)$ and the fluid layer thickness $h = h(t) = h_{\min}(t)$ were derived in Chapter 2. In this special case, since the fluid layer thickness $h = h(t)$ is a function of t only the Reynolds equation (2.63) governing the fluid pressure $p = p(r,t)$ simplifies to

$$\frac{\mathrm{d}h}{\mathrm{d}t} = \frac{h^2(\alpha h^2 + 4k^{1/2}h + 6\delta\alpha k) + 12k(\alpha h + k^{1/2})}{12r(\alpha h + k^{1/2})}\frac{\partial}{\partial r}\left(r\frac{\partial p}{\partial r}\right). \tag{3.1}$$

Furthermore, since the bearing is of a finite (dimensional) radius $r = \mathcal{R}$ the boundary condition (2.48) is applied at the finite (dimensionless) radius $r = 1$, i.e.

$$p = 0 \quad \text{at} \quad r = 1, \tag{3.2}$$

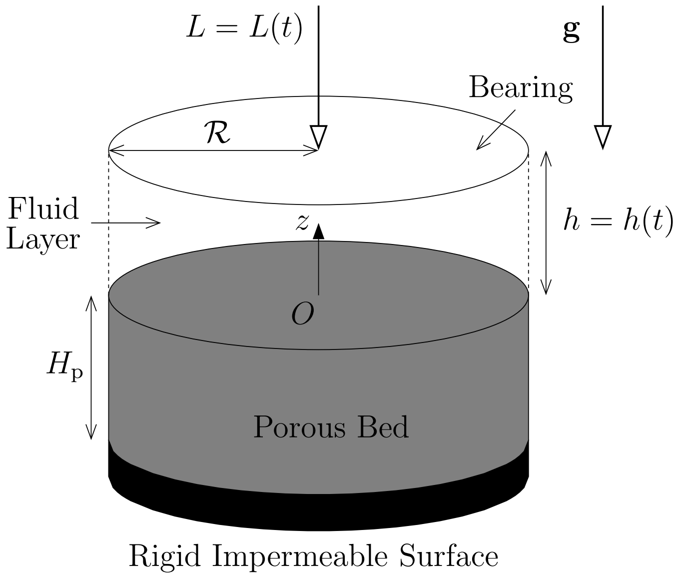

Figure 3.1: The geometry of the axisymmetric problem

and the load condition (2.59) becomes

$$L = 2\pi \int_0^1 p\, r\, \mathrm{d}r. \tag{3.3}$$

In §3.1 the Reynolds equation (3.1) and the load condition (3.3) are solved subject to the boundary conditions (2.49) and (3.2) and the initial condition (2.51) yielding a simple explicit solution for the fluid pressure $p = p(r, t)$ (§3.1.1) and a semi-analytic explicit solution for $t(h)$ in terms of an integral that is evaluated numerically (§3.1.2). It is shown that, in contrast to the case when the bed is impermeable (see, for example, Stefan [63], Reynolds [50] and Stone [66]), the fluid layer thickness h always reaches zero in a finite contact time t_c, i.e. the bearing and the porous bed contact in a finite time, and in §3.1 a semi-analytic explicit solution for the contact time t_c is obtained in terms of an integral that is evaluated numerically. Furthermore, leading order solutions for the contact time t_c that are valid in the limits of small permeability $k \to 0$ and large permeability $k \to \infty$

are calculated in §3.2.1 and §3.3.1, respectively, these solutions being expressed in terms of elementary functions. In particular, it is shown that to leading order in the limit of small permeability $k \to 0$ the contact time t_c is the same for all three choices of boundary condition (2.17)–(2.19).

The fluid particle paths (r, z) of fluid particles initially situated in the fluid layer and fluid particles initially situated in the porous bed are also calculated numerically in §3.1.4, and the extent to which the fluid particles initially situated in the fluid layer/porous bed penetrate into the porous bed (the penetration depth z_pen) is also calculated. Asymptotic solutions for the fluid particle paths (r, z) and penetration depth z_pen that are valid in the limits of small permeability $k \to 0$ and large permeability $k \to \infty$ are calculated in §3.2.2 and §3.3.2, respectively.

Similar problems have been considered by other authors (see, for example, Wu [76, 77], Prakash and Vij [47, 48] and Lin *et al.* [33]). However, these authors were primarily concerned with the effect of the permeability and velocity slip on the interface between the fluid and porous layers on the time-height (t-h) relationship and did not explicitly calculate the contact time t_c. In addition they did not calculate the fluid particle paths and penetration depths. Furthermore, asymptotic limits likely to be of practical interest, in particular the limit of small permeability $k \to 0$, were not investigated.

The squeeze-film flow described in this Chapter is axisymmetric, but the corresponding two-dimensional problem is also of some interest and is treated in Appendix A. In particular, as we show in Appendix A, the solutions for the fluid layer thickness $h = h(t)$ and the fluid particle paths (x, y) may be readily obtained from the corresponding solutions in the axisymmetric case.

3.1 General Solution

3.1.1 Fluid Pressure and Velocities

Integrating the unsteady Reynolds equation (3.1) twice with respect to r and applying the pressure boundary conditions (3.2) and (2.49) we obtain

$$p = -\frac{3(\alpha h + k^{1/2})(1 - r^2)}{h^2(\alpha h^2 + 4k^{1/2}h + 6\delta\alpha k) + 12k(\alpha h + k^{1/2})}\frac{\mathrm{d}h}{\mathrm{d}t}. \tag{3.4}$$

Applying the load condition (3.3) yields a separable first-order ordinary differential equation for the fluid layer thickness $h = h(t)$:

$$L(t) = -\frac{3\pi(\alpha h + k^{1/2})}{2\left[h^2(\alpha h^2 + 4k^{1/2}h + 6\delta\alpha k) + 12k(\alpha h + k^{1/2})\right]}\frac{\mathrm{d}h}{\mathrm{d}t}. \tag{3.5}$$

Re-arranging (3.5) for $\mathrm{d}h/\mathrm{d}t$ and substituting into (3.4) reveals that the pressure is simply

$$p = \frac{2(1 - r^2)L(t)}{\pi}, \tag{3.6}$$

showing that the pressure is parabolic in r and independent of k, and that its only temporal dependence is via that of the load $L(t)$. Substituting (3.6) into (2.54) shows that the Darcy velocity is given by

$$\mathbf{u} = (u_r, 0, u_z) = \frac{4L(t)k}{\pi}(r, 0, -2(1 + z)), \tag{3.7}$$

which is independent of both α and δ, and so is the same for all three choices of boundary condition (2.17)–(2.19). Substituting (3.6) into (2.60) and (2.61) shows that the fluid velocity is given by $\mathbf{v} = (v_r, 0, v_z)$, where

$$v_r = \frac{2L(t)(h - z)\left[(\alpha h + k^{1/2})z + k^{1/2}(h + 2\delta\alpha k^{1/2})\right]r}{\pi(\alpha h + k^{1/2})} \tag{3.8}$$

and

$$v_z = -\frac{2L(t)\mathcal{F}(h,z)}{3\pi(\alpha h + k^{1/2})}, \tag{3.9}$$

where $\mathcal{F}(h,z)$ is given by (2.62). In particular, (3.7)–(3.9) show that both u_r and v_r are linear in r, but that both u_z and v_z are independent of r.

3.1.2 Fluid Layer Thickness and Contact Time

Integrating (3.5) from 0 to t and imposing the initial condition (2.51) yields an implicit solution for the fluid layer thickness $h = h(t)$:

$$\int_0^t L(\tau)\,\mathrm{d}\tau = \frac{3\pi}{2}\int_h^d \frac{\alpha s + k^{1/2}}{s^2(\alpha s^2 + 4k^{1/2}s + 6\delta\alpha k) + 12k(\alpha s + k^{1/2})}\,\mathrm{d}s. \tag{3.10}$$

For simplicity in the remainder of the present work, we concentrate on the case of constant (dimensional) load $L = L_0 > 0$, corresponding to taking the constant (dimensionless) load to be equal to unity, i.e. $L_0 = 1$, without loss of generality. We shall, however, retain the constant (dimensionless) load L_0 explicitly in what follows for clarity of presentation.

In the case of constant load $L = L_0$ equation (3.10) yields an explicit expression for the time $t = t(h)$ taken for the fluid layer to reduce to a thickness h:

$$t(h) = \frac{3\pi}{2L_0}\int_h^d \frac{\alpha s + k^{1/2}}{s^2(\alpha s^2 + 4k^{1/2}s + 6\delta\alpha k) + 12k(\alpha s + k^{1/2})}\,\mathrm{d}s. \tag{3.11}$$

In the special case in which the bed is impermeable, i.e. when $k = 0$, the fluid layer thickness $h = h(t)$ is given explicitly by

$$h = \left(\frac{3\pi d^2}{3\pi + 4d^2 L_0 t}\right)^{1/2}, \tag{3.12}$$

so that

$$h \sim \left(\frac{3\pi}{4L_0 t}\right)^{1/2} \to 0^+ \quad \text{as} \quad t \to \infty, \tag{3.13}$$

i.e. an infinite time is required to squeeze all of the fluid out of the fluid layer (see, for example, Stone [66]).

In the general case $k \neq 0$ the integral in (3.11) was evaluated numerically using the `int` tool (with its default numerical method) in the computer algebra and numerical analysis package MAPLE. (Note that the integral in (3.11) may, in principle, be evaluated analytically, though this involves the zeros of the quartic expression appearing in the denominator of the integrand. These zeros may, in principle, be found using standard formulae; however, in practice, they are very unwieldy and so we always evaluated the integral numerically.)

Figure 3.2(a) shows plots of h as a function of $\ln t$ for different values of the permeability k. Figure 3.2(a) shows that, as expected, increasing k decreases the time taken for the fluid layer to reduce to a thickness h. Figure 3.2(a) also shows that when the bed is permeable, i.e. when $k \neq 0$, the bearing always makes contact with the porous bed in a finite time. This finite contact time is denoted by t_c, and is given by setting $h = 0$ in (3.11) to yield

$$t_c = \frac{3\pi}{2L_0} \int_0^d \frac{\alpha s + k^{1/2}}{s^2(\alpha s^2 + 4k^{1/2}s + 6\delta\alpha k) + 12k(\alpha s + k^{1/2})} \, \mathrm{d}s. \tag{3.14}$$

Figure 3.2(b) shows a plot of $\ln t_c$ as a function of $\ln k$. Figure 3.2(b) shows that, in agreement with Figure 3.2(a), increasing k decreases the contact time t_c. (In fact, it will be shown in §3.2.1 that $t_c = O(k^{-2/3}) \gg 1$ in the limit $k \to 0$ and in §3.3.1 that $t_c = O(k^{-1}) \ll 1$ in the limit $k \to \infty$.)

While the effect of varying the permeability k is relatively straightforward to understand, the effect of varying the Beavers–Joseph constant α is more subtle. Figure

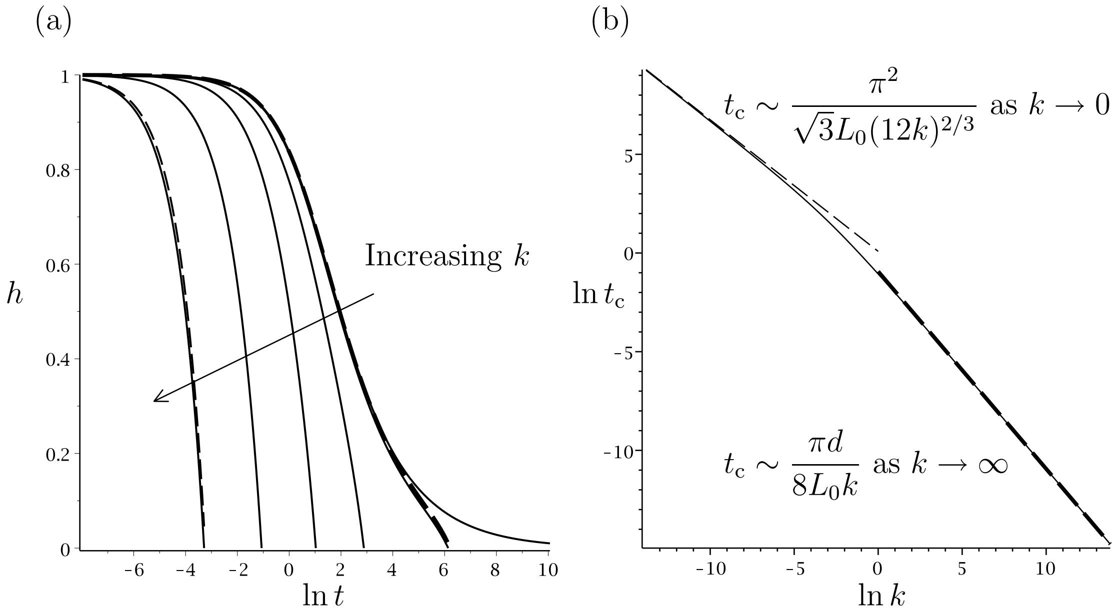

Figure 3.2: (a) Plots of the fluid layer thickness h as a function of $\ln t$ given by (3.11) for $k = 0$, 10^{-4}, 10^{-2}, 10^{-1}, 1 and 10 (solid lines), the uniformly valid leading order small-k asymptotic solution (3.59) for $k = 10^{-4}$ (bold dashed line) and the leading order large-k asymptotic solution (3.87) for $k = 10$ (dashed line). (b) Plots of $\ln t_c$ as a function of $\ln k$ given by (3.14) (solid line), the leading order small-k asymptotic solution (3.58) (dashed line) and the leading order large-k asymptotic solution (3.89) (bold dashed line). In all of the plots $\alpha = 1$

3.3 shows plots of h as a function of t for different values of α for two values of k. In particular, Figure 3.3(a) shows that for a "small" value of k (specifically $k = 10^{-2}$) as α increases the time taken for the fluid layer to reduce to a thickness h increases, whereas Figure 3.3(b) shows that for a "large" value of k (specifically $k = 5$) as α increases the time taken for the fluid layer to reduce to a thickness h decreases. This qualitative change in behaviour is confirmed by the analysis of the asymptotic limits $k \to 0$ and $k \to \infty$ given subsequently in §3.2 and §3.3, respectively.

To understand the physical reason why varying the Beavers–Joseph constant α has a qualitatively different effect for small and large values of the permeability k it is instructive to examine the radial fluid velocity v_r and the radial Darcy

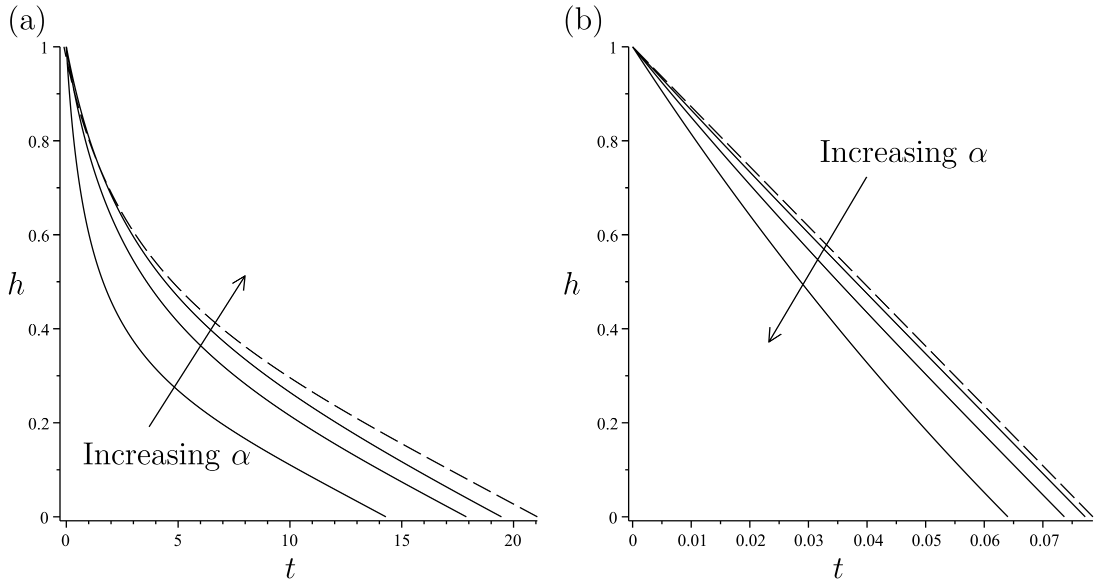

Figure 3.3: (a) Plots of the fluid layer thickness h as a function of t given by (3.11) for $\alpha = 10^{-2}$, $\alpha = 1$ and $\alpha = 100$ with $k = 10^{-2}$ (solid lines) and the uniformly valid leading order small-k asymptotic solution (3.59) with $k = 10^{-2}$ (dashed line). (b) Plots of h as a function of t given by (3.11) for $\alpha = 10^{-2}$, $\alpha = 1$ and $\alpha = 100$ with $k = 5$ (solid lines) and the leading order large-k asymptotic solution (3.87) with $k = 5$ (dashed line)

velocity u_r. Figure 3.4 shows plots of v_r as a function of z for $0 \leq z \leq h$ and of u_r as a function of z for $-1 \leq z \leq 0$ for different values of α for three values of the permeability k. (Note that all of the plots shown in Figure 3.4, and also all of those shown subsequently in Figure 3.5, are for the same value of the fluid layer thickness, namely $h = 1/2$, and so are therefore not at the same instant t.) Figure 3.4(a) shows the flow in the special case in which the bed is impermeable, i.e. when $k = 0$ and hence $l_{\mathrm{s}} = 0$, in which case there is, of course, no flow in the porous bed and no-slip between the fluid and the porous bed at the interface $z = 0$. Figures 3.4(b) and 3.4(c) show the flow for different values of α for a "small" (specifically $k = 10^{-2}$) and a "large" (specifically $k = 10$) value of the permeability k, respectively. Note that, since u_r is independent of both α and z, there is only a single uniform velocity profile in the porous bed in Figures 3.4(b) and 3.4(c).

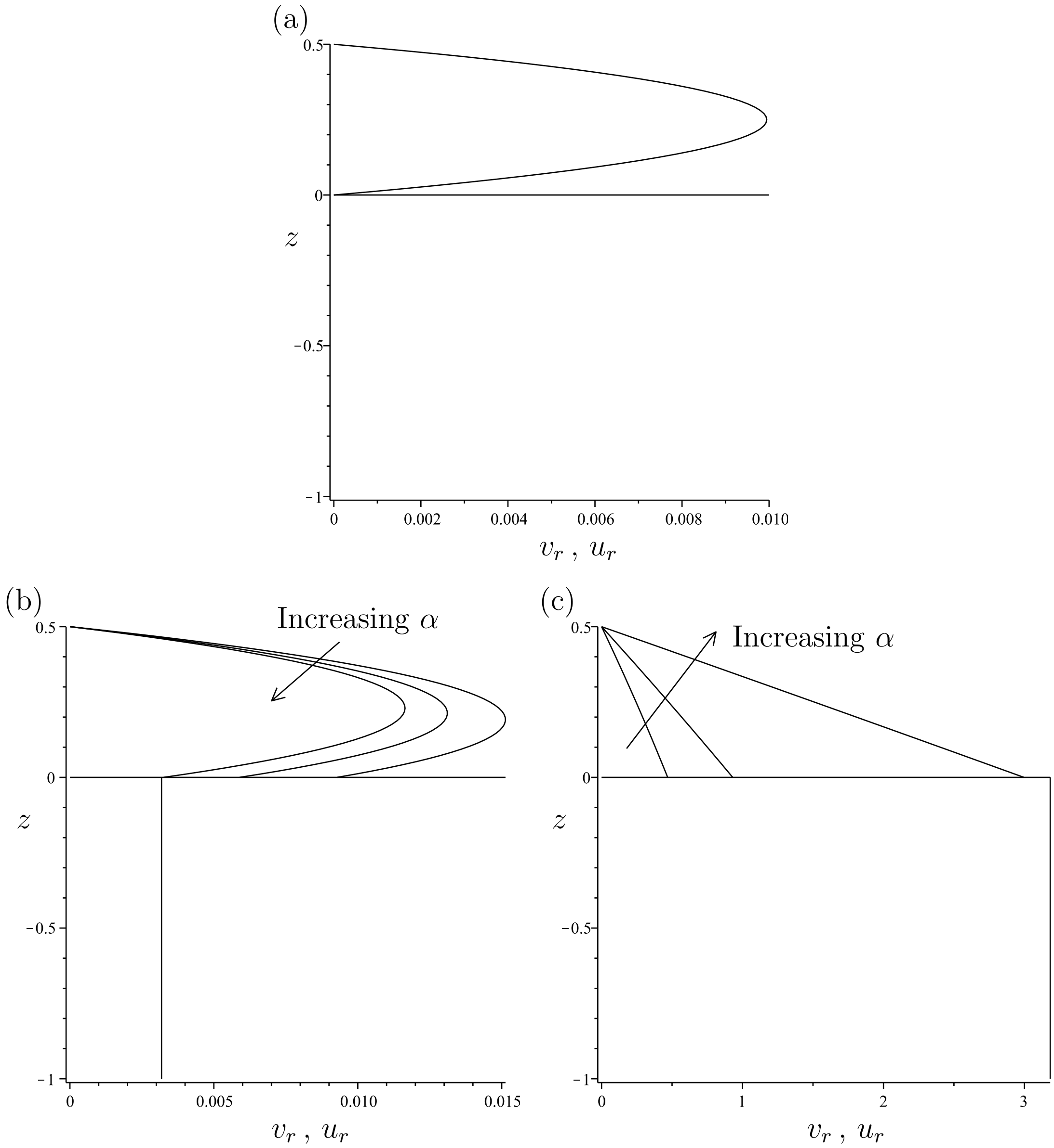

Figure 3.4: Plots of the radial fluid velocity v_r as a function of z for $0 \leq z \leq h$ and of the radial Darcy velocity u_r as a function of z for $-1 \leq z \leq 0$ at $r = 1/4$ when $h = 1/2$ for $\alpha = 1$, 2.5 and 100 with (a) $k = 0$, (b) $k = 10^{-2}$ and (c) $k = 10$

These figures also clearly show the effect of velocity slip at the interface $z = 0$, and that the fastest flow is in the fluid layer for small k but in the porous bed for large k. In particular, Figure 3.4(b) shows that when k is small increasing α (i.e. decreasing the slip length l_{s}) decreases v_r and hence decreases the fluid volume flux out of the fluid layer into the region beyond $r = 1$, denoted by Q_{out} and given by

$$Q_{\text{out}} = 2\pi \int_0^h v_r\, r\big|_{r=1}\, \mathrm{d}z = \frac{2L_0 h^2(\alpha h^2 + 4k^{1/2}h + 6\delta\alpha k)}{3(\alpha h + k^{1/2})}. \tag{3.15}$$

Since the fluid volume flux into the porous bed, denoted by Q_{bed} and given by

$$Q_{\text{bed}} = 2\pi \int_0^1 v_z\, r\big|_{z=0}\, \mathrm{d}r = -8L_0 k, \tag{3.16}$$

is constant and independent of α, this decrease in Q_{out} causes the time taken for the fluid layer to reduce to a thickness h to increase, consistent with the behaviour for small k shown in Figure 3.3(a). On the other hand, Figure 3.4(c) shows that when k is large increasing α (i.e. decreasing the slip length l_{s}) increases v_r and hence increases Q_{out}, causing the time taken for the fluid layer to reduce to a thickness h to decrease, consistent with the behaviour for large k shown in Figure 3.3(b).

3.1.3 Instantaneous Streamlines

Substituting (3.6) into (2.67) and (2.68), we deduce that the streamfunction $\psi = \psi(r, z, t)$ is given by

$$\psi = -\frac{r^2 \mathcal{F}(h, z) L_0}{3\pi(\alpha h + k^{1/2})} \tag{3.17}$$

in the fluid layer $0 \leq z \leq h$, where $\mathcal{F}(h, z)$ is again given by (2.62), and

$$\psi = -\frac{4kr^2(1 + z)L_0}{\pi} \tag{3.18}$$

in the porous bed $-1 \leq z \leq 0$. Figure 3.5 shows plots of the instantaneous streamlines for three values of the permeability k. Figure 3.5(a) shows the streamlines in the special case in which the bed is impermeable, i.e. when $k = 0$, in which

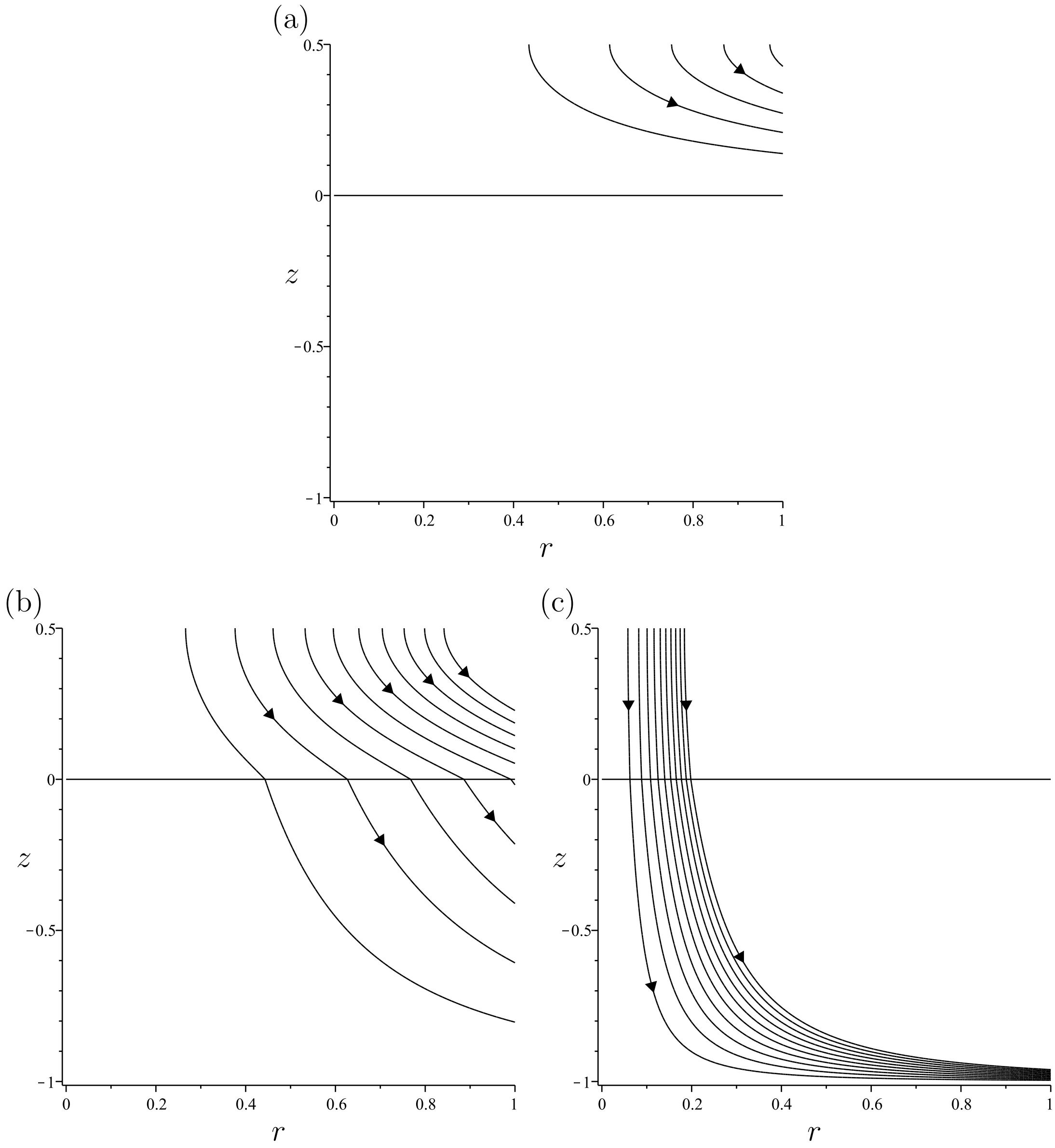

Figure 3.5: Plots of the instantaneous streamlines $\psi = \text{constant} = -j/4 \times 10^{-2}$ for $j = 1, 2, \ldots, 10$ with ψ given by (3.17) for $0 \leq z \leq h$ and (3.18) for $-1 \leq z < 0$ when $h = 1/2$ for (a) $k = 0$, (b) $k = 10^{-2}$ and (c) $k = 1/2$. In all of the plots $\alpha = 1$

case there is, of course, no flow in the porous bed. Figures 3.5(b) and 3.5(c) show the streamlines for two non-zero values of the permeability k. In particular, they show that when the bed is permeable the vertical fluid velocity v_z on the interface $z = 0$ (which is given by $v_z|_{z=0} = u_z|_{z=0} = -8L_0k/\pi$) is always negative, and hence that fluid always flows from the fluid layer into the porous bed and never flows the other way. They also show that as k increases so do Q_{out} and Q_{bed}, and hence that the contact time t_{c} decreases, consistently with the behaviour shown in Figure 3.2.

3.1.4 Fluid Particle Paths and Penetration Depths

Substituting (3.7), (3.8) and (3.9) into (2.69) and (2.70), and using (3.5) to eliminate t, we deduce that the differential equations that govern the path (r, z) taken by a fluid particle are

$$\frac{1}{r}\frac{\mathrm{d}r}{\mathrm{d}h} = -\frac{3(h-z)\left[(\alpha h + k^{1/2})z + k^{1/2}(h + 2\delta\alpha k^{1/2})\right]}{h^2(\alpha h^2 + 4k^{1/2}h + 6\delta\alpha k) + 12k(\alpha h + k^{1/2})}, \tag{3.19}$$

$$\frac{\mathrm{d}z}{\mathrm{d}h} = \frac{\mathcal{F}(h, z)}{h^2(\alpha h^2 + 4k^{1/2}h + 6\delta\alpha k) + 12k(\alpha h + k^{1/2})} \tag{3.20}$$

in the fluid layer $0 \le z \le h$, where $\mathcal{F}(h, z)$ is again given by (2.62), and

$$\frac{1}{r}\frac{\mathrm{d}r}{\mathrm{d}h} = -\frac{6k(\alpha h + k^{1/2})}{\phi\left[h^2(\alpha h^2 + 4k^{1/2}h + 6\delta\alpha k) + 12k(\alpha h + k^{1/2})\right]}, \tag{3.21}$$

$$\frac{1}{1+z}\frac{\mathrm{d}z}{\mathrm{d}h} = \frac{12k(\alpha h + k^{1/2})}{\phi\left[h^2(\alpha h^2 + 4k^{1/2}h + 6\delta\alpha k) + 12k(\alpha h + k^{1/2})\right]} \tag{3.22}$$

in the porous bed $-1 \le z \le 0$, subject to the initial conditions

$$r = r_0 \quad \text{and} \quad z = z_0 \quad \text{when} \quad t = 0, \quad \text{i.e.} \quad \text{when} \quad h = d. \tag{3.23}$$

Integrating (3.21) and (3.22) subject to (3.23) shows that the particle paths in the porous bed are given by

$$\left(\frac{r}{r_0}\right)^2 = \frac{1+z_0}{1+z} = \exp\left[-\frac{12k}{\phi}\int_d^h \frac{\alpha s + k^{1/2}}{s^2(\alpha s^2 + 4k^{1/2}s + 6\delta\alpha k) + 12k(\alpha s + k^{1/2})}\,\mathrm{d}s\right], \tag{3.24}$$

and so, in particular, always satisfy $r^2(1+z) = r_0^2(1+z_0) = \text{constant}$.

Figure 3.6 shows the paths (r, z) taken by several fluid particles from their initial positions (r_0, z_0) at $t = 0$ for three values of the permeability k.

In the special case in which the bed is impermeable, i.e. when $k = 0$, equations (3.19) and (3.20) may be solved exactly subject to (3.23) to yield

$$r = r_0\left(\frac{4d(d-z_0)z_0 + (d-2z_0)^2 h}{d^2 h}\right)^{3/4}, \tag{3.25}$$

$$z = \frac{h}{2}\left[1 - (d-2z_0)\left(\frac{h}{4d(d-z_0)z_0 + (d-2z_0)^2 h}\right)^{1/2}\right] \tag{3.26}$$

for $z_0 \geq 0$. Figure 3.6(a) shows the paths of several fluid particles in this case and, in particular, shows that all of the fluid particles eventually flow out of the fluid layer into the region beyond $r = 1$.

In the general case $k \neq 0$ the differential equations (3.19)–(3.22) were solved numerically using the `dsolve` tool (with its default numerical method) in MAPLE subject to (3.23). Figures 3.6(b) and 3.6(c) show the paths of several fluid particles for two non-zero values of the permeability k. In particular, they show that fluid particles initially in the fluid layer can either flow out of the fluid layer into the region beyond $r = 1$ or flow into the porous bed and then, in some cases, out of the porous bed into the region beyond $r = 1$. Since the vertical Darcy velocity $u_z = -8L_0k(1+z)/\pi$ is less than or equal to zero, fluid particles that enter the porous bed never re-enter the fluid layer, and fluid particles that are initially in

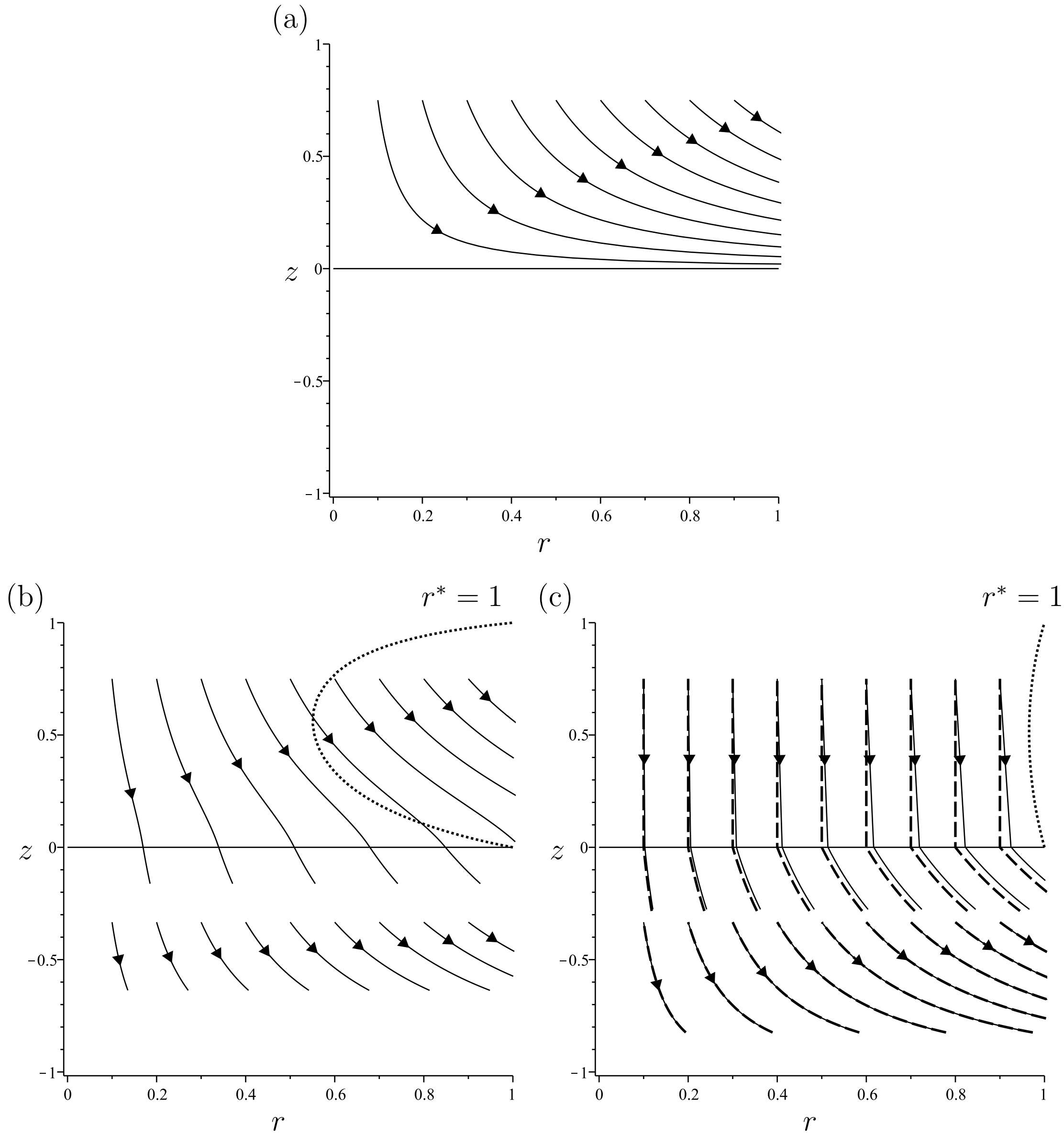

Figure 3.6: Plots of fluid particle paths (r, z) with r and z given by (a) (3.25) and (3.26) for $(r_0, z_0) = (0.1, 0.75)$, $(0.2, 0.75)$, $\ldots$, $(0.9, 0.75)$, (b,c) (3.19)–(3.22) subject to $(r_0, z_0) = (0.1, 0.75)$, $(0.2, 0.75)$, $\ldots$, $(0.9, 0.75)$ and $(r_0, z_0) = (0.1, -1/3)$, $(0.2, -1/3)$, $\ldots$, $(0.9, -1/3)$ for (b) $k = 10^{-2}$ and (c) $k = 10$ (solid lines) and the leading order large-k asymptotic solutions (3.92), (3.96), (3.97), (3.99) and (3.100) (dashed lines) for $\alpha = 1$ and $\phi = 3/4$. Parts (b) and (c) also include plots of the curve $r^* = 1$ (dotted lines)

the porous bed never enter the fluid layer. Figures 3.6(b) and 3.6(c) also show that as k increases then v_z increases relative to v_r so that the flow in the fluid layer is increasingly directed towards the porous bed, and consequently the fraction of the fluid particles initially in the fluid layer that flow into the porous bed increases. Fluid particles initially in the fluid layer that enter the porous bed do so by crossing the interface $z = 0$ at some point $(r^*, 0)$, where $r^* = r^*(r_0, z_0)$, at $t = t^*$ corresponding to $h = h(t^*) = h^*$, and so the critical curve that divides the region of particles that enter the porous bed (with $r^* < 1$) from the region of those that do not is given by $r^* = 1$. The curve $r^* = 1$ is found by solving (3.19) and (3.20) subject to $r = 1$ and $z = 0$ at $h = h^*$ backwards in time, i.e. from $h = h^*$ to $h = d$. Evaluating the solution for (r, z) when $h = d$ yields the initial position (r_0, z_0) of the fluid particle that passes through the point $(r, z) = (1, 0)$ when $h = h^*$. Repeating this procedure for $0 \leq h^* \leq d$ yields the curve $r^* = 1$. Figures 3.6(b) and 3.6(c) include plots of the curve $r^* = 1$ calculated in this way and confirm that fluid particles that initially lie to the left of $r^* = 1$ flow from the fluid layer into the porous bed, and the fluid particles that initially lie to the right of $r^* = 1$ flow out of the fluid layer into the region beyond $r = 1$. Figure 3.7 shows plots of the curve $r^* = 1$ for different values of the permeability k. In particular, Figure 3.7 shows that as k increases the curve $r^* = 1$ moves to the right, i.e. less fluid flows out of the fluid layer into the region beyond $r = 1$ and more fluid flows into the porous bed.

Also of considerable practical interest are the depths to which fluid particles (which may be initially situated in either the fluid layer or the porous bed) penetrate into the porous bed, denoted by z_{pen} and given by $z_{\text{pen}} = z(t_{\text{c}}) < 0$. Since both v_z and u_z are independent of r, z_{pen} is independent of r_0. However, the value of r_0 does affect whether or not a fluid particle flows into the region beyond $r = 1$. Figure 3.8(a) shows plots of $\ln |z_{\text{pen}}|$ as a function of $\ln k$ for "small" values of the permeability k for three fluid particles initially situated in the fluid layer with $r_0 = O(k^{1/4})$.

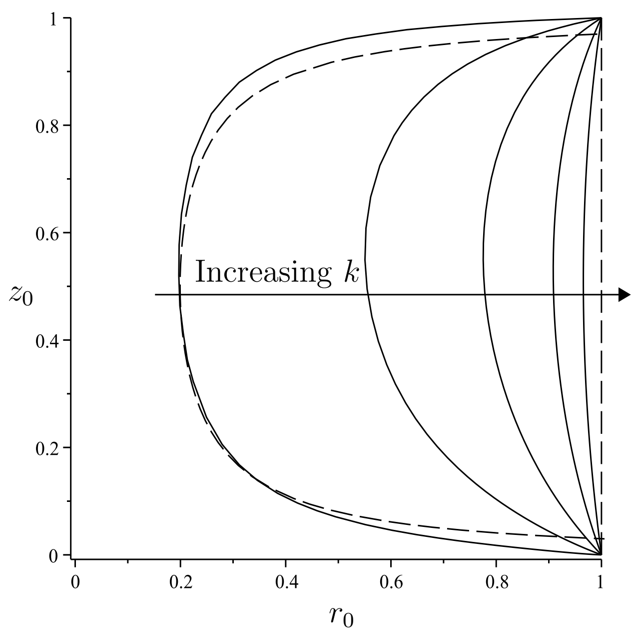

Figure 3.7: Plots of the critical curve $r^* = 1$ which divides the region of particles that enter the porous bed (with $r^* < 1$) from those that do not (with $r^* > 1$) for $k = 10^{-4}$, 10^{-2}, 10^{-1}, 1 and 10 (solid lines), the leading order small-k asymptotic solution (3.70) for $k = 10^{-4}$ (dashed line) and the leading order large-k asymptotic solution $r_0 = 1$ (dashed line). In all of the plots $\alpha = 1$

In particular, Figure 3.8(a) shows that $|z_{\text{pen}}|$ decreases as k decreases and/or z_0 increases. Moreover, the effect of z_0 on z_{pen} becomes less pronounced as k decreases. (In fact, it will be shown in §3.2.2 that at leading order in the limit of small permeability $k \to 0$ the penetration depth $z_{\text{pen}} = O(k^{1/3}) \ll 1$ of a fluid particle initially situated in the fluid layer with $r_0 = O(k^{1/4})$ is small and independent of z_0.) Figure 3.8(b) shows plots of z_{pen} as a function of $\ln k$ for "large" values of the permeability k for three fluid particles initially situated in the fluid layer. In particular, Figure 3.8(b) shows that again $|z_{\text{pen}}|$ decreases as k decreases and/or z_0 increases. However, in this case, the effect of k on z_{pen} becomes less pronounced as k increases. (In fact, it will be shown in §3.3.2 that at leading order in the limit $k \to \infty$ the penetration depth $z_{\text{pen}} = O(1)$ of a fluid particle initially situated in the fluid layer is independent of k and its magnitude decreases monotonically

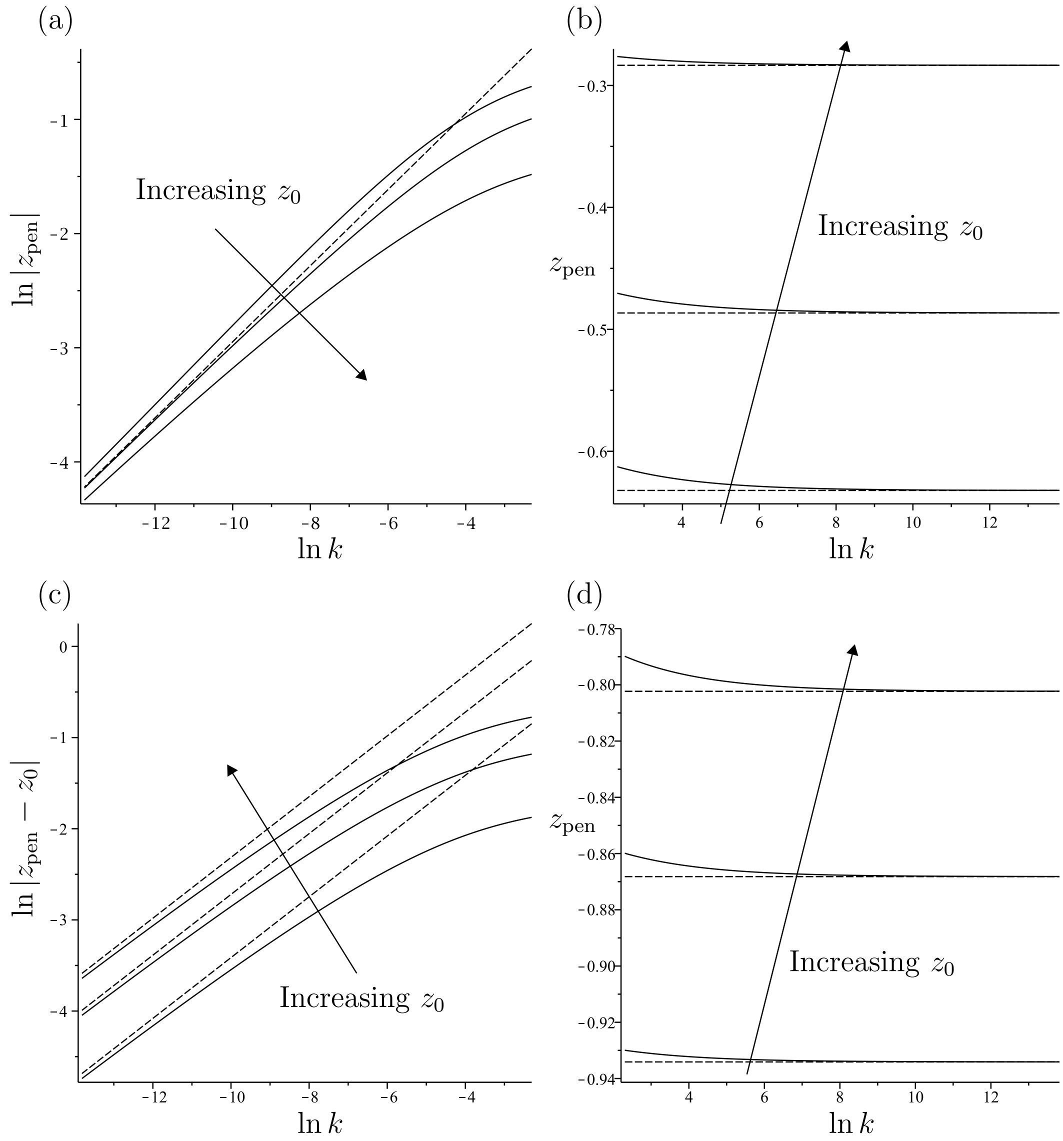

Figure 3.8: (a) Plots of $\ln |z_{\text{pen}}|$ as a function of $\ln k$ given by (3.19)–(3.22) subject to $(r_0, z_0) = (0.5 \times (12k)^{1/4}, 0.25)$, $(0.5 \times (12k)^{1/4}, 0.5)$ and $(0.5 \times (12k)^{1/4}, 0.75)$ (solid lines) and the leading order small-k asymptotic solution given by (3.75) (dashed line). (b) Plots of z_{pen} as a function of $\ln k$ given by (3.19)–(3.22) subject to $(r_0, z_0) = (0.5, 0.25)$, $(0.5, 0.5)$ and $(0.5, 0.75)$ (solid lines) and the leading order large-k asymptotic solution given by (3.98) (dashed lines). (c) Plots of $\ln |z_{\text{pen}} - z_0|$ as a function of $\ln k$ given by (3.21) and (3.22) subject to $(r_0, z_0) = (0.5, -0.25), (0.5, -0.5)$ and $(0.5, -0.75)$ (solid lines) and the leading order small-k asymptotic solution given by (3.80) (dashed lines). (d) Plots of z_{pen} as a function of $\ln k$ given by (3.21) and (3.22) subject to $(r_0, z_0) = (0.5, -0.25), (0.5, -0.5)$ and $(0.5, -0.75)$ (solid lines) and the leading order large-k asymptotic solution given by (3.101) (dashed lines). In all of the plots $\alpha = 1$ and $\phi = 3/4$

as z_0 increases.) Figure 3.8(c) shows plots of $\ln|z_{\text{pen}} - z_0|$ as a function of $\ln k$ for "small" values of the permeability k for three fluid particles initially situated in the porous bed. In particular, Figure 3.8(c) shows that $|z_{\text{pen}} - z_0|$ decreases as k decreases and/or z_0 decreases. (In fact, it will be shown in §3.2.2 that at leading order in the limit $k \to 0$ the magnitude of the relative penetration depth $|z_{\text{pen}} - z_0| = O(k^{1/3}) \ll 1$ of a fluid particle initially situated in the porous bed is small and decreases monotonically as z_0 decreases.) Figure 3.8(d) shows plots of z_{pen} as a function of $\ln k$ for "large" values of the permeability k for three fluid particles initially situated in the porous bed. In particular, Figure 3.8(d) shows that, as in Figure 3.8(b), $|z_{\text{pen}}|$ decreases as k decreases and/or z_0 increases. Moreover, the effect of k on z_{pen} becomes less pronounced as k increases. (In fact, it will be shown in §3.3.2 that at leading order in the limit of large permeability $k \to \infty$ the penetration depth $z_{\text{pen}} = O(1)$ of a fluid particle initially situated in the porous bed is independent of k and its magnitude decreases monotonically as z_0 increases.)

As we have already seen, there is qualitatively different behaviour for small and large values of the permeability k, and so in §3.2 and §3.3 we investigate the asymptotic behaviour of the solution in the limits $k \to 0$ and $k \to \infty$, respectively, in detail.

3.2 Limit of Small Permeability $k \to 0$

In this section asymptotic solutions for the fluid layer thickness $h = h(t)$ (§3.2.1) and the fluid particle paths (r, z) (§3.2.2) in the limit of small permeability $k \to 0$ are obtained.

In this limit it will transpire that the contact time $t_c = O(k^{-2/3}) \gg 1$ is large, and a regular perturbation solution for $h = h(t)$ in powers of $k^{1/2} \ll 1$ turns out to be valid only for "short" times $t = O(1)$ (more precisely, for $t = o(k^{-1/2})$), and additional asymptotic solutions valid for "intermediate" times $t = O(k^{-1/2})$ and "long" times $t = O(k^{-2/3})$ are required in order to obtain a complete description of the behaviour up to the contact time.

3.2.1 Asymptotic Solution for the Fluid Layer Thickness and Contact Time

3.2.1.1 Solution for "Short" Times $t = O(1)$

Seeking a regular perturbation solution to (3.5) with $L = L_0$ of the form

$$h(t) = h_0(t) + k^{1/2}h_1(t) + kh_2(t) + O(k^{3/2}), \tag{3.27}$$

at $O(1)$, $O(k^{1/2})$ and $O(k)$ we have

$$\frac{\mathrm{d}h_0}{\mathrm{d}t} = -\frac{2L_0 h_0^3}{3\pi}, \tag{3.28}$$

$$\frac{\mathrm{d}h_1}{\mathrm{d}h_0} - \frac{3}{h_0}h_1 = \frac{3}{\alpha h_0}, \tag{3.29}$$

$$\frac{\mathrm{d}h_2}{\mathrm{d}h_0} - \frac{3}{h_0}h_2 = \frac{3\left[h_0(\alpha^2 h_1^2 + 2\alpha h_1 + 2\delta\alpha^2 - 1) + 4\alpha^2\right]}{\alpha^2 h_0^3}, \tag{3.30}$$

respectively, where t has been eliminated from (3.29) and (3.30) using (3.28). Solving (3.28)–(3.30) subject to the initial conditions $h_0(0) = d$, $h_1(0) = 0$ and $h_2(0) = 0$ yields the solutions

$$h_0 = \left(\frac{3\pi d^2}{3\pi + 4d^2 L_0 t}\right)^{1/2}, \tag{3.31}$$

$$h_1 = -\frac{(d^3 - {h_0}^3)}{\alpha d^3}, \tag{3.32}$$

$$h_2 = \frac{3\left[5{h_0}^7 + (5\delta\alpha^2 d^2 + 8\alpha^2 d - 10d^2){h_0}^5 + 5(1-\delta\alpha^2)d^6 h_0 - 8\alpha^2 d^6\right]}{10\alpha^2 d^6 {h_0}^2}. \tag{3.33}$$

The leading order solution for h_0 given by (3.31) is simply the solution for an impermeable bed given by (3.12), i.e., as expected, the porous bed is effectively impermeable at leading order. The effect of permeability first appears at first order and, since h_1 given by (3.32) is negative for all $t > 0$, its effect is, as expected, to decrease the time t taken for the fluid layer to reduce to a thickness h. However, since

$$h_0 \sim \left(\frac{3\pi}{4L_0 t}\right)^{1/2} \to 0^+, \quad h_1 \to -\frac{1}{\alpha}, \quad h_2 \sim -\frac{16L_0 t}{5\pi} \to -\infty \quad \text{as} \quad t \to \infty, \tag{3.34}$$

the expansion (3.27) is not uniformly valid for all t. Comparing the leading and first order terms suggests that the expansion remains uniformly valid provided that

$$t \ll \frac{\alpha^2}{L_0 k}, \quad \text{i.e.} \quad t = o(k^{-1}). \tag{3.35}$$

However, comparing the first and second order terms shows that in fact the expansion remains uniformly valid only provided that

$$t \ll \frac{1}{L_0 \alpha k^{1/2}}, \quad \text{i.e.} \quad t = o(k^{-1/2}), \tag{3.36}$$

and hence a second asymptotic solution valid for "intermediate" times $t = O(k^{-1/2})$ for which $h = O(k^{1/4})$ is necessary.

3.2.1.2 Solution for "Intermediate" Times $t = O(k^{-1/2})$

For "intermediate" times $t = O(k^{-1/2})$ we re-scale t and h according to

$$t = k^{-1/2}\hat{t}, \quad h = k^{1/4}\hat{h}, \tag{3.37}$$

where $\hat{t}$ and $\hat{h}$ are $O(1)$ in the limit $k \to 0$. Seeking a regular perturbation solution to (3.5) with $L = L_0$ of the form

$$\hat{h}(\hat{t}) = \hat{h}_0(\hat{t}) + k^{1/4}\hat{h}_1(\hat{t}) + O(k^{1/2}), \tag{3.38}$$

at $O(1)$ and $O(k^{1/4})$ we have

$$\frac{\mathrm{d}\hat{h}_0}{\mathrm{d}\hat{t}} = -\frac{2L_0\hat{h}_0^3}{3\pi}, \tag{3.39}$$

$$\frac{\mathrm{d}\hat{h}_1}{\mathrm{d}\hat{h}_0} - \frac{3}{\hat{h}_0}\hat{h}_1 = \frac{3(4\alpha + \hat{h}_0^2)}{\alpha\hat{h}_0^3}, \tag{3.40}$$

respectively. Solving (3.39) and (3.40) subject to the appropriate matching conditions with the solution at "short" times, namely

$$\hat{h}_0 \sim \left(\frac{3\pi}{4L_0\hat{t}}\right)^{1/2} \to \infty, \quad \hat{h}_1 \to -\frac{1}{\alpha} \quad \text{as} \quad \hat{t} \to 0, \tag{3.41}$$

yields the solutions

$$\hat{h}_0 = \left(\frac{3\pi}{4L_0\hat{t}}\right)^{1/2}, \tag{3.42}$$

$$\hat{h}_1 = -\frac{12\alpha + 5\hat{h}_0^2}{5\alpha\hat{h}_0^2}. \tag{3.43}$$

This solution for "intermediate" times is qualitatively similar to that for "short" times. However, since

$$\hat{h}_0 = \left(\frac{3\pi}{4L_0\hat{t}}\right)^{1/2} \to 0^+, \quad \hat{h}_1 \sim -\frac{16L_0\hat{t}}{5\pi} \to -\infty \quad \text{as} \quad \hat{t} \to \infty, \tag{3.44}$$

now the expansion remains uniformly valid provided that

$$\hat{t} \ll \frac{1}{L_0 k^{1/6}}, \quad \text{i.e.} \quad t \ll \frac{1}{L_0 k^{2/3}}, \tag{3.45}$$

and hence a third (and final) asymptotic solution valid for "long" times $t = O(k^{-2/3})$ for which $h = O(k^{1/3})$ is necessary.

3.2.1.3 Solution for "Long" Times $t = O(k^{-2/3})$

For "long" times $t = O(k^{-2/3})$ we re-scale t and h according to

$$t = (12k)^{-2/3}T, \quad h = (12k)^{1/3}H, \tag{3.46}$$

where T and H are $O(1)$ in the limit $k \to 0$ and the factor 12 has been introduced into the scalings for convenience. Seeking a regular perturbation solution to (3.5) with $L = L_0$ of the form

$$H(T) = H_0(T) + (12k)^{1/6}H_1(T) + O(k^{1/3}), \tag{3.47}$$

at $O(1)$ and $O(k^{1/6})$ we have

$$\frac{\mathrm{d}H_0}{\mathrm{d}T} = -\frac{2L_0(H_0^3+1)}{3\pi}, \tag{3.48}$$

$$\frac{\mathrm{d}H_1}{\mathrm{d}H_0} - \frac{3H_0^2}{H_0^3+1}H_1 = \frac{\sqrt{3}H_0^2}{2\alpha(H_0^3+1)}, \tag{3.49}$$

respectively. Solving (3.48) and (3.49) subject to the appropriate matching conditions with the solution at "intermediate" times, namely

$$H_0 \sim \left(\frac{3\pi}{4L_0T}\right)^{1/2} \to \infty, \quad H_1 \to -\frac{1}{2\sqrt{3}\alpha} \quad \text{as} \quad T \to 0, \tag{3.50}$$

yields the solutions

$$T = \frac{\pi[f(\infty) - f(H_0)]}{2L_0}, \tag{3.51}$$

$$H_1 = -\frac{1}{2\sqrt{3}\alpha}, \tag{3.52}$$

where the function $f = f(H_0)$ is given by

$$f(H_0) = \ln\left(\frac{H_0 + 1}{\sqrt{H_0^2 - H_0 + 1}}\right) + \sqrt{3}\tan^{-1}\left(\frac{2H_0 - 1}{\sqrt{3}}\right) \tag{3.53}$$

and satisfies $f(0) = -\sqrt{3}\pi/6$ and $f(\infty) = \sqrt{3}\pi/2$. Unlike for the solutions for "short" and "intermediate" times, the permeability now appears in the leading order solution and the solution remains uniformly valid up to the contact time $t = t_c$ given by $t_c = (12k)^{-2/3}T_c$, where T_c satisfies $H(T_c) = 0$, and has the asymptotic expansion

$$T_c = T_{c0} + (12k)^{1/6}T_{c1} + O(k^{1/3}), \tag{3.54}$$

where

$$H_0(T_{c0}) = 0, \quad T_{c1} = -\frac{H_1(T_{c0})}{H_0'(T_{c0})}, \tag{3.55}$$

so that

$$T_{c0} = \frac{\pi^2}{\sqrt{3}L_0}, \quad T_{c1} = -\frac{\sqrt{3}\pi}{4L_0\alpha}. \tag{3.56}$$

Expressed in terms of the original variables the asymptotic expansion for the contact time (3.54) is therefore

$$t_{\mathrm{c}} = \frac{\pi^2}{\sqrt{3}L_0(12k)^{2/3}} - \frac{\pi}{8L_0\alpha k^{1/2}} + O(k^{-1/3}). \tag{3.57}$$

In particular, the leading order small-k solution for the contact time given by

$$t_{\mathrm{c}} = \frac{\pi^2}{\sqrt{3}L_0(12k)^{2/3}} \tag{3.58}$$

is independent of both α and δ, and so is the same for all three choices of boundary condition (2.17)–(2.19). Figure 3.2(b) compares the leading order small-k asymptotic solution for t_{c} given by (3.58) with the exact solution given by (3.14). The Beavers–Joseph constant α appears at first order in the asymptotic expansion for t_{c} given by (3.57), and inspection of the first order term reveals that decreasing α (i.e. increasing the slip length l_{s}) decreases the contact time t_{c}, consistent with the behaviour shown in Figure 3.3(a).

3.2.1.4 A Uniformly Valid Leading Order Composite Solution for $t(h)$

A uniformly valid leading order composite solution for $t = t(h)$ is

$$t(h) = -\frac{3\pi}{4d^2L_0} + (12k)^{-2/3}T\left(\frac{h}{(12k)^{1/3}}\right), \tag{3.59}$$

where T is given by (3.51). Figures 3.2(a) and 3.3(a) compare the uniformly valid leading order small-k asymptotic solution for $t = t(h)$ given by (3.59) with the exact solution for $t = t(h)$ given by (3.11). (Note that setting $h = d$ in (3.59) yields $t(d) = O(k)$ as $k \to 0$, so that (3.59) satisfies the initial condition (2.51) at leading order in the limit $k \to 0$. Similarly, setting $h = 0$ in (3.59) yields

$t(0) \sim \pi^2/\sqrt{3}L_0(12k)^{2/3}$ as $k \to 0$, so that (3.59) coincides with (3.58) at leading order in the limit $k \to 0$.)

3.2.2 Asymptotic Solution for the Fluid Particle Paths and Penetration Depths

3.2.2.1 Fluid Particles Initially Situated in the Fluid Layer $z_0 > 0$

The analysis in §3.2.1 shows that in the limit of small permeability $k \to 0$ the porous bed is effectively impermeable for "short" and "intermediate" times, i.e. for $t = o(k^{-2/3})$, and so at leading order the paths of fluid particles initially situated in the fluid layer (i.e. with $z_0 > 0$) are given by the solution for an impermeable bed given by (3.25) and (3.26). When $t = O(k^{-2/3})$ and $h = O(k^{1/3})$ the solution for an impermeable bed yields

$$r \sim r_0 \left(\frac{4(d - z_0)z_0}{dh} \right)^{3/4} = O\left(\frac{r_0((d - z_0)z_0)^{3/4}}{k^{1/4}} \right), \tag{3.60}$$

$$z \sim \frac{h}{2} = O(k^{1/3}), \tag{3.61}$$

showing that only those fluid particles whose initial positions are close to the axis $r = 0$ (specifically, those with $r_0 = O(k^{1/4})$) or are close to either the porous bed or the bearing (specifically, those with $z_0 = O(k^{1/3})$ or $d - z_0 = O(k^{1/3})$, respectively) have not flowed out of the fluid layer into the region beyond $r = 1$ at "long" times. In order to analyse the path of a fluid particle initially situated in the fluid layer close to the axis $r = 0$ with $r_0 = O(k^{1/4})$ and $z_0 > 0$ when $t = O(k^{-2/3})$ and $h = O(k^{1/3})$, we re-scale r_0, z, t and h according to

$$r_0 = (12k)^{1/4}R_0, \quad z = (12k)^{1/3}Z, \quad t = (12k)^{-2/3}T, \quad h = (12k)^{1/3}H, \tag{3.62}$$

where R_0, Z, T and H are $O(1)$ in the limit $k \to 0$ and the factor 12 has again been introduced into the scalings for convenience.

From (3.19) and (3.20) the leading order equations for the path of a fluid particle in the fluid layer are

$$\frac{1}{r}\frac{\mathrm{d}r}{\mathrm{d}H} = -\frac{3(H-Z)Z}{H^3+1}, \tag{3.63}$$

$$\frac{\mathrm{d}Z}{\mathrm{d}H} = \frac{-2Z^3+3HZ^2+1}{H^3+1}. \tag{3.64}$$

The solutions to (3.63) and (3.64) must match with the $h \to 0$ limits of (3.25) and (3.26) as $H \to \infty$, namely

$$r \sim R_0\left(\frac{4(d-z_0)z_0}{dH}\right)^{3/4} \to 0 \quad \text{as} \quad H \to \infty, \tag{3.65}$$

$$Z \sim \frac{H}{2} \to \infty \quad \text{as} \quad H \to \infty. \tag{3.66}$$

The leading order vertical position of the fluid particle $Z(T)$, which is independent of the initial height of the fluid particle z_0, was obtained numerically by posing (3.64) as an initial value problem by shooting from the value $Z = 0$ at the unknown value of the fluid layer thickness $H = H^*$ at which the fluid particle crosses the interface $Z = 0$ to $Z = H_\infty/2$ at some large value $H = H_\infty \gg 1$ approximating the matching condition (3.66) to within a prescribed tolerance, namely 10^{-6}. This procedure yielded the solution $H^* \simeq 0.4958$ corresponding to $T = T^* = T(H^*)$, which from (3.46) and (3.51) corresponds to the time

$$t = t^* = (12k)^{-2/3}T(H^*) \simeq \frac{0.6540}{L_0 k^{2/3}}. \tag{3.67}$$

The leading order radial position of the fluid particle $R(T)$ is calculated by integrating (3.63) from $H = H^*$ to H to obtain $r = r^* g(H)$, where $r = r^*$ is again

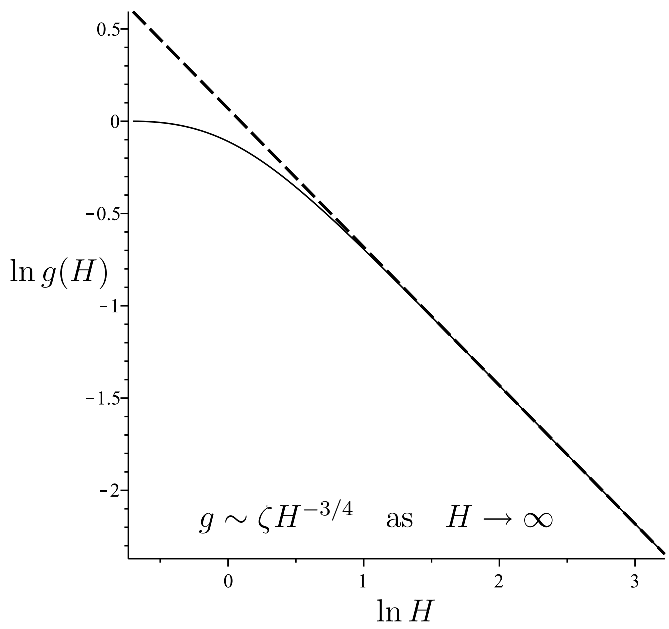

Figure 3.9: Plots of $\ln g(H)$ as a function of $\ln H$ given by (3.68) (solid line) and its large-H asymptotic behaviour $g \sim \zeta H^{-3/4}$, where $\zeta \simeq 1.0708$, (dashed line)

the radial position at which the fluid particle crosses the interface $Z = 0$ and the function $g = g(H)$ is defined by

$$g(H) = \exp\left[-3\int_{H^*}^{H} \frac{(s-Z)Z}{s^3+1}\,\mathrm{d}s\right]. \tag{3.68}$$

Figure 3.9 shows a plot of $\ln g(H)$ as a function of $\ln H$ together with its large-H asymptotic behaviour $g \sim \zeta H^{-3/4}$ where $\zeta \simeq 1.0708$ as $H \to \infty$. Imposing the matching condition (3.65) yields

$$r^* = \frac{R_0}{\zeta}\left(\frac{4(d-z_0)z_0}{d}\right)^{3/4}. \tag{3.69}$$

In particular, the leading order solution for the critical curve $r^* = 1$ is therefore given by

$$r_0 = \zeta\left(\frac{d}{4(d-z_0)z_0}\right)^{3/4}(12k)^{1/4}. \tag{3.70}$$

Figure 3.7 compares the leading order small-k asymptotic solution (3.70) with the exact solution for $r^* = 1$ for $k = 10^{-4}$. In particular, it shows that the asymptotic solution compares favourably with the exact solution when $z_0 = O(1)$. However, as Figure 3.7 also shows, the asymptotic solution fails for $z_0 = O(k^{1/3}) \ll 1$ and for $d - z_0 = O(k^{1/3}) \ll 1$, i.e. for fluid particles that are initially close to either the porous bed or the bearing; for brevity these cases are not considered further here. From (3.21) and (3.22) the leading order equations for the path of a fluid particle after it has entered the porous bed at $r = r^*$ are

$$\frac{\mathrm{d}R}{\mathrm{d}H} = -\frac{r^*}{2\phi(H^3+1)}, \tag{3.71}$$

$$\frac{\mathrm{d}Z}{\mathrm{d}H} = \frac{1}{\phi(H^3+1)}, \tag{3.72}$$

where we have written $r = r^* + (12k)^{1/3}R$. Solving (3.71) and (3.72) subject to the initial conditions $R = 0$ and $Z = 0$ at $H = H^*$ yields

$$r = r^*\left(1 + \frac{[f(H^*) - f(H)](12k)^{1/3}}{6\phi}\right), \tag{3.73}$$

$$z = -\frac{[f(H^*) - f(H)](12k)^{1/3}}{3\phi} \tag{3.74}$$

for $0 \leq H < H^*$, where the function $f = f(H)$ is given by (3.53) and satisfies $f(H^*) \simeq 0.5381$, showing that the fluid particle remains close to $r = r^*$ and $z = 0$. In particular, setting $H = 0$ in (3.74) shows that the leading order asymptotic solution for z_{pen} is

$$z_{\mathrm{pen}} = -\frac{[f(H^*) - f(0)](12k)^{1/3}}{3\phi} \simeq -\frac{1.1027k^{1/3}}{\phi}, \tag{3.75}$$

which depends on k but is independent of z_0. Figure 3.8(a) compares the leading order small-k asymptotic solution for z_{pen} given by (3.75) with the exact solution.

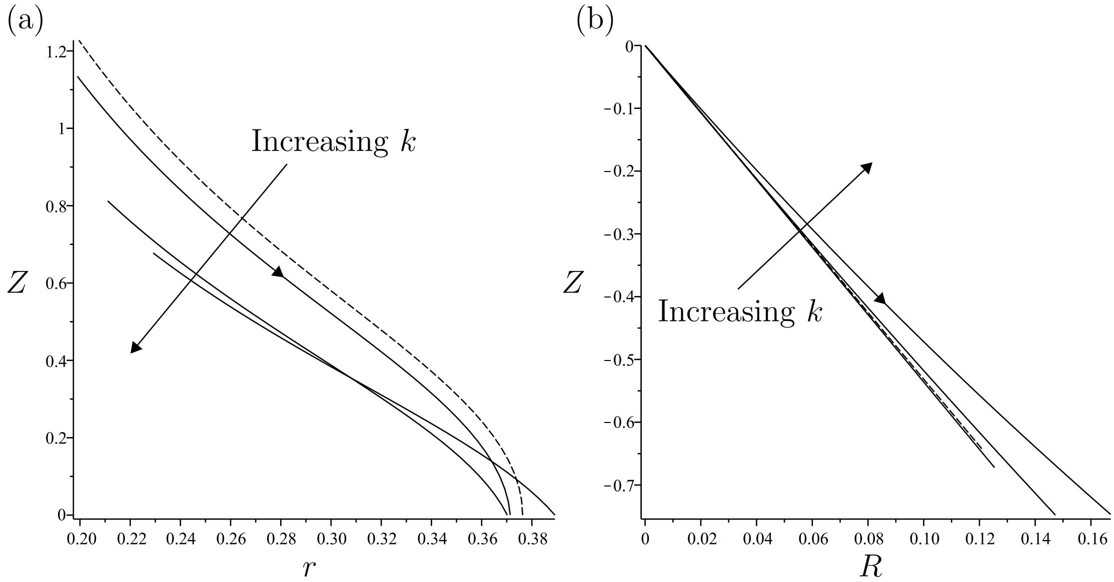

Figure 3.10: (a) Plots of the scaled fluid particle paths (r, Z) in the fluid layer where $Z = z/(12k)^{1/3}$ given by (3.19)–(3.22) subject to $(r_0, z_0) = (0.5 \times (12k)^{1/4}, 0.25)$ for $k = 10^{-3}$, 10^{-4} and 10^{-8} (solid lines) and the leading order small-k asymptotic solution given by $r = r^* g(H)$ and the numerical solution of (3.64) for $H \geq H^*$ (dashed line). (b) Plots of the scaled fluid particle paths (R, Z) in the porous bed where $R = (r - r^*)/(12k)^{1/3}$ and $Z = z/(12k)^{1/3}$ given by (3.19)–(3.22) subject to $(r_0, z_0) = (0.5 \times (12k)^{1/4}, 0.25)$ for $k = 10^{-3}$, 10^{-4} and 10^{-8} and the leading order small-k asymptotic solution given by (3.73) and (3.74) for $0 \leq H < H^*$ (dashed line). In all of the plots $\alpha = 1$ and $\phi = 3/4$

Figure 3.10 compares the scaled fluid particle paths in (a) the fluid layer and (b) the porous bed with the leading order small-k asymptotic solution given by $r = r^* g(H)$ and the numerical solution of (3.64) for $H \geq H^*$, and by (3.73) and (3.74) for $0 \leq H < H^*$.

3.2.2.2 Fluid Particles Initially Situated in the Porous Bed $z_0 < 0$

As we have already seen, the analysis in §3.2.1 shows that in the limit of small permeability $k \to 0$ the porous bed is effectively impermeable for "short" and "intermediate" times, i.e. for $t = o(k^{-2/3})$, and so at leading order fluid particles initially situated in the porous bed (i.e. with $z_0 < 0$) remain close to their initial positions, specifically

$$r = r_0\left(1+\frac{3(d^2-h^2)k}{\phi d^2 h^2}\right), \tag{3.76}$$

$$z = z_0-(1+z_0)\frac{6(d^2-h^2)k}{\phi d^2 h^2}. \tag{3.77}$$

For "long" times, i.e. for $t = O(k^{-2/3})$, a similar analysis to that described previously in §3.2.2.1 yields

$$r = r_0\left(1+\frac{[f(\infty)-f(H)](12k)^{1/3}}{6\phi}\right), \tag{3.78}$$

$$z = z_0-(1+z_0)\frac{[f(\infty)-f(H)](12k)^{1/3}}{3\phi}, \tag{3.79}$$

$$z_{\text{pen}} = z_0-(1+z_0)\frac{[f(\infty)-f(0)](12k)^{1/3}}{3\phi} = z_0-\frac{2\pi(1+z_0)(12k)^{1/3}}{3\sqrt{3}\phi}, \tag{3.80}$$

which depends on k and z_0. Figure 3.8(c) compares the leading order small-k asymptotic solution for z_{pen} given by (3.80) with the exact solution.

3.3 Limit of Large Permeability $k \to \infty$

In this section asymptotic solutions for the fluid layer thickness $h = h(t)$ (§3.3.1) and the fluid particle paths (r, z) (§3.3.2) in the limit of large permeability $k \to \infty$ are obtained.

In this limit it will transpire that the contact time $t_c = O(k^{-1}) \ll 1$ is small, and, unlike in the limit of small permeability $k \to 0$ described in §3.2, a regular perturbation expansion for $h(t)$ in powers of $k^{-1/2} \ll 1$ is uniformly valid up to the contact time, making this limit somewhat easier to analyse.

3.3.1 Asymptotic Solution for the Fluid Layer Thickness and Contact Time

Since the contact time $t_c = O(k^{-1})$ we re-scale time t according to

$$t = k^{-1}T, \tag{3.81}$$

where T is $O(1)$ in the limit $k \to \infty$. Seeking a regular perturbation solution to (3.5) with $L = L_0$ of the form

$$h(T) = h_0(T) + k^{-1/2}h_1(T) + O(k^{-1}), \tag{3.82}$$

at $O(1)$ and $O(k^{-1/2})$ we have

$$\frac{\mathrm{d}h_0}{\mathrm{d}T} = -\frac{8L_0}{\pi}, \tag{3.83}$$

$$\frac{\mathrm{d}h_1}{\mathrm{d}h_0} = \frac{\delta\alpha h_0^2}{2}, \tag{3.84}$$

respectively. Solving (3.83) and (3.84) subject to the initial conditions $h_0(0) = d$ and $h_1(0) = 0$ yields the solutions

$$h_0 = d - \frac{8L_0T}{\pi}, \tag{3.85}$$

$$h_1 = -\frac{\delta\alpha(d^3 - h_0^3)}{6}. \tag{3.86}$$

Note that, unlike in the limit of small permeability $k \to 0$, the effect of permeability appears at leading order and the leading order solution h_0 given by (3.85) becomes zero at the finite time $T = T_c = \pi d/8L_0$. Figures 3.2(a) and 3.3(b) compare the leading order large-k asymptotic solution for $h = h(t)$, i.e.

$$h = d - \frac{8L_0kt}{\pi}, \tag{3.87}$$

with the exact solution for $t = t(h)$ given by (3.11). The contact time $t = t_\mathrm{c}$ has the asymptotic expansion

$$t_\mathrm{c} = \frac{\pi d}{8L_0k} - \frac{\pi\delta\alpha d^3}{48L_0k^{3/2}} + O(k^{-2}). \tag{3.88}$$

Figure 3.2(b) compares the leading order large-k asymptotic solution for t_c, i.e.

$$t_\mathrm{c} = \frac{\pi d}{8L_0k}, \tag{3.89}$$

with the exact solution given by (3.14). As for the corresponding result in the limit of small permeability $k \to 0$ given by (3.57), the Beavers–Joseph constant α appears at first order in the large-k asymptotic expansion for t_c given by (3.88), but inspection of the first order term reveals that increasing the slip length l_s now increases (rather than decreases) the contact time t_c, consistent with the behaviour shown in Figure 3.3(b). However, unlike in the limit of small permeability $k \to 0$, the asymptotic expansion for t_c given by (3.88) is not uniformly valid in the limit $\alpha \to \infty$ (i.e. in the special case of zero slip length, $l_\mathrm{s} = 0$) corresponding to the boundary condition (2.18), and so this case is treated separately in Appendix B.

3.3.2 Asymptotic Solution for the Fluid Particle Paths and Penetration Depths

3.3.2.1 Fluid Particles Initially Situated in the Fluid Layer $z_0 > 0$

From (3.19) and (3.20) the leading order equations for the path of a fluid particle in the fluid layer are simply

$$\frac{\mathrm{d}r}{\mathrm{d}h} = 0, \tag{3.90}$$

$$\frac{\mathrm{d}z}{\mathrm{d}h} = 1. \tag{3.91}$$

Solving (3.90) and (3.91) subject to (3.23) yields

$$r = r_0 \quad \text{and} \quad z = h - h^*, \tag{3.92}$$

where $h^* = d - z_0$, showing that (since $v_z = O(k) \gg 1$ is larger than $v_r = O(k^{1/2}) \gg 1$) at leading order the particle moves vertically downwards through the fluid layer, reaching the interface $z = 0$ when $h = h^*$ corresponding to $T = T^* = \pi z_0/8L_0$, which from (3.81) corresponds to the time

$$t = t^* = \frac{\pi z_0}{8L_0 k}. \tag{3.93}$$

In particular, this means that the leading order large-k asymptotic approximation to the curve $r^* = 1$ is simply the straight line $r_0 = 1$. Figure 3.7 compares the straight line $r_0 = 1$ with the exact solution for $r^* = 1$ for $k = 10$.

From (3.21) and (3.22) the leading order equations for the path of a fluid particle after it has entered the porous bed are

$$\frac{1}{r}\frac{\mathrm{d}r}{\mathrm{d}h} = -\frac{1}{2\phi}, \tag{3.94}$$

$$\frac{1}{1+z}\frac{\mathrm{d}z}{\mathrm{d}h} = \frac{1}{\phi}. \tag{3.95}$$

Solving (3.94) and (3.95) subject to the initial conditions $r = r_0$ and $z = 0$ at $h = h^*$ yields

$$r = r_0 \exp\left(\frac{h^* - h}{2\phi}\right), \tag{3.96}$$

$$z = -1 + \exp\left(-\frac{h^* - h}{\phi}\right) \tag{3.97}$$

for $0 \leq h < h^*$. In particular, setting $h = 0$ in (3.97) shows that the leading order asymptotic solution for z_{pen} is

$$z_{\text{pen}} = -1 + \exp\left(-\frac{h^*}{\phi}\right), \tag{3.98}$$

which, in contrast to the corresponding result in the limit of small permeability $k \to 0$ given by (3.75), depends on z_0 (via h^*) but is independent of k. Figure 3.6(c) compares the fluid particle paths (r, z) with the leading order large-k asymptotic solution given by (3.92), (3.96) and (3.97). Figure 3.8(b) compares the leading order large-k asymptotic solution for z_{pen} given by (3.98) with the exact solution.

3.3.2.2 Fluid Particles Initially Situated in the Porous Bed $z_0 < 0$

A similar analysis for fluid particles initially situated in the porous bed (i.e. with $z_0 < 0$) yields

$$r = r_0 \exp\left(\frac{d-h}{2\phi}\right), \tag{3.99}$$

$$z = -1 + (1+z_0)\exp\left(-\frac{d-h}{\phi}\right), \tag{3.100}$$

$$z_{\text{pen}} = -1 + (1+z_0)\exp\left(-\frac{d}{\phi}\right). \tag{3.101}$$

Figure 3.6(c) compares the fluid particle paths (r, z) with the leading order large-k asymptotic solution given by (3.99) and (3.100). Figure 3.8(d) compares the leading order large-k asymptotic solution for z_{pen} given by (3.101) with the exact solution.

3.4 Conclusions

In this Chapter we considered the axisymmetric squeeze-film flow of a thin layer of Newtonian fluid filling the cylindrical gap between a flat bearing moving under a prescribed constant load and a thin stationary porous bed of uniform thickness bonded to an impermeable surface. The Reynolds equation (3.1) that governs the fluid pressure $p = p(r, t)$ and the load condition (3.3) were solved subject to the boundary conditions (2.49) and (3.2) and the initial condition (2.51) yielding a simple explicit solution for the fluid pressure $p = p(r, t)$, given by (3.6), and a semi-analytic explicit solution for the time $t(h)$ taken for the fluid layer thickness to reduce to a value h, given by (3.11), in terms of an integral that was evaluated numerically.

It was shown that, in contrast to the case when the bed is impermeable treated by, for example, Stefan [63], Reynolds [50] and Stone [66], the fluid layer thickness h always reaches zero in a finite contact time t_c given by (3.14), i.e. the bearing and the porous bed contact in a finite time. The contact time t_c was shown to increase as the permeability k of the porous bed decreases. In particular, the contact time t_c was shown to satisfy $t_c = O(k^{-2/3}) \gg 1$ in the limit of small permeability $k \to 0$ and $t_c = O(k^{-1}) \ll 1$ in the limit of large permeability $k \to \infty$. Furthermore, it was shown that for "small" values of k the velocity slip on the interface $z = 0$ between the fluid and porous layers, introduced via the application of the Beavers–Joseph boundary condition (2.17) on this interface, had a negligible effect on the contact time t_c. In fact to leading order in the limit of small permeability $k \to 0$ the contact time t_c, given by (3.58), was shown to be independent of the Beavers-Joseph constant α and identical for all three choices of boundary condition (2.17)–(2.19). However, it was shown that for "large" values of k the velocity slip on the interface $z = 0$ has a non-negligible effect on the contact time t_c. The leading order term in the large-k expansion for the contact time t_c, given by (3.88), was shown to be independent of the Beavers-Joseph constant α. However, this expansion is not valid in the limit $\alpha \to \infty$, i.e. in the case when the slip length $l_s = 0$ corresponding to the boundary condition (2.18), and the (different) leading order large-k solution for the contact time t_c that is valid in this limit is calculated in Appendix B.

The fluid particle paths and penetration depths of fluid particles initially situated in fluid layer and fluid particles initially situated in the porous bed were also calculated. Furthermore, the curve that divides the region of fluid particles initially situated in fluid layer that enter the porous bed from the region of those that do not was also calculated and it was shown that as the permeability k increases more fluid particles flow from the fluid layer into the porous bed. In particular, it was shown that to leading order in the limit of small permeability $k \to 0$ the penetration depth z_{pen} (into the porous bed) of fluid particles initially situated in the fluid layer such that their initial radial position $r_0 = O(k^{1/4})$ satisfies $z_{\text{pen}} = O(k^{1/3}) \ll 1$. Furthermore, the relative penetration depth $z_{\text{pen}} - z_0$ of fluid particles initially situated in the porous bed was shown to satisfy $z_{\text{pen}} - z_0 = O(k^{1/3})$.

Chapter 4

Squeeze-film Flow between a Curved Bearing and a Porous Bed

4.1 Introduction

In Chapter 3 we considered the axisymmetric thin film flow in the gap between a thin stationary porous bed and a flat impermeable bearing of radius $\mathcal{R}$, the bearing moving towards the porous bed under a prescribed constant load. The time $t(h)$ taken for the minimum fluid layer thickness to reduce to a value h and the fluid particle paths were calculated. In particular, it was shown that contact between the bearing and the porous bed always occurs in a finite contact time t_c. In this Chapter we consider the axisymmetric squeeze-film flow in the thin gap between a thin stationary porous bed and a smooth rigid impermeable *curved* (i.e. non-flat) bearing with shape $H \propto r^{2n}$, where n is an integer (see Figure 4.1).

The equations governing the fluid pressure $p = p(r,t)$ and the minimum fluid layer thickness $h_{\min} = h_{\min}(t)$ were derived in Chapter 2. The Reynolds equation

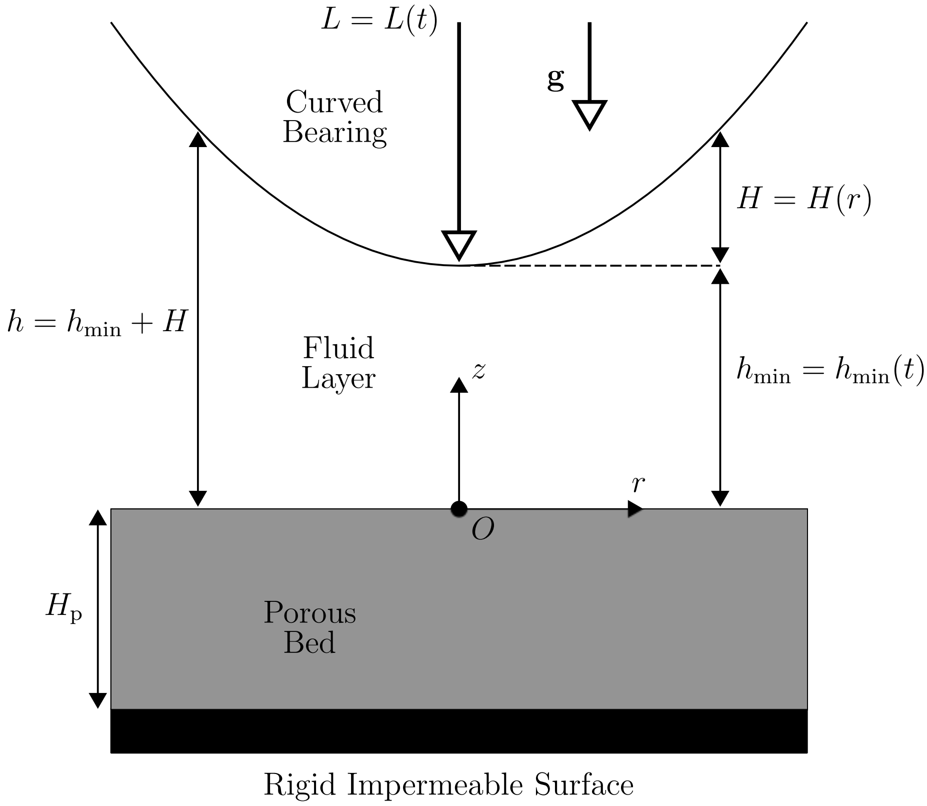

Figure 4.1: The geometry of the axisymmetric problem

governing the fluid pressure p is

$$\frac{\mathrm{d}h_{\min}}{\mathrm{d}t} = \frac{1}{12r}\frac{\partial}{\partial r}\left(\frac{r[h^2(\alpha h^2 + 4k^{1/2}h + 6\delta\alpha k) + 12k(\alpha h + k^{1/2})]}{\alpha h + k^{1/2}}\frac{\partial p}{\partial r}\right), \quad (4.1)$$

where, from (2.58) with $H = r^{2n}$, the fluid layer thickness h is given by

$$h(r,t) = h_{\min}(t) + r^{2n}. \quad (4.2)$$

In §4.2 the Reynolds equation (4.1) and the load condition (2.59) are solved subject to the boundary conditions (2.48) and (2.49) and the initial condition (2.51), yielding semi-analytic explicit solutions for the fluid pressure $p = p(r,t)$ and $t(h_{\min})$ in terms of integrals that are evaluated numerically. It is shown that, in contrast to the case when the bed is impermeable (see Stone [66]), the minimum fluid layer thickness h_{min} always reaches zero in a finite contact time t_{c}, i.e. the bearing and the porous bed contact in a finite time, and in §4.2 a semi-analytic explicit solution for the contact time t_{c} is obtained in terms of a double integral that is evaluated numerically. Furthermore, leading order solutions for the contact time t_{c} that are valid in the limits of small permeability $k \to 0$ and large permeability $k \to \infty$ are calculated in §4.3 and §4.4, respectively, and these solutions are expressed in terms of elementary functions. The paths of fluid particles initially situated in the fluid layer and fluid particles initially situated in the porous bed are also calculated numerically in §4.2, and the extent to which the fluid particles penetrate into the porous bed/fluid layer is determined.

Since solutions for different values of n are compared, in §4.2 the solutions are presented in terms of the dimensionless variables (2.26). (Recall that the scalings used in the non-dimensionalisation (2.26) are independent of n.) The ratio $H_{\mathrm{p}}/\mathcal{R}$ was chosen to be $H_{\mathrm{p}}/\mathcal{R} = 10^{-2}$ in all of the plots presented in this Chapter.

Similar problems have been considered by other authors (see, for example, Goren [24], Nir [42], Davis [20], Stone [66] and Ramon *et al.* [49]). The problem that we consider in this Chapter is a natural extension to the work of Stone [66] (who considered the impermeable case $k = 0$). Furthermore, in order to determine the extent to which fluid particles penetrate into the porous bed/fluid layer, we calculate the fluid particle paths. This aspect (and that of the contact time t_{c}) was not addressed by Goren [24], Nir [42], Davis [20], Stone [66] or Ramon *et al.* [49].

4.2 General Solution

Integrating the unsteady Reynolds equation (4.1) once with respect to r and applying the pressure boundary condition (2.49) we obtain

$$\frac{\partial p}{\partial r} = \frac{6r(\alpha h + k^{1/2})}{h^2(\alpha h^2 + 4k^{1/2}h + 6\delta\alpha k) + 12k(\alpha h + k^{1/2})}\frac{\mathrm{d}h_{\mathrm{min}}}{\mathrm{d}t}, \tag{4.3}$$

where the fluid layer thickness $h = h(r,t)$ is given by (4.2). A further integration, applying the remaining pressure boundary condition (2.48), yields an expression for the fluid pressure $p = p(r,t)$:

$$p = -6\left(\int_r^\infty \frac{\tilde{r}(\alpha h + k^{1/2})}{h^2(\alpha h^2 + 4k^{1/2}h + 6\delta\alpha k) + 12k(\alpha h + k^{1/2})}\,\mathrm{d}\tilde{r}\right)\frac{\mathrm{d}h_{\mathrm{min}}}{\mathrm{d}t}. \tag{4.4}$$

Applying the load condition (2.59) yields a separable first-order ordinary differential equation for the minimum fluid layer thickness $h_{\mathrm{min}} = h_{\mathrm{min}}(t)$:

$$L(t) = -6\pi\left(\int_0^\infty \frac{\tilde{r}^3(\alpha h + k^{1/2})}{h^2(\alpha h^2 + 4k^{1/2}h + 6\delta\alpha k) + 12k(\alpha h + k^{1/2})}\,\mathrm{d}\tilde{r}\right)\frac{\mathrm{d}h_{\mathrm{min}}}{\mathrm{d}t}. \tag{4.5}$$

Integrating (4.5) from 0 to t and imposing the initial condition (2.51) yields an implicit solution for the minimum fluid layer thickness $h_{\mathrm{min}} = h_{\mathrm{min}}(t)$:

$$\int_0^t L(\tau)\,\mathrm{d}\tau = 6\pi\int_{h_{\mathrm{min}}}^d \int_0^\infty \frac{\tilde{r}^3(\alpha h + k^{1/2})}{h^2(\alpha h^2 + 4k^{1/2}h + 6\delta\alpha k) + 12k(\alpha h + k^{1/2})}\,\mathrm{d}\tilde{r}\,\mathrm{d}s, \tag{4.6}$$

For simplicity in the remainder of this Chapter we concentrate on the case of constant (dimensional) load $L = L_0 > 0$, corresponding to taking the constant (dimensionless) load to be equal to unity, i.e. $L_0 = 1$, without loss of generality. Furthermore, in all of the plots presented subsequently in this Chapter we take $d = 1$, corresponding to the initial thickness of the fluid layer H_{f} being the same as the thickness of the porous bed H_{p}. We shall, however, retain the constant (dimensionless) load L_0 and d explicitly in what follows for clarity of presentation.

4.2.1 Minimum Fluid Layer Thickness and Contact Time

In the case of constant load $L = L_0$ equation (4.6) yields an explicit expression for the time $t = t(h_{\min})$ taken for the minimum fluid layer thickness to reduce to a value $h_{\min}$:

$$t(h_{\min}) = \frac{6\pi}{L_0} \int_{h_{\min}}^{d} \int_0^{\infty} \frac{\tilde{r}^3(\alpha h + k^{1/2})}{h^2(\alpha h^2 + 4k^{1/2}h + 6\delta\alpha k) + 12k(\alpha h + k^{1/2})} \, \mathrm{d}\tilde{r} \, \mathrm{d}s. \quad (4.7)$$

In the special case when the bed is impermeable, i.e. when $k = 0$, the minimum fluid layer thickness $h_{\min} = h_{\min}(t)$ is given explicitly by

$$h_{\min} = \begin{cases} d \exp\left(-\dfrac{2L_0}{3\pi} t\right) & \text{when} \quad n = 1, \\ \dfrac{3\pi d}{3\pi + 4dL_0 t} & \text{when} \quad n = 2, \\ \left(d^{-2(n-1)/n} + \dfrac{2n^2 \sin(2\pi/n) L_0}{3\pi^2(n-2)} t\right)^{-n/2(n-1)} & \text{when} \quad n \geq 3, \end{cases} \quad (4.8)$$

so that

$$h_{\min} = \left\{ \begin{array}{ll} O\left(\exp\left(-\dfrac{2L_0}{3\pi} t\right)\right) & \text{when} \quad n = 1 \\ O\left(t^{-n/2(n-1)}\right) & \text{when} \quad n \geq 2 \end{array} \right\} \to 0^+ \quad \text{as} \quad t \to \infty, \quad (4.9)$$

i.e. an infinite amount of time is required for the minimum fluid layer thickness to reduce to zero. The solution for $h_{\min} = h_{\min}(t)$ in the case $k = 0$ given by (4.8) is equivalent[1] to the solution for $h_{\min}$ given by Stone [66], who, recall, considered

[1]Note that in the dimensional solution for $h_{\min} = h_{\min}(t)$ given by Stone [66] (equation 12 in Stone [66]) the exponent of the radius $\mathcal{R}$ is incorrectly given as $3(2n-1)/2n$ when it should in

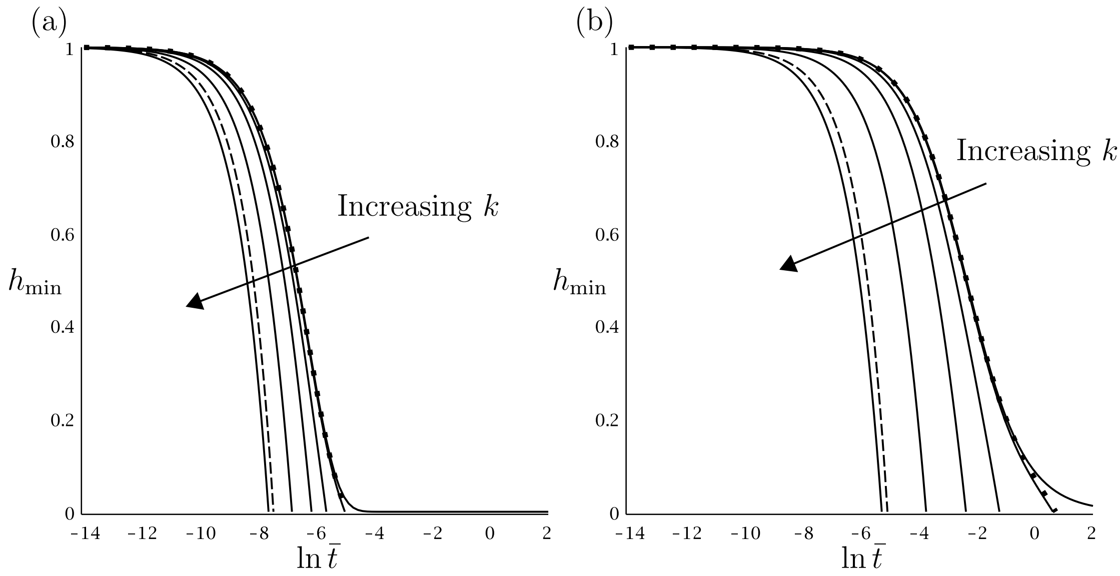

Figure 4.2: (a) Plots of $h_{\min}$ as a function of $\ln \bar{t}$ for (a) $n = 1$ and (b) $n = 2$ given by (4.7) for $k = 0, 10^{-4}, 10^{-2}, 10^{-1}, 1$ and 10 (solid lines), the uniformly valid leading order small-k asymptotic solutions (a) (4.82) and (b) (4.129) for $k = 10^{-4}$ (dotted lines) and the leading order large-k asymptotic solutions (a) (4.145) and (b) (4.153) for $k = 10$ (dashed lines). In all plots $\alpha = 1$

the approach of bearings with shape $H \propto r^{2n}$, where n is an integer, through a thin layer of fluid towards a stationary flat impermeable bed. However, whereas the solution for $h_{\min}$ given by Stone [66] involved a double integral dependent on n, the solution given by (4.8) is expressed in terms of elementary functions, i.e. we have spotted that by simply changing the order of integration this double integral can be evaluated.

In the general case $k \neq 0$ the integral in (4.7) was evaluated numerically using the `int` tool (with its default numerical method) in MAPLE. (The integral in (4.7) may, in principle, be evaluated in closed form, but again the resulting expression is unwieldy.)

Figure 4.2 shows plots of $h_{\min}$ as a function of $\ln \bar{t}$ for different values of the permeability k and two different values of n. Figure 4.2 shows that, as expected,

fact be $2(2n-1)/n$.

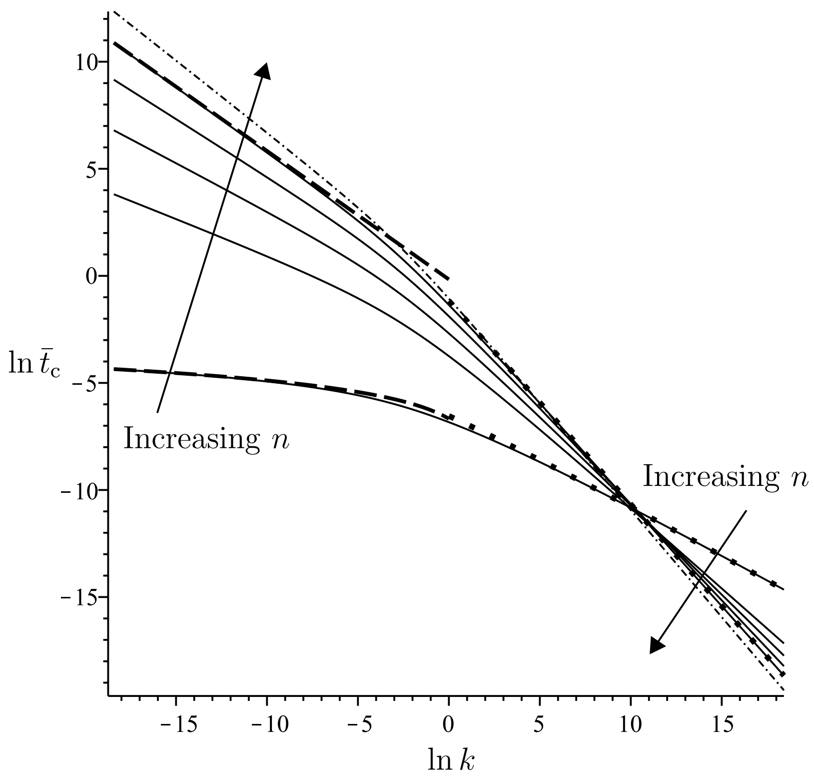

Figure 4.3: Plots of $\ln \bar{t}_{\mathrm{c}}$ as a function of $\ln k$ given by (4.10) for $n = 1, 2, 3, 5$ and 10 (solid lines), the leading order small-k asymptotic solutions (4.75) and (4.124) (dashed lines) for $n = 1$ and $n = 10$, respectively, the leading order large-k asymptotic solutions (4.147) and (4.155) (dotted lines) for $n = 1$ and $n = 10$, respectively, and the solution for a flat bearing given by (3.14) (dash-dotted line). In all plots $\alpha = 1$

increasing the permeability k decreases the time $t(h_{\mathrm{min}})$ taken for the minimum fluid layer thickness to reduce to a value h_{min}. Figure 4.2 also shows that for "small" values of k (specifically $k = 0, 10^{-4}, 10^{-2}$ and 10^{-1}) increasing n increases $t(h_{\mathrm{min}})$, whereas for "large" values of k (specifically $k = 1$ and 10) increasing n decreases $t(h_{\mathrm{min}})$. Furthermore, Figure 4.2 shows that when the bed is permeable, i.e. when $k > 0$, the bearing and the porous bed always make contact in a finite time. This finite contact time is denoted by t_{c}, and is given by setting $h_{\mathrm{min}} = 0$ in

(4.7) to yield

$$t_c = \frac{6\pi}{L_0} \int_0^d \int_0^\infty \frac{\tilde{r}^3(\alpha h + k^{1/2})}{h^2(\alpha h^2 + 4k^{1/2}h + 6\delta\alpha k) + 12k(\alpha h + k^{1/2})} \, d\tilde{r} \, ds, \tag{4.10}$$

where $h = s + \tilde{r}^{2n}$. Figure 4.3 shows plots of $\ln \bar{t}_c$, where $\bar{t}_c = (2nH_p/\mathcal{R})^{2/n} t_c$, as a function of $\ln k$ for five values of n and also, for comparison, for the case of a flat bearing treated in Chapter 3. Figure 4.3 shows that, in agreement with Figure 4.2, increasing k decreases the contact time $\bar{t}_c$. Figure 4.3 also shows, in agreement with Figure 4.2, that when the permeability $k \ll 1$ is small increasing n increases the contact time $\bar{t}_c$, whereas when the permeability $k \gg 1$ is large increasing n decreases the contact time $\bar{t}_c$. This qualitative change in behaviour is confirmed by the analysis of the asymptotic limits $k \to 0$ and $k \to \infty$ given subsequently in §4.3 and §4.4, respectively. Furthermore, Figure 4.3 shows that as n increases from $n = 1$ to $n = 10$ the solution for $\ln \bar{t}_c$ as a function of $\ln k$ becomes almost indistinguishable from the solution in the case of a flat bearing (Chapter 3). The physical reason for this is that as n increases the bearing becomes flatter around the axis of symmetry $r = 0$; in fact as $n \to \infty$ the bearing resembles a flat bearing of (dimensional) radius $r = \mathcal{R}$.

The effect of varying the permeability k is relatively simple to understand; however, the effect of varying the Beavers–Joseph constant α is, again, less obvious. Figure 4.4 shows plots of $h_{\min}$ as a function of $\ln \bar{t}$ for different values of α for two values of k and two values of n. In particular, Figures 4.4(a) and 4.4(b) show that, similarly to the case of a flat bearing treated in Chapter 3, for a "small" value of k (specifically $k = 10^{-2}$) as α increases the time $t(h_{\min})$ increases, whereas Figures 4.4(c) and 4.4(d) show that for a "large" value of k (specifically $k = 5 \times 10^4$) as α increases the time $t(h_{\min})$ decreases. Again, this qualitative change in behaviour is confirmed by the analysis of the asymptotic limits $k \to 0$ and $k \to \infty$ given

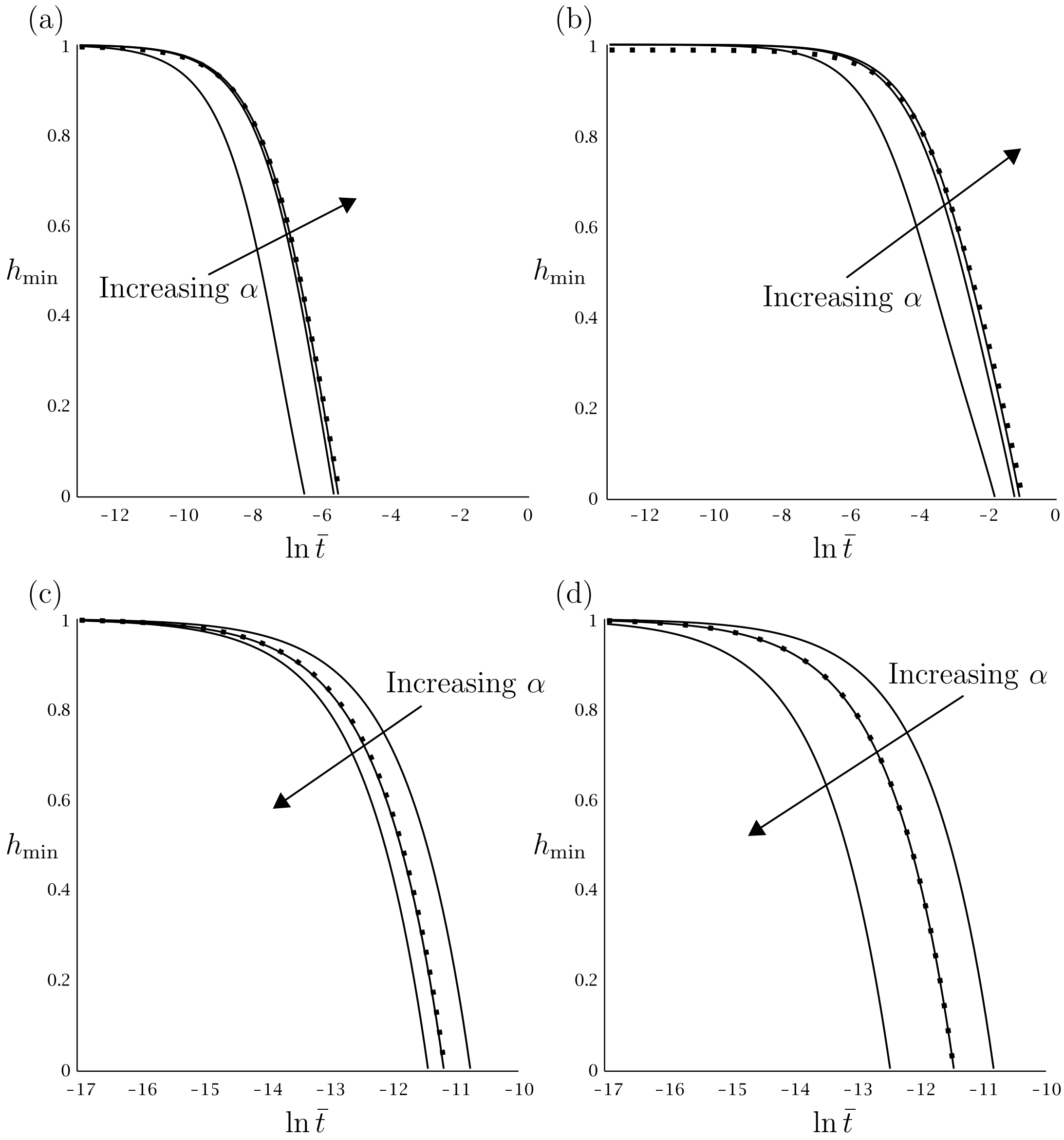

Figure 4.4: Plots of $h_{\min}$ as a function of $\ln \bar{t}$ for (a) $k = 10^{-2}$, $n = 1$, (b) $k = 10^{-2}$, $n = 2$, (c) $k = 5 \times 10^4$, $n = 1$, and (d) $k = 5 \times 10^4$, $n = 2$ given by (4.7) for $\alpha = 10^{-2}$, 1 and 100 (solid lines), the uniformly valid leading order small-k asymptotic solutions (a) (4.82) and (b) (4.129) (dotted lines), and the leading order large-k asymptotic solutions (c) (4.145) and (d) (4.153) for $\alpha = 1$ (dotted lines)

subsequently in §4.3 and §4.4, respectively.

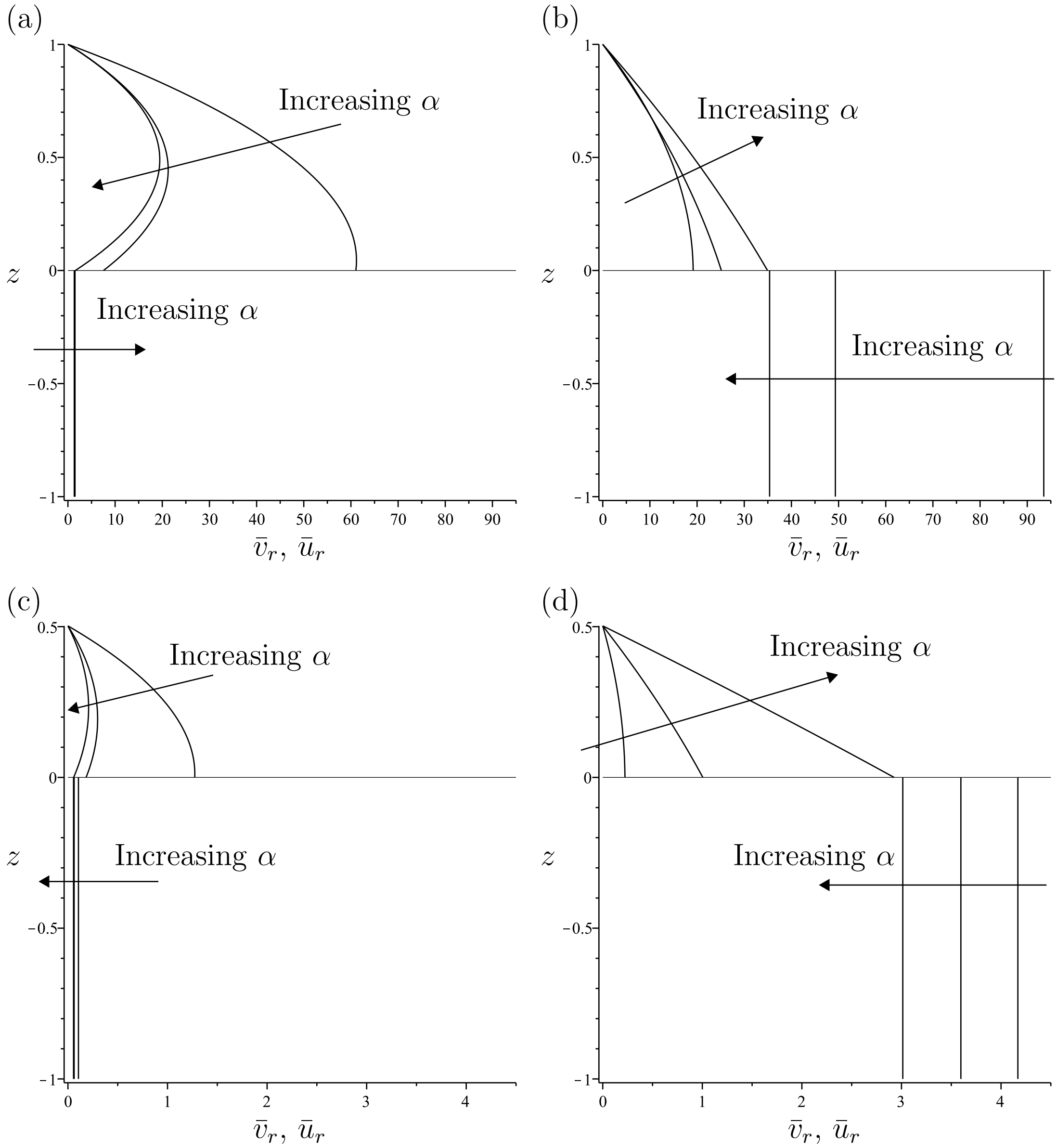

Figure 4.5: Plots of the radial fluid velocity $\bar{v}_r$ at $\bar{r} = 0.1$ as a function of z in $0 \le z \le h(r,t)$ given by (2.60) and plots of the radial Darcy velocity $\bar{u}_r$ at $\bar{r} = 0.1$ as a function of z in $-1 \le z \le 0$ given by (2.54) at the times when $h_{\min} = 1/2$ for $\alpha = 10^{-2}, 1$ and 100, and (a) $k = 10^{-2}$, $n = 1$, (b) $k = 2.5$, $n = 1$, (c) $k = 10^{-2}$, $n = 2$, and (d) $k = 2.5$, $n = 2$

4.2.2 Velocity and Instantaneous Streamlines

To understand the physical reason why varying the Beavers–Joseph constant α has a different qualitative effect for small and large values of the permeability k it

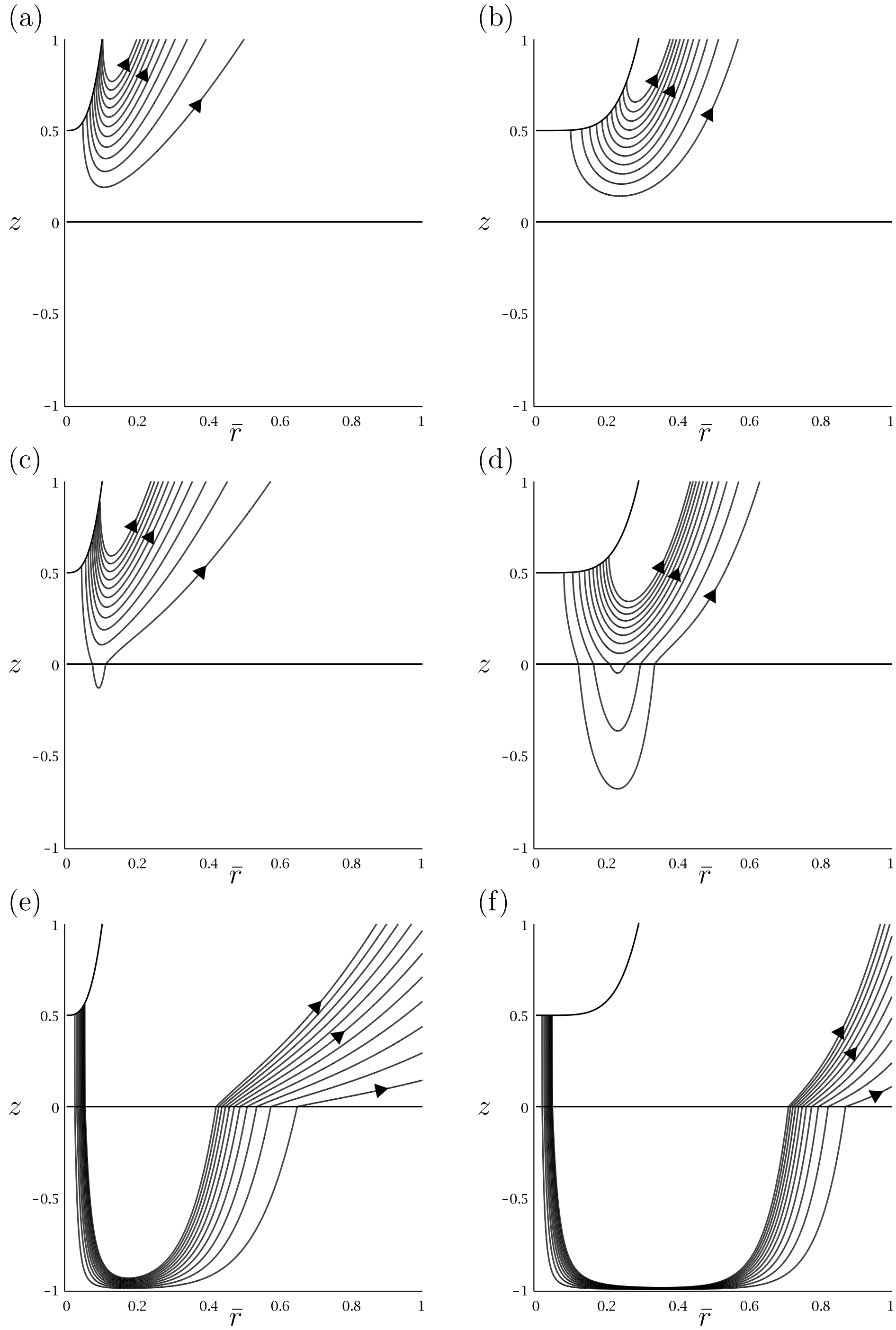

Figure 4.6: Plots of instantaneous streamlines ψ = constant $= -j/4 \times 10^{-2}$ for $j = 1, 2, \ldots, 11$ with ψ given by (2.67) in $0 \le z \le h$ and (2.68) in $-1 \le z \le 0$ at the times when $h_{\min} = 1/2$ for (a) $k = 0$, $n = 1$, (b) $k = 0$, $n = 2$, (c) $k = 10^{-2}$, $n = 1$, (d) $k = 10^{-2}$, $n = 2$, (e) $k = 10$, $n = 1$, and (f) $k = 10$, $n = 2$. In all plots $\alpha = 1$

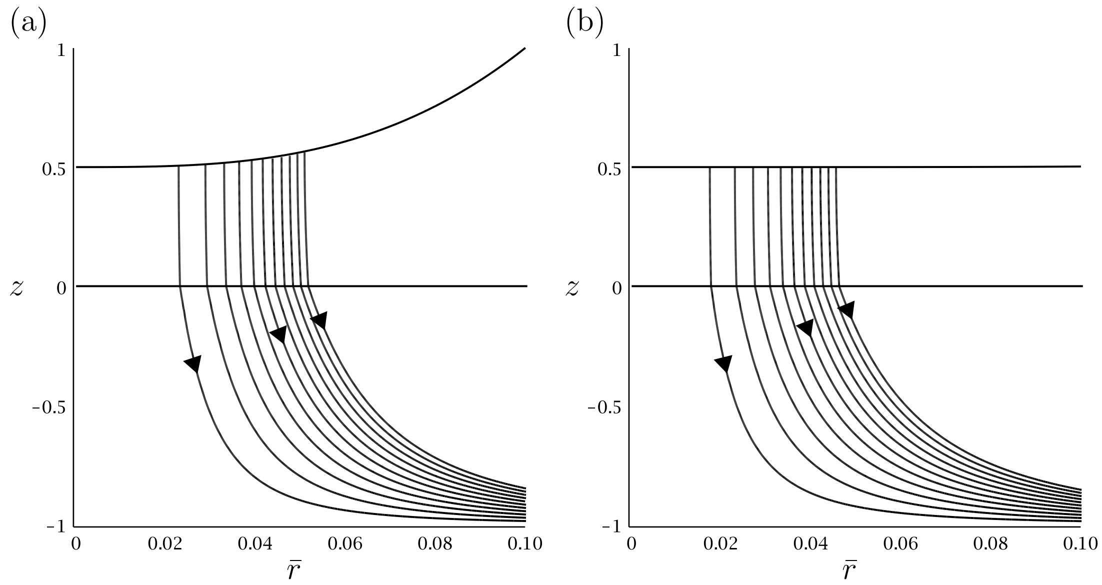

Figure 4.7: Enlargements of (a) Figure 4.6(e) and (b) Figure 4.6(f)

is, again, instructive to examine the radial fluid velocity $\bar{v}_r$ and the radial Darcy velocity $\bar{u}_r$. Figure 4.5 shows plots of $\bar{v}_r$ as a function of z in $0 \leq z \leq h$ and plots of $\bar{u}_r$ as a function of z in $-1 \leq z \leq 0$ for three values of the Beavers–Joseph constant α for two values of the permeability k and two values of n. (Note that all of the plots shown in Figure 4.5, and also all of those subsequently shown in Figures 4.6 and 4.7, are for the same value of the minimum fluid layer thickness, namely $h_{\min} = 1/2$, and so are not, therefore, at the same instant $\bar{t}$.) Figures 4.5(a) and 4.5(c) and Figures 4.5(b) and 4.5(d) show the flow for a "small" (specifically $k = 10^{-2}$) and a "large" (specifically $k = 2.5$) value of the permeability k, respectively. These figures show that when k is small the fastest flow is in the fluid layer and when k is large the fastest flow is in the porous bed. In particular, Figures 4.5(a) and 4.5(c) show that when k is small increasing α (i.e. decreasing the slip length l_s) decreases $\bar{v}_r$ and hence decreases the volume flux of fluid out of the fluid layer

$\bar{Q}_{\text{out}} = (2nH_{\text{p}}/\mathcal{R})^{-1/n}Q_{\text{out}}$, where $Q_{\text{out}} = Q_{\text{out}}(r,t)$ is given by

$$Q_{\text{out}} = 2\pi \int_0^h v_r r \, \mathrm{d}z = -\frac{\pi r h^2(\alpha h^2 + 4k^{1/2}h + 6\delta\alpha k)}{6(\alpha h + k^{1/2})}\frac{\partial p}{\partial r}. \tag{4.11}$$

As shown in Figures 4.4(a) and 4.4(b), this decrease in $\bar{Q}_{\text{out}}$ causes the time $t(h_{\text{min}})$ to increase. On the other hand, Figures 4.5(b) and 4.5(d) show that when k is large increasing α increases $\bar{v}_r$ and hence increases $\bar{Q}_{\text{out}}$, meaning that, as shown in Figures 4.4(c) and 4.4(d), the time $t(h_{\text{min}})$ decreases.

Figure 4.6 shows plots of instantaneous streamlines for three values of the permeability k and two values of n. Figures 4.6(a) and 4.6(b) show the streamlines in the case in which the bed is impermeable $k = 0$, in which there is no flow in the porous bed. As n increases the spacing between the streamlines increases, meaning that the volume flux of fluid out of the fluid layer $\bar{Q}_{\text{out}}$ decreases and hence that the time $t(h_{\text{min}})$ increases.

Figures 4.6(c) and 4.6(d) show the streamlines for a "small" value of k (specifically $k = 10^{-2}$) and Figures 4.6(e) and 4.6(f) show the streamlines for a "large" value of k (specifically $k = 10$). As k increases the spacing between the streamlines decreases, meaning that both the volume flux of fluid out of the fluid layer $\bar{Q}_{\text{out}}$ and the volume flux of fluid into the porous bed $\bar{Q}_{\text{bed}} = (2nH_{\text{p}}/\mathcal{R})^{-1/n}Q_{\text{bed}}$, where $Q_{\text{bed}} = Q_{\text{bed}}(r,t)$ is given by

$$Q_{\text{bed}} = 2\pi \int_0^r v_z\Big|_{z=0} \tilde{r} \, \mathrm{d}\tilde{r} = 2\pi k r \frac{\partial p}{\partial r}, \tag{4.12}$$

increase and hence that the time $t(h_{\text{min}})$ decreases. Furthermore, Figures 4.6(c) and 4.6(d) also show that for a "small" value of k increasing n increases the spacing between the streamlines, meaning that both $\bar{Q}_{\text{out}}$ and $\bar{Q}_{\text{bed}}$ decrease and hence that the time $t(h_{\text{min}})$ increases, consistently with the behaviour for small k shown in

Figures 4.2, 4.4(a) and 4.4(b). Figures 4.6(e) and 4.6(f) also show that for a “large” value of k increasing n decreases the spacing between the streamlines, meaning that both $\bar{Q}_{\text{out}}$ and $\bar{Q}_{\text{bed}}$ increase and hence that the time $t(h_{\min})$ decreases, consistent with the behaviour for large k shown in Figures 4.4(c) and 4.4(d). The latter behaviour can be seen more readily from Figures 4.7(a) and 4.7(b) which show enlargements of Figures 4.6(e) and 4.6(f), respectively.

4.2.3 Fluid Pressure

In the special case when the bed is impermeable, i.e. when $k = 0$, the fluid pressure $p = p(r, t)$ is given by

$$p = \begin{cases} \dfrac{L_0 h_{\min}}{\pi(h_{\min} + r^2)^2} & \text{when} \quad n = 1, \\ \dfrac{L_0}{2\pi h_{\min}^{1/2}} \left[3 \left(\dfrac{\pi}{2} - \tan^{-1}\left(\dfrac{r^2}{h_{\min}^{1/2}} \right) \right) - \dfrac{h_{\min}^{1/2} r^2 (5h_{\min} + 3r^4)}{(h_{\min} + r^4)^2} \right] & \text{when} \quad n = 2, \\ \dfrac{2n^3 \sin(2\pi/n) L_0 h_{\min}^{(3n-2)/n}}{\pi^2 (n-1)(n-2)} \displaystyle\int_r^\infty \dfrac{\tilde{r}}{(h_{\min} + \tilde{r}^{2n})^3} \, \mathrm{d}\tilde{r} & \text{when} \quad n \geq 3, \end{cases} \tag{4.13}$$

where (4.8) has been used in (4.4), and, in particular, the maximum fluid pressure $p_{\max} = p(0, t)$ is given by

$$p_{\max} = \begin{cases} \dfrac{L_0}{\pi h_{\min}} & \text{when} \quad n = 1, \\ \dfrac{3L_0}{4h_{\min}^{1/2}} & \text{when} \quad n = 2, \\ \dfrac{(2n-1)\cos(\pi/n) L_0}{\pi(n-2) {h_{\min}}^{1/n}} & \text{when} \quad n \geq 3. \end{cases} \tag{4.14}$$

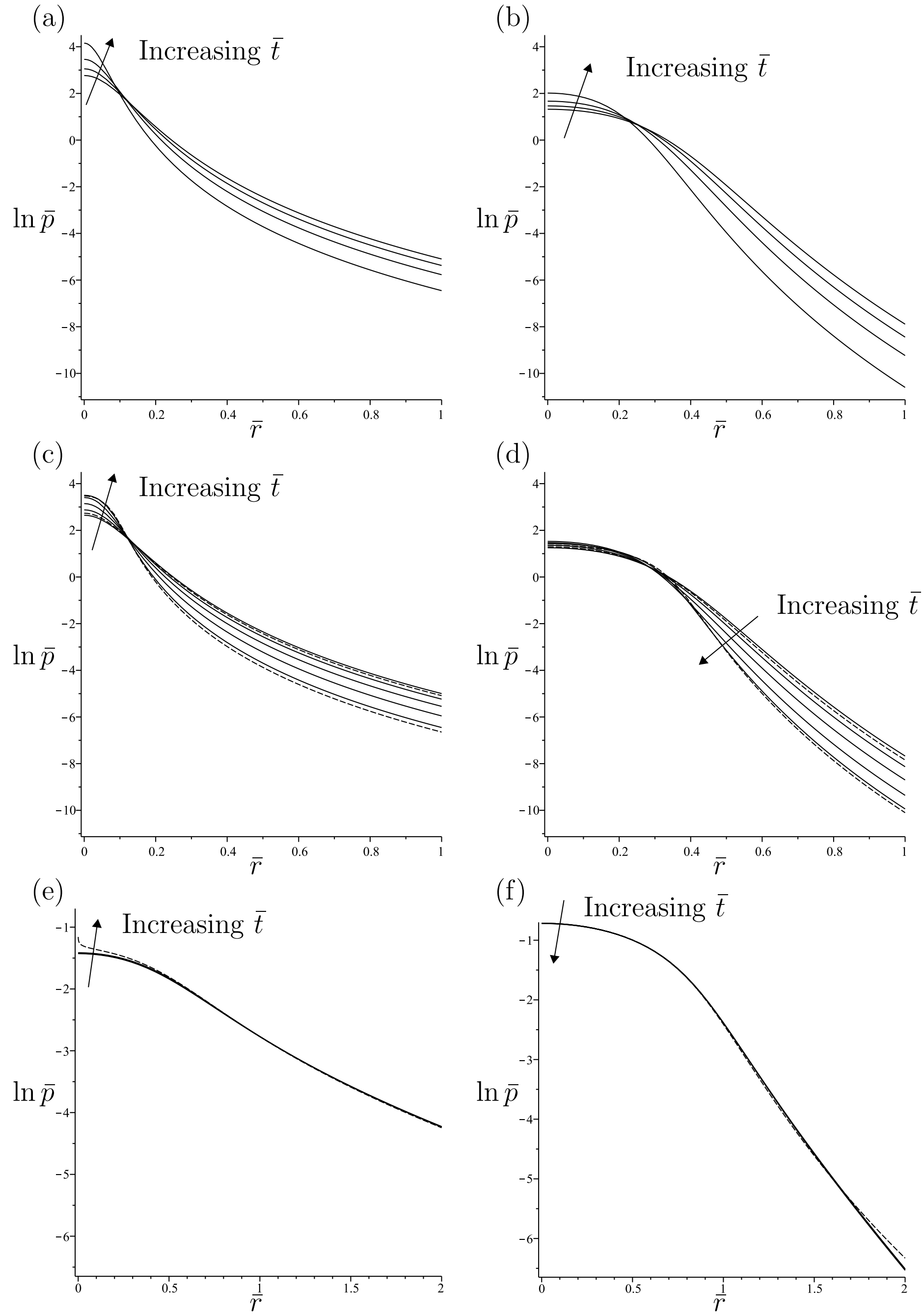

Figure 4.8: Plots of $\ln \bar{p}$ as a function of $\bar{r}$ given by (4.4) at the times when $h_{\min} = d, 3d/4, d/2, d/4$ and 0 (solid lines), the uniformly valid leading order small-k asymptotic solutions (c) (4.80) and (d) (4.127) at the times when $h_{\min} = d$ and 0 (dashed lines), and the leading order large-k asymptotic solutions (e) (4.141) and (f) (4.150) (dashed lines) for (a) $k = 0$, $n = 1$, (b) $k = 0$, $n = 2$, (c) $k = 10^{-2}$, $n = 1$, (d) $k = 10^{-2}$, $n = 2$, (e) $k = 5 \times 10^4$, $n = 1$, (f) $k = 5 \times 10^4$, $n = 2$. In all plots $\alpha = 1$

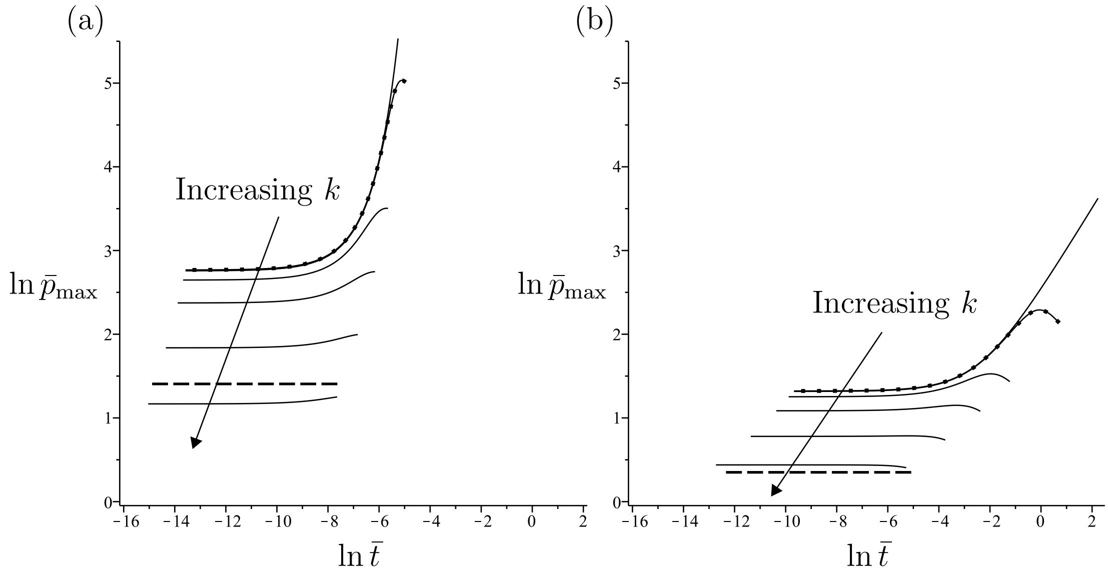

Figure 4.9: Plots of $\ln \bar{p}_{\max}$ as a function of $\ln \bar{t}$ given by (4.4) for $k = 0, 10^{-4}, 10^{-2}, 10^{-1}, 1$ and 10 (solid lines), the uniformly valid leading order small-k asymptotic solutions (a) (4.81) and (b) (4.128) for $k = 10^{-4}$ (dotted lines), and the leading order large-k asymptotic solutions (a) (4.144) and (b) (4.152) for $k = 10$ (dashed lines) for (a) $n = 1$ and (b) $n = 2$. In all plots $\alpha = 1$

In this case the maximum fluid pressure

$$p_{\max} = \left\{ \begin{array}{ll} O\left(\exp\left(\dfrac{2L_0 t}{3\pi}\right)\right) & \text{when} \quad n = 1 \\ O(t^{1/2(n-1)}) & \text{when} \quad n \geq 2 \end{array} \right\} \to \infty \quad \text{as} \quad t \to \infty. \qquad (4.15)$$

In the general case $k \neq 0$ the fluid pressure p is given by (4.4) and was evaluated numerically using MAPLE. Figure 4.8 shows plots of $\ln \bar{p}$ as a function of $\bar{r}$ for three values of the permeability k and two values of n. Figure 4.8 shows that, as expected, increasing k decreases the maximum fluid pressure $\bar{p}_{\max} = \bar{p}(0, \bar{t}) = (2nH_{\mathrm{p}}/\mathcal{R})^{-1/n} p_{\max}$ and distributes the fluid pressure $\bar{p}$ over a larger area. Furthermore, Figure 4.8 shows that increasing k decreases the temporal variations in $\bar{p}$. (In fact, it will be shown subsequently in §4.4 that to leading order in the limit $k \to \infty$ the fluid pressure p is independent of t.)

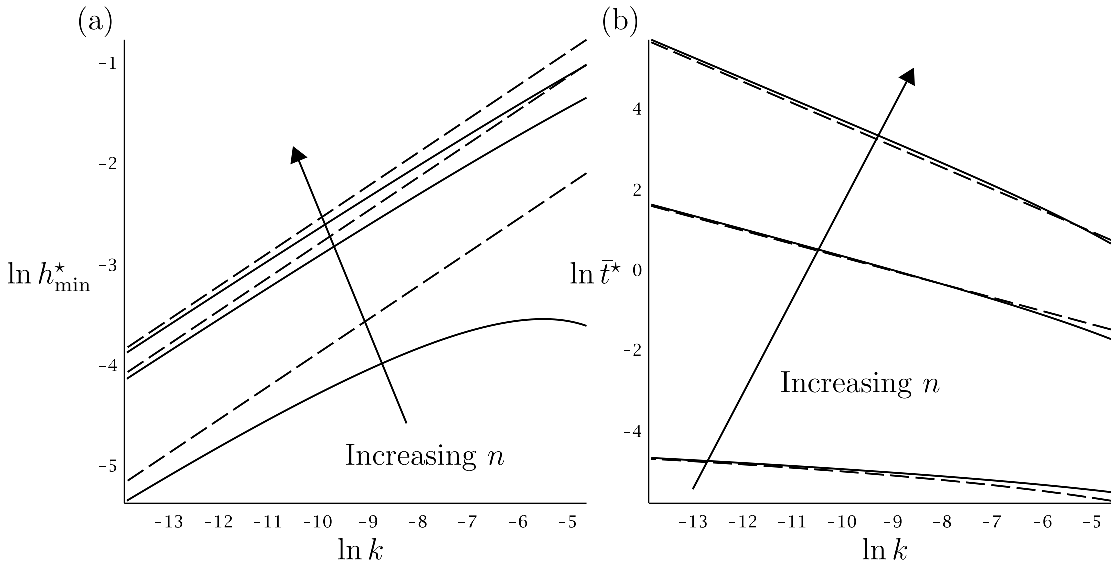

Figure 4.10: (a) Plots of $\ln h^\star_{\min}$ as a function of $\ln k$ for $n = 1, 2$ and 5 given by the numerical solution (solid lines) and the leading order small-k asymptotic solutions (4.78) ($n = 1$) and (4.126) ($n \geq 2$) (dashed lines). (b) Plots of $\ln \bar{t}^\star$ as a function of $\ln k$ for $n = 1, 2$ and 5 given by the numerical solution (solid lines) and the leading order small-k asymptotic solutions (4.79) ($n = 1$) and (4.125) ($n \geq 2$) (dashed lines). In all plots $\alpha = 1$

Figures 4.8(a)–(d) show that for small values of k (specifically $k = 0$ and $k = 10^{-2}$) increasing n decreases $\bar{p}_{\max}$ and distributes the fluid pressure $\bar{p}$ over a larger area, whereas Figures 4.8(e) and 4.8(f) show that for a large value of k (specifically $k = 5 \times 10^4$) increasing n increases $\bar{p}_{\max}$ and concentrates the fluid pressure $\bar{p}$ over a smaller area. Again, this qualitative change in behaviour is confirmed by the analysis of the asymptotic limits $k \to 0$ and $k \to \infty$ given subsequently in §4.3 and §4.4, respectively.

Figure 4.9 shows plots of $\ln \bar{p}_{\max}$ as a function of $\ln \bar{t}$ for six values of the permeability k and two values of n. Figure 4.9 shows that for small values of k the solution for $\bar{p}_{\max}$ as a function of $\bar{t}$ has a maximum turning point. The maximum fluid pressure $\bar{p}_{\max}$ increases monotonically in time to its maximum value $\bar{p}^\star_{\max}$, which it attains at some time $\bar{t} = \bar{t}^\star$ satisfying $0 < \bar{t}^\star < \bar{t}_c$, and then decreases to its value at $\bar{t} = \bar{t}_c$. The physical reason for this is the fact that, as the analysis of the solution in the asymptotic limit $k \to 0$ given subsequently in §4.3 shows, the porous bed is effectively impermeable when $h_{\min} \gg O(k^{1/3})$ is sufficiently "large", and the effects of the permeability k on the fluid pressure $\bar{p}$ become significant only when $h_{\min} = O(k^{1/3})$. The maximum fluid pressure $\bar{p}_{\max}$ increases monotonically in time while $h_{\min} \gg O(k^{1/3})$, and when $h_{\min} = O(k^{1/3})$ the fluid volume flux into the porous bed $\bar{Q}_{\text{bed}}$ is sufficiently large that it causes a decrease in $\bar{p}_{\max}$. Consequently the maximum fluid pressure $\bar{p}_{\max} = \bar{p}_{\max}(\bar{t})$ does not attain its maximum value $\bar{p}^{\star}_{\max}$ at the contact time $\bar{t}_c$. This is somewhat similar to an observation made by Goren [24]. Goren calculated the force exerted on a sphere as it approaches a permeable membrane through a fluid layer at a constant velocity and found that the maximum force exerted on the sphere does not occur when the sphere and the membrane are in contact.

Figure 4.10(a) shows plots of $\ln h^{\star}_{\min}$ as a function of $\ln k$ for three values of n, where $h^{\star}_{\min} = h_{\min}(\bar{t}^{\star})$ is the (unique) value of $h_{\min}$ at which the maximum fluid pressure $\bar{p}_{\max}$ attains its maximum value $\bar{p}^{\star}_{\max}$, and Figure 4.10(b) shows plots of $\ln \bar{t}^{\star}$ as a function of $\ln k$ for the same three values of n. Figure 4.10(a) shows that decreasing k decreases $h^{\star}_{\min}$ and that increasing n increases $h^{\star}_{\min}$. Figure 4.10(b) shows that decreasing k and/or increasing n increases the time $\bar{t}^{\star}$ at which $\bar{p}_{\max}$ attains its maximum value $\bar{p}^{\star}_{\max}$. The physical reason for this is that as k decreases and/or n increases the time $\bar{t}(h_{\min})$ taken for the minimum fluid layer thickness to reduce to a value $h_{\min} = O(k^{1/3})$, when, recall, the effects of k finally become significant resulting in a decrease in $\bar{p}_{\max}$, increases and hence $\bar{t}^{\star}$ also increases. This behaviour is confirmed by the analysis of the asymptotic limit $k \to 0$ given subsequently in §4.3.

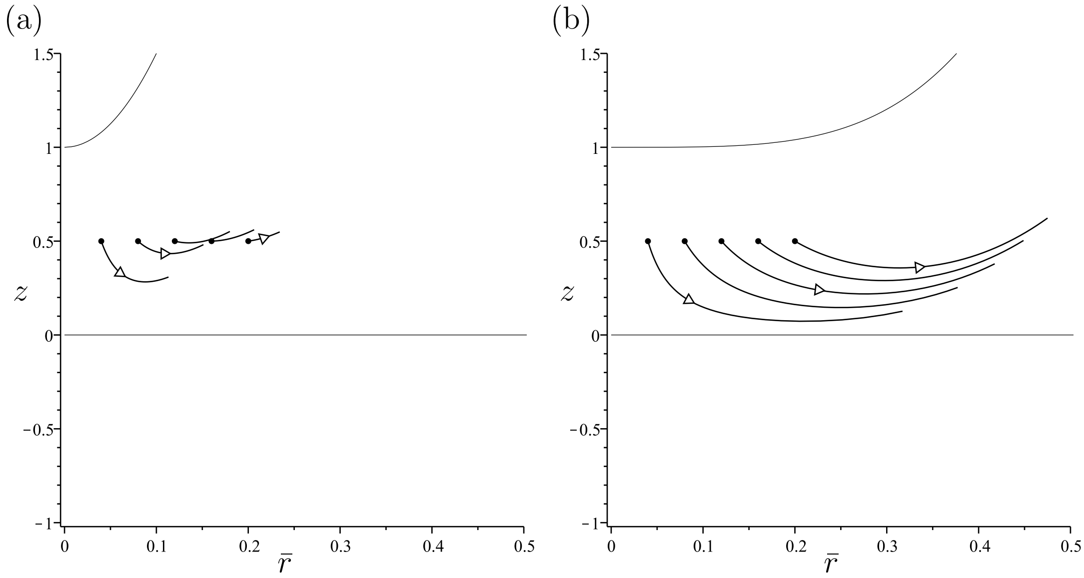

Figure 4.11: Plots of the paths of fluid particles, z as a function of $\bar{r}$, in the impermeable case $k = 0$, with $\bar{r} = \bar{r}(h_{\min})$ and $z = z(h_{\min})$ given by (4.16) and (4.17) subject to $(\bar{r}_0, z_0) = (0.04, 0.5), (0.08, 0.5), (0.12, 0.5), (0.16, 0.5)$ and $(0.2, 0.5)$ for (a) $n = 1$ and (b) $n = 2$

4.2.4 Fluid Particle Paths and Penetration Depths

Substituting (4.3) into (2.69) and (2.70) and then using the chain rule to eliminate t, we obtain the differential equations that govern the path (r, z) taken by a fluid particle:

$$\frac{1}{r}\frac{\mathrm{d}r}{\mathrm{d}h_{\min}} = -\frac{3(h-z)[(\alpha h + k^{1/2})z + k^{1/2}(h + 2\delta\alpha k^{1/2})]}{h^2(\alpha h^2 + 4k^{1/2}h + 6\delta\alpha k) + 12k(\alpha h + k^{1/2})}, \tag{4.16}$$

$$\frac{\mathrm{d}z}{\mathrm{d}h_{\min}} = \frac{1}{2r}\frac{\partial}{\partial r}\left(\frac{\mathcal{F}(h,z)r^2}{h^2(\alpha h^2 + 4k^{1/2}h + 6\delta\alpha k) + 12k(\alpha h + k^{1/2})}\right), \tag{4.17}$$

in the fluid layer $0 \le z \le h$, where $\mathcal{F}(h, z)$ is given by (2.62), and

$$\frac{1}{r}\frac{\mathrm{d}r}{\mathrm{d}h_{\min}} = -\frac{6k(\alpha h + k^{1/2})}{\phi\,[h^2(\alpha h^2 + 4k^{1/2}h + 6\delta\alpha k) + 12k(\alpha h + k^{1/2})]}, \tag{4.18}$$

$$\frac{1}{1+z}\frac{\mathrm{d}z}{\mathrm{d}h_{\min}} = \frac{6k}{\phi r}\frac{\partial}{\partial r}\left(\frac{(\alpha h + k^{1/2})r^2}{h^2(\alpha h^2 + 4k^{1/2}h + 6\delta\alpha k) + 12k(\alpha h + k^{1/2})}\right), \tag{4.19}$$

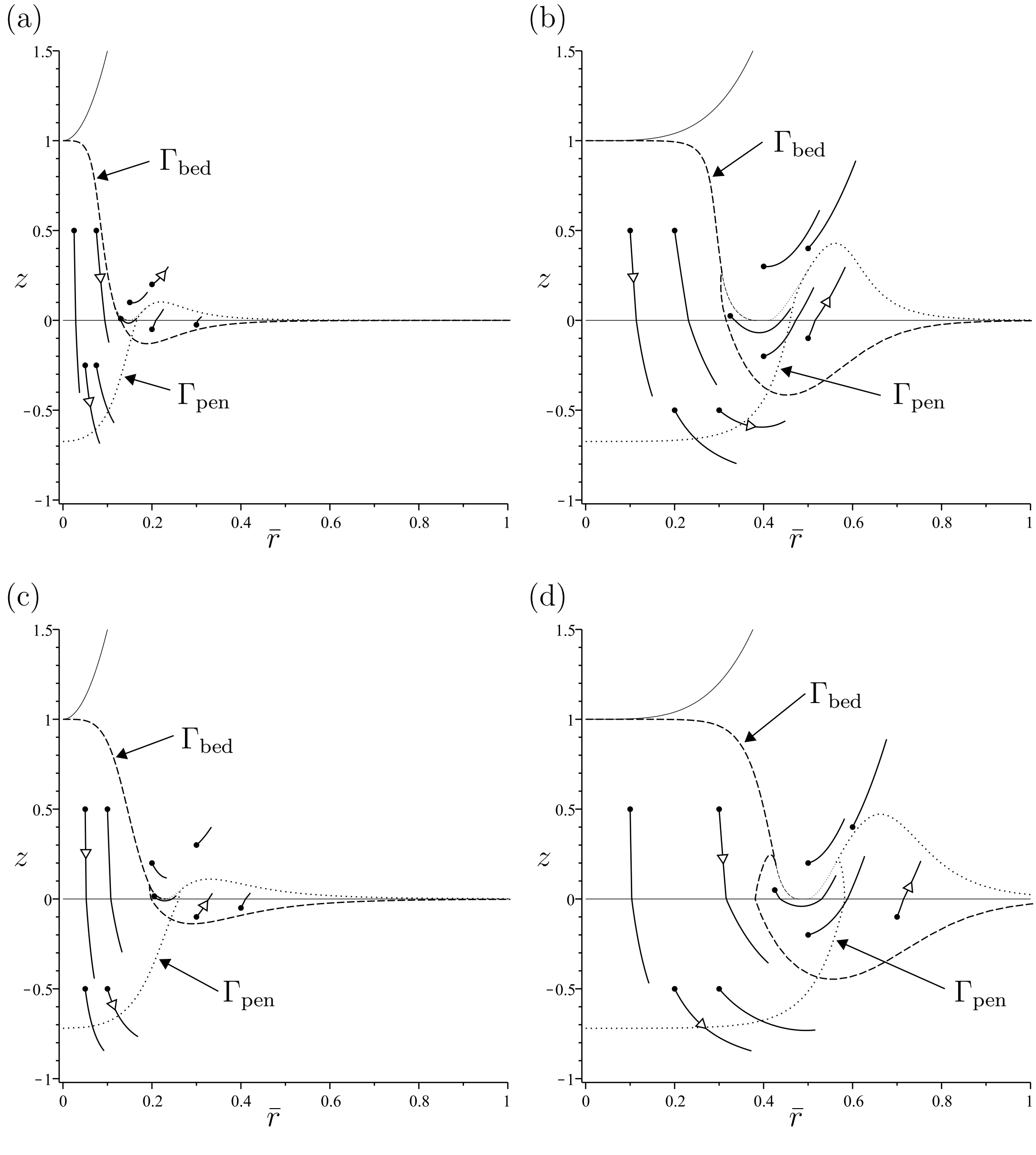

Figure 4.12: Plots of the paths of fluid particles, z as a function of $\bar{r}$, in the permeable case $k > 0$, with $\bar{r} = \bar{r}(h_{\text{min}})$ and $z = z(h_{\text{min}})$ given by (4.16)–(4.19) (solid lines), and plots of the curves Γ_{bed} (thick dashed lines), Γ_{pen} (thick dotted lines), Γ_{bed^*} (thin dashed lines) and Γ_{pen^*} (thin dotted lines) for (a) $k = 0.5$, $n = 1$, (b) $k = 0.5$, $n = 2$, (c) $k = 10$, $n = 1$, and (d) $k = 10$, $n = 2$. In all plots $\alpha = 1$ and $\phi = 3/4$

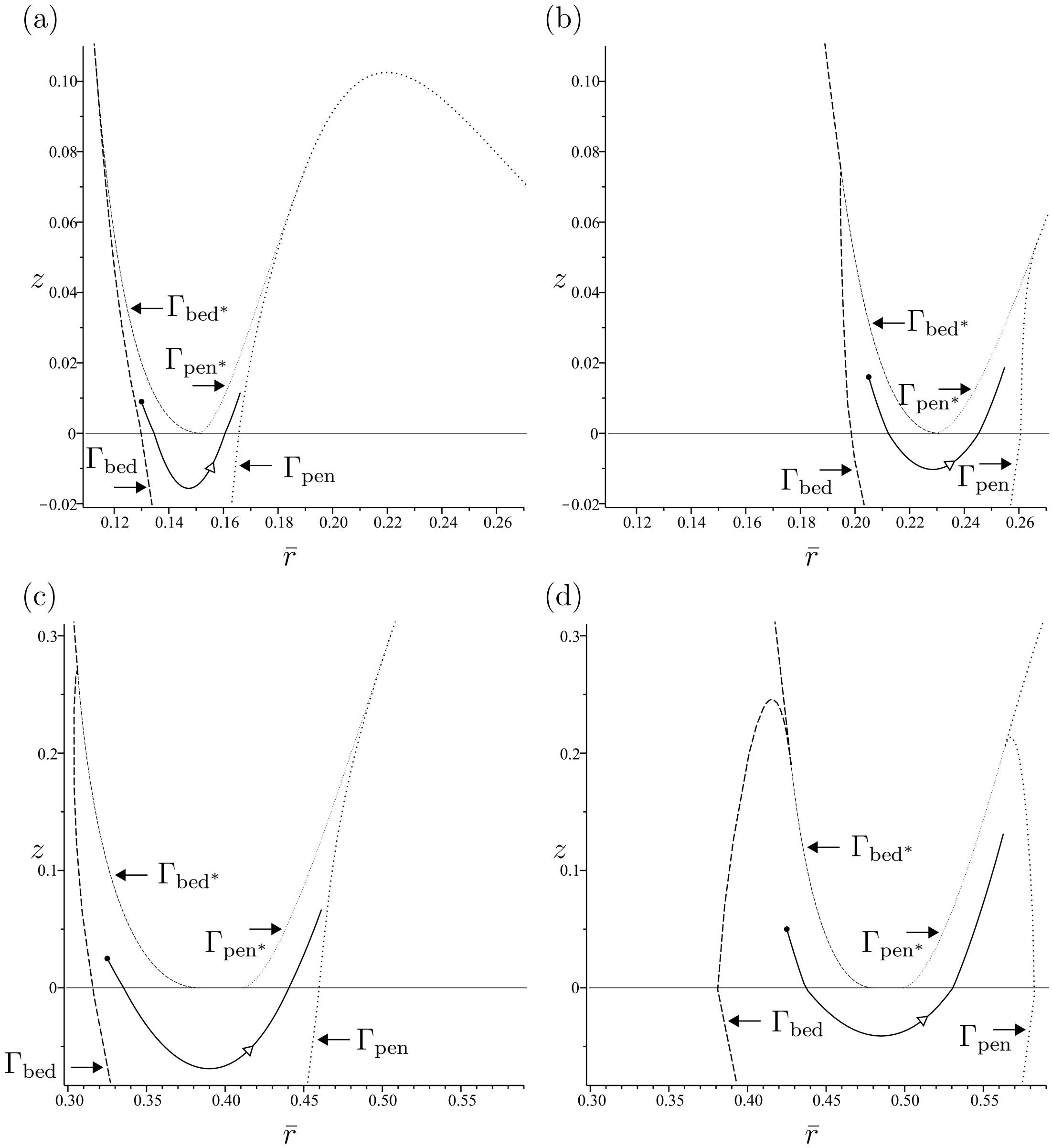

Figure 4.13: Enlargements of Figure 4.12 showing only the paths of the fluid particles that flow from the fluid layer into the porous bed and then re-emerge into the fluid layer, namely the particles initially situated at the points (a) $(\bar{r}_0, z_0) = (0.13, 0.009)$, (b) $(\bar{r}_0, z_0) = (0.325, 0.025)$, (c) $(\bar{r}_0, z_0) = (0.205, 0.016)$, and (d) $(\bar{r}_0, z_0) = (0.425, 0.05)$

in the porous bed $-1 \leq z \leq 0$, subject to the initial conditions

$$r = r_0 \quad \text{and} \quad z = z_0 \quad \text{when} \quad h_{\text{min}} = d. \tag{4.20}$$

The differential equations (4.16)–(4.19) were solved numerically using the `dsolve` tool (with its default numerical method) in MAPLE subject to the initial condition (4.20).

Figure 4.11 shows the paths $(\bar{r}, z)$ taken by several fluid particles from their initial positions $(\bar{r}_0, z_0)$, where $\bar{r}_0 = (2nH_{\text{p}}/\mathcal{R})^{1/2n} r_0$, in the special case when the bed is impermeable, i.e. when $k = 0$, for two values of n. In this case the fluid particles can flow only through the fluid layer.

Figure 4.12 shows the paths taken by several fluid particles for two non-zero values of k and two values of n. Figure 4.12 shows that there are three possible behaviours for the fluid particles that are initially situated in the fluid layer: they can flow through the fluid layer without passing into the porous bed, they can flow from the fluid layer into the porous bed, or they can flow from the fluid layer into the porous bed and then re-emerge into the fluid layer. On the other hand, there are only two possibilities for the fluid particles initially situated in the porous bed: they can either flow through the porous bed without passing into the fluid layer or they can flow from the porous bed into the fluid layer.

The curve Γ_{bed}, which consists of the initial positions $(\bar{r}_0, z_0)$ of the fluid particles that are situated on $z = 0$ when $h_{\text{min}} = 0$, i.e. at the contact time $\bar{t} = \bar{t}_{\text{c}}$, is also plotted in Figure 4.12; it separates the fluid particles that are situated in the porous bed when $h_{\text{min}} = 0$ from those that are situated in the fluid layer when $h_{\text{min}} = 0$. The fluid particles that are initially situated to the left of Γ_{bed} (as it is traversed towards $\bar{r} = 0$) are in the porous bed at the contact time $\bar{t} = \bar{t}_{\text{c}}$ and the fluid particles that are initially situated to the right of Γ_{bed} are in the fluid layer at the contact time $\bar{t} = \bar{t}_{\mathrm{c}}$. Furthermore, Figure 4.12 shows that as k increases (with n fixed) or as n increases (with k fixed) the area bounded by the curves Γ_{bed}, $z = 0$ and $r = 0$ increases, meaning that more fluid flows from the fluid layer into the porous bed. Consequently, mass conservation in the porous bed requires that more fluid flows from the porous bed into the fluid layer and thus the area of the finite region bounded by the curves Γ_{bed} and $z = 0$ also increases.

The final positions $(\bar{r}_{\mathrm{pen}}, z_{\mathrm{pen}}) = (\bar{r}(0), z(0))$ of the fluid particles that flow from the fluid layer into the porous bed and vice versa are also of interest. The curve Γ_{pen}, which consists of the final positions $(\bar{r}_{\mathrm{pen}}, z_{\mathrm{pen}}) = (\bar{r}(0), z(0))$ of the fluid particles initially situated on $z = 0$, is also plotted in Figure 4.12; it shows the extent to which the fluid particles initially situated in the fluid layer penetrate into the porous bed (the part of the curve below $z = 0$) and the extent to which the fluid particles initially situated in the porous bed can penetrate into the fluid layer (the part of the curve above $z = 0$). Figure 4.12 shows that as k increases the fluid particles penetrate deeper and wider into the porous bed. Furthermore, Figure 4.12 shows that the fluid particle initially situated at the point $(\bar{r}_0, z_0) = (0, 0)$ is the one that penetrates deepest into the porous bed. Since the radial fluid velocity $\bar{v}_r = 0$ at $\bar{r} = 0$ and the radial Darcy velocity $\bar{u}_r = 0$ at $\bar{r} = 0$ are both zero for all times, the fluid particles initially situated at $\bar{r} = 0$ move vertically downwards only. Thus setting $r = 0$ in (4.19) and solving the resulting differential equation for $z(h_{\mathrm{min}})$ subject to the initial condition $z(d) = 0$ we deduce that the penetration depth z_{pen} of the fluid particle initially situated at $(\bar{r}_0, z_0) = (0, 0)$ is given by

$$z_{\mathrm{pen}} = -1 + \exp\left(-\frac{12k}{\phi}\int_0^d \frac{\alpha s + k^{1/2}}{s^2(\alpha s^2 + 4k^{1/2}s + 6\delta\alpha) + 12k(\alpha s + k^{1/2})}\,\mathrm{d}s\right), \quad (4.21)$$

which, we note, does not depend on n. Though the maximum penetration depth z_{pen} of fluid particles initially situated in the fluid layer into the porous bed given by (4.21) does not depend on n, Figure 4.12 shows that increasing n widens the region over which these fluid particles penetrate into the porous bed and increases the maximum penetration depth z_{pen} into the the fluid layer of fluid particles initially situated in the porous bed.

As discussed earlier, the fluid particles that lie to the right of the curve Γ_{bed} are situated in the fluid layer when $h_{\mathrm{min}} = 0$. However, as shown in Figure 4.12, some of these fluid particles flow from the fluid layer into the porous bed and then re-emerge into the fluid layer. The curve Γ_{bed^*}, which consists of the initial positions $(\bar{r}_0, z_0)$ of the fluid particles that flow from the fluid layer into the porous bed at the point where the vertical fluid velocity $\bar{v}_z = 0$ vanishes, is also plotted in Figure 4.12. Figure 4.12 shows that the finite region bounded by the curves Γ_{bed}, Γ_{bed^*} and $z = 0$ contains those fluid particles that flow from the fluid layer into the porous bed and then re-emerge into the fluid layer. This behaviour can be more readily seen from Figure 4.13 which is an enlargement of Figure 4.12. When $h_{\mathrm{min}} = 0$ these fluid particles are situated (in the fluid layer) in the finite region bounded by the curves Γ_{pen}, $z = 0$ and Γ_{pen^*}, where the curve Γ_{pen^*}, which is also plotted in Figure 4.12, consists of the final positions $(\bar{r}_{\mathrm{pen}}, z_{\mathrm{pen}})$ of the fluid particles that flow from the fluid layer into the porous bed at the point where the vertical fluid velocity $\bar{v}_z = 0$ vanishes. Again, this behaviour can be seen more readily from Figure 4.13.

4.3 Limit of Small Permeability $k \to 0$

In this section asymptotic solutions for the fluid pressure $p = p(r, t)$ and the minimum fluid layer thickness $h_{\mathrm{min}} = h_{\mathrm{min}}(t)$ in the limit of small permeability

$k \to 0$ are obtained. In this limit it will transpire that the contact time

$$t_c = \left\{ \begin{array}{ll} O\left(\ln\left(\frac{1}{k}\right)\right) & \text{when} \quad n = 1 \\ O(k^{-2(n-1)/3n}) & \text{when} \quad n \geq 2 \end{array} \right\} \gg 1 \tag{4.22}$$

is large, and, as in the case of a flat bearing treated in Chapter 3, regular perturbation solutions for $p = p(r, t)$ and $h_{\min} = h_{\min}(t)$ in powers of $k^{1/2} \ll 1$ turn out to be valid only for "short" times $t = O(1)$ when $h_{\min} = O(1)$. Additional asymptotic solutions that are valid for "intermediate" times

$$t = \left\{ \begin{array}{ll} O\left(\ln\left(\frac{1}{k}\right)\right) & \text{when} \quad n = 1, \\ O(k^{-(n-1)/2n}) & \text{when} \quad n \geq 2, \end{array} \right. \tag{4.23}$$

when $h_{\min} = O(k^{1/4})$, and "long" times

$$t = \left\{ \begin{array}{ll} O\left(\ln\left(\frac{1}{k}\right)\right) & \text{when} \quad n = 1, \\ O(k^{-2(n-1)/3n}) & \text{when} \quad n \geq 2, \end{array} \right. \tag{4.24}$$

when $h_{\min} = O(k^{1/3})$, are required in order to obtain a full description of the behaviour up to the contact time.

Note that when the bearing is parabolic, i.e. when $n = 1$, time t is the same asymptotic order, specifically $t = O(\ln(1/k))$, for "intermediate" and "long" times. However, the minimum fluid layer thickness $h_{\min}$, the fluid pressure p and, consequently, r are different asymptotic orders for "intermediate" and "long" times.

When $n \geq 2$ it is found that an algebraic rescaling of time t is required for "intermediate" and "long" times, whereas when $n = 1$ a logarithmic shift forward in time t is required for "intermediate" and "long" times. Thus the case of a parabolic bearing $n = 1$ is treated separately in §4.3.1. All other cases, namely the cases when $n \geq 2$, are treated in §4.3.2.

4.3.1 Parabolic Bearing $n = 1$

4.3.1.1 Solution for "Short" Times $t = O(1)$ when $h_{\min} = O(1)$

Seeking a regular perturbation solution to (4.3) of the form

$$p(r,t) = p_0(r,t) + k^{1/2}p_1(r,t) + O(k) \tag{4.25}$$

and

$$h_{\min}(t) = h_0(t) + k^{1/2}h_1(t) + O(k), \tag{4.26}$$

at $O(1)$ and $O(k^{1/2})$ we have

$$\frac{\partial p_0}{\partial r} = \frac{6r}{(h_0 + r^2)^3}\frac{\mathrm{d}h_0}{\mathrm{d}t} \tag{4.27}$$

and

$$\frac{\partial p_1}{\partial r} = \frac{6r}{(h_0 + r^2)^3}\frac{\mathrm{d}h_1}{\mathrm{d}t} - \frac{18r(1 + \alpha h_1)}{\alpha(h_0 + r^2)^4}\frac{\mathrm{d}h_0}{\mathrm{d}t}, \tag{4.28}$$

respectively. Solving (4.27) and (4.28) subject to the boundary conditions $p_0 \to 0$ and $p_1 \to 0$ as $r \to \infty$ yields the solutions

$$p_0 = -\frac{3}{2(h_0 + r^2)^2}\frac{\mathrm{d}h_0}{\mathrm{d}t} \tag{4.29}$$

and

$$p_1 = -\frac{3}{2(h_0 + r^2)^2}\frac{\mathrm{d}h_1}{\mathrm{d}t} + \frac{3(1 + \alpha h_1)}{\alpha(h_0 + r^2)^3}\frac{\mathrm{d}h_0}{\mathrm{d}t}. \tag{4.30}$$

The solutions p_0 and p_1 must satisfy the load conditions

$$\int_0^\infty p_0 r\,\mathrm{d}r = \frac{L_0}{2\pi} \quad \text{and} \quad \int_0^\infty p_1 r\,\mathrm{d}r = 0 \tag{4.31}$$

and so at $O(1)$ and $O(k^{1/2})$ we have

$$L_0 = -\frac{3\pi}{2h_0}\frac{\mathrm{d}h_0}{\mathrm{d}t} \tag{4.32}$$

and

$$\frac{\mathrm{d}h_1}{\mathrm{d}h_0} - \frac{1}{h_0}h_1 = \frac{1}{\alpha h_0}, \tag{4.33}$$

respectively, where t has been eliminated from (4.33) using (4.32). Solving (4.32) and (4.33) subject to the initial conditions $h_0(0) = d$ and $h_1(0) = 0$ yields the solutions

$$h_0 = d\exp\left(-\frac{2L_0}{3\pi}t\right) \tag{4.34}$$

and

$$h_1 = -\frac{d - h_0}{\alpha d}. \tag{4.35}$$

The leading order solutions for $p = p(r,t)$ and $h_{\min} = h_{\min}(t)$, namely p_0 and h_0, given by (4.29) and (4.34) are the well-known solutions in the case when a parabolic bearing approaches an impermeable ($k = 0$) bed under constant load previously given by (4.13) and (4.8), i.e., as expected, the porous bed is effectively impermeable at leading order. The effects of the permeability first occur at first order. Eliminating $\mathrm{d}h_0/\mathrm{d}t$ and h_1 from (4.29) and (4.30) using (4.32) and (4.35) we have

$$p_0 = \frac{L_0 h_0}{\pi(h_0 + r^2)^2} \quad \text{and} \quad p_1 = -\frac{L_0 h_0\,(h_0 - r^2)}{\pi\alpha d\,(h_0 + r^2)^3}. \tag{4.36}$$

Since p_1 given by (4.36) is negative when $r < h_0^{1/2}$ and positive when $r > h_0^{1/2}$ and h_1 given by (4.35) is negative for all $t > 0$, the effect of the permeability k at first order is to decrease $p_{\max}$, to distribute the fluid pressure p over a larger area, and to decrease the time $t(h_{\min})$ taken for the minimum fluid layer thickness to reduce to a value $h_{\min}$. However, since $h_0 = O(\exp(-2L_0t/3\pi)) \to 0^+$ and $h_1 \to -1/\alpha$ as $t \to \infty$, the expansions (4.25) and (4.26) are not uniformly valid for all t. Comparing the leading and first order terms in the expansion (4.26) suggests that the expansion is uniformly valid provided that

$$t \ll \frac{1}{L_0} \ln\left(\frac{1}{k}\right) \quad \text{and} \quad h_{\min} \gg \frac{k^{1/2}}{\alpha}. \tag{4.37}$$

However, it can be shown that the second order term h_2 satisfies $|h_2| = O(h_0^{-2}) = O(\exp(4L_0t/3\pi)) \to \infty$ as $t \to \infty$ and so comparing the first and second order terms shows that the expansion in fact remains uniformly valid only when

$$t \ll \frac{1}{L_0} \ln\left(\frac{1}{k}\right) \quad \text{and} \quad h_{\min} \gg \frac{k^{1/4}}{\alpha^{1/2}}, \tag{4.38}$$

and therefore a second asymptotic solution that is valid for "intermediate" times $t = O(\ln(1/k))$ when $h_{\min} = O(k^{1/4})$ is required.

4.3.1.2 Solution for "Intermediate" Times $t = O(\ln(1/k))$ when $h_{\min} = O(k^{1/4})$

For "intermediate" times $t = O(\ln(1/k))$ when $h_{\min} = O(k^{1/4})$ we re-scale r, p and $h_{\min}$ and shift t according to

$$r = k^{1/8}\hat{r}, \quad t = \frac{3\pi}{8L_0} \ln\left(\frac{1}{k}\right) + \hat{t}, \quad p = k^{-1/4}\hat{p}, \quad h_{\min} = k^{1/4}\hat{h}, \tag{4.39}$$

where $\hat{r}$, $\hat{t}$, $\hat{p}$ and $\hat{h}$ are $O(1)$ in the limit $k \to 0$. Seeking a regular perturbation solution to (4.3) of the form

$$\hat{p} = \hat{p}_0(\hat{r}, \hat{t}) + k^{1/4}\hat{p}_1(\hat{r}, \hat{t}) + O(k^{1/2}) \tag{4.40}$$

and

$$\hat{h} = \hat{h}_0(\hat{t}) + k^{1/4}\hat{h}_1(\hat{t}) + O(k^{1/2}), \tag{4.41}$$

at $O(1)$ and $O(k^{1/4})$ we have

$$\frac{\partial \hat{p}_0}{\partial \hat{r}} = \frac{6\hat{r}}{(\hat{h}_0 + \hat{r}^2)^3}\frac{\mathrm{d}\hat{h}_0}{\mathrm{d}\hat{t}} \tag{4.42}$$

and

$$\frac{\partial \hat{p}_1}{\partial \hat{r}} = \frac{6\hat{r}}{\alpha(\hat{h}_0 + \hat{r}^2)^6}\left[\alpha(\hat{h}_0 + \hat{r}^2)^3\frac{\mathrm{d}\hat{h}_1}{\mathrm{d}\hat{t}} - 3\left(4\alpha + (1 + \alpha\hat{h}_1)(\hat{h}_0 + \hat{r}^2)^2\right)\frac{\mathrm{d}\hat{h}_0}{\mathrm{d}\hat{t}}\right], \tag{4.43}$$

respectively. Solving (4.42) and (4.43) subject to the boundary conditions $\hat{p}_0 \to 0$ and $\hat{p}_1 \to 0$ as $\hat{r} \to \infty$ yields the solutions

$$\hat{p}_0 = -\frac{3}{2(\hat{h}_0 + \hat{r}^2)^2}\frac{\mathrm{d}\hat{h}_0}{\mathrm{d}\hat{t}} \tag{4.44}$$

and

$$\hat{p}_1 = -\frac{3}{10\alpha(\hat{h}_0 + \hat{r}^2)^5}\left[5\alpha(\hat{h}_0 + \hat{r}^2)^3\frac{\mathrm{d}\hat{h}_1}{\mathrm{d}\hat{t}} - 2\left(12\alpha + 5(1 + \alpha\hat{h}_1)(\hat{h}_0 + \hat{r}^2)^2\right)\frac{\mathrm{d}\hat{h}_0}{\mathrm{d}\hat{t}}\right]. \tag{4.45}$$

The solutions $\hat{p}_0$ and $\hat{p}_1$ must satisfy the load conditions

$$\int_0^\infty \hat{p}_0\hat{r}\,\mathrm{d}\hat{r} = \frac{L_0}{2\pi} \quad \text{and} \quad \int_0^\infty \hat{p}_1\hat{r}\,\mathrm{d}\hat{r} = 0 \tag{4.46}$$

and so at $O(1)$ and $O(k^{1/4})$ we have

$$L_0 = -\frac{3\pi}{2\hat{h}_0}\frac{\mathrm{d}\hat{h}_0}{\mathrm{d}\hat{t}} \tag{4.47}$$

and

$$\frac{\mathrm{d}\hat{h}_1}{\mathrm{d}\hat{h}_0} - \frac{1}{\hat{h}_0}\hat{h}_1 = \frac{6\alpha + 5\hat{h}_0^2}{5\alpha\hat{h}_0^3}, \tag{4.48}$$

respectively. Solving (4.47) and (4.48) subject to the appropriate matching conditions with the solution that is valid at "short" times, namely

$$\hat{h}_0 \sim d\exp\left(-\frac{2L_0}{3\pi}\hat{t}\right) \to \infty, \quad \hat{h}_1 \to -\frac{1}{\alpha} \quad \text{as} \quad \hat{t} \to -\infty, \tag{4.49}$$

yields the solutions

$$\hat{h}_0 = d\exp\left(-\frac{2L_0}{3\pi}\hat{t}\right) \tag{4.50}$$

and

$$\hat{h}_1 = -\frac{2\alpha + 5\hat{h}_0^2}{5\alpha\hat{h}_0^2}. \tag{4.51}$$

This solution, which is valid for "intermediate" times, is qualitatively similar to the solution that is valid for "short" times obtained previously. However, since $\hat{h}_0 = O(\exp(-2L_0\hat{t}/3\pi)) \to 0^+$ and $|\hat{h}_1| = O(\exp(4L_0\hat{t}/3\pi)) \to \infty$ as $\hat{t} \to \infty$, these expansions remain uniformly valid provided only that

$$\hat{t} \ll \frac{1}{L_0}\ln\left(\frac{1}{k}\right) \quad \text{and} \quad \hat{h} \gg k^{1/12}, \quad \text{i.e.} \quad t \ll \frac{1}{L_0}\ln\left(\frac{1}{k}\right) \quad \text{and} \quad h_{\mathrm{min}} \gg k^{1/3}, \tag{4.52}$$

and hence a third (and final) asymptotic solution that is valid for "long" times $t = O(\ln(1/k))$ when $h_{\mathrm{min}} = O(k^{1/3})$ is required.

4.3.1.3 Solution for "Long" Times $t = O(\ln(1/k))$ when $h_{\min} = O(k^{1/3})$

For "long" times $t = O(\ln(1/k))$ when $h_{\min} = O(k^{1/3})$ we re-scale r, p and $h_{\min}$ and shift t according to

$$r = (12k)^{1/6}R, \quad t = \frac{\pi}{2L_0}\ln\left(\frac{1}{k}\right) + T, \quad p = (12k)^{-1/3}P, \quad h_{\min} = (12k)^{1/3}H_{\min}, \tag{4.53}$$

where R, T, P and $H_{\min}$ are $O(1)$ in the limit $k \to 0$ and the factor 12 has been introduced into the scalings for convenience. Seeking a regular perturbation solution to (4.3) of the form

$$P = P_0(R,T) + (12k)^{1/6}P_1(R,T) + O(k^{1/3}) \tag{4.54}$$

and

$$H_{\min} = H_0(T) + (12k)^{1/6}H_1(T) + O(k^{1/3}), \tag{4.55}$$

at $O(1)$ and $O(k^{1/6})$ we have

$$\frac{\partial P_0}{\partial R} = \frac{6R}{(H_0 + R^2)^3 + 1}\frac{\mathrm{d}H_0}{\mathrm{d}T} \tag{4.56}$$

and

$$\begin{aligned}\frac{\partial P_1}{\partial R} \quad = \quad & \frac{3R}{\alpha\left((H_0 + R^2)^3 + 1\right)^2}\left(2\alpha\left((H_0 + R^2)^3 + 1\right)\frac{\mathrm{d}H_1}{\mathrm{d}T}\right. \\ & \left. -\sqrt{3}(1 + 2\sqrt{3}\alpha H_1)(H_0 + R^2)^2\frac{\mathrm{d}H_0}{\mathrm{d}T}\right),\end{aligned} \tag{4.57}$$

respectively. Solving (4.56) and (4.57) subject to the boundary conditions $P_0 \to 0$ and $P_1 \to 0$ as $R \to \infty$ yields the solutions

$$P_0 = -6I_{0,1}(R, H_0, 1)\frac{\mathrm{d}H_0}{\mathrm{d}T} \tag{4.58}$$

and

$$P_1 = -6I_{0,1}(R, H_0, 1)\frac{\mathrm{d}H_1}{\mathrm{d}T} + \frac{3\sqrt{3}(1+2\sqrt{3}\alpha H_1)}{\alpha}I_{2,2}(R, H_0, 1)\frac{\mathrm{d}H_0}{\mathrm{d}T}, \tag{4.59}$$

where we have defined the integral

$$I_{M,N}(R, H_0, n) := \int_R^\infty \frac{s(H_0 + s^{2n})^M}{[(H_0 + s^{2n})^3 + 1]^N}\,\mathrm{d}s \tag{4.60}$$

for any n. The solutions P_0 and P_1 must satisfy the load conditions

$$\int_0^\infty P_0 R\,\mathrm{d}R = \frac{L_0}{2\pi} \quad \text{and} \quad \int_0^\infty P_1 R\,\mathrm{d}R = 0 \tag{4.61}$$

and so at $O(1)$ and $O(k^{1/6})$ we have

$$L_0 = -6\pi J_{0,1}(H_0, 1)\frac{\mathrm{d}H_0}{\mathrm{d}T} \tag{4.62}$$

and

$$J_{0,1}(H_0, 1)\frac{\mathrm{d}H_1}{\mathrm{d}H_0} = \frac{\sqrt{3}(1+2\sqrt{3}\alpha H_1)}{2\alpha}J_{2,2}(H_0, 1), \tag{4.63}$$

respectively, where we have defined the integral

$$J_{M,N}(H_0, n) := \int_0^\infty \frac{s^3(H_0 + s^{2n})^M}{[(H_0 + s^{2n})^3 + 1]^N}\,\mathrm{d}s \tag{4.64}$$

for any n. Note that

$$J_{0,1}(H_0, 1) = \frac{1}{6}\sum_{j=1}^{3} \omega_j (H_0 + \omega_j) \ln(H_0 + \omega_j), \tag{4.65}$$

where

$$\omega_1 = 1, \quad \omega_2 = -\frac{1}{2}(1+\sqrt{3}\mathrm{i}) \quad \text{and} \quad \omega_3 = -\frac{1}{2}(1-\sqrt{3}\mathrm{i}) \tag{4.66}$$

are the cube roots of unity, and so equation (4.62) may be written

$$L_0 = -\pi \left(\sum_{j=1}^{3} \omega_j (H_0 + \omega_j) \ln(H_0 + \omega_j) \right) \frac{\mathrm{d}H_0}{\mathrm{d}T}. \tag{4.67}$$

Solving (4.67) and (4.63) subject to the appropriate the matching conditions with the solution that is valid at "intermediate" times, namely

$$H_0 \sim \frac{d}{12^{1/3}} \exp\left(-\frac{2L_0 T}{3\pi}\right) \to \infty, \quad H_1 \to -\frac{1}{2\sqrt{3}\alpha} \quad \text{as} \quad T \to -\infty, \tag{4.68}$$

yields the solutions

$$T = \frac{\pi}{4L_0}\left(2\left(3(1+\ln d) - \ln 12\right) + \sum_{j=1}^{3} \omega_j (H_0 + \omega_j)^2 \left(1 - 2\ln(H_0 + \omega_j)\right)\right) \tag{4.69}$$

and

$$H_1 = -\frac{1}{2\sqrt{3}\alpha}. \tag{4.70}$$

Unlike the solutions that are valid for "short" and "intermediate" times obtained previously, the permeability k now appears at leading order in the solutions for $p = p(r,t)$ and $h_{\mathrm{min}} = h_{\mathrm{min}}(t)$, and these solutions remain uniformly valid up to the contact time $t = t_{\mathrm{c}}$, which is given by $t_{\mathrm{c}} = (\pi/2L_0)\ln(1/k) + T_{\mathrm{c}}$, where T_{c}

satisfies $H_{\min}(T_{\rm c}) = 0$ and has the asymptotic expansion

$$T_{\rm c} = T_{\rm c0} + (12k)^{1/6} T_{\rm c1} + O(k^{1/3}), \tag{4.71}$$

where

$$H_0(T_{\rm c0}) = 0, \quad T_{\rm c1} = -\frac{H_1(T_{\rm c0})}{H_0'(T_{\rm c0})}, \tag{4.72}$$

so that

$$T_{\rm c0} = \frac{\pi}{4L_0}(9 - 2\ln 12 + 6\ln d), \quad T_{\rm c1} = -\frac{\pi^2}{3\alpha L_0}. \tag{4.73}$$

Therefore, in terms of the original variables the asymptotic expansion for the contact time $t_{\rm c}$ given by (4.71) is

$$t_{\rm c} = \frac{\pi}{2L_0}\ln\left(\frac{1}{12k}\right) + \frac{3\pi}{4L_0}(3 + 2\ln d) - \frac{\pi^2(12k)^{1/6}}{3\alpha L_0} + O(k^{1/3}). \tag{4.74}$$

As in the case of a flat bearing treated in Chapter 3, the leading-order small-k solution for the contact time given by

$$t_{\rm c} = \frac{\pi}{2L_0}\ln\left(\frac{1}{12k}\right) + \frac{3\pi}{4L_0}(3 + 2\ln d) \tag{4.75}$$

does not depend on α or δ, and is, therefore, the same for all three choices of boundary condition (2.17)–(2.19). Figure 4.3 compares the leading-order small-k solution for $t_{\rm c}$ given by (4.75) with the exact solution given by (4.10). The Beavers–Joseph constant α appears at $O(k^{1/6})$ in the small-k expansion for $t_{\rm c}$ given by (4.74), and inspection of the $O(k^{1/6})$ term shows that increasing α (i.e. decreasing the slip length $l_{\rm s}$) increases the contact time $t_{\rm c}$, which is consistent with the behaviour shown in Figure 4.4(a).

The leading-order small-k solution for the maximum fluid pressure $p_{\max} = p(0, t)$, given by setting $R = 0$ in (4.58), has a maximum turning point when $H_0 = H^\star_{\min}$, where $H^\star_{\min} \simeq 0.2478$ (correct to 4 decimal places) is the real positive solution of the equation

$$\left(J_{0,1}(H_0, n)\frac{\mathrm{d}I_{0,1}(0, H_0, n)}{\mathrm{d}H_0} - I_{0,1}(0, H_0, n)\frac{\mathrm{d}J_{0,1}(H_0, n)}{\mathrm{d}H_0} \right)\Bigg|_{H_0=H^\star_{\min}} = 0, \qquad (4.76)$$

i.e.

$$\left(\sum_{j=1}^{3} \omega_j (H^\star_{\min} + \omega_j) \ln(H^\star_{\min} + \omega_j) \right) \sum_{j=1}^{3} \frac{\omega_j}{H^\star_{\min} + \omega_j} = \left(\sum_{j=1}^{3} \omega_j \ln(H^\star_{\min} + \omega_j) \right)^2 . \qquad (4.77)$$

Therefore to leading order in the limit $k \to 0$ and in terms of the original variables, the maximum fluid pressure $p_{\max}$ attains its maximum value when

$$h_{\min} = h^\star_{\min} \simeq 0.5673 \times k^{1/3} \qquad (4.78)$$

which from (4.53) and (4.69) corresponds to the time

$$t = t^\star \simeq \frac{1}{L_0}\left(1.5708 \times \ln\left(\frac{1}{k}\right) + 0.6673 + 4.7124 \times \ln d \right). \qquad (4.79)$$

Figures 4.10(a) and 4.10(b) compare the exact solutions for $h^\star_{\min}$ and $t^\star$ with the leading order small-k solutions given by (4.78) and (4.79), respectively.

4.3.1.4 A Uniformly Valid Leading Order Composite Solution for $p(r, t)$ and $t(h_{\min})$

A uniformly valid leading order composite solution for $p = p(r, t)$ is

$$p(r, t) = \frac{L_0 I_{0,1}(R, H_{\min}, 1)}{\pi (12k)^{1/3} J_{0,1}(H_{\min}, 1)}, \qquad (4.80)$$

where $R = (12k)^{-1/6}r$ and $H_{\min} = (12k)^{-1/3}h_{\min}$. Figure 4.8(c) compares the uniformly valid leading order small-k solution for $p = p(r,t)$ given by (4.80) with the exact solution for $p = p(r,t)$ given by (4.4).

A uniformly valid leading order composite solution for $p_{\max} = p(0,t)$ is given by setting $r = 0$ in (4.80), which yields

$$p_{\max}(t) = -\frac{L_0 \sum_{j=1}^{3} \omega_j \ln(H_{\min} + \omega_j)}{\pi(12k)^{1/3} \sum_{j=1}^{3} \omega_j (H_{\min} + \omega_j) \ln(H_{\min} + \omega_j)}. \tag{4.81}$$

Figure 4.9(a) compares the uniformly valid leading order small-k solution for $p_{\max} = p(0,t)$ given by (4.81) with the exact solution for $p_{\max} = p(0,t)$ given by setting $r = 0$ in (4.4).

A uniformly valid leading order composite solution for the time $t(h_{\min})$ taken for the minimum fluid layer thickness to reduce to a value $h_{\min}$ is

$$\begin{aligned} t(h_{\min}) \quad &= \quad \frac{\pi}{4L_0}\left(2\left[3(1+\ln d) + \ln\left(\frac{1}{12k}\right)\right]\right. \\ &\left. + \sum_{j=1}^{3} \omega_j (H_{\min} + \omega_j)^2 \left[1 - 2\ln(H_{\min} + \omega_j)\right]\right), \end{aligned} \tag{4.82}$$

where $H_{\min} = (12k)^{-1/3}h_{\min}$. Figures 4.2 and 4.4 compare the uniformly valid leading order small-k solution for $t = t(h_{\min})$ given by (4.82) with the exact solution for $t = t(h_{\min})$ given by (4.7). (Note that setting $h_{\min} = d$ in (4.82) yields $t(d) = O(k^{1/3})$ as $k \to 0$, so that to leading order in the limit $k \to 0$ the initial condition (2.51) is satisfied. Similarly, setting $h_{\min} = 0$ in (4.82) we see that to leading order in the limit $k \to 0$ it coincides with (4.75).)

4.3.2 General Bearing Shapes $n \geq 2$

4.3.2.1 Solution for "Short" Times $t = O(1)$

As in §4.3.1.1, seeking a regular perturbation solution to (4.3) in powers of $k^{1/2}$, at $O(1)$ and $O(k^{1/2})$ we have

$$\frac{\partial p_0}{\partial r} = \frac{6r}{(h_0 + r^{2n})^3}\frac{\mathrm{d}h_0}{\mathrm{d}t} \tag{4.83}$$

and

$$\frac{\partial p_1}{\partial r} = \frac{6r}{(h_0 + r^{2n})^3}\frac{\mathrm{d}h_1}{\mathrm{d}t} - \frac{18r(1+\alpha h_1)}{\alpha(h_0 + r^{2n})^4}\frac{\mathrm{d}h_0}{\mathrm{d}t}, \tag{4.84}$$

respectively. Solving (4.83) and (4.84) subject to the boundary conditions $p_0 \to 0$ and $p_1 \to 0$ as $r \to \infty$ yields the solutions

$$p_0 = -6K_3(r, h_0, n)\frac{\mathrm{d}h_0}{\mathrm{d}t} \tag{4.85}$$

and

$$p_1 = -6K_3(r, h_0, n)\frac{\mathrm{d}h_1}{\mathrm{d}t} + \frac{18(1+\alpha h_1)}{\alpha}K_4(r, h_0, n)\frac{\mathrm{d}h_0}{\mathrm{d}t}, \tag{4.86}$$

where we have defined the integral

$$K_M(r, h_0, n) := \int_r^\infty \frac{s}{(h_0 + s^{2n})^M}\,\mathrm{d}s. \tag{4.87}$$

The solutions p_0 and p_1 must, again, satisfy the load conditions (4.31) and so at $O(1)$ and $O(k^{1/2})$ we have

$$L_0 = \begin{cases} -\dfrac{3\pi}{4h_0^2}\dfrac{\mathrm{d}h_0}{\mathrm{d}t} & \text{when} \quad n = 2, \\ -\dfrac{3\pi^2(n-1)(n-2)}{n^3\sin(2\pi/n)h_0^{(3n-2)/n}}\dfrac{\mathrm{d}h_0}{\mathrm{d}t} & \text{when} \quad n \geq 3, \end{cases} \tag{4.88}$$

and

$$\frac{\mathrm{d}h_1}{\mathrm{d}h_0} - \frac{3n-2}{nh_0}h_1 = \frac{3n-2}{\alpha n h_0}, \tag{4.89}$$

respectively. Solving (4.88) and (4.89) subject to the initial conditions $h_0(0) = d$ and $h_1(0) = 0$ yields the solutions

$$h_0 = \begin{cases} \dfrac{3\pi d}{3\pi + 4dL_0 t} & \text{when} \quad n = 2, \\ \left(d^{-2(n-1)/n} + \dfrac{2n^2 \sin(2\pi/n) L_0}{3\pi^2(n-2)} t\right)^{-n/2(n-1)} & \text{when} \quad n \geq 3, \end{cases} \tag{4.90}$$

and

$$h_1 = -\frac{d^{(3n-2)/n} - h_0^{(3n-2)/n}}{\alpha d^{(3n-2)/n}}. \tag{4.91}$$

The leading order solutions for $p = p(r,t)$ and $h_{\min} = h_{\min}(t)$, namely p_0 and h_0 given by (4.85) and (4.90), are the well-known solutions in the case when a bearing of shape $H = r^{2n}$, where $n \geq 2$, approaches an impermeable ($k = 0$) bed under constant load given by (4.13) and (4.8), i.e. as expected, the porous bed is effectively impermeable at leading order. The effect of the permeability first occurs at first order, and since

$$p_1 = \begin{cases} \dfrac{8L_0 h_0^3 (2K_3 - 3h_0 K_4)}{\pi \alpha d^2} & \text{when} \quad n = 2, \\ \dfrac{2n^2 \sin(2\pi/n) L_0 h_0^{(5n-4)/n} \left((3n-2)K_3 - 3nh_0 K_4\right)}{\pi^2 (n-1)(n-2) \alpha d^{(3n-2)/n}} & \text{when} \quad n \geq 3, \end{cases} \tag{4.92}$$

where $K_3 = K_3(r, h_0, n)$ and $K_4 = K_4(r, h_0, n)$ are given by (4.87), is negative when $r < r_1 h_0^{1/2n}$ and positive when $r > r_1 h_0^{1/2n}$, where r_1 is the real positive solution of the equation

$$3nK_4(r_1, 1, n) - (3n-2)K_3(r_1, 1, n) = 0, \tag{4.93}$$

and h_1 given by (4.90) is negative for all $t > 0$, the effect of the permeability k at first order is to decrease $p_{\max} = p(0, t)$ and distribute the fluid pressure p over a larger area, and to decrease the time $t(h_{\min})$ taken for the minimum fluid layer thickness to reduce to a value $h_{\min}$. However, since $h_0 = O(t^{-n/2(n-1)}) \to 0^+$ and $h_1 \to -1/\alpha$ as $t \to \infty$ the expansions in powers of $k^{1/2}$ for $p = p(r, t)$ and $h_{\min} = h_{\min}(t)$ are not uniformly valid for all t. Comparing the leading and first order terms in the expansions suggests that they are uniformly valid provided that

$$t \ll k^{-(n-1)/n}. \tag{4.94}$$

However, it can be shown that the second order term h_2 satisfies $h_2 = O(t^{n/(n-1)}) \to \infty$ as $t \to \infty$, and so comparing the first and second order terms shows that in fact the expansions are only uniformly valid provided that

$$t \ll k^{-(n-1)/2n}, \tag{4.95}$$

and therefore a second asymptotic solution that is valid for "intermediate" times $t = O(k^{-(n-1)/2n})$ is required.

4.3.2.2 Solution for "Intermediate" Times $t = O(k^{-(n-1)/2n})$

For "intermediate" times $t = O(k^{-(n-1)/2n})$ we re-scale r, t, p and $h_{\min}$ according to

$$r = k^{1/8n}\hat{r}, \quad t = k^{-(n-1)/2n}\hat{t}, \quad p = k^{-1/4n}\hat{p}, \quad h_{\min} = k^{1/4}\hat{h}, \tag{4.96}$$

where $\hat{r}$, $\hat{t}$, $\hat{p}$ and $\hat{h}$ are $O(1)$ in the limit $k \to 0$. Like in §4.3.1.2, seeking a regular perturbation solution to (4.3) in powers of $k^{1/4}$, at $O(1)$ and $O(k^{1/4})$ we have

$$\frac{\partial \hat{p}_0}{\partial \hat{r}} = \frac{6\hat{r}}{(\hat{h}_0 + \hat{r}^{2n})^3} \frac{\mathrm{d}\hat{h}_0}{\mathrm{d}\hat{t}} \tag{4.97}$$

and

$$\frac{\partial \hat{p}_1}{\partial \hat{r}} = \frac{6\hat{r}}{\alpha(\hat{h}_0 + \hat{r}^{2n})^6} \left(\alpha(\hat{h}_0 + \hat{r}^{2n})^3 \frac{\mathrm{d}\hat{h}_1}{\mathrm{d}\hat{t}} - 3\left[4\alpha + (1 + \alpha\hat{h}_1)(\hat{h}_0 + \hat{r}^{2n})^2\right] \frac{\mathrm{d}\hat{h}_0}{\mathrm{d}\hat{t}} \right), \tag{4.98}$$

respectively. Solving (4.97) and (4.98) subject to the boundary conditions $\hat{p}_0 \to 0$ and $\hat{p}_1 \to 0$ as $\hat{r} \to \infty$ yields the solutions

$$\hat{p}_0 = -6K_3(\hat{r}, \hat{h}_0, n) \frac{\mathrm{d}\hat{h}_0}{\mathrm{d}\hat{t}} \tag{4.99}$$

and

$$\hat{p}_1 = -6K_3(\hat{r}, \hat{h}_0) \frac{\mathrm{d}\hat{h}_1}{\mathrm{d}\hat{t}} + \frac{18}{\alpha} \left[(1 + \alpha\hat{h}_1)K_4(\hat{r}, \hat{h}_0, n) + 4\alpha K_6(\hat{r}, \hat{h}_0, n)\right] \frac{\mathrm{d}\hat{h}_0}{\mathrm{d}\hat{t}}. \tag{4.100}$$

The solutions $\hat{p}_0$ and $\hat{p}_1$ must, again, satisfy the load conditions (4.46) and so at $O(1)$ and $O(k^{1/4})$ we have

$$L_0 = \begin{cases} -\dfrac{3\pi}{4\hat{h}_0^2} \dfrac{\mathrm{d}\hat{h}_0}{\mathrm{d}\hat{t}} & \text{when} \quad n = 2, \\ -\dfrac{3\pi^2(n-1)(n-2)}{n^3 \sin(2\pi/n)\hat{h}_0^{(3n-2)/n}} \dfrac{\mathrm{d}\hat{h}_0}{\mathrm{d}\hat{t}} & \text{when} \quad n \geq 3, \end{cases} \tag{4.101}$$

and

$$\frac{\mathrm{d}\hat{h}_1}{\mathrm{d}\hat{h}_0} - \frac{(3n-2)}{n\hat{h}_0}\hat{h}_1 = \frac{3n-2}{5\alpha n^3 \hat{h}_0^3} \left[2\alpha(2n-1)(5n-2) + 5n^2\hat{h}_0^2\right], \tag{4.102}$$

respectively. Solving (4.101) and (4.102) subject to the appropriate matching conditions with the solution that is valid at "short" times, namely

$$\hat{h}_0 \sim \left\{ \begin{array}{cc} \dfrac{3\pi}{4L_0\hat{t}} & \text{when} \quad n = 2 \\ \left(\dfrac{3\pi^2(n-2)}{2n^2\sin(2\pi/n)L_0\hat{t}}\right)^{n/2(n-1)} & \text{when} \quad n \geq 3 \end{array} \right\} \to \infty \quad \text{as} \quad \hat{t} \to 0, \tag{4.103}$$

and

$$\hat{h}_1 \to -\frac{1}{\alpha} \quad \text{as} \quad \hat{t} \to 0, \tag{4.104}$$

yields the solutions

$$\hat{h}_0 = \left\{ \begin{array}{cc} \dfrac{3\pi}{4L_0\hat{t}} & \text{when} \quad n = 2, \\ \left(\dfrac{3\pi^2(n-2)}{2n^2\sin(2\pi/n)L_0\hat{t}}\right)^{n/2(n-1)} & \text{when} \quad n \geq 3, \end{array} \right. \tag{4.105}$$

and

$$\hat{h}_1 = -\frac{1}{\alpha} - \frac{2(3n-2)(2n-1)}{5n^2\hat{h}_0^2}. \tag{4.106}$$

This solution, which is valid for "intermediate" times, is qualitatively similar to the solution that is valid for "short" times obtained previously. However, since $\hat{h}_0 = O(\hat{t}^{-n/2(n-1)}) \to 0^+$ and $|\hat{h}_1| = O(\hat{t}^{n/(n-1)}) \to \infty$ as $\hat{t} \to \infty$, the expansions remain uniformly valid provided only that

$$\hat{t} \ll \frac{1}{L_0 k^{(n-1)/6n}}, \quad \text{i.e.} \quad t \ll \frac{1}{L_0 k^{2(n-1)/3n}}, \tag{4.107}$$

and hence a third (and final) asymptotic solution that is valid for "long" times $t = O(k^{-2(n-1)/3n})$ is required.

4.3.2.3 Solution for "Long" Times $t = O(k^{-2(n-1)/3n})$

For "long" times $t = O(k^{-2(n-1)/3n})$ we re-scale r, t, p and $h_{\min}$ according to

$$r = (12k)^{1/6n} R, \quad t = (12k)^{-2(n-1)/3n} T, \quad p = (12k)^{-1/3n} P, \quad h_{\min} = (12k)^{1/3} H_{\min}, \tag{4.108}$$

where R, T, P and $H_{\min}$ are $O(1)$ in the limit $k \to 0$ and the factor 12 has been introduced into the scalings for convenience. As in §4.3.1.3, seeking a regular perturbation solution to (4.3) in powers of $k^{1/6}$, at $O(1)$ and $O(k^{1/6})$ we have

$$\frac{\partial P_0}{\partial R} = \frac{6R}{(H_0 + R^{2n})^3 + 1} \frac{\mathrm{d}H_0}{\mathrm{d}T} \tag{4.109}$$

and

$$\begin{aligned} \frac{\partial P_1}{\partial R} = \; & \frac{3R}{\alpha\left[(H_0 + R^{2n})^3 + 1\right]^2} \left(2\alpha \left[(H_0 + R^{2n})^3 + 1\right] \frac{\mathrm{d}H_1}{\mathrm{d}T} \right. \\ & \left. -\sqrt{3}(1 + 2\sqrt{3}\alpha H_1)(H_0 + R^{2n})^2 \frac{\mathrm{d}H_0}{\mathrm{d}T} \right), \end{aligned} \tag{4.110}$$

respectively. Solving (4.109) and (4.110) subject to the boundary conditions $P_0 \to 0$ and $P_1 \to 0$ as $R \to \infty$ yields the solutions

$$P_0 = -6 I_{0,1}(R, H_0, n) \frac{\mathrm{d}H_0}{\mathrm{d}T} \tag{4.111}$$

and

$$P_1 = -6 I_{0,1}(R, H_0, n) \frac{\mathrm{d}H_1}{\mathrm{d}T} + \frac{3\sqrt{3}(1 + 2\sqrt{3}\alpha H_1)}{\alpha} I_{2,2}(R, H_0, n) \frac{\mathrm{d}H_0}{\mathrm{d}T}. \tag{4.112}$$

The solutions P_0 and P_1 must, again, satisfy the load conditions (4.61) and so at $O(1)$ and $O(k^{1/6})$ we have

$$L_0 = -6\pi J_{0,1}(H_0, n)\frac{\mathrm{d}H_0}{\mathrm{d}T} \tag{4.113}$$

and

$$J_{0,1}(H_0, n)\frac{\mathrm{d}H_1}{\mathrm{d}H_0} = \frac{\sqrt{3}\left(1 + 2\sqrt{3}\alpha H_1\right)}{2\alpha} J_{2,2}(H_0, n), \tag{4.114}$$

respectively. Note that

$$\begin{aligned} J_{0,1}(H_0, n) &= \frac{1}{3}\sum_{j=1}^{3}\omega_j \int_0^\infty \frac{u^3}{H_0 + \omega_j + u^{2n}}\,\mathrm{d}u \\ &= \frac{1}{3n}\sum_{j=1}^{3}\omega_j (H_0+\omega_j)^{(2-n)/n}\int_{C_j}\frac{z^{(4-n)/n}}{1+z^2}\,\mathrm{d}z \\ &= \begin{cases} -\dfrac{1}{12}\displaystyle\sum_{j=1}^{3}\omega_j \ln(H_0+\omega_j) & \text{when} \quad n = 2, \\ \dfrac{\pi}{6n\sin(2\pi/n)}\displaystyle\sum_{j=1}^{3}\omega_j (H_0+\omega_j)^{(2-n)/n} & \text{when} \quad n \geq 3, \end{cases} \end{aligned} \tag{4.115}$$

where ω_j, $j = 1, 2, 3$, are, again, the cube roots of unity given by (4.66) and C_j, $j = 1, 2, 3$, are the rays emanating from the origin in the complex plane in the direction of $(H_0 + \omega_j)^{-1/2}$. Furthermore, noting that $-\pi/2 < \mathrm{Arg}((H_0 + \omega_j)^{-1/2}) < \pi/2$, $j = 1, 2, 3$, in order to evaluate the contour integrals in (4.115) for $n \geq 3$ we have made use of the result obtained in Appendix E. In Appendix E it is shown that the integral

$$I = \int_C \frac{z^a}{1+z^2}\,\mathrm{d}z, \quad a \in \mathbb{R}, \tag{4.116}$$

where C is a ray that emanates from the origin in the complex plane and makes an angle ϕ, satisfying $-\pi/2 < \phi < \pi/2$, with the positive real axis, is independent of the direction of the ray provided that $-1 < a < 1$. Therefore, in (4.115) we have made use of the fact that when $n \geq 3$ the integrals

$$\int_{C_j} \frac{z^{(4-n)/n}}{1+z^2}\,\mathrm{d}z = \int_0^\infty \frac{z^{(4-n)/n}}{1+z^2}\,\mathrm{d}z = \frac{\pi}{2\sin(2\pi/n)}, \quad j = 1, 2, 3. \tag{4.117}$$

Thus equation (4.113) may be written

$$L_0 = \begin{cases} \dfrac{\pi}{2}\left(\displaystyle\sum_{j=1}^{3} \omega_j \ln(H_0+\omega_j)\right)\dfrac{\mathrm{d}H_0}{\mathrm{d}T} & \text{when} \quad n = 2, \\ -\dfrac{\pi^2}{n\sin(2\pi/n)}\left(\displaystyle\sum_{j=1}^{3} \omega_j (H_0+\omega_j)^{-(n-2)/n}\right)\dfrac{\mathrm{d}H_0}{\mathrm{d}T} & \text{when} \quad n \geq 3. \end{cases} \tag{4.118}$$

Solving (4.118) and (4.114) subject to the appropriate matching conditions with the solution that is valid at "intermediate" times, namely

$$H_0 \sim \left.\begin{cases} \dfrac{3\pi}{4L_0T} & \text{when} \quad n = 2 \\ \left(\dfrac{3\pi^2(n-2)}{2n^2\sin(2\pi/n)L_0T}\right)^{n/2(n-1)} & \text{when} \quad n \geq 3 \end{cases}\right\} \to \infty \quad \text{as} \quad T \to 0 \tag{4.119}$$

and

$$H_1 \to -\frac{1}{2\sqrt{3}\alpha} \quad \text{as} \quad T \to 0, \tag{4.120}$$

yields the solutions

$$T = \begin{cases} \dfrac{\pi}{2L_0}\displaystyle\sum_{j=1}^{3} \omega_j (H_0+\omega_j)\left[\ln(H_0+\omega_j) - 1\right] & \text{when} \quad n = 2, \\ -\dfrac{\pi^2}{2\sin(2\pi/n)L_0}\displaystyle\sum_{j=1}^{3} \omega_j (H_0+\omega_j)^{2/n} & \text{when} \quad n \geq 3, \end{cases} \tag{4.121}$$

and

$$H_1 = -\frac{1}{2\sqrt{3}\alpha}. \tag{4.122}$$

Unlike the solutions that are valid for "short" and "intermediate" times obtained previously, the permeability k now appears at leading order in the solutions for $p = p(r,t)$ and $h_{\rm min} = h_{\rm min}(t)$, and these solutions remain uniformly valid up to the contact time $t = t_{\rm c}$, which has the asymptotic expansion

$$t_{\rm c} = \frac{\pi^2 \csc[(2+n)\pi/3n]}{2L_0(12k)^{2(n-1)/3n}} - \frac{\pi^2 \csc(2\pi/3n)}{2\sqrt{3}\alpha n L_0(12k)^{(3n-4)/6n}} + O(k^{-(n-2)/3n}). \qquad (4.123)$$

(Note that letting $n \to \infty$ in (4.123) we recover the result for a flat bearing obtained in Chapter 3.) As in the cases of a flat bearing (Chapter 3) and a parabolic bearing (§4.3.1), the leading order small-k solution for the contact time, given by

$$t_{\rm c} = \frac{\pi^2 \csc[(2+n)\pi/3n]}{2L_0(12k)^{2(n-1)/3n}} \qquad (4.124)$$

does not depend on α or δ, and is, therefore, the same for all three choices of boundary condition (2.17)–(2.19). Figure 4.3 compares the leading order small-k solution for $t_{\rm c}$ given by (4.124) with the exact solution given by (4.10). The Beavers–Joseph constant α appears at first order in the small-k expansion for $t_{\rm c}$ given by (4.123), and inspection of the first-order term shows that increasing α (i.e. decreasing the slip length $l_{\rm s}$) increases the contact time $t_{\rm c}$, which is consistent with the behaviour shown in Figure 4.4(b).

The leading order small-k solution for the maximum fluid pressure $p_{\rm max} = p(0,t)$, given by setting $R = 0$ in (4.111), has a maximum turning point at the time

$$t = t^\star = (12k)^{-2(n-1)/3n} T(H^\star_{\rm min}) \qquad (4.125)$$

n	$H^{\star}_{\min}$
1	0.2478
2	0.7317
3	0.8492
5	0.9363
10	0.9987
25	1.0351

Table 4.1: The real positive solutions of (4.76)

when the minimum fluid layer thickness satisfies

$$h_{\min} = h^{\star}_{\min} = H^{\star}_{\min}(12k)^{1/3}, \tag{4.126}$$

where $H^{\star}_{\min}$ is the real positive solution of (4.76). Table 4.1 contains the real positive solutions of (4.76) (correct to 4 decimal places) for several values of n. Figures 4.10(a) and 4.10(b) compare the exact solutions for $h^{\star}_{\min}$ and $t^{\star}$ with the leading order small-k solutions given by (4.126) and (4.125), respectively.

4.3.2.4 A Uniformly Valid Leading Order Composite Solution for $p(r,t)$ and $t(h_{\min})$

A uniformly valid leading-order composite solution for the fluid pressure $p = p(r,t)$ is

$$p(r,t) = \frac{L_0 I_{0,1}(R, H_{\min}, n)}{\pi(12k)^{1/3n} J_{0,1}(H_{\min}, n)}, \tag{4.127}$$

where $R = (12k)^{-1/6n} r$ and $H_{\min} = (12k)^{-1/3} h_{\min}$. Figure 4.8(d) compares the leading order small-k solution for $p = p(r,t)$ given by (4.127) with the exact solution for $p = p(r,t)$ given by (4.4).

A uniformly valid leading-order composite solution for $p_{\max} = p(0,t)$ is given by setting $r = 0$ in (4.127), which yields

$$p_{\max}(t) = \begin{cases} \dfrac{6L_0 \displaystyle\sum_{j=1}^{3} \omega_j (H_{\min} + \omega_j)^{-1/2}}{(12k)^{1/6} \displaystyle\sum_{j=1}^{3} \omega_j \ln(H_{\min} + \omega_j)} & \text{when} \quad n = 2, \\ -\dfrac{2L_0 \cos(\pi/n) \displaystyle\sum_{j=1}^{3} \omega_j \left(H_{\min} + \omega_j\right)^{-(n-1)/n}}{\pi (12k)^{1/3n} \displaystyle\sum_{j=1}^{3} \omega_j \left(H_{\min} + \omega_j\right)^{-(n-2)/n}} & \text{when} \quad n \geq 3. \end{cases} \tag{4.128}$$

Figure 4.9(b) compares the uniformly valid leading order small-k solution for $p_{\max} = p(0,t)$ given by (4.128) with the exact solution for $p_{\max} = p(0,t)$ given by setting $r = 0$ in (4.4).

Uniformly valid leading order composite solutions for the time $t(h_{\min})$ taken for the minimum fluid layer thickness to reduce to a value $h_{\min}$ are

$$t(h_{\min}) = \frac{\pi \left(-3(12k)^{1/3} + 2d \displaystyle\sum_{j=1}^{3} \omega_j (H_{\min} + \omega_j) \left[\ln(H_{\min} + \omega_j) - 1\right] \right)}{4L_0 d (12k)^{1/3}} \tag{4.129}$$

when $n = 2$, and

$$t(h_{\min}) = \frac{\pi^2 \left(3(2-n)(12k)^{2(n-1)/3n} - n^2 d^{2(n-1)/n} \displaystyle\sum_{j=1}^{3} \omega_j (H_{\min} + \omega_j)^{2/n} \right)}{2n^2 \sin(2\pi/n) L_0 \left(12d^3 k\right)^{2(n-1)/3n}} \tag{4.130}$$

when $n \geq 3$, where $H_{\min} = (12k)^{-1/3} h_{\min}$. Figures 4.2 and 4.4 compare the uniformly valid leading order small-k solution for $t = t(h_{\min})$ given by (4.129) with the exact solution for $t = t(h_{\min})$ given by (4.7). (Note that setting $h_{\min} = d$ in both (4.129) and (4.130) yields $t(d) = O(k)$ as $k \to 0$, so that both (4.129) and

(4.130) satisfy the initial condition (2.51) to leading order in the limit $k \to 0$. Similarly, setting $h_{\min} = 0$ in both (4.129) and (4.130) we see that they both coincide with (4.124) to leading order in the limit $k \to 0$.)

4.4 Limit of Large Permeability $k \to \infty$

In this section asymptotic solutions for the fluid pressure $p = p(r,t)$ and the minimum fluid layer thickness $h_{\min} = h_{\min}(t)$ in the limit of large permeability $k \to \infty$ are obtained. In this limit it will transpire that the contact time

$$t_c = \left\{ \begin{array}{ll} O(k^{-1/2} \ln k) & \text{when} \quad n = 1 \\ O(k^{-(2n-1)/2n}) & \text{when} \quad n \geq 2 \end{array} \right\} \ll 1 \tag{4.131}$$

is small, and, unlike in the limit of small permeability $k \to 0$ treated in §4.3, there are inner $r = O(k^{1/8n})$ and outer $r = O(k^{1/4n})$ regions in which different (uniformly valid in time) large-k solutions for the fluid pressure $p = p(r,t)$ are valid. In the case of a parabolic bearing $n = 1$ the contributions to the normal force F_z exerted on the bearing by the fluid in the inner and the outer regions are both algebraically $O(1)$ and so we must, therefore, obtain the asymptotic solution for $p = p(r,t)$ in both regions in order to obtain the correct leading order asymptotic solution for the minimum fluid layer thickness $h_{\min} = h_{\min}(t)$. The case of a parabolic bearing $n = 1$ is treated in §4.4.1. However, for bearings of shape $H = r^{2n}$, where $n \geq 2$, the contribution to the normal force F_z exerted on the bearing by the fluid in the outer region is smaller than the contribution from the inner region and, therefore, we need only obtain the asymptotic solution for $p = p(r,t)$ in the inner region in order to obtain the correct leading order asymptotic solution for the minimum fluid layer thickness $h_{\min} = h_{\min}(t)$. The case $n \geq 2$ is treated in §4.4.2.

4.4.1 Parabolic Bearing $n = 1$

Since the contact time $t_c = O(k^{-1/2} \ln k)$ we re-scale time t according to

$$t = k^{-1/2}(\ln k)T, \tag{4.132}$$

where T is $O(1)$ in the limit $k \to \infty$. There are inner and outer regions in which different large-k solutions for the fluid pressure $p = p(r, t)$ are valid.

4.4.1.1 Inner Solution for $p(r, t)$ valid when $r = O(k^{1/8})$

In the inner region $r = O(k^{1/8})$ we re-scale r and p according to

$$r = k^{1/8}\hat{r}, \quad p = k^{-1/4}(\ln k)^{-1}\hat{p}, \tag{4.133}$$

where $\hat{r}$ and $\hat{p}$ are $O(1)$ in the limit $k \to \infty$. In terms of the re-scaled variables (4.132) and (4.133) and to leading order in the limit $k \to \infty$ equation (4.3) is

$$\frac{\partial \hat{p}}{\partial \hat{r}} = \frac{\hat{r}}{2 + \alpha \hat{r}^4} \frac{\mathrm{d}h_{\min}}{\mathrm{d}T}. \tag{4.134}$$

Solving (4.134) subject to the boundary condition $\hat{p} \to 0$ as $\hat{r} \to \infty$ yields, in terms of the original variables, the solution

$$p = -\frac{1}{\sqrt{8\alpha}k^{3/4}} \left[\frac{\pi}{2} - \tan^{-1}\left(\sqrt{\frac{\alpha}{2}} \frac{r^2}{k^{1/4}} \right) \right] \frac{\mathrm{d}h_{\min}}{\mathrm{d}t}, \tag{4.135}$$

so that

$$p \sim -\frac{1}{2\alpha k^{1/2} r^2} \frac{\mathrm{d}h_{\min}}{\mathrm{d}t} \quad \text{as} \quad r \to \infty. \tag{4.136}$$

Note that if the solution for $p = p(r, t)$ given by (4.135) is used in the load condition (2.59) then the integral diverges logarithmically in the limit $r \to \infty$, showing that

(4.135) is not valid in the limit $r \to \infty$. In fact, there is an outer region $r = O(k^{1/4})$ in which a different large-k solution for the fluid pressure $p = p(r,t)$ is valid. This singularity is resolved subsequently in §4.4.1.3 where a uniformly valid leading order composite solution for $p = p(r,t)$ is constructed.

4.4.1.2 Outer Solution for $p(r,t)$ valid when $r = O(k^{1/4})$

In the outer region $r = O(k^{1/4})$ we re-scale r and p according to

$$r = k^{1/4}R, \quad p = k^{-1/2}(\ln k)^{-1}P, \tag{4.137}$$

where R and P are $O(1)$ in the limit $k \to \infty$. In terms of the re-scaled variables (4.132) and (4.137) and to leading order in the limit $k \to \infty$ equation (4.3) is

$$\frac{\partial P}{\partial R} = \frac{6(1+\alpha R^2)}{R^3(6\alpha + 4R^2 + \alpha R^4)} \frac{\mathrm{d}h_{\min}}{\mathrm{d}T}. \tag{4.138}$$

Solving (4.138) subject to the boundary condition $P \to 0$ as $R \to \infty$ yields, in terms of the original variables, the solution

$$p = -\frac{6}{k}\left(\int_{r/k^{1/4}}^{\infty} \frac{1+\alpha u^2}{u^3(6\alpha + 4u^2 + \alpha u^4)}\,\mathrm{d}u\right)\frac{\mathrm{d}h_{\min}}{\mathrm{d}t}, \tag{4.139}$$

so that

$$p \sim -\frac{1}{2\alpha k^{1/2} r^2}\frac{\mathrm{d}h_{\min}}{\mathrm{d}t} \quad \text{as} \quad r \to 0. \tag{4.140}$$

The solution for $p = p(r,t)$ given by (4.139) is singular at leading (and first) order in the limit $r \to 0$, and if it is used in the load condition (2.59) then the integral diverges logarithmically in the limit $r \to 0$, showing that (4.139) is not valid in the limit $r \to 0$. This singularity is resolved in the following subsection §4.4.1.3 where a uniformly valid leading order composite solution for $p = p(r,t)$ is constructed.

(Note that the outer limit, i.e. the limit $r \to \infty$, of the inner solution (4.135) automatically matches (at leading order) with the inner limit, i.e. the limit $r \to 0$, of the outer solution (4.139).)

4.4.1.3 A Uniformly Valid Leading Order Composite Solution for $p(r, t)$

A uniformly valid leading order composite solution for $p = p(r, t)$ is

$$\begin{aligned} p(r,t) \quad &= \quad -\frac{1}{8\alpha k}\left[\sqrt{8\alpha}k^{1/4}\left(\frac{\pi}{2}-\tan^{-1}\left(\sqrt{\frac{\alpha}{2}}\frac{r^2}{k^{1/4}}\right)\right)\right. \\ &\quad \left. +48\alpha\int_{r/k^{1/4}}^{\infty}\frac{1+\alpha\tilde{r}^2}{\tilde{r}^3(\alpha\tilde{r}^4+4\tilde{r}^2+6\alpha)}\,\mathrm{d}\tilde{r}-\frac{4k^{1/2}}{r^2}\right]\frac{\mathrm{d}h_{\min}}{\mathrm{d}t}. \end{aligned} \tag{4.141}$$

Applying the load condition (2.59) to (4.141) yields the equation governing the leading order large-k solution for $h_{\min} = h_{\min}(t)$:

$$L_0 = -\frac{\pi(\ln k + g(\alpha))}{8\alpha k^{1/2}}\frac{\mathrm{d}h_{\min}}{\mathrm{d}t}, \tag{4.142}$$

where the function $g = g(\alpha)$ is defined by

$$g(\alpha) := 2\ln(3\alpha) + \frac{4(1-3\alpha^2)}{\sqrt{2(2-3\alpha^2)}}\ln\left(\frac{2-\sqrt{2(2-3\alpha^2)}}{2+\sqrt{2(2-3\alpha^2)}}\right). \tag{4.143}$$

Figure 4.14 shows a plot of g given by (4.143) as a function of α. Figure 4.8(e) compares the uniformly valid leading order large-k solution for $p = p(r, t)$ given by (4.141) with the exact solution for $p = p(r, t)$ given by (4.4). Note that the solution given by (4.141) is logarithmically singular in the limit $r \to 0$. This is a consequence of the fact that the leading order outer solution for $p = p(r, t)$ given by (4.139) is singular at both leading and first order in the limit $r \to 0$. However, since the singularity is logarithmic it does not result in an infinite normal force F_z being exerted on the bearing by the fluid, and therefore the load condition (2.59)

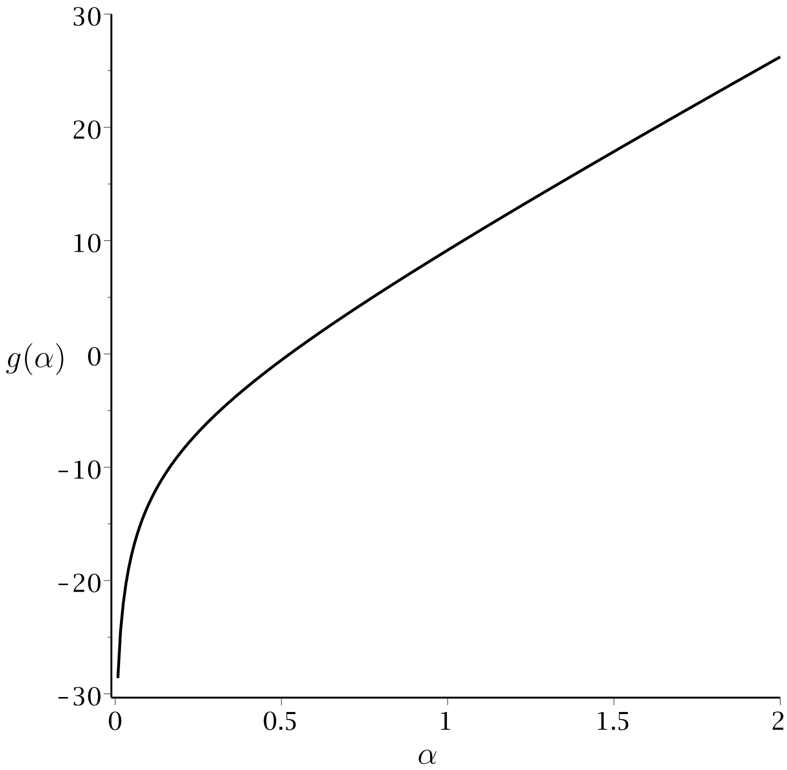

Figure 4.14: A plot of $g(\alpha)$ given by (4.143) as a function of α

can be applied to the uniformly valid leading order large-k solution for $p = p(r,t)$ given by (4.141) to obtain the equation governing the leading order large-k solution for $h_{\min} = h_{\min}(t)$.

Setting $r = 0$ in (4.135), where $\mathrm{d}h_{\min}/\mathrm{d}t$ is given by (4.142), we obtain the leading order large-k solution for the maximum fluid pressure $p_{\max}$:

$$p_{\max} = \frac{\sqrt{2\alpha}L_0}{k^{1/4}(\ln k + g(\alpha))}. \tag{4.144}$$

Figure 4.9(a) compares the leading order large-k solution for $p_{\max}$ given by (4.144) with the exact solution given by setting $r = 0$ in (4.4).

4.4.1.4 Asymptotic Solution for the Minimum Fluid Layer Thickness and Contact Time

Solving (4.142) subject to the initial condition (2.51) yields the solution

$$t = \frac{\pi(\ln k + g(\alpha))}{8\alpha L_0 k^{1/2}}(d - h_{\mathrm{min}}), \tag{4.145}$$

i.e.

$$h_{\mathrm{min}} = d - \frac{8\alpha L_0 k^{1/2}}{\pi(\ln k + g(\alpha))}t. \tag{4.146}$$

Figures 4.2(a) and 4.4(c) compare the leading order large-k asymptotic solution for $t = t(h_{\mathrm{min}})$ given by (4.145) with the exact solution given by (4.7). Setting $h_{\mathrm{min}} = 0$ in (4.145) we obtain the leading order large-k solution for the contact time t_{c}:

$$t_{\mathrm{c}} = \frac{\pi d(\ln k + g(\alpha))}{8\alpha L_0 k^{1/2}}. \tag{4.147}$$

Figure 4.3 compares the leading order large-k solution for the contact time t_{c} given by (4.147) with the exact solution given by (4.10). In contrast to the limit of small permeability $k \to 0$, the leading order large-k solution for the contact time t_{c} given by (4.147) depends on α. Inspection of (4.147) shows that increasing α (i.e. decreasing the slip length l_{s}) decreases the contact time t_{c}, which is consistent with the behaviour shown in Figure 4.4(c). Note that the asymptotic solution for t_{c} given by (4.147) is not uniformly valid in the limit $\alpha \to \infty$ (i.e. in the special case of zero slip length $l_{\mathrm{s}} = 0$) corresponding to the boundary conditions (2.18) and (2.19). These cases are treated separately in Appendices C and D, respectively.

4.4.2 General Bearing Shapes $n \geq 2$

Since the contact time $t_c = O(k^{-(2n-1)/2n})$ and the maximum fluid pressure $p_{\max} = O(k^{-1/4n})$ we re-scale r, p and t according to

$$r = k^{1/8n} R, \quad t = k^{-(2n-1)/2n} T, \quad p = k^{-1/4n} P, \tag{4.148}$$

where R, T and P are $O(1)$ in the limit $k \to \infty$.

4.4.2.1 Asymptotic Solution for the Fluid Pressure

In terms of the re-scaled variables (4.148) and to leading order in the limit $k \to \infty$ equation (4.3) is

$$\frac{\partial P}{\partial R} = \frac{R}{2 + \alpha R^{4n}} \frac{\mathrm{d}h_{\min}}{\mathrm{d}T}. \tag{4.149}$$

Solving (4.149) subject to the boundary condition $P \to 0$ as $R \to \infty$ yields, in terms of the original variables, the solution

$$p = -\frac{1}{k^{(4n-1)/4n}} \left(\int_{k^{-1/8n} r}^{\infty} \frac{\tilde{r}}{2 + \alpha \tilde{r}^{4n}} \, \mathrm{d}\tilde{r} \right) \frac{\mathrm{d}h_{\min}}{\mathrm{d}t}. \tag{4.150}$$

Applying the load condition (2.59) to (4.150) yields the equation governing the leading order large-k solution for $h_{\min} = h_{\min}(t)$:

$$L_0 = -\frac{\pi^2 \csc(\pi/n)}{8n k^{(2n-1)/2n}} \left(\frac{2}{\alpha} \right)^{1/n} \frac{\mathrm{d}h_{\min}}{\mathrm{d}t}. \tag{4.151}$$

Figure 4.8(f) compares the leading order large-k solution for $p = p(r,t)$ given by (4.150) with the exact solution given by (4.4). Note that the solution for $p = p(r,t)$ given by (4.150) diverges from the exact solution given by (4.4) as $r \to \infty$. This is a consequence of the fact that (4.150) is not uniformly valid in r. There is an outer region $r = O(k^{1/4n})$ in which a different large-k solution for $p = p(r,t)$ is valid. However, the contribution to the normal force F_z exerted on the bearing by the fluid in this outer region is $o(1)$ and so we do not, therefore, need to pursue this any further.

Setting $r = 0$ in (4.150) we obtain the leading order large-k solution for the maximum fluid pressure $p_{\max}$:

$$p_{\max} = \frac{2\cos(\pi/2n)L_0}{\pi k^{1/4n}} \left(\frac{\alpha}{2}\right)^{1/2n}. \tag{4.152}$$

Figure 4.9(b) compares the leading order large-k solution for $p_{\max}$ given by (4.152) with the exact solution given by setting $r = 0$ in (4.4).

4.4.2.2 Asymptotic Solution for the Minimum Fluid Layer Thickness and Contact Time

Solving (4.151) subject to the initial condition (2.51) yields the solution

$$t = \frac{\pi^2 \csc(\pi/n)}{8nL_0 k^{(2n-1)/2n}} \left(\frac{2}{\alpha}\right)^{1/n} (d - h_{\min}), \tag{4.153}$$

i.e.

$$h_{\min} = d - \frac{8n\sin(\pi/n)L_0 k^{(2n-1)/2n}}{\pi^2} \left(\frac{\alpha}{2}\right)^{1/n} t. \tag{4.154}$$

Figures 4.2(b) and 4.4(d) compare the leading order large-k solution for $t = t(h_{\min})$ given by (4.153) with the exact solution given by (4.7). Setting $h_{\min} = 0$ in (4.153) we obtain the leading order large-k solution for the contact time t_c:

$$t_c = \frac{\pi^2 d \csc(\pi/n)}{8nL_0 k^{(2n-1)/2n}} \left(\frac{2}{\alpha}\right)^{1/n}. \tag{4.155}$$

Figure 4.3 compares the leading order large-k solution for the contact time t_c given by (4.155) with the exact solution given by (4.10). As in the case of a parabolic bearing $n = 1$ (§4.4.1), when $n \geq 2$ the leading order large-k solution for the contact time t_c given by (4.155) depends on α, and inspection of (4.155) shows that increasing α decreases the contact time t_c, which is consistent with the behaviour shown in Figure 4.4(d). As in the case of a parabolic bearing $n = 1$ (§4.4.1), the asymptotic solution for t_c given by (4.155) is not uniformly valid in the limit $\alpha \to \infty$ corresponding to the boundary conditions (2.18) and (2.19). These cases are treated separately in Appendices C and D, respectively.

Note that letting $n \to \infty$ in (4.155) we recover the result for a flat bearing obtained in Chapter 3.

4.5 Conclusions

In this Chapter we considered the axisymmetric squeeze-film flow in the thin gap between a thin stationary porous bed and a smooth rigid impermeable curved bearing with shape $H \propto r^{2n}$, where n is an integer, moving towards the porous bed under a prescribed constant load L_0. The Reynolds equation that governs the fluid pressure $p = p(r, t)$ was solved yielding an explicit solution for p given by (4.4) in terms of an integral that was evaluated numerically. This solution for p was then used in the load condition (2.59) to yield the differential equation (4.5) governing the minimum fluid layer thickness $h_{\min} = h_{\min}(t)$, which was then solved yielding an explicit expression for the time $t(h_{\min})$ taken for the minimum fluid layer thickness to reduce to a value $h_{\min}$, given by (4.7), in terms of a double integral that was evaluated numerically. It was shown that, in contrast to the case $k = 0$ treated by Stone [66], the bearing and the porous bed always touch in a finite contact time t_c, given by (4.10). The contact time t_c was shown to increase as the permeability k decreased, and, in fact, it was shown in §4.3 that to leading order in the limit of small permeability $k \to 0$ the contact time

$$t_c = \left\{ \begin{array}{lll} O\left(\ln\left(\frac{1}{k}\right)\right) & \text{when} & n = 1 \\ O(k^{-2(n-1)/3n}) & \text{when} & n \geq 2 \end{array} \right\} \gg 1 \tag{4.156}$$

is large, and it was shown in §4.4 that to leading order in the limit of large permeability $k \to \infty$ the contact time

$$t_c = \left\{ \begin{array}{lll} O(k^{-1/2}\ln k) & \text{when} & n = 1 \\ O(k^{-(2n-1)/2n}) & \text{when} & n \geq 2 \end{array} \right\} \ll 1 \tag{4.157}$$

is small.

For "small" values of k it was found that increasing n increased t_c, i.e. the contact time t_c is longer for flatter bearings, whereas for "large" values of k increasing n decreased t_c, i.e. the contact time t_c is shorter for flatter bearings. This behaviour was confirmed by the analysis of the asymptotic limits $k \to 0$ and $k \to \infty$ given in §4.3 and §4.4, respectively, and is readily seen from equations (4.156) and (4.157). Furthermore, it was shown that, similarly to the case of a flat bearing treated in Chapter 3, for "small" values of k the velocity slip on the interface $z = 0$ between the fluid and porous layers, introduced via the application of the Beavers–Joseph boundary condition (2.17) on this interface, has a negligible effect on the contact time t_c, and in fact to leading order in the limit of small permeability $k \to 0$ the contact time t_c, given by (4.75) when $n = 1$ and (4.124) when $n \geq 2$, was found to be independent of the Beavers–Joseph constant α and identical for all three choices of boundary condition (2.17)–(2.19). However, it was shown that for "large" values of k the velocity slip on the interface $z = 0$ has a non-negligible effect on the contact time t_c. In fact, to leading order in the limit of large permeability $k \to \infty$ the contact time t_c, given by (4.147) when $n = 1$ and (4.155) when $n \geq 2$, depends on the Beavers–Joseph constant α and increasing α, i.e. decreasing the slip length l_s, decreases the contact time t_c.

As well as calculating the contact time t_c, the fluid pressure $p = p(r, t)$ was also calculated and is given by (4.4). In contrast to the case $k = 0$, it was shown that when the bed is permeable, i.e. when $k > 0$, the fluid pressure p remains finite as the bearing approaches the porous bed. The maximum fluid pressure $p_{\max}$ was shown to increase as k decreases, and, in fact, it was shown in §4.3 that to leading order in the limit of small permeability $k \to 0$ the maximum fluid pressure

$$p_{\max} = O(k^{-1/3n}) \gg 1 \tag{4.158}$$

is large, and it was shown in §4.4 that to leading order in the limit of large permeability $k \to \infty$ the maximum fluid pressure

$$p_{\max} = \left\{ \begin{array}{ccc} O(k^{-1/4}(\ln k)^{-1}) & \text{when} & n = 1 \\ O(k^{-1/4n}) & \text{when} & n \geq 2 \end{array} \right\} \ll 1 \tag{4.159}$$

is small. For "small" values of k it was shown that increasing n decreases $p_{\max}$, i.e. for flatter bearings $p_{\max}$ decreases and p is distributed over a larger area, whereas for "large" values of k increasing n increases $p_{\max}$, i.e. for flatter bearings $p_{\max}$ increases and p becomes localised over a smaller area. This behaviour was confirmed by the analysis of the asymptotic limits $k \to 0$ and $k \to \infty$ given in §4.3 and §4.4, respectively, and is readily seen from equations (4.158) and (4.159). Furthermore, it was shown that for small values of k the maximum value of $p_{\max}$

does not occur at the contact time t_c. The maximum fluid pressure $p_{\max}$ increases monotonically in time to its maximum value $p^{\star}_{\max}$ which it attains at some time $t^{\star} < t_c$ and then decreases to its value at the contact time t_c. This behaviour was confirmed by the analysis of the asymptotic limit $k \to 0$ given in §4.3.

The paths of fluid particles initially situated in the fluid layer and fluid particles initially situated in the porous bed were calculated in §4.2.4. It was shown that as the permeability k increases the fluid particles that flow from the fluid layer into the porous bed penetrate deeper and wider into the porous bed. It was also shown that, though the maximum penetration depth z_{pen} of these fluid particles, given by (4.21), is independent of n, increasing n widens the region into which these fluid particles penetrate into the porous bed. Furthermore it was shown that, unlike in the case of a flat bearing treated in Chapter 3, there are fluid particles, initially situated in the porous bed, that flow from the porous bed into the fluid layer. In fact it was shown that there are fluid particles, initially situated in the fluid layer, that flow from the fluid layer into the porous bed and then re-emerge into the fluid layer. The region in the fluid layer in which these fluid particles are initially situated was calculated.

Chapter 5

Squeeze-film Flow between a Curved Bearing Coated with an Elastic Layer and a Porous Bed

5.1 Introduction

In Chapter 4 we considered the axisymmetric thin film flow in the gap between a thin stationary porous bed and a smooth rigid impermeable curved bearing (with shape $H \propto r^{2n}$, where n is an integer). In particular, it was shown that when the bearing approaches the stationary porous bed under a constant load, contact between the bearing and the porous bed always occurs in a finite contact time t_c. In this Chapter we consider the effect of coating the bearing with a thin elastic layer, i.e. we consider the axisymmetric squeeze-film flow in the thin gap between a thin stationary porous bed and a smooth rigid impermeable curved bearing (again with shape $H \propto r^{2n}$, where $n \geq 1$ is an integer) coated with a thin elastic layer (see Figure 5.1). The equations governing the fluid pressure p and the minimum

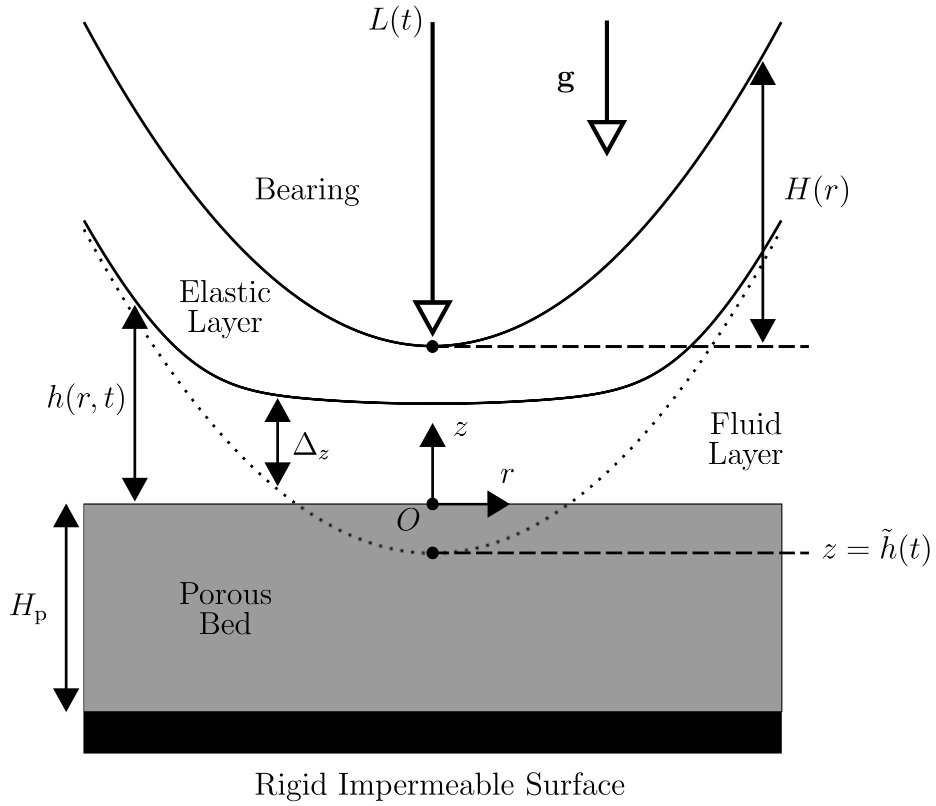

Figure 5.1: The geometry of the axisymmetric problem. The dotted line shows the lower surface of the undeformed elastic layer given by $z = \tilde{h}(t) + H(r)$

height of the undeformed interface between the fluid layer and the elastic layer $\tilde{h}$ (which, when both are known, yield the fluid layer thickness via (2.58)) were derived in Chapter 2. In this Chapter we focus solely on the case when there is no slip relative to the stationary porous bed at the interface between the fluid layer and the porous bed at $z = 0$, i.e. the radial fluid velocity v_r satisfies $v_r = 0$ on this interface, corresponding to the boundary condition (2.19). Recall that this choice of boundary condition corresponds to the parameter choices $\alpha \to \infty$, i.e. the slip-length $l_s = 0$, and $\delta = 0$. In Chapters 3 and 4 it was shown that to leading order in the limit of small permeability $k \to 0$, the limit most relevant to the knee, the solutions for the fluid pressure p and the fluid layer thickness h are identical for all three choices of boundary condition (2.17)–(2.19). Since we are primarily interested in small values of the permeability k, in order to facilitate the analysis in this Chapter, we are justified in considering only the simplest of the three boundary conditions (2.17)–(2.19), namely the boundary condition (2.19). With this choice of boundary condition, from (2.63) the Reynolds equation governing the fluid pressure p is

$$\frac{\partial h}{\partial t} = \frac{1}{12r}\frac{\partial}{\partial r}\left(r\left(h^3 + 12k\right)\frac{\partial p}{\partial r}\right), \tag{5.1}$$

where, from (2.58) with $H = r^{2n}$, the fluid layer thickness h is given by

$$h(r,t) = \tilde{h}(t) + r^{2n} + \eta p(r,t), \tag{5.2}$$

where the compliance of the elastic layer η is given by (2.39). The Reynolds equation (5.1) and the load condition (2.59) are solved subject to the pressure boundary conditions (2.48) and (2.49), and the initial conditions (2.50) and (2.51). It is assumed that initially the fluid layer thickness $h \gg 1$ is large so that the initial fluid pressure $\mathcal{P}_0 \ll 1$ is small. Specifically, we take the initial fluid pressure

$$\mathcal{P}_0 = 0 \tag{5.3}$$

to be zero, and the initial minimum height of the undeformed interface between the fluid layer and the elastic layer

$$\tilde{h}(0) = d \gg 1 \tag{5.4}$$

to be large (specifically, we take $d = 5$ in the subsequent numerical calculations) so that the initial minimum fluid layer thickness $h_{\min}(0) = d \gg 1$ is large, consistently with our assumption that initially the fluid layer thickness $h \gg 1$ is large and the fluid pressure $p \ll 1$ is small.

In §5.2 the Reynolds equation (5.1) and the load condition (2.59) are solved numerically[1] subject to the boundary conditions (2.48) and (2.49) and the initial conditions (5.3) and (5.4) for different values of the permeability k, different values of the compliance of the elastic layer η and different values of n. Since solutions for different values of n are compared, the equations are solved, and the solutions are presented, in terms of the dimensionless variables (2.26).

Since the initial fluid pressure is zero, i.e. $\mathcal{P}_0 = 0$, in order to satisfy the load condition (2.59) the prescribed load $L(t)$ must be equal to zero initially. As in Chapters 3 and 4 we are interested in the case when the prescribed load L is constant. Thus we take the load L to be

$$L(\bar{t}) = \begin{cases} \dfrac{L_0}{2}\left(1 - \cos(\pi \bar{t})\right) & \text{when} \quad 0 \leq \bar{t} < 1, \\ L_0 & \text{when} \quad \bar{t} \geq 1, \end{cases} \tag{5.5}$$

so that the load L increases from an initial value of zero (satisfying the load condition (2.59)) to a constant value $L_0 > 0$ for $\bar{t} \geq 1$. Note that the load $L = L(\bar{t})$, given by (5.5), that we prescribe is similar to that prescribed by Weekley [70].

For simplicity, in the remainder of this Chapter we will concentrate on the case of a constant dimensional load $L = L_0 > 0$ for $\bar{t} \geq 1$, corresponding to taking the dimensionless load given by (5.5) to be equal to unity for $\bar{t} \geq 1$, i.e. $L_0 = 1$ for $\bar{t} \geq 1$, without loss of generality. We shall, however, retain L_0 explicitly in what follows for clarity of presentation.

Recall from (2.39) that the compliance of the elastic layer η is given by

$$\eta = \frac{L_0}{(2G + \lambda)l^2} = \left(\frac{\mathcal{R}}{2nH_\text{p}}\right)^{1/n} \bar{\eta}, \tag{5.6}$$

[1]The numerical procedure used is described subsequently in §5.2.1.

where

$$\bar{\eta} = \frac{L_0}{(2G+\lambda)\mathcal{R}^2}. \tag{5.7}$$

In Chapter 2 it was shown that the vertical displacement U_z of the elastic layer (from its undeformed state) on the interface between the fluid layer and the elastic layer at $z = h$ is proportional to the fluid pressure $p = p(r,t)$, i.e.

$$U_z|_{z=\tilde{h}(t)+H(r)} = \eta p(r,t). \tag{5.8}$$

For a physically consistent solution, the maximum value of $U_z|_{z=\tilde{h}(t)+H(r)}$, which occurs at $r = 0$, cannot exceed unity (i.e. the dimensionless thickness of the elastic layer) since a displacement exceeding unity would correspond to the interface between the fluid layer and the elastic layer at $z = h$ intersecting the interface between the elastic layer and the bearing, i.e. the elastic layer would have penetrated into the bearing, which is not physically possible. Thus for a physically consistent solution the maximum fluid pressure $p_{\max} = p(0,t)$ must satisfy

$$\eta p_{\max} < 1, \tag{5.9}$$

or equivalently

$$\bar{\eta}\bar{p}_{\max} < 1, \tag{5.10}$$

where $\bar{p}_{\max} = (2nH_{\mathrm{p}}/\mathcal{R})^{-1/n}p_{\max}$. Note from (2.56) that $\eta p_{\max}$ is the maximum size of the axial strain in the elastic layer at the interface between the fluid and elastic layers $z = h$. Therefore, the stricter condition $\eta p_{\max} \ll 1$, or equivalently $\bar{\eta}\bar{p}_{\max} \ll 1$, must be satisfied, otherwise the small strain assumption which leads to the Navier–Lamé equations (2.6) is violated. Values of η satisfying the less stringent condition (5.9), or equivalently values of $\bar{\eta}$ satisfying (5.10), are chosen *a posteriori* for use in the work presented in this Chapter. However, it should be noted that if, for the physical application, η is such that the small strain assumption is violated then finite strain theory should be used to describe the displacements in the elastic layer.

5.2 General Solution

5.2.1 Numerical Procedure

The Reynolds equation (5.1) and the load condition (2.59) were solved, subject to the pressure boundary conditions (2.48) and (2.49), and the initial conditions (5.3) and (5.4), on the finite domain $0 \leq \bar{r} \leq 50$ using COMSOL Multiphysics version 3.5a. The software package COMSOL Multiphysics is a finite element solver that can be used to simulate many physical systems, for example, chemical, electrical, fluid and mechanical systems. A mesh consisting of 10,000 elements of length $\Delta\bar{r} = 5 \times 10^{-3}$ was used in all simulations, quadratic basis functions were chosen and the absolute and relative tolerances were set to 10^{-7}.
The ratio $H_{\mathrm{p}}/\mathcal{R}$ was chosen to be $H_{\mathrm{p}}/\mathcal{R} = 0.1$ in all simulations.

5.2.2 Fluid Layer Thickness and Contact Time

Figure 5.2 shows plots of the fluid layer thickness h as a function of $\bar{r}$ at ten equally spaced times for two different values of the permeability k in the case when the bearing shape is parabolic, i.e. when $n = 1$. In Figures 5.2(a) and 5.2(b), in which $k = 0$ and $k = 10^{-5}$, respectively, we see that h decreases monotonically as time $\bar{t}$ increases. Furthermore, the elastic layer deforms in such a way that a fluid layer of approximately uniform thickness is formed in $\bar{r} < \bar{r}_{\mathrm{C}}$, where $\bar{r}_{\mathrm{C}}$ is the radial position of a "corner" $\bar{r} = \bar{r}_{\mathrm{C}}$ that forms in the interface $z = h$ between the elastic

(a)

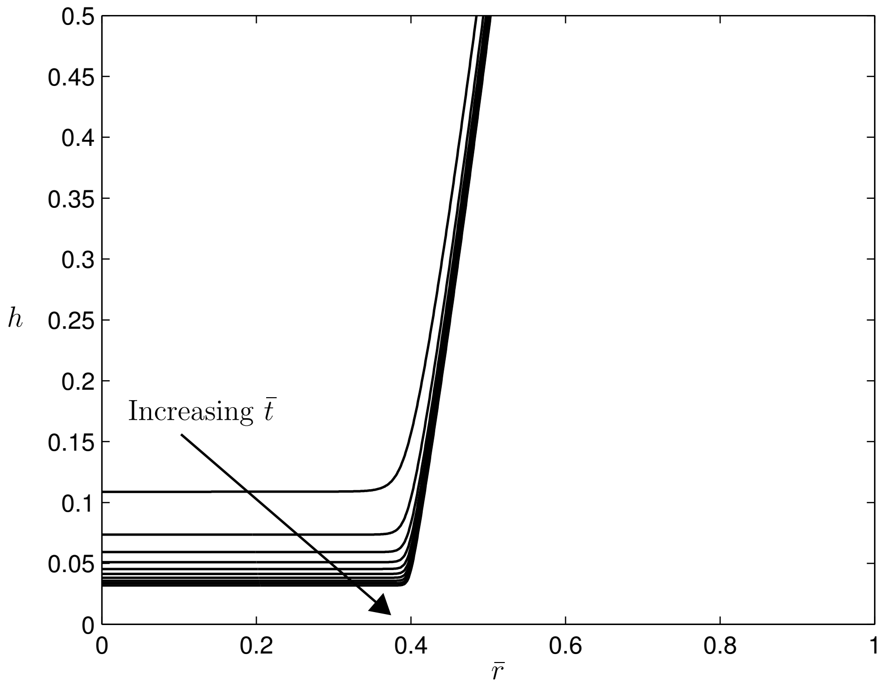

(b)

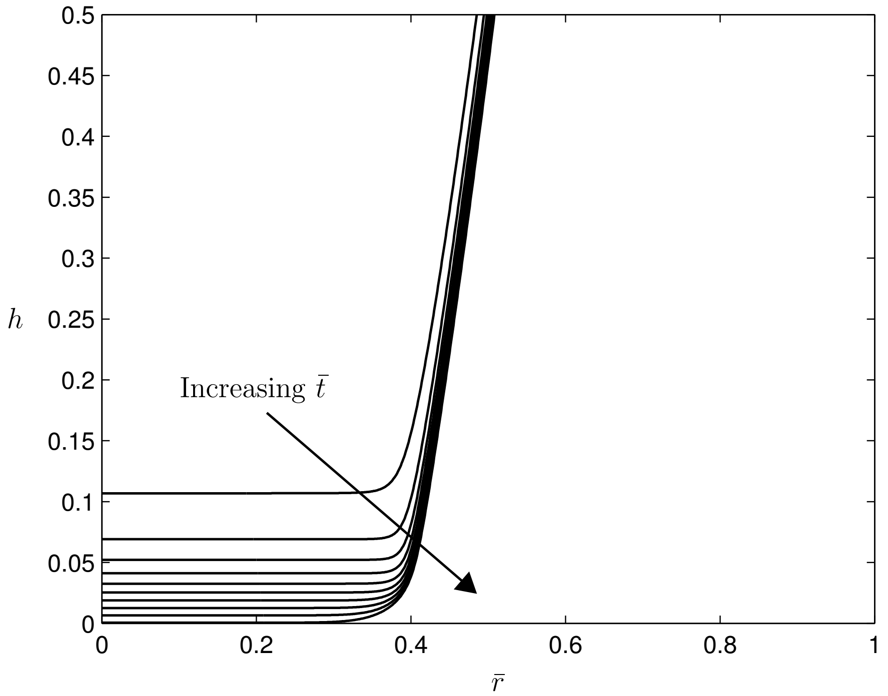

Figure 5.2: Plots of h as a function of $\bar{r}$ for two values of k, namely (a) $k = 0$ and (b) $k = 10^{-5}$, at the times $\bar{t} = 6j$, $j = 1, 2, \ldots, 10$. In both plots $n = 1$ and $\bar{\eta} = 0.2$

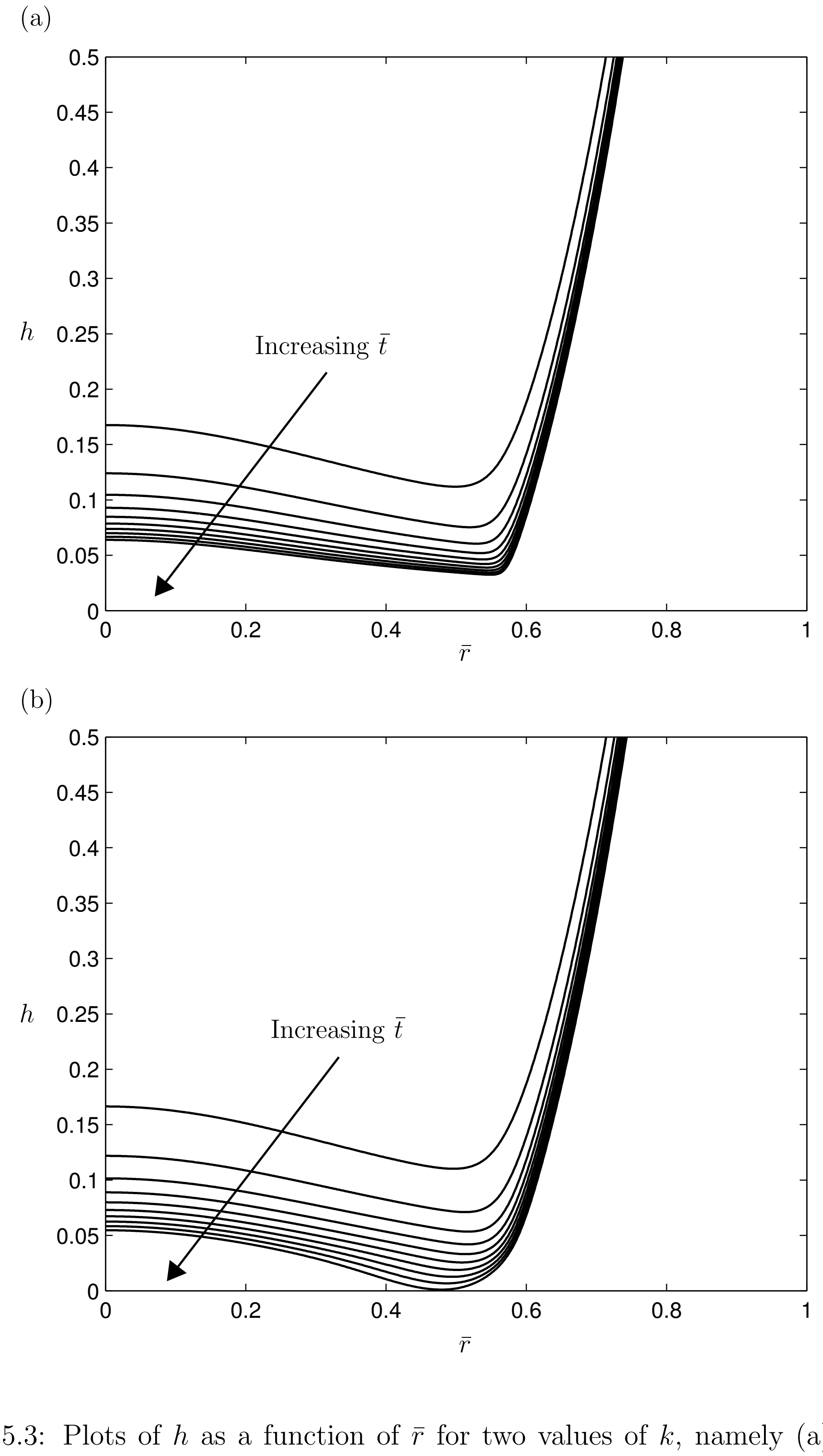

Figure 5.3: Plots of h as a function of $\bar{r}$ for two values of k, namely (a) $k = 0$ and (b) $k = 10^{-5}$, at the times $\bar{t} = 23j$, $j = 1, 2, \ldots, 10$. In both plots $n = 2$ and $\bar{\eta} = 0.2$

layer and the fluid layer. Once formed, these features are maintained thereafter. Similar structures have been observed in two dimensions when a parabolic bearing approaches a flat stationary surface coated with a thin elastic layer through a thin layer of fluid (see, for example, Weekley *et al.* [71] and Balmforth *et al.* [8]); however, the corresponding axisymmetric flow (which, when $k = 0$ and $n = 1$, is mathematically equivalent to the axisymmetric flow considered in this Chapter) seems not to have been previously studied.

Comparing Figures 5.2(a) and 5.2(b) we see that at each time $\bar{t}$ the minimum fluid layer thickness $h_{\min} = h(0, \bar{t})$ is smaller in Figure 5.2(b), in which $k = 10^{-5}$, than it is in Figure 5.2(a), in which $k = 0$, i.e. the time taken for the minimum fluid layer thickness to reduce to a value $h_{\min}$ decreases as the permeability k increases, as expected. Furthermore, we see that increasing k from $k = 0$ to $k = 10^{-5}$ has almost no effect on the radial position of the corner $\bar{r} = \bar{r}_{\mathrm{C}}$ that forms in the interface $z = h$.

Figure 5.3 shows plots of the fluid layer thickness h as a function of $\bar{r}$ at ten equally spaced times for two different values of the permeability k in the case when the bearing shape is quartic, i.e. when $n = 2$. In Figures 5.3(a) and 5.3(b), in which $k = 0$ and $k = 10^{-5}$, respectively, we see that h decreases monotonically as time $\bar{t}$ increases. In contrast to the case when the bearing is parabolic, as time $\bar{t}$ increases a fluid layer of approximately uniform thickness does not form. The fluid layer thickness h decreases from its value at $\bar{r} = 0$ to a minimum value $h_{\min}$, which it attains at $\bar{r} = \bar{r}_{\min} > 0$, and then increases monotonically in $\bar{r}$ beyond $\bar{r} = \bar{r}_{\min}$. Figures 5.2 and 5.3 show that a region of approximately uniform fluid layer thickness h is formed when the bearing is parabolic, i.e. when $n = 1$, but not when the bearing is quartic, i.e. when $n = 2$. In fact, a region of approximately uniform fluid layer thickness h forms only when the bearing is parabolic, i.e. when

$n = 1$.

Similarly to the case when the bearing is parabolic, i.e. when $n = 1$, comparing Figures 5.3(a) and 5.3(b) it is clear that increasing k decreases the time taken for the minimum fluid layer thickness to reduce to a value $h_{\rm min}$, as expected. Furthermore, we see that increasing k from $k = 0$ to $k = 10^{-5}$ decreases, at a given time $\bar{t}$, the radial position $\bar{r} = \bar{r}_{\rm min}$ at which h attains its minimum value $h_{\rm min}$.

Note that when the bearing was parabolic, i.e. when $n = 1$, and $\bar{\eta} > 0$ and in the cases when $\bar{\eta} = 0$ considered in Chapters 3 and 4, the minimum fluid layer thickness $h_{\rm min}$ always occurred at $\bar{r} = 0$. It will subsequently be shown, by the numerical results presented in §5.2.3, that when $n \geq 2$ and $\bar{\eta} > 0$ the minimum fluid layer thickness $h_{\rm min}$ occurs at some position $\bar{r} = \bar{r}_{\rm min} > 0$. Note that Balmforth *et al.* [8], who considered the approach of a two-dimensional parabolic bearing towards a stationary elastic layer through a thin layer of fluid, also found that the minimum fluid layer thickness occurred away from the axis of symmetry when the elastic layer was modelled as a beam, a membrane or an elastic half space.

Figure 5.4 shows plots of the fluid filled gap between the porous bed and the elastic layer for $n = 1, 2, 3, 4, 5$ and 10. (Note that all of the plots in Figure 5.4 are for the same value of the minimum fluid layer thickness $h_{\rm min} = 0.1$, and are not, therefore, at the same instant in time.) In all cases the deformation of the elastic layer is largest at $\bar{r} = 0$ and decreases as $\bar{r}$ increases. As n increases the deformations are smaller but occur over a larger area. Figure 5.4(a), in which $n = 1$, shows that far beyond the corner at $\bar{r} = \bar{r}_{\rm C}$ the elastic layer is indistinguishable from its undeformed state and the fluid layer thickness $h = O(\bar{r}^2)$ as $\bar{r} \to \infty$. Similarly, Figures 5.4(b)–(f), in which $n = 2, 3, 4, 5$ and 10, respectively, show that far beyond $\bar{r} = \bar{r}_{\rm min}$ the elastic layer is indistinguishable from its undeformed state and $h =$

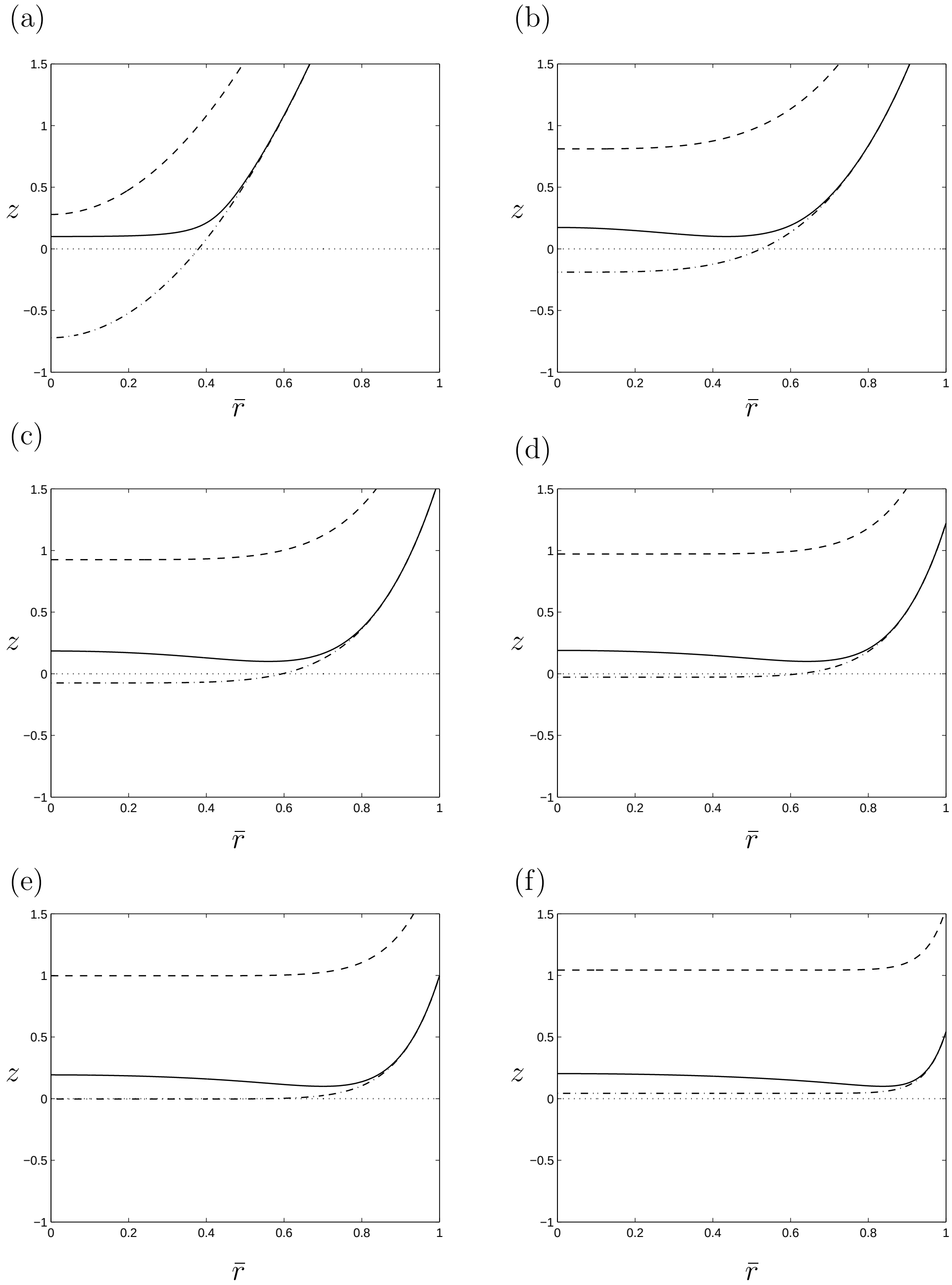

Figure 5.4: Plots of the interface between the porous bed and the fluid layer $z = 0$ (dotted lines), the interface between the fluid layer and the elastic layer $z = h$ (solid lines) and the interface between the elastic layer and the bearing $z = \tilde{h} + H(\bar{r}) + 1$ (dashed lines), for (a) $n = 1$, (b) $n = 2$, (c) $n = 3$, (d) $n = 4$, (e) $n = 5$ and (f) $n = 10$ at the times (a) $\bar{t} = 3.1730$, (b) $\bar{t} = 12.8187$, (c) $\bar{t} = 23.3686$, (d) $\bar{t} = 31.8709$, (e) $\bar{t} = 38.2097$ and (f) $\bar{t} = 52.5185$ when the minimum fluid layer thickness $h_{\min} = 0.1$. The dash-dot lines are given by $z = \tilde{h} + H(\bar{r})$, i.e. plots of the lower surface of the undeformed elastic layer. In all plots $k = 10^{-3}$ and $\bar{\eta} = 0.25$

$O(\bar{r}^{2n})$ as $\bar{r} \to \infty$. Furthermore, Figures 5.4(b)–(f) show that $\bar{r}_{\min}$ increases as n increases.

Figure 5.5 shows plots of the minimum fluid layer thickness $h_{\min}$ as a function of $\ln \bar{t}$ for three values of the permeability k, two values of n and three values of $\bar{\eta}$. Figure 5.5 shows that, similarly to the case $\bar{\eta} = 0$ treated in Chapter 4, increasing the permeability k decreases the time taken for the minimum fluid layer thickness to reduce to a value $h_{\min}$. For the values[2] of k considered in Figure 5.5, namely $k = 0, 10^{-5}$ and 10^{-3}, increasing n increases this time. Furthermore, and again similarly to the case $\bar{\eta} = 0$ treated in Chapter 4, Figure 5.5 shows that when the bed is permeable, i.e. when $k > 0$, the elastic layer and the porous bed always make contact in a finite time, the contact time $\bar{t} = \bar{t}_{\mathrm{c}} = (2nH_{\mathrm{p}}/\mathcal{R})^{2/n} t_{\mathrm{c}}$, where $\bar{t}_{\mathrm{c}}$ satisfies $h_{\min}(\bar{t}_{\mathrm{c}}) = 0$. Figure 5.6 shows plots of $\ln \bar{t}_{\mathrm{c}}$ as a function of $\ln k$ for five values of n. Both Figures 5.5 and 5.6 show that, as expected, increasing k or decreasing n decreases the contact time $\bar{t}_{\mathrm{c}}$.

The effect of increasing or decreasing the compliance of the elastic layer $\bar{\eta}$ on the time taken for the minimum fluid layer thickness to reduce to a value $h_{\min}$ can also be seen from Figure 5.5, which shows that increasing $\bar{\eta}$ increases this time and, in particular, increases the contact time $\bar{t}_{\mathrm{c}}$ when $k > 0$. To understand the physical reason why increasing the compliance of the elastic layer $\bar{\eta}$ increases the time taken for the minimum fluid layer thickness to reduce to a value $h_{\min}$ it is instructive to examine the fluid pressure $p = p(r, t)$, which we shall do in §5.2.3.

Figure 5.7 shows plots of $\tilde{h}$, the minimum height of the undeformed interface between the fluid layer and the elastic layer, as a function of $\ln \bar{t}$ for three different

[2]Recall that in Chapter 4 it was shown that when $\bar{\eta} = 0$ and the permeability $k \gg 1$ is large, increasing n decreases the time taken for the minimum fluid layer thickness to reduce to a thickness $h_{\min}$. We anticipate similar behaviour when $\bar{\eta} > 0$. However, only "small" values of k are considered in this Chapter and we, therefore, describe the behaviour only for "small" values of k.

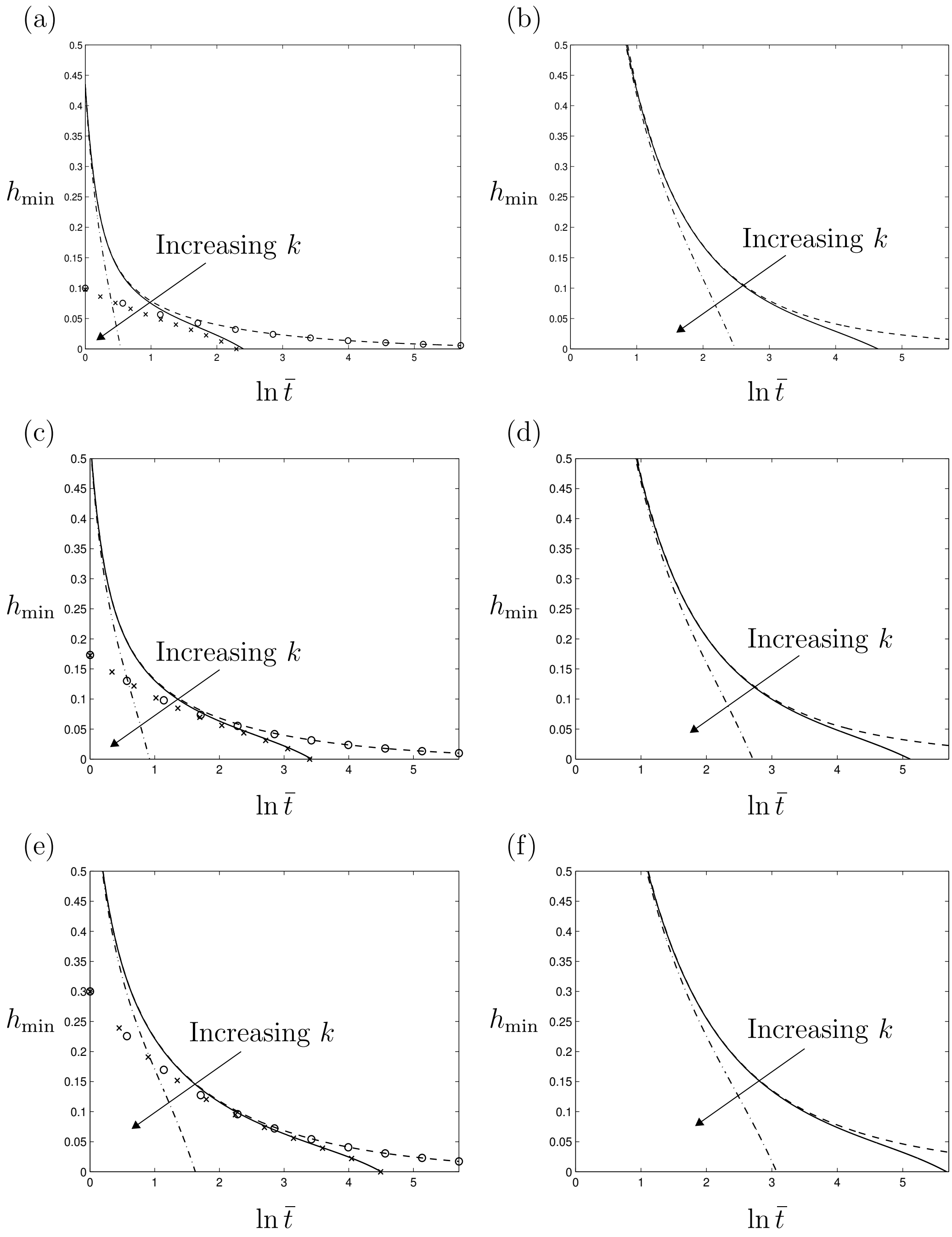

Figure 5.5: Plots of $h_{\min}$ as a function of $\ln \bar{t}$ for three values of k, namely $k = 0$ (dashed lines), 10^{-5} (solid lines) and 10^{-3} (dash-dot lines), for (a) $n = 1$ and $\bar{\eta} = 1/30$, (b) $n = 2$ and $\bar{\eta} = 1/30$, (c) $n = 1$ and $\bar{\eta} = 0.1$, (d) $n = 2$ and $\bar{\eta} = 0.1$, (e) $n = 1$ and $\bar{\eta} = 0.3$, and (f) $n = 2$ and $\bar{\eta} = 0.3$. In (a), (c) and (e) the circles correspond to the large-t asymptotic solution for $h_{\min}$ in the case $n = 1$ given by (5.19) and the crosses correspond to the small-k asymptotic solution for $h_{\min}$ in the case $n = 1$ given by (5.46)

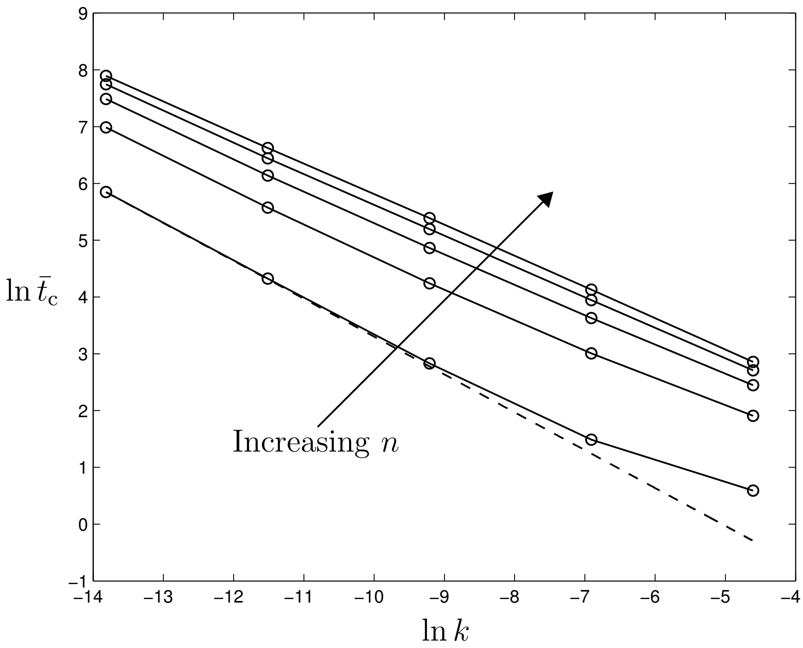

Figure 5.6: Plots of $\ln \bar{t}_c$ as a function of $\ln k$ for $n = 1, 2, 3, 4$ and 5 (solid lines). The dashed line corresponds to the leading order small-k asymptotic solution for the contact time when $n = 1$ given by (5.47). In all plots $\bar{\eta} = 1/4$

values of the permeability k, for two values of n and three values of $\bar{\eta}$. Figure 5.7 shows that in the special case when the bed is impermeable, i.e. when $k = 0$, $\tilde{h}$ decreases monotonically in time from its initial value $\tilde{h}(0) = d$ and asymptotes to a constant negative value for large times $\bar{t} \to \infty$, the magnitude of which increases as $\bar{\eta}$ increases or n decreases. Analogous behaviour is observed when the bed is permeable, i.e. when $k > 0$: $\tilde{h}$ decreases monotonically in time from its initial value $\tilde{h}(0) = d$ to its value at the contact time $\bar{t} = \bar{t}_c$, and the value of $\tilde{h}$ at $\bar{t} = \bar{t}_c$ increases as k increases.

5.2.3 Fluid Pressure

Figures 5.8(a) and 5.8(b) show plots of the fluid pressure $\bar{p}$ as a function of $\bar{r}$ at ten equally spaced times for two different values of the permeability k in the

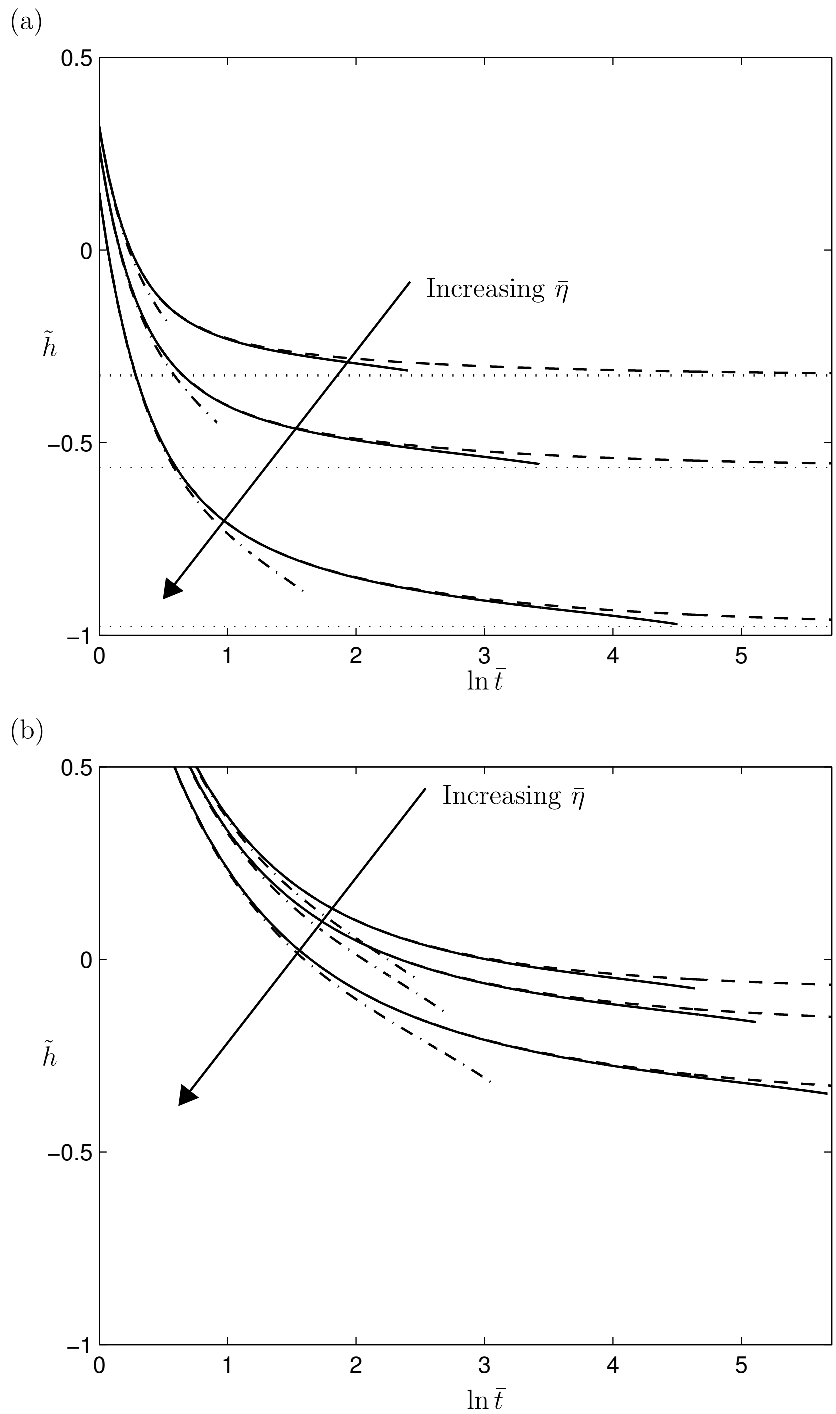

Figure 5.7: Plots of $\tilde{h}$ as a function of $\ln \bar{t}$ for three values of $\bar{\eta}$, namely $\bar{\eta} = 1/30, 0.1$ and 0.3, each for three values of k, namely $k = 0$ (dashed lines), $k = 10^{-5}$ (solid lines) and $k = 10^{-3}$ (dash-dot lines), and two values of n, namely (a) $n = 1$ and (b) $n = 2$. The dotted lines in (a) correspond to the leading order large-t and small-k asymptotic solutions for $\tilde{h}$, both of which are given by (5.30)

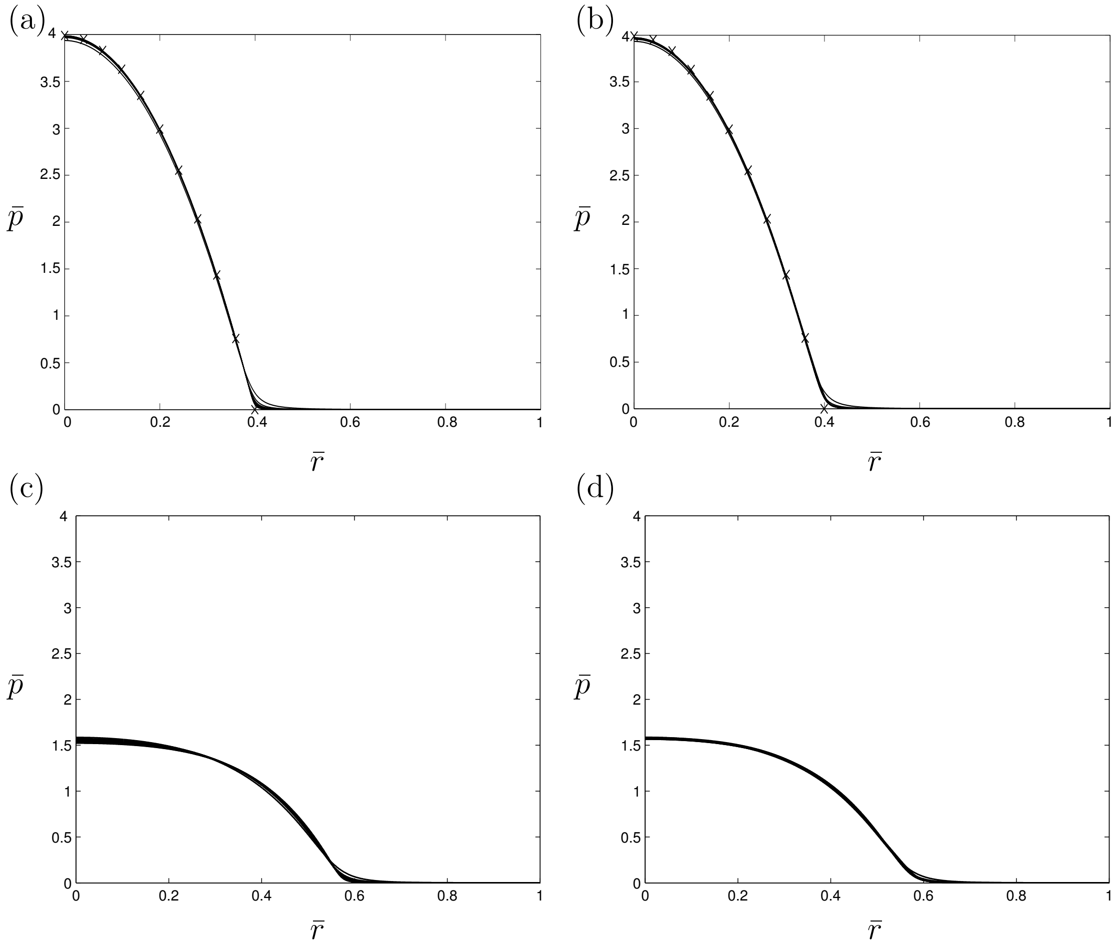

Figure 5.8: (a,b) Plots of the fluid pressure $\bar{p}$ as a function of $\bar{r}$ at the times $\bar{t} = 6j$, $j = 1, 2, \ldots, 10$, for (a) $n = 1$ and $k = 0$, and (b) $n = 1$ and $k = 10^{-5}$. In (a) and (b) the crosses correspond to the leading order large-t and small-k asymptotic solutions for p in the case $n = 1$, both of which are given by (5.32). (c,d) Plots of the fluid pressure $\bar{p}$ as a function of $\bar{r}$ at the times $\bar{t} = 23j$, $j = 1, 2, \ldots, 10$, for (c) $n = 2$ and $k = 0$, and (d) $n = 2$ and $k = 10^{-5}$. In all plots $\bar{\eta} = 0.2$

case when the bearing is parabolic, i.e. when $n = 1$. Between the chosen times, temporal variations in the fluid pressure $\bar{p}$ are small. Figures 5.8(c) and 5.8(d) show plots of the fluid pressure $\bar{p}$ as a function of $\bar{r}$ at ten equally spaced times (different from those in Figures 5.8(a) and 5.8(b)) for two different values of the permeability k in the case when the bearing is quartic, i.e. when $n = 2$; again, the temporal variations in the fluid pressure $\bar{p}$ are small. Comparing Figures 5.8(a) and 5.8(b) and Figures 5.8(c) and 5.8(d) we see that increasing the permeability k (with n fixed) has almost no effect on the fluid pressure $\bar{p}$. Furthermore, Figures 5.8(a) and 5.8(b) show that when the bearing is parabolic, i.e. when $n = 1$, the fluid pressure $\bar{p}$ is approximately parabolic in $\bar{r} < \bar{r}_C$. For the values[3] of k considered in Figure 5.8, namely $k = 0$ and 10^{-5}, comparing Figures 5.8(a) and 5.8(b) with Figures 5.8(c) and 5.8(d) shows that increasing n from $n = 1$ (a parabolic bearing) to $n = 2$ (a quartic bearing) with k fixed decreases the maximum fluid pressure $\bar{p}_{\max}$ and distributes the fluid pressure $\bar{p}$ over a larger area.

Figure 5.9 shows plots of $\bar{p}$ as a function of $\bar{r}$ for three values of $\bar{\eta} > 0$ for a fixed value of the permeability k for two values of n at the times when the minimum fluid layer thickness $h_{\min}$ takes the value $h_{\min} = 0.05$. Figure 5.9 shows that increasing $\bar{\eta}$, with both k and n fixed, decreases the maximum fluid pressure $\bar{p}_{\max}$ and distributes the fluid pressure $\bar{p}$ over a larger area.

Figure 5.10 shows plots of $\ln \bar{p}_{\max}$ as a function of $\ln \bar{t}$ for three values of k, each for three values of $\bar{\eta} > 0$, and two values of n. In Figure 5.10(a) the bearing is parabolic ($n = 1$). Figure 5.10(a) shows that when the permeability $k = 0$ the maximum fluid pressure $\bar{p}_{\max}$ increases from its initial value $\bar{p}_{\max}(0) = 0$ and asymptotes to a maximum constant value as $\bar{t} \to \infty$. This constant value decreases as $\bar{\eta}$ increases.

[3]In Appendix D it is shown that when $\bar{\eta} = 0$ and the permeability $k \gg 1$ is large, increasing n increases $\bar{p}_{\max}$ and distributes the fluid pressure $\bar{p}$ over a larger area. We anticipate similar behaviour when $\bar{\eta} > 0$. However, only "small" values of k are considered in this Chapter and again we, therefore, describe the behaviour only for "small" values of k.

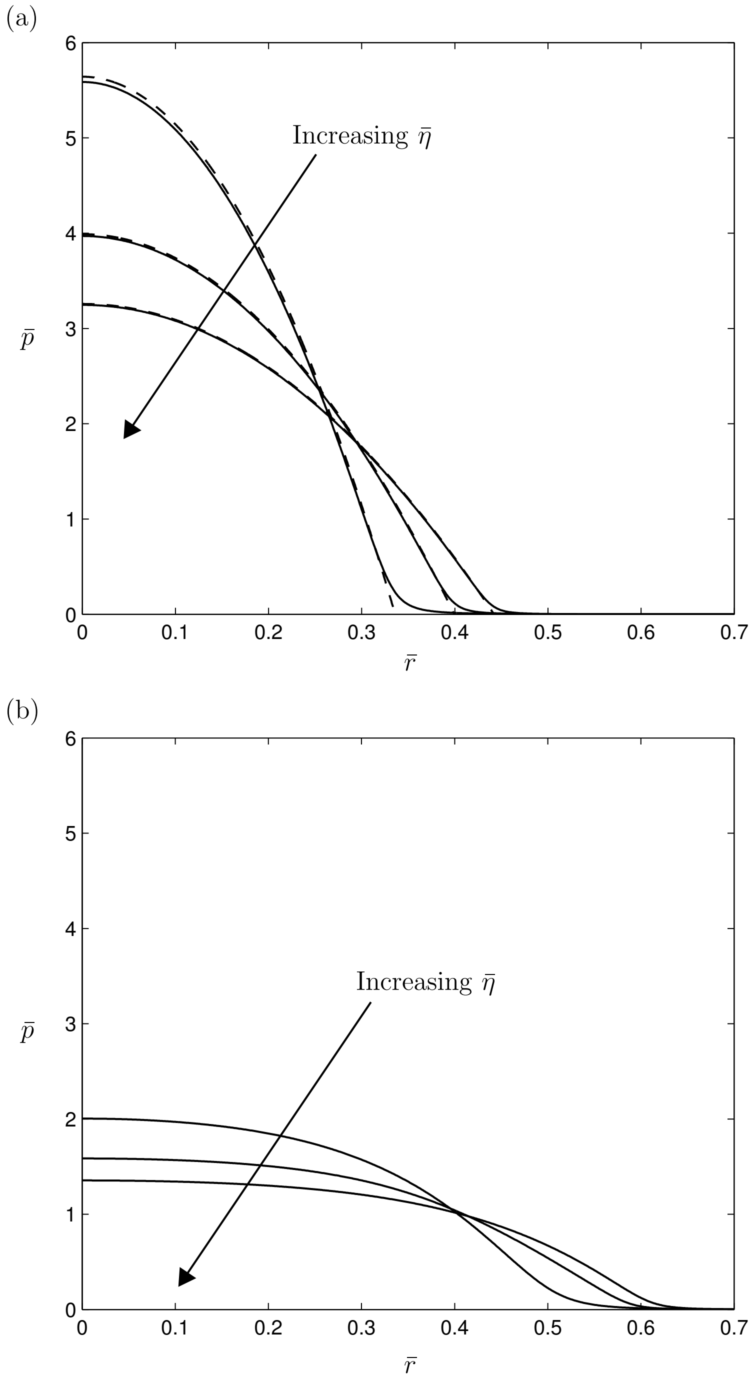

Figure 5.9: (a) Plots of the fluid pressure $\bar{p}$ as a function of $\bar{r}$ for $\bar{\eta} = 0.1, 0.2$ and 0.3 and $n = 1$ at the times $\bar{t} = 10.0478, 19.0261$ and 28.0327, respectively, when $h_{\min} = 0.05$. The dashed lines correspond to the leading order small-k asymptotic solution for $\bar{p}$ given by (5.32). (b) Plots of the fluid pressure $\bar{p}$ as a function of $\bar{r}$ for $\bar{\eta} = 0.1, 0.2$ and 0.3 and $n = 2$ at the times $\bar{t} = 52.3009, 75.1892$ and 95.1841, respectively, when $h_{\min} = 0.05$. In both plots $k = 10^{-5}$

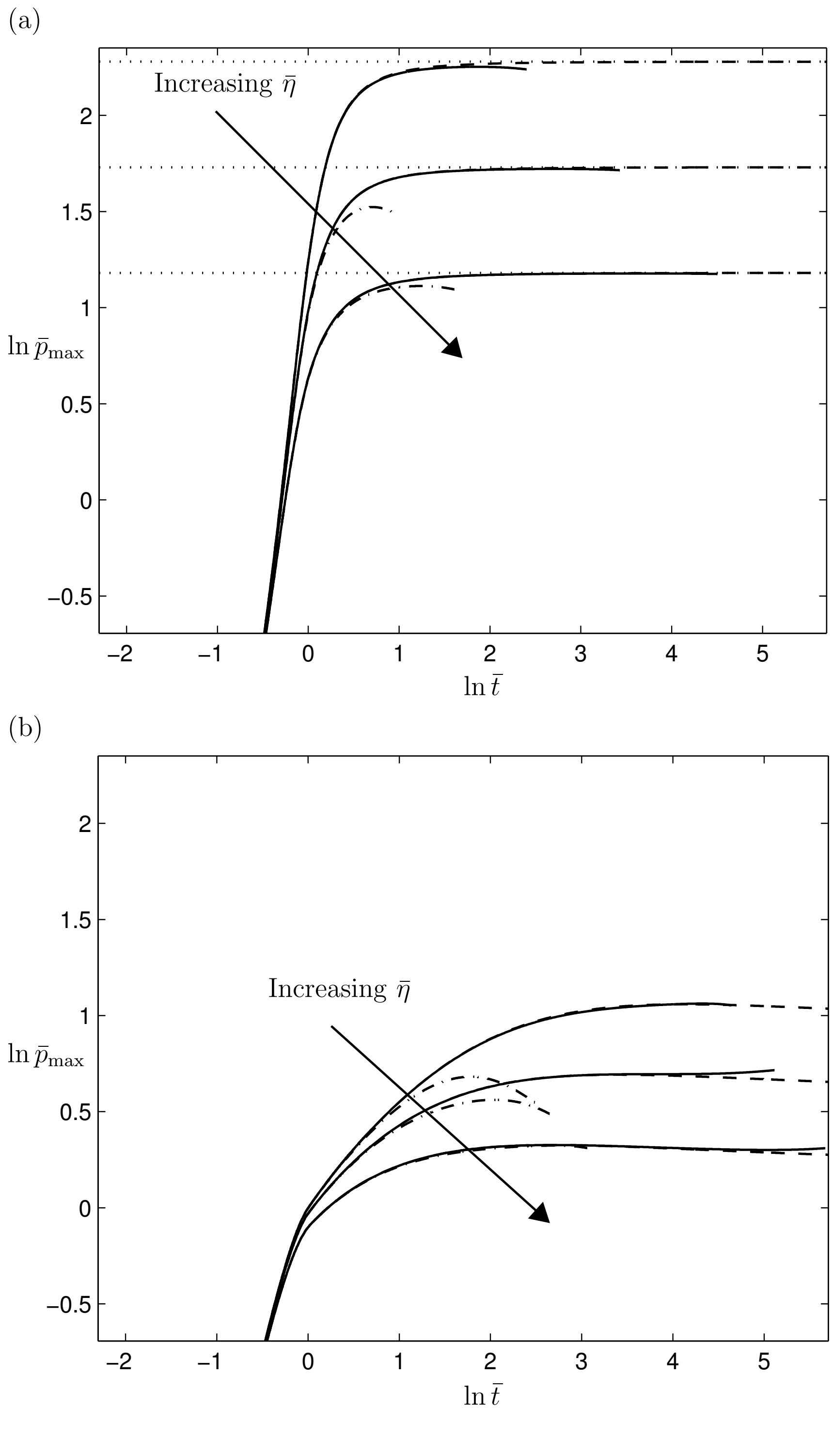

Figure 5.10: Plots of $\ln \bar{p}_{\max}$ as a function of $\ln \bar{t}$ for three values of k, namely $k = 0$ (dashed curves), $k = 10^{-5}$ (solid curves) and $k = 10^{-3}$ (dash-dot curves), for three values of $\bar{\eta}$, namely $\bar{\eta} = 1/30$, 0.1 and 0.3, with (a) $n = 1$ and (b) $n = 2$. The dotted lines in (a) correspond to the asymptotic solution for $p_{\max}$ given by (5.33)

This behaviour is qualitatively different from that in the case when $\bar{\eta} = 0$ treated in Chapter 4, in which $\bar{p}_{\text{max}}$ increases exponentially as time $\bar{t}$ increases. When $\bar{\eta} > 0$ the pressure $\bar{p}$ in the fluid layer causes the elastic layer to deform, which in turn decreases the fluid pressure $\bar{p}$, distributing it over a larger area and preventing its unbounded growth.

Figure 5.10(a) shows that when $k > 0$, similarly to the case when $\bar{\eta} = 0$ treated in Chapter 4, $\bar{p}_{\text{max}}$ has a maximum turning point in time $\bar{t}$. The maximum fluid pressure $\bar{p}_{\text{max}}$ increases monotonically in time from its initial value $\bar{p}_{\text{max}}(0) = 0$ to its maximum value, which it attains at some time $\bar{t} < \bar{t}_{\text{c}}$, and then relaxes to its value at $\bar{t} = \bar{t}_{\text{c}}$. Similarly to the case $\bar{\eta} = 0$ treated in Chapter 4, the physical reason for this is that the porous bed is effectively impermeable when the fluid layer thickness h is sufficiently large and the effects of the permeability k become significant only when $h = O(k^{1/3})$ (see the analysis of the asymptotic limit $k \to 0$ given subsequently in §5.3). The maximum fluid pressure $\bar{p}_{\text{max}}$ increases monotonically in time $\bar{t}$ while $h \gg O(k^{1/3})$. However, after a "long" time $\bar{t} = O(k^{-2/3})$, when $h = O(k^{1/3})$, the fluid volume flux into the porous bed $\bar{Q}_{\text{bed}}$ is sufficiently large that it causes a relaxation in $\bar{p}_{\text{max}}$. It should be noted that this relaxation is less pronounced as the permeability k decreases. In fact, the analysis of the asymptotic limit $k \to 0$ given subsequently in §5.3 shows that this phenomenon is not observed at leading order in this limit.

In Figure 5.10(b) the bearing is quartic ($n = 2$). Figure 5.10(b) shows that when $k = 0$, similarly to the case when the bearing is parabolic, i.e. when $n = 1$, $\bar{p}_{\text{max}}$ increases from its initial value and asymptotes to a constant value that decreases as $\bar{\eta}$ increases. This behaviour is, again, qualitatively different from that observed in the case $\bar{\eta} = 0$ (see Chapter 4).

Figure 5.10(b) shows that when $k > 0$, initially the maximum fluid pressure $\bar{p}_{\text{max}}$

increases in a manner similar to the case $k = 0$. As the minimum fluid layer thickness h_{min} (which we recall occurs at some radial position $\bar{r} = \bar{r}_{\text{min}} > 0$ when $n \geq 2$) approaches zero it becomes increasingly difficult for the fluid in $\bar{r} < \bar{r}_{\text{min}}$ to flow out through the fluid layer, and if there is an insufficient flow of fluid from $\bar{r} < \bar{r}_{\text{min}}$ into the porous bed the maximum fluid pressure $\bar{p}_{\text{max}}$ can increase as the fluid that is "trapped" in $\bar{r} < \bar{r}_{\text{min}}$ is squeezed between the elastic layer and the porous bed. Figure 5.10(b) shows that this is in fact the case when $k = 10^{-5}$ with either $\bar{\eta} = 0.1$ or $\bar{\eta} = 0.3$; in both cases we see that $\bar{p}_{\text{max}}$ increases towards its value at the contact time $\bar{t}_{\text{c}}$. Furthermore, Figure 5.10(b) shows that this phenomenon is not observed when $k = 10^{-3}$ and $\bar{\eta} = 1/30$, $k = 10^{-3}$ and $\bar{\eta} = 0.1$, $k = 10^{-3}$ and $\bar{\eta} = 0.3$, and $k = 10^{-5}$ and $\bar{\eta} = 1/30$.

When the permeability $k = 0$ the fluid in $\bar{r} < \bar{r}_{\text{min}}$ can only flow out through the fluid layer; however, for large times $\bar{t} \gg 1$ the maximum fluid pressure p_{max} does not increase as the fluid in $\bar{r} < \bar{r}_{\text{min}}$ is squeezed between the elastic layer and the impermeable bed. In this case the minimum fluid layer thickness h_{min}, which is such that $h_{\text{min}} \to 0^+$ as $\bar{t} \to \infty$, approaches zero at a sufficiently slow rate that the fluid volume flux into $\bar{r} > \bar{r}_{\text{min}}$ is sufficiently large that there is no increase in $\bar{p}_{\text{max}}$.

Figure 5.11 shows plots of $\bar{r}_{\text{min}}$, the radial position at which the fluid layer thickness h attains its minimum value h_{min}, as a function of $\ln \bar{t}$ for three values of k, each for three values of $\bar{\eta} > 0$, and two values of $n \geq 2$, namely, (a) $n = 2$ and (b) $n = 5$. (Recall that in the case when the bearing is parabolic, i.e. when $n = 1$, the fluid layer thickness attains its minimum value h_{min} at $\bar{r} = 0$ for all times.) Figure 5.11 shows that when the bed is impermeable, i.e. when $k = 0$, $\bar{r}_{\text{min}}$ increases monotonically in time $\bar{t}$. Furthermore, Figure 5.11 shows that increasing n or increasing the compliance of the elastic layer $\bar{\eta}$ increases the value of $\bar{r}_{\text{min}}$ at any

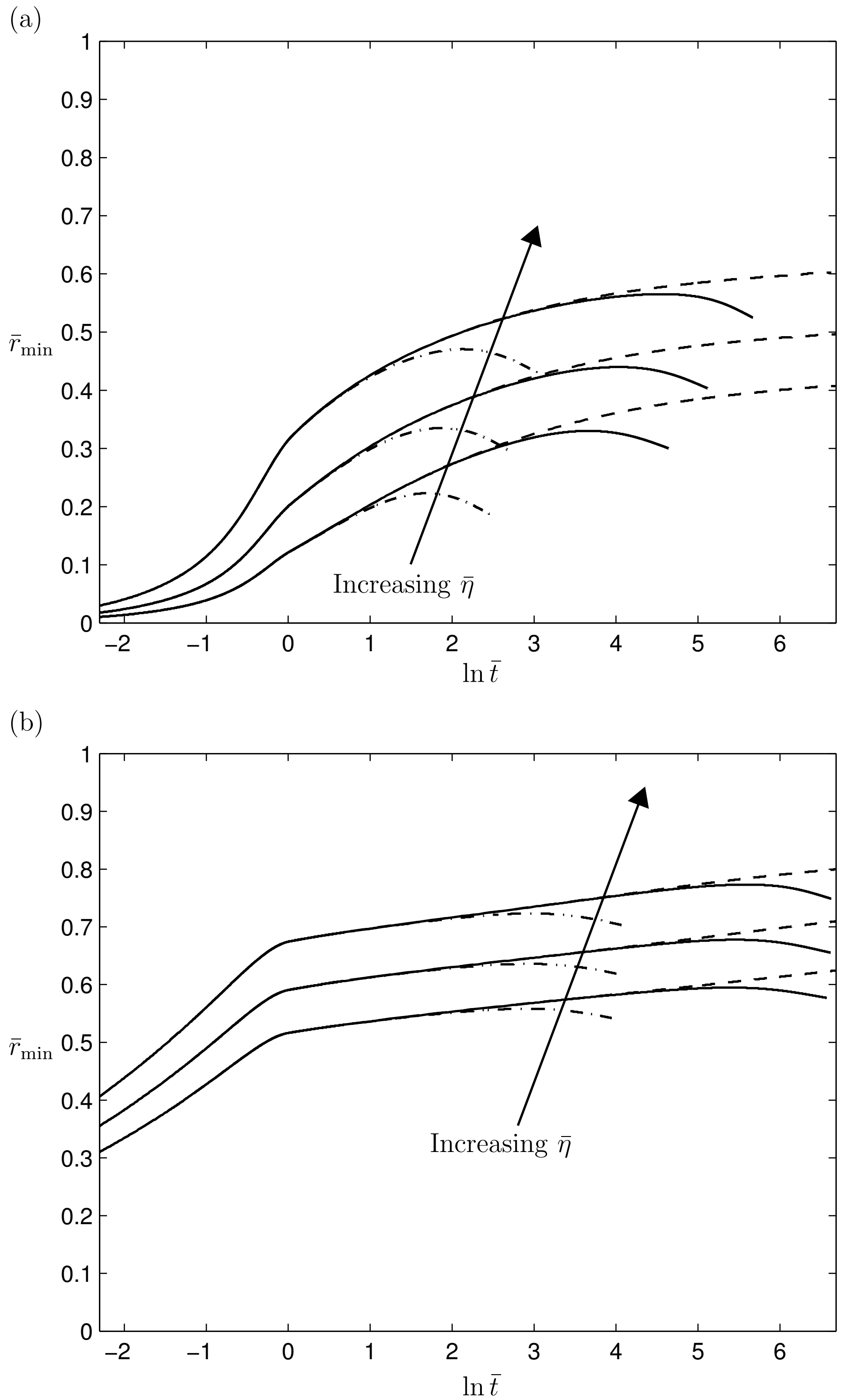

Figure 5.11: Plots of $\bar{r}_{\min}$ as a function of $\ln \bar{t}$ for three values of $\bar{\eta}$, namely $\bar{\eta} = 1/30$, 0.1 and 0.3, each for three values of k, namely $k = 0$ (dashed lines), $k = 10^{-5}$ (solid lines) and $k = 10^{-3}$ (dash-dot lines), for (a) $n = 2$ and (b) $n = 5$

given time $\bar{t} > 0$. However, when $k > 0$ there is qualitatively different behaviour. Figure 5.11 shows that when the bed is permeable, i.e. when $k > 0$, $\bar{r}_{\min}$ increases monotonically in time to its maximum value, which it attains at some time $\bar{t} < \bar{t}_{\mathrm{c}}$, and then decreases to its value at $\bar{t} = \bar{t}_{\mathrm{c}}$. This is qualitatively different from the monotonic increase in $\bar{r}_{\min} = \bar{r}_{\min}(\bar{t})$ observed in the case when $k = 0$. However, Figure 5.11 shows that, similarly to the case when $k = 0$, when $k > 0$ increasing n or increasing the compliance of the elastic layer $\bar{\eta}$ increases the value of $\bar{r}_{\min}$ at any given time $\bar{t} \leq \bar{t}_{\mathrm{c}}$.

Since $\bar{r}_{\min} > 0$ is a local minimum of the fluid layer thickness h it satisfies

$$\left.\frac{\partial h}{\partial \bar{r}}\right|_{\bar{r}=\bar{r}_{\min}} = 0, \tag{5.11}$$

and hence we deduce from equation (5.2) that

$$\bar{r}_{\min} \propto \left(-\bar{\eta}\left.\frac{\partial \bar{p}}{\partial \bar{r}}\right|_{\bar{r}=\bar{r}_{\min}}\right)^{1/(2n-1)}. \tag{5.12}$$

The radial position $\bar{r} = \bar{r}_{\min}(\bar{t})$ at which h attains its minimum value $h_{\min}$ is, therefore, determined by the pressure gradient $-\partial\bar{p}/\partial\bar{r} > 0$ at $\bar{r} = \bar{r}_{\min}$. When the pressure gradient $-\partial\bar{p}/\partial\bar{r}$ increases $\bar{r}_{\min}$ increases, and when the pressure gradient $-\partial\bar{p}/\partial\bar{r}$ decreases $\bar{r}_{\min}$ decreases.

In order to understand why, when $k > 0$, the radial position $\bar{r} = \bar{r}_{\min}$ increases monotonically in time to its maximum value and then decreases to its value at $\bar{t} = \bar{t}_{\mathrm{c}}$ (a phenomenon not observed in the special case when the bed is impermeable $k = 0$) it is instructive to compare the maximum fluid pressure $\bar{p}_{\max}$ and the fluid pressure at $\bar{r}_{\min}$ as functions of $\ln \bar{t}$.

Figures 5.12(a) and 5.12(b) show plots of the maximum fluid pressure $\bar{p}_{\max}$ and the fluid pressure $\bar{p}$ at $\bar{r}_{\min}$, respectively, as a functions of $\ln \bar{t}$ for three values of the permeability k, each for three values of $\bar{\eta} > 0$, in the case when the bearing is quartic, i.e. when $n = 2$. Figures 5.12(a) and 5.12(b) show that when $k = 0$ the fluid pressure $\bar{p}$ initially increases at both $\bar{r} = 0$ and $\bar{r} = \bar{r}_{\mathrm{min}}$, with $\bar{p}_{\mathrm{max}}$ increasing faster than the fluid pressure $\bar{p}$ at $\bar{r}_{\mathrm{min}}$, meaning that the pressure gradient $-\partial\bar{p}/\partial\bar{r}$ at $\bar{r} = \bar{r}_{\mathrm{min}}$ increases and consequently $\bar{r}_{\mathrm{min}}$ increases, i.e. $\bar{r}_{\mathrm{min}}$ moves radially outwards. As the pressure $\bar{p}$ in the fluid layer increases it causes the elastic layer to deform, which in turn decreases the fluid pressure $\bar{p}$ (at both $\bar{r} = 0$ and $\bar{r} = \bar{r}_{\mathrm{min}}$) and distributes it over a larger area. The fluid pressure $\bar{p}$ at $\bar{r} = \bar{r}_{\mathrm{min}}$ decreases faster than $\bar{p}_{\mathrm{max}}$, meaning that the pressure gradient $-\partial\bar{p}/\partial\bar{r}$ at $\bar{r} = \bar{r}_{\mathrm{min}}$ increases and consequently $\bar{r}_{\mathrm{min}}$ continues to increase, i.e. $\bar{r}_{\mathrm{min}}$ continues to move radially outwards.

Figure 5.12 shows that when the permeability $k > 0$ the initial evolution of the fluid pressure $\bar{p}$ is similar to the case when $k = 0$, and consequently $\bar{r}_{\mathrm{min}}$ moves radially outwards. However, for larger times the behaviour is qualitatively different. Figure 5.12(b) shows that when the permeability $k > 0$ there is an increase in the fluid pressure $\bar{p}$ at $\bar{r} = \bar{r}_{\mathrm{min}}$ as the minimum fluid layer thickness h_{min} (which, we recall, occurs at $\bar{r} = \bar{r}_{\mathrm{min}} > 0$) decreases to zero in a finite contact time $\bar{t} = \bar{t}_{\mathrm{c}}$. The increase in the fluid pressure $\bar{p}$ at $\bar{r} = \bar{r}_{\mathrm{min}}$ means that, following its initial increase, the pressure gradient $-\partial\bar{p}/\partial\bar{r}$ at $\bar{r} = \bar{r}_{\mathrm{min}}$ decreases and $\bar{r}_{\mathrm{min}}$ decreases. Thus, $\bar{r}_{\mathrm{min}}$ increases from its initial value $\bar{r}_{\mathrm{min}} = 0$ to its maximum value, which it attains at some time $\bar{t} < \bar{t}_{\mathrm{c}}$, and then, because of the increase in the fluid pressure $\bar{p}$ at $\bar{r} = \bar{r}_{\mathrm{min}}$ as h_{min} decreases to zero in a finite contact time $\bar{t} = \bar{t}_{\mathrm{c}}$, decreases to its value at the contact time $\bar{t}_{\mathrm{c}}$.

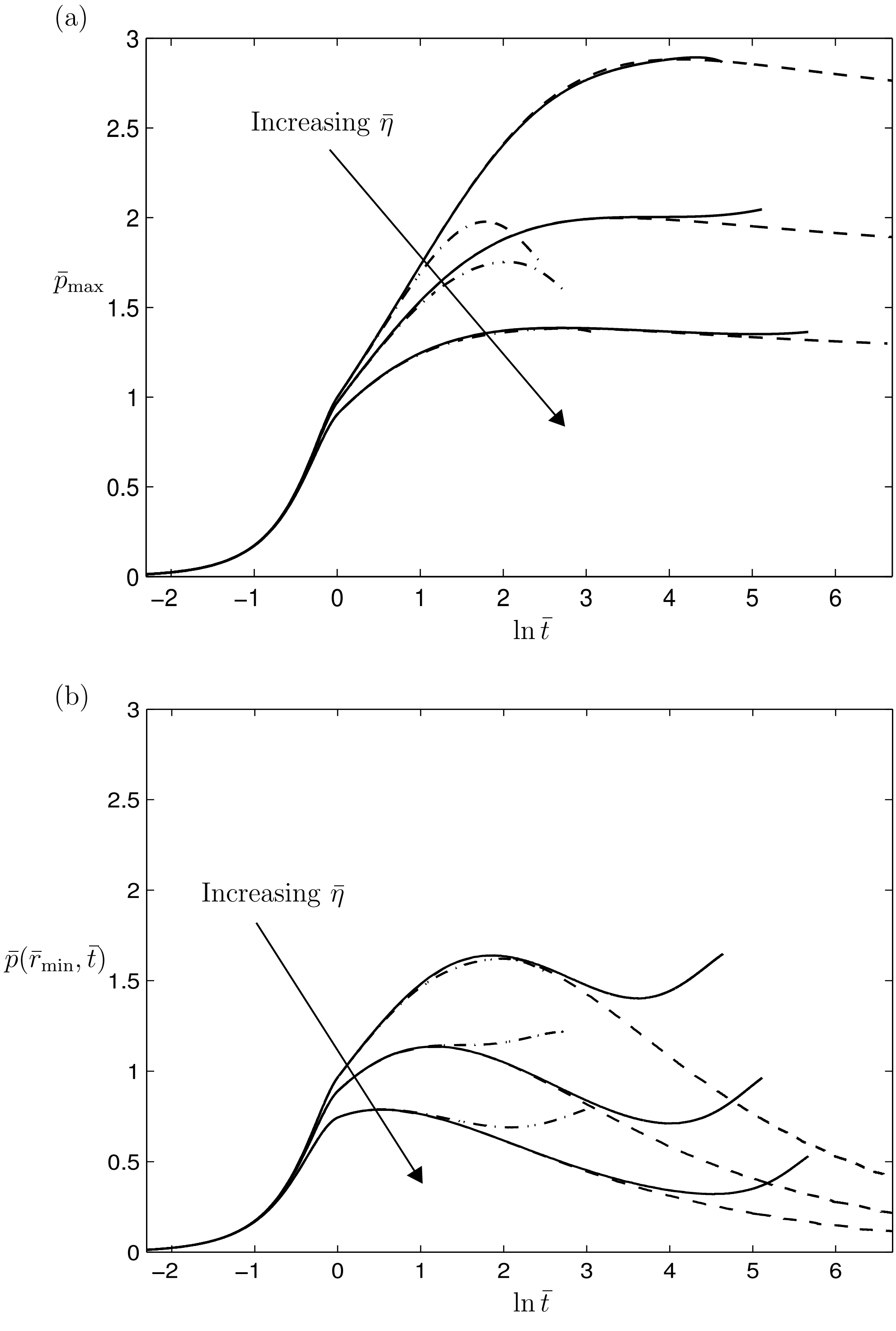

Figure 5.12: Plots of (a) $\bar{p}_{\max}$ and (b) $\bar{p}(\bar{r}_{\min}, \bar{t})$ as functions of $\ln \bar{t}$ for three values of $\bar{\eta}$, namely $\bar{\eta} = 1/30$, 0.1 and 0.3, each for three values of k, namely $k = 0$ (dashed lines), $k = 10^{-5}$ (solid lines) and $k = 10^{-3}$ (dash-dot lines), in the case when $n = 2$

5.3 Limit of Small Permeability $k \to 0$ in the Special Case when the Bearing is Parabolic, i.e. when $n = 1$

In this section asymptotic solutions for the fluid layer thickness h and the fluid pressure p that are valid in the limit of small permeability $k \to 0$ are obtained in the special case when the bearing is parabolic, i.e. when $n = 1$. Using (5.2) to eliminate the fluid pressure p from (5.1), we deduce that in this special case h satisfies

$$\frac{\partial h}{\partial t} = \frac{1}{12\eta r}\frac{\partial}{\partial r}\left(r\left(h^3 + 12k\right)\left(\frac{\partial h}{\partial r} - 2r\right)\right). \tag{5.13}$$

In the limit of small permeability $k \to 0$ it will transpire that, similarly to the inelastic cases for a flat bearing and a curved bearing with $n \to \infty$ treated in Chapter 3 and 4, respectively, the contact time $t_c = O(k^{-2/3}) \gg 1$ is large, and solutions for h and p that are valid for "short" times $t = O(1)$ (more precisely, $t = o(k^{-2/3})$) and "long" times $t = O(k^{-2/3})$ are required in order to obtain a complete description of the behaviour up to the contact time. Furthermore, and in contrast to the inelastic cases treated in Chapters 3 and 4, for both "short" and "long" times different asymptotic solutions for h and p are valid in the three spatial regions $r < r_C$, $|r - r_C| \ll 1$ and $r > r_C$. The leading order small-k asymptotic solutions for h and p that are valid in $r < r_C$ and $|r - r_C| \ll 1$ are determined for both "short" and "long" times and, in particular, it is shown that to leading order in the limit of small permeability $k \to 0$ the radial position $r = r_C$ of the corner that forms in the interface $z = h$ between the elastic layer and the fluid layer is identical for "short" and "long" times.

5.3.1 Solution for "Short" Times $t = O(1)$

Figures 5.5(a), 5.5(c) and 5.5(e) show that when $k \ll 1$ is small the solution for the minimum fluid layer thickness $h_{\min}$ is indistinguishable from the solution in the case when the bed is impermeable, i.e. when $k = 0$, for "short" times $t = O(1)$. Indeed, for "short" times $t = O(1)$ the bed is effectively impermeable and the leading order small-k asymptotic solution for h is given by the solution for h in the special case when the bed is impermeable, i.e. when $k = 0$. Setting $k = 0$ in (5.13) we deduce that in this special case the fluid layer thickness h satisfies

$$\frac{\partial h}{\partial t} = \frac{1}{12\eta r}\frac{\partial}{\partial r}\left(rh^3\left(\frac{\partial h}{\partial r} - 2r\right)\right). \tag{5.14}$$

It is not possible to obtain the analytical solution to (5.14) for h that is valid for all times t. However, similarly to Weekley *et al.* [71] and Balmforth *et al.* [8], both of whom considered the approach of a two-dimensional parabola through a thin layer of fluid towards a flat surface coated with a thin elastic layer, we can obtain the solution for h that is valid to leading order in the limit of large time $t \to \infty$, i.e. the large-t asymptotic behaviour of the leading order small-k asymptotic solution for h that is valid for "short" times $t = O(1)$.

5.3.1.1 Solution to (5.14) Valid in $r < r_{\mathrm{C}}$ for Large Times $t \to \infty$

When $k = 0$ and $n = 1$, the minimum fluid layer thickness $h_{\min} = h(0,t) = O\left(t^{-1/2}\right) \to 0^+$ as $t \to \infty$, and thus we re-scale t and h according to

$$t = T, \quad h = T^{-1/2}H, \tag{5.15}$$

where H is $O(1)$ in the limit $t \to \infty$. Seeking a regular perturbation solution to (5.14) of the form

$$H(r,T) = H_0(r) + O(T^{-1/2}), \tag{5.16}$$

at $O(1)$ we have

$$\frac{1}{r}\frac{\mathrm{d}}{\mathrm{d}r}\left(r^2 H_0^3\right) = 3\eta H_0. \tag{5.17}$$

Solving (5.17) subject to the boundary condition $\mathrm{d}H_0/\mathrm{d}r = 0$ at $r = 0$ yields the simple solution

$$H_0 = \sqrt{\frac{3\eta}{2}}. \tag{5.18}$$

Therefore, in terms of the original variables the leading order large-t asymptotic solution for the fluid layer thickness h is

$$h = \sqrt{\frac{3\eta}{2t}} \simeq 1.2247 \times \sqrt{\frac{\eta}{t}}, \tag{5.19}$$

showing that to leading order in the limit of large time $t \to \infty$ the elastic layer deforms in such a way as to produce a fluid layer of uniform thickness. Figures 5.5(a), 5.5(c) and 5.5(e) compare the leading order large-t asymptotic solution for the minimum fluid layer thickness h_{min} given by (5.19) with full numerical solutions. The elastic layer deforms in such a way as to produce a fluid layer of uniform thickness in $r < r_{\mathrm{C}}$, and consequently the approach of the parabolic bearing towards the stationary impermeable bed is qualitatively the same as the approach of a flat impermeable bearing towards a stationary impermeable bed (see §3.2.1.1 or, for example, Stone [66]). This is consistent with the numerical results discussed in §5.2.2 which showed that, when $k = 0$ and $n = 1$, a fluid layer of approximately uniform thickness h is formed in $r < r_{\mathrm{C}}$ for large times (see Figure 5.2(a)).

Seeking regular perturbation solutions for $p = p(r,t)$ and $\tilde{h} = \tilde{h}(t)$ of the form[4]

$$p(r,T) = p_0(r) + O(T^{-1/2}) \tag{5.20}$$

and

$$\tilde{h}(T) = \tilde{h}_0 + \tilde{h}_1 T^{-1/2} + O(T^{-1}), \tag{5.21}$$

at $O(1)$ we see from (5.2) that

$$p_0 = -\frac{\tilde{h}_0 + r^2}{\eta}, \tag{5.22}$$

i.e. to leading order in the limit of large time $t \to \infty$ the fluid pressure is parabolic and independent of t. This is consistent with the numerical results discussed in §5.2.3 which showed that, when $k = 0$ and $n = 1$, the fluid pressure p in $r < r_C$ is approximately parabolic in r and independent of time t for large times (see Figure 5.8(a)).

Clearly the leading order large-t asymptotic solutions for h and p given by (5.19) and (5.22), respectively, are not uniformly valid in r, and there is in fact a corner region $|r - r_C| \ll 1$ (corresponding to the corner that forms in the interface $z = h$ that can be seen in Figure 5.2(a)) in which different large-t asymptotic solutions for h and p are valid. This corner region $|r - r_C| \ll 1$ is analysed in the following subsection §5.3.1.2 and the leading order large-t solution for h that is valid in this region is calculated.

---

[4]Note that the first order term $\tilde{h}_1$ in the expansion for $\tilde{h}$ given by (5.21) is retained as it will be required later.

5.3.1.2 Solution to (5.14) Valid in $|r - r_C| = O(t^{-1/2})$ for Large Times $t \to \infty$

In the corner region $|r - r_C| \ll 1$ we re-scale r, h and p according to

$$r = r_C + T^{-1/2}\hat{r}, \quad t = T, \quad h = T^{-1/2}\hat{h}, \quad p = T^{-1/2}\hat{p}, \tag{5.23}$$

where $\hat{r}$, $\hat{h}$ and $\hat{p}$ are $O(1)$ in the limit $t \to \infty$. Seeking a regular perturbation solution to (5.14) of the form

$$\hat{h}(\hat{r}, T) = \hat{h}_0(\hat{r}) + O(T^{-1/2}), \tag{5.24}$$

at $O(1)$ we have

$$\frac{\mathrm{d}}{\mathrm{d}\hat{r}}\left(\hat{h}_0^3\left(\frac{\mathrm{d}\hat{h}_0}{\mathrm{d}\hat{r}} - 2r_C\right)\right) = 0. \tag{5.25}$$

Substituting (5.21) and (5.24) into (5.2) and re-arranging we find that, in terms of the re-scaled variables (5.23), the fluid pressure $\hat{p}$ is given by

$$\hat{p} = -T^{1/2}\frac{\tilde{h}_0 + r_C^2}{\eta} + \frac{\hat{h}_0 - \tilde{h}_1 - 2r_C\hat{r}}{\eta} + O(T^{-1/2}). \tag{5.26}$$

Since $\hat{p} = O(1)$ as $t \to \infty$ we deduce from (5.26) that the radial position of the corner $r = r_C$ must satisfy

$$\tilde{h}_0 + r_C^2 = 0, \quad \text{i.e.} \quad r_C = \sqrt{-\tilde{h}_0}. \tag{5.27}$$

In order to determine explicitly the leading order large-t solution for the fluid layer thickness $\hat{h}_0$ we must first determine (to first order) the large-t asymptotic solution for the minimum height of the undeformed interface between the fluid layer and the elastic layer $\tilde{h}$, which then yields the radial position $r = r_C$ of the corner in

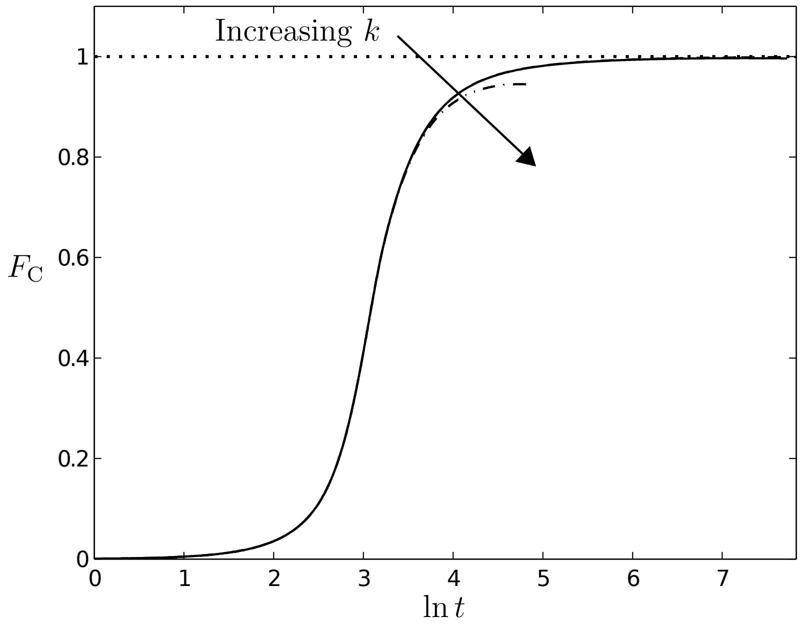

Figure 5.13: Plots of F_C, defined by (5.28), as a function of $\ln t$ for three values of k, namely $k = 0$ (dashed line), $k = 10^{-5}$ (solid line) and $k = 10^{-3}$ (dash-dot line), for $n = 1$ and $\eta = 3/2$. The dotted line shows a plot of L_0 as a function of $\ln t$. Note that the solid ($k = 10^{-5}$) and dashed lines ($k = 0$) are indistinguishable

the fluid layer thickness h via (5.27).

The normal force $F_C = F_C(t)$ exerted on the bearing by the elastic layer in $r < r_C$ is given by

$$F_C = 2\pi \int_0^{r_C} rp \, dr, \tag{5.28}$$

where $r_C = \sqrt{-\tilde{h}_0}$, and Figure 5.13 shows plots of F_C as a function of $\ln t$ for three values of the permeability k. In the special case $k = 0$, Figure 5.13 shows that $F_C \to L_0^-$ as $t \to \infty$, i.e. to leading order in the limit of large time $t \to \infty$ the normal force exerted on the bearing by the elastic layer in $r < r_C$ balances the prescribed constant load $L = L_0$ acting vertically downwards through the bearing. Hence, we deduce that the normal force exerted on the bearing by the elastic layer in $r > r_C$ is small. From (5.23) we see that the normal force exerted on the bearing by the elastic layer in the corner region is $O(t^{-3/2})$, which is small. Furthermore, using a similar argument to Weekley [70], it can be shown that the normal force exerted on the bearing by the elastic layer in $r > r_{\mathrm{C}}$ is at most $O(t^{-3/2})$. Thus in the limit of large time $t \to \infty$ the leading and first order contributions to the normal force exerted on the bearing by the elastic layer occur in $r < r_{\mathrm{C}}$, and hence at $O(1)$ and $O(t^{-1/2})$ the load condition (2.59) requires that

$$\tilde{h}_0 = -\sqrt{\frac{2\eta L_0}{\pi}} \quad \text{and} \quad \tilde{h}_1 = \sqrt{\frac{3\eta}{2}}, \tag{5.29}$$

respectively, i.e. to leading order in the limit of large time $t \to \infty$ the minimum height of the undeformed interface between the fluid layer and the elastic layer satisfies

$$\tilde{h} = -\sqrt{\frac{2\eta L_0}{\pi}} \simeq -0.7979 \times \sqrt{\eta L_0}, \tag{5.30}$$

and hence the radial position $r = r_{\mathrm{C}}$ of the corner that forms in the interface $z = h$ is given by

$$r_{\mathrm{C}} = \left(\frac{2\eta L_0}{\pi}\right)^{1/4} \simeq 0.8932 \times (\eta L_0)^{1/4}. \tag{5.31}$$

Figure 5.7(a) compares the leading order large-t solution for $\tilde{h}$, given by (5.30), with full numerical solutions. Substituting $\tilde{h}_0$, given by (5.29), into (5.22) we deduce that to leading order in the limit of large time $t \to \infty$ the fluid pressure p in $r < r_{\mathrm{C}}$ is given by

$$p = \frac{1}{\eta}\left(\sqrt{\frac{2\eta L_0}{\pi}} - r^2\right), \tag{5.32}$$

and hence to leading order in the limit of large time $t \to \infty$ the maximum fluid pressure $p_{\max} = p(0, t)$ is given by

$$p_{\max} = \sqrt{\frac{2L_0}{\pi\eta}} \simeq 0.7979 \times \sqrt{\frac{L_0}{\eta}}. \tag{5.33}$$

Figures 5.8(a) and 5.10(a) compare the leading order large-t solutions for the fluid pressure p and the maximum fluid pressure p_{max}, given by (5.32) and (5.33), respectively, with full numerical solutions.

Substituting (5.33) into (5.9) we deduce that for a physically consistent leading order large-t solution we require that

$$\eta < \frac{\pi}{2L_0} \simeq \frac{1.5708}{L_0}. \tag{5.34}$$

Note that throughout this Chapter we have used (5.34) as an upper bound on η in all of the numerical calculations.

The physical effect of increasing η is readily seen from equations (5.19), (5.31) and (5.33). As η increases the maximum fluid pressure $p_{\text{max}} \propto \eta^{-1/2}$ decreases and the corner in the fluid layer thickness at $r = r_{\text{C}} \propto \eta^{1/4}$ occurs further from the axis of symmetry $r = 0$, i.e. the fluid pressure p is distributed over a larger area which reduces the magnitude of the pressure gradient $\partial p/\partial r$, increasing the time $t \propto \eta$ taken for the minimum fluid layer thickness to reduce to a thickness h_{min}.

Solving (5.25) subject to the appropriate matching condition with the solution that is valid in $r < r_{\text{C}}$, namely

$$\hat{h}_0 \sim \sqrt{\frac{3\eta}{2}} \quad \text{as} \quad \hat{r} \to -\infty, \tag{5.35}$$

and the boundary condition (2.21), which, from (5.26), at $O(1)$ requires that

$$\hat{h}_0 \sim \tilde{h}_1 + 2r_{\text{C}}\hat{r} \quad \text{as} \quad \hat{r} \to \infty, \tag{5.36}$$

where $\tilde{h}_1$ and r_C are given by (5.29) and (5.31), respectively, yields the solution

$$\hat{r} = \left(\frac{9\pi\eta}{128L_0}\right)^{1/4}\left[s + \frac{\sqrt{3}\pi}{6} - 1 - \frac{1}{\sqrt{3}}\tan^{-1}\left(\frac{2s+1}{\sqrt{3}}\right) + \frac{1}{3}\ln\left(\frac{s-1}{\sqrt{s^2+s+1}}\right)\right], \tag{5.37}$$

where

$$s = \sqrt{\frac{2}{3\eta}}\hat{h}_0. \tag{5.38}$$

Figure 5.14(a) compares the leading order large-t solution for h given by (5.37) with full numerical solutions.

Note that Weekley *et al.* [71] considered the approach of a two-dimensional parabolic surface towards a stationary thin elastic layer through a thin layer of fluid and found that a solution similar to (5.37) describes the fluid layer thickness h in the vicinity of the corner that forms in the interface between the fluid and elastic layers. However, Weekley *et al.* [71] did not retain the first order term in the asymptotic expansion for $\tilde{h}$ in their matching condition equivalent to (5.36). Consequently, the leading order solution for h in the vicinity of the corner given by Weekley *et al.* [71], though giving the correct shape of the corner, is shifted horizontally to the right of the corner, and an unspecified $O(1)$ horizontal shift to the left is required to correct the leading order solution for h. It is not, therefore, possible to determine the fluid layer thickness h_C at the corner from this solution.

Setting $\hat{r} = 0$ in (5.37) we deduce that to leading order in the limit of large time $t \to \infty$ the fluid layer thickness $h_C = h(r_C, t)$ at the corner $r = r_C$ is given by

$$h_C = \sqrt{\frac{3\eta s_0^2}{2t}} \simeq 1.6428 \times \sqrt{\frac{\eta}{t}}, \tag{5.39}$$

(a)

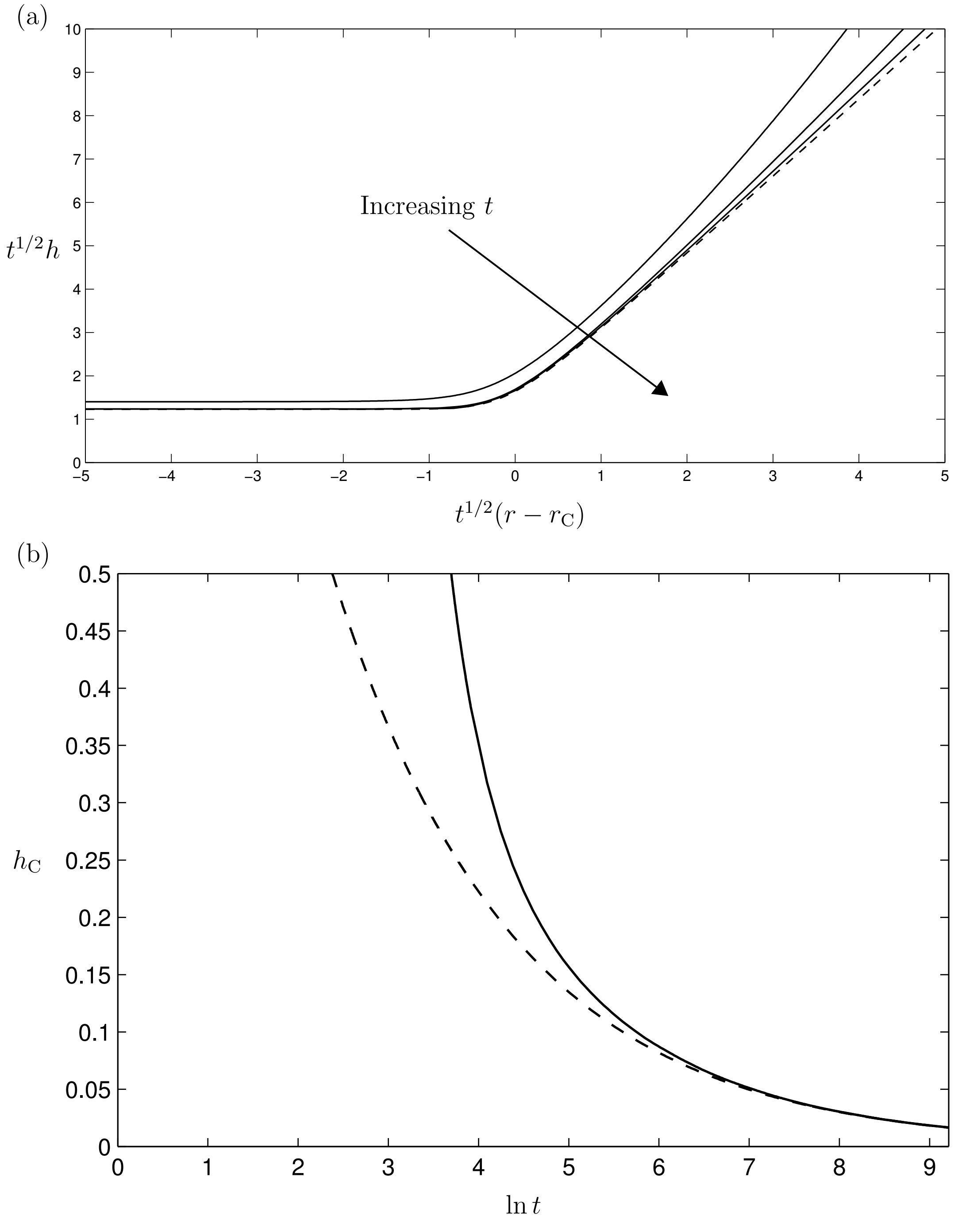

Figure 5.14: (a) Plots of the re-scaled fluid layer thickness $t^{1/2}h$ as a function of $t^{1/2}(r - r_C)$ for $t = 100$, 1000 and 10000. The dashed line corresponds to the leading order large-t asymptotic solution for h given by (5.37). (b) A plot of the fluid layer thickness h_C at the corner $r = r_C$ as a function of $\ln t$. The dashed line corresponds to the leading order large-t asymptotic solution for h_C given by (5.39). In both plots $k = 0$, $n = 1$ and $\eta = 1$

where $s_0 \simeq 1.3413$ satisfies

$$s_0 + \frac{\sqrt{3}\pi}{6} - 1 - \frac{1}{\sqrt{3}}\tan^{-1}\left(\frac{2s_0+1}{\sqrt{3}}\right) + \frac{1}{3}\ln\left(\frac{s_0-1}{\sqrt{s_0^2+s_0+1}}\right) = 0. \quad (5.40)$$

Figure 5.14(b) compares the leading order large-t solution for the fluid layer thickness h_C at the corner $r = r_C$ given by (5.39) with a full numerical solution.

The large-t asymptotic behaviour of the leading order small-k, "short" time $t = O(1)$ asymptotic solutions for h in $r < r_C$ and $|r - r_C| = O(t^{-1/2})$ are given by (5.19) and (5.39), respectively. Since these solutions are valid only for "short" times $t = O(1)$ when the bed is effectively impermeable, neither solution reaches zero in a finite contact time t_c. After a "long" time $t = O(k^{-2/3})$ the effects of the permeability k become significant and asymptotic solutions that are valid for "long" times $t = O(k^{-2/3})$ are required in order to describe the behaviour right up to the contact time t_c. These solutions are calculated in the following subsection §5.3.2.

5.3.2 Solution for "Long" Times $t = O(k^{-2/3})$

The effects of the permeability k become significant when the fluid volume flux into the porous bed Q_{bed} is the same size as, or larger than, the fluid volume flux out of the fluid layer Q_{out}. Thus, when the permeability $k \ll 1$ is small its effects become significant only after a "long" time $t = O(k^{-2/3}) \gg 1$ when the fluid layer thickness $h = O(k^{1/3}) \ll 1$ is small. Note that in Chapter 3 it was shown that when a flat rigid impermeable bearing and a stationary porous bed (of permeability $k \ll 1$), separated by a thin fluid layer of thickness h, approach each other under constant load, the effects of the permeability k are, similarly, significant only after a "long" time $t = O(k^{-2/3}) \gg 1$ when $h = O(k^{1/3}) \ll 1$ is small.

The leading order small-k asymptotic solutions for h and p that are valid for "long" times $t = O(k^{-2/3})$ inherit the spatial structure of the leading order small-k asymptotic solutions that are valid for "short" times $t = o(k^{-2/3})$, i.e. the solutions in the case $k = 0$ calculated in §5.3.1, and, therefore, different small-k asymptotic solutions for h and p are, again, valid in $r < r_C$, $|r - r_C| \ll 1$ and $r > r_C$.

5.3.2.1 Solution to (5.13) Valid in $r < r_C$

For "long" times we re-scale t and h according to

$$t = (12k)^{-2/3}T, \quad h = (12k)^{1/3}H, \tag{5.41}$$

where T and H are $O(1)$ in the limit $k \to 0$ and the factor 12 has again been introduced into the scalings for convenience. Seeking a regular perturbation solution to (5.13) of the form

$$H(r,T) = H_0(r,T) + O(k^{1/3}), \tag{5.42}$$

at $O(1)$ we have

$$3rH_0^2 \frac{\partial H_0}{\partial r} + 6\eta \frac{\partial H_0}{\partial T} = -2(H_0^3 + 1). \tag{5.43}$$

Solving (5.43) subject to the appropriate matching condition with the solution for h given by (5.19) that is valid at "short" times, namely

$$H_0 \sim \sqrt{\frac{3\eta}{2T}} \quad \text{as} \quad T \to 0, \tag{5.44}$$

yields the solution

$$T = \eta[f(\infty) - f(H_0)], \tag{5.45}$$

where f is again given by (3.53). Therefore, in terms of the original variables the leading order small-k asymptotic solution for the fluid layer thickness h that is valid for "long" times $t = O(k^{-2/3})$ is

$$t = \frac{\eta}{(12k)^{2/3}} \left[f(\infty) - f\left(h/(12k)^{1/3} \right) \right], \tag{5.46}$$

i.e. to leading order in the limit of small permeability $k \to 0$ the fluid layer thickness h in $r < r_{\rm C}$ is uniform. Figures 5.5(a), 5.5(c) and 5.5(e) compare the leading order small-k asymptotic solution for h given by (5.46) with full numerical solutions. It was shown in §5.3.1 that for "short" times $t = o(k^{-2/3})$, when the effects of the permeability k are negligible and the bed is effectively impermeable, the thin elastic layer that coats the bearing deforms in such a way as to produce a fluid layer of uniform thickness h, given by (5.19), in $r < r_{\rm C}$. For "large" times $t = O(k^{-2/3})$ when the effects of the permeability k are no longer negligible the fluid layer thickness h, given by (5.46), in $r < r_{\rm C}$ remains uniform. The main difference between the leading order small-k solutions for h that are valid in $r < r_{\rm C}$ for "short" $t = o(k^{-2/3})$ and "long" times $t = O(k^{-2/3})$ is that the solution for h that is valid for "long" times, given by (5.46), reaches zero in a finite contact time $t_{\rm c}$ whereas the solution for h that is valid for "short" times, given by (5.19), does not. Setting the fluid layer thickness $h = 0$ in (5.46), we deduce that to leading order in the limit of small permeability $k \to 0$ the contact time $t_{\rm c}$ is given by

$$t_{\rm c} = \frac{2\pi\eta}{\sqrt{3}(12k)^{2/3}}. \tag{5.47}$$

Figure 5.6 compares the leading order small-k asymptotic solution for the contact time $t_{\rm c}$ given by (5.47) with the full numerical solution. Since h is uniform in $r < r_{\rm C}$ the approach of the parabolic bearing towards the stationary porous bed is qualitatively the same as the approach of a flat bearing towards a stationary porous bed through a thin layer of fluid, a problem that was treated in Chapter 3. The leading order small-k solution for the contact time t_c given by (5.47) is, therefore, similar to the corresponding result obtained in Chapter 3, namely (3.58). In particular, in both cases the contact time $t_c \propto k^{-2/3}$.

Seeking regular perturbation solutions for $p = p(r, t)$ and $\tilde{h} = \tilde{h}(t)$ of the form[5]

$$p(r, T) = p_0(r) + O(k^{1/3}) \tag{5.48}$$

and

$$\tilde{h}(T) = \tilde{h}_0(T) + (12k)^{1/3}\tilde{h}_1(T) + O(k^{2/3}), \tag{5.49}$$

we see from (5.2) that

$$p_0 = -\frac{\tilde{h}_0(T) + r^2}{\eta}, \tag{5.50}$$

i.e. to leading order in the limit of small permeability $k \to 0$ for "long" times $t = O(k^{-2/3})$ the fluid pressure p is, again, parabolic and independent of the permeability k. This is consistent with the numerical results discussed in §5.2.3 which showed that, when the permeability $k \ll 1$ is small, $n = 1$ and time $t \gg 1$ is large, the fluid pressure p in $r < r_C$ is approximately parabolic in r and independent of k (see Figures 5.8(a), 5.8(b) and 5.9(a)).

Recall that for "short" times $t = o(k^{-2/3})$ the leading order small-k asymptotic solutions for h and p given by (5.19) and (5.32), respectively, are not uniformly valid in r, and there is a corner region $|r - r_C| \ll 1$ in which different leading order small-k asymptotic solutions for h and p are valid. Similarly, for "large" times $t = O(k^{-2/3})$ the leading order small-k asymptotic solutions for h and p given by

[5]Note that the first order term $\tilde{h}_1$ in the expansion for $\tilde{h}$ given by (5.49) is, again, retained as it will be required later.

(5.46) and (5.50), respectively, are not uniformly valid in r, and different small-k asymptotic solutions for h and p are valid in the corner region $|r - r_{\text{C}}| = O(k^{1/3})$. The corner region is analysed in the following subsection §5.3.2.2.

5.3.2.2 Solution to (5.13) Valid in $|r - r_{\text{C}}| = O(k^{1/3})$

In the corner region $|r - r_{\text{C}}| = O(k^{1/3})$ we re-scale r, t, h and p according to

$$r = r_{\text{C}} + (12k)^{1/3}\hat{r}, \quad t = (12k)^{-2/3}T, \quad h = (12k)^{1/3}\hat{h}, \quad p = (12k)^{1/3}\hat{p}, \quad (5.51)$$

where $\hat{r}$, $\hat{t}$, $\hat{h}$ and $\hat{p}$ are $O(1)$ in the limit $k \to 0$. Seeking a regular perturbation solution to (5.1) of the form

$$\hat{h}(\hat{r}, T) = \hat{h}_0(\hat{r}, T) + O(k^{1/3}), \quad (5.52)$$

at $O(1)$ we have

$$\frac{\partial}{\partial \hat{r}}\left((\hat{h}_0^3 + 1)\left(\frac{\partial \hat{h}_0}{\partial \hat{r}} - 2r_{\text{C}}\right)\right) = 0. \quad (5.53)$$

Substituting (5.49) and (5.52) into (5.2) and re-arranging we find that, in terms of the re-scaled variables (5.51), the fluid pressure $\hat{p}$ is given by

$$\hat{p} = -\frac{\tilde{h}_0 + r_{\text{C}}^2}{\eta(12k)^{1/3}} + \frac{\hat{h}_0 - \tilde{h}_1 - 2r_{\text{C}}\hat{r}}{\eta} + O(k^{1/3}). \quad (5.54)$$

Since $\hat{p} = O(1)$ as $t \to \infty$ we deduce from (5.54) that the radial position of the corner $r = r_{\text{C}}$ must, just as it did for "short" times $t = o(k^{-2/3})$, satisfy $r_{\text{C}} = (-\tilde{h}_0)^{1/2}$.

In order to determine explicitly the leading order small-k solution for the fluid layer thickness $\hat{h}_0$ that is valid for "long" times $t = O(k^{-2/3})$ in the vicinity of the corner $|r - r_{\text{C}}| = O(k^{1/3})$ we must first determine (to first order) the asymptotic solution for $\tilde{h}$, which then yields, via $r_C = (-\tilde{h}_0)^{1/2}$, the radial position $r = r_C$ of the corner.

Figure 5.13 shows that when the permeability $k \ll 1$ is small $F_C \to L_0^-$ after a "long" time $t = O(k^{-2/3})$, i.e. the normal force exerted on the bearing by the elastic layer in $r < r_C$ balances the prescribed constant load $L = L_0$ acting vertically downwards through the bearing. Hence, we deduce that for long times $t = O(k^{-2/3})$ the normal force exerted on the bearing by the elastic layer in $r > r_C$ is small. (Recall that in §5.3.1 this force was shown to be small for short times $t = o(k^{-2/3})$.) From (5.51) we see that the normal force exerted on the bearing by the elastic layer in the corner region is $O(k)$, which is small. Furthermore, it can be shown that the normal force exerted on the bearing by the elastic layer in $r > r_C$ is at most $O(k)$. Thus, similarly to §5.3.1, in the limit of small permeability $k \to 0$ for "long" times $t = O(k^{-2/3})$ the leading and first order contributions to the normal force exerted on the bearing by the elastic layer occur in $r < r_C$ and hence at $O(1)$ and $O(k^{1/3})$ the load condition (2.59) requires that

$$\tilde{h}_0 = -\sqrt{\frac{2\eta L_0}{\pi}} \quad \text{and} \quad \tilde{h}_1 = H_0(T). \tag{5.55}$$

Consequently, a similar analysis to §5.3.1.2 shows that to leading order in the limit of small permeability $k \to 0$ for "long" times $t = O(k^{-2/3})$ the minimum height of the undeformed interface between the fluid layer the elastic layer $\tilde{h}$, the fluid pressure p in $r < r_C$, the maximum fluid pressure $p_{\max}$ and the radial position of the corner $r = r_C$ are, again, given by (5.30), (5.32), (5.33), and (5.31), respectively. Figures 5.7(a), 5.8(a), 5.8(b) and 5.9(a), and 5.10(a) compare the leading order small-k solutions for $\tilde{h}$, p and $p_{\max}$ given by (5.30), (5.32) and (5.33), respectively, with full numerical solutions. Furthermore, for a physically consistent solution it is required that η, again, satisfies (5.34).

The physical effect of increasing η is identical to that described in §5.3.1.2 for "short" times $t = o(k^{-2/3})$ (when, to leading order in the limit of small permeability $k \to 0$, the bed is effectively impermeable). In fact, the leading order small-k solutions for h and p that are valid for "long" times $t = O(k^{-2/3})$ in $r < r_\mathrm{C}$ are similar to those that are valid for "short" times $t = o(k^{-2/3})$. The leading order solutions for p in $r < r_\mathrm{C}$ and the radial position of the corner $r = r_\mathrm{C}$ are identical for "short" $t = o(k^{-2/3})$ and "long" $t = O(k^{-2/3})$ times, i.e. to leading order in the limit of small permeability $k \to 0$ both the fluid pressure p in $r < r_\mathrm{C}$ and the radial position of the corner $r = r_\mathrm{C}$ are unaffected by the permeability k when its effects become significant after a "long" time $t = O(k^{-2/3})$.

Solving (5.53) subject to the appropriate matching condition with the solution that is valid in $r < r_\mathrm{C}$, namely

$$\hat{h}_0 \sim H_0 \quad \text{as} \quad \hat{r} \to -\infty, \tag{5.56}$$

where H_0 is given by (5.45), and the boundary condition (2.21), which, from (5.54) at $O(1)$ requires that

$$\hat{h}_0 \sim \tilde{h}_1(T) + 2r_\mathrm{C}\hat{r} \quad \text{as} \quad \hat{r} \to \infty, \tag{5.57}$$

where r_C and $\tilde{h}_1$ are given by (5.31) and (5.55), respectively, yields the solution

$$\begin{aligned} \hat{r} \;=\; & \left(\frac{\pi}{32\eta L_0}\right)^{1/4}\left[\hat{h}_0 - H_0 + \frac{H_0^3+1}{3H_0^2}\ln\left(\frac{\hat{h}_0 - H_0}{\sqrt{\hat{h}_0^2 + H_0\hat{h}_0 + H_0^2}}\right)\right. \\ & \left. + \frac{H_0^3+1}{\sqrt{3}H_0^2}\left(\frac{\pi}{2} - \tan^{-1}\left(\frac{2\hat{h}_0 + H_0}{\sqrt{3}H_0}\right)\right)\right]. \end{aligned} \tag{5.58}$$

Figure 5.15(a) compares the leading order small-k solution for the fluid layer thick-

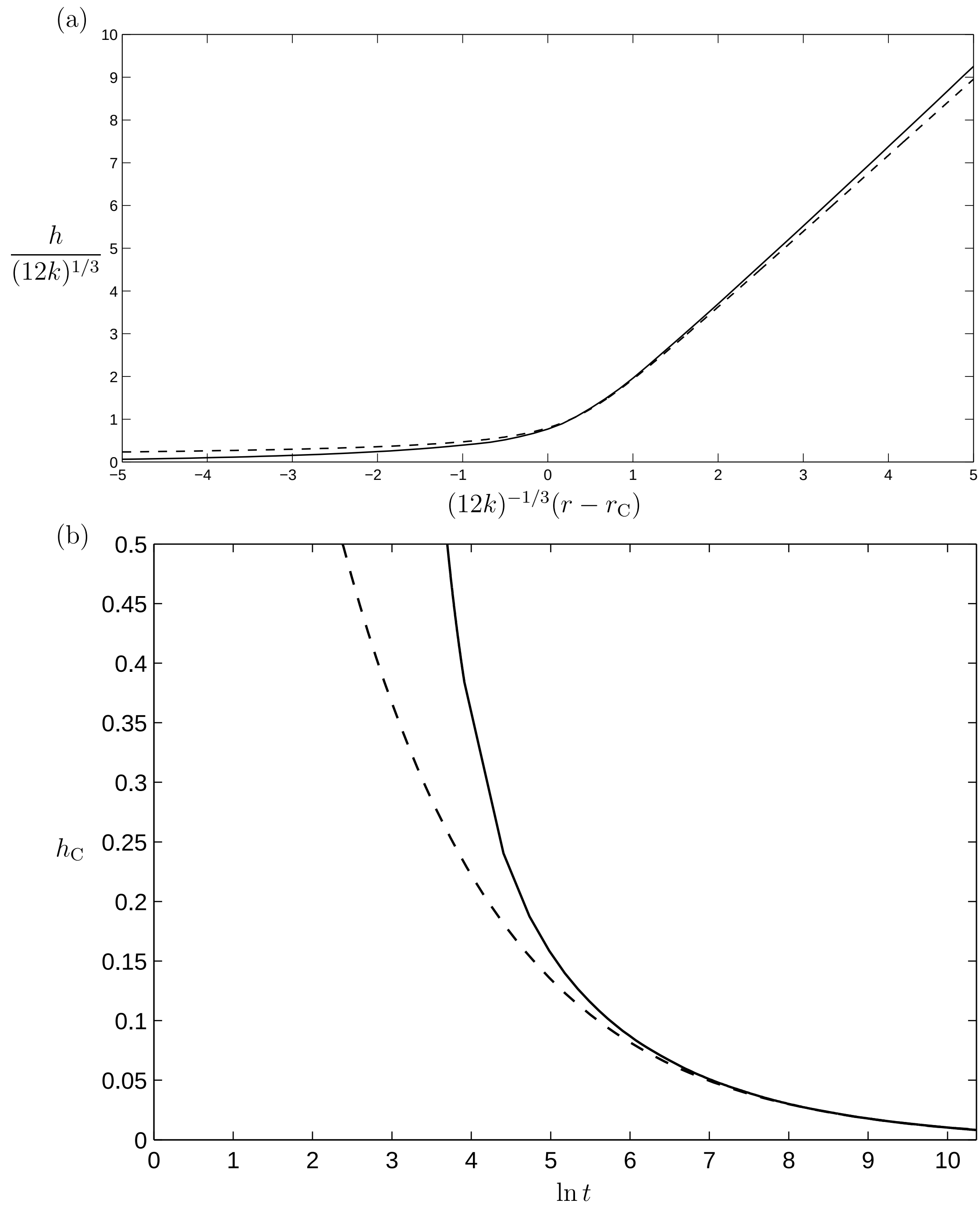

Figure 5.15: (a) Plots of the re-scaled fluid layer thickness $(12k)^{-1/3}h$ as a function of $(12k)^{-1/3}(r - r_C)$ for $t = 31700$. The dashed line corresponds to the leading order small-k asymptotic solution for h given by (5.58). (b) A plot of the fluid layer thickness h_C at the corner $r = r_C$ as a function of $\ln t$. The dashed line corresponds to the leading-order small-k asymptotic solution for h_C given by (5.59). In both plots $k = 10^{-7}$, $n = 1$ and $\eta = 1$

ness h given by (5.58) with full numerical solutions. Setting $\hat{r} = 0$ in (5.58) we deduce that to leading order in the limit of small permeability $k \to 0$ for "large" times $t = O(k^{-2/3})$ the fluid layer thickness $h_{\mathrm{C}} = h(r_{\mathrm{C}}, t)$ at the corner $r = r_{\mathrm{C}}$ is given by

$$h_{\mathrm{C}} = (12k)^{1/3}\hat{h}_{\mathrm{C}}(t), \tag{5.59}$$

where $\hat{h}_{\mathrm{C}} = \hat{h}_{\mathrm{C}}(t)$ satisfies

$$\ln\left(\frac{\hat{h}_{\mathrm{C}} - H_0}{\sqrt{\hat{h}_{\mathrm{C}}^2 + H_0\hat{h}_{\mathrm{C}} + H_0^2}}\right) + \sqrt{3}\left(\frac{\pi}{2} - \tan^{-1}\left(\frac{2\hat{h}_{\mathrm{C}} + H_0}{\sqrt{3}H_0}\right)\right) = \frac{3H_0^2(H_0 - \hat{h}_{\mathrm{C}})}{H_0^3 + 1}, \tag{5.60}$$

where H_0 is given implicitly by (5.46). Figure 5.15(b) compares the leading order small-k solution for h_{C} given by (5.59) with a full numerical solution. Taking the limit $H_0 \to 0^+$ in (5.60) we deduce that, to leading order in the limit of small permeability $k \to 0$, at the contact time t_{c} the fluid layer thickness h_{C} at the corner $r = r_{\mathrm{C}}$ is given by

$$h_{\mathrm{C}}(t_{\mathrm{c}}) = (6k)^{1/3}. \tag{5.61}$$

5.4 Conclusions

In this Chapter we have considered the squeeze-film flow of a thin layer of Newtonian fluid filling the gap between a curved impermeable bearing (with shape $H \propto r^{2n}$, where n is an integer) coated with a thin elastic layer, moving under a prescribed load L, and a flat impermeable surface coated with a thin stationary porous bed of permeability k. The governing Reynolds equation was derived in §2 and was solved numerically using COMSOL Multiphysics. Numerical solutions for the fluid layer thickness $h = h(r, t)$, the contact time t_{c} and the fluid pressure $p = p(r, t)$ were obtained and interpreted physically. Furthermore, in the special case when the bearing is parabolic, i.e. when $n = 1$, the asymptotic limit of small permeability $k \to 0$ was investigated and asymptotic solutions for the fluid layer thickness $h = h(r, t)$, the contact time t_c and the fluid pressure $p = p(r, t)$ were obtained.

In the special case when the bearing is parabolic, i.e. when $n = 1$, for the range of permeabilities k used in the numerical calculations, namely $0 \le k \le 10^{-3}$, it was shown that a region of approximately uniform fluid layer thickness h forms in $r < r_C$ as the elastic layer approaches the porous bed, where $r = r_C$ is the radial position of a corner that forms in the interface $z = h$ between the elastic and fluid layers. For flatter bearing shapes, i.e. for $n \ge 2$, and in particular when the bearing is quartic, i.e. when $n = 2$, qualitatively different behaviour was observed. In these cases it was shown that a region of approximately uniform fluid layer thickness h does not form as the elastic layer approaches the porous bed. Furthermore, it was shown that when $n \ge 2$ the fluid layer thickness h attains its minimum value at $r = r_{\min} > 0$, whereas when the bearing is parabolic, i.e. when $n = 1$, the fluid layer thickness h attains its minimum value at $r = 0$.

In all of the numerical calculations presented in this Chapter in which $k = 0$, the fluid layer thickness h never reached zero in a finite time t. However, in all of the numerical calculations presented in this Chapter in which $k > 0$, the fluid layer thickness h always reached zero in a finite contact time t_c. The contact time t_c was found to increase as the permeability k decreases, or as n increases, i.e. when a flatter bearing shape $H \propto r^{2n}$ is chosen, or as the compliance of the elastic layer η increases.

In the special case of a parabolic bearing (the geometry most relevant to the human knee), i.e. when $n = 1$, the asymptotic limit of small permeability $k \to 0$ (the asymptotic limit most relevant to the human knee) was investigated. It was shown that for "short" times $t = o(k^{-2/3})$ the bed is effectively impermeable and, therefore, on this "short" timescale the solution in the case of an impermeable bed, i.e. the solution in the case $k = 0$, is valid to leading order in the limit of small permeability $k \to 0$. On this "short" timescale $t = o(k^{-2/3})$ it was shown that to leading order a fluid layer of uniform thickness h given by (5.19) is formed in $r < r_{\mathrm{C}}$, where $r = r_{\mathrm{C}}$ is the radial position of the corner that forms in the interface $z = h$ between the elastic and fluid layers and is given by (5.31). Furthermore, it was shown that to leading order in the limit of small permeability $k \to 0$ the fluid pressure p in $r < r_{\mathrm{C}}$, which is given by (5.32), is parabolic in r and independent of time t.

The leading order small-k asymptotic solution for the fluid layer thickness h that is valid on this "short" timescale is similar to those calculated by Weekley *et al.* [71] and Balmforth *et al.* [8], both of whom considered the approach of a two-dimensional parabola through a thin layer of fluid towards a flat stationary surface coated with a thin elastic layer. In particular, a fluid layer of uniform thickness $h = O(t^{-1/2}) \to 0^+$ as $t \to \infty$ is formed around the axis of symmetry in both cases.

It was shown that the effects of the permeability k become significant only after a "long" time $t = O(k^{-2/3})$, and a second leading order small-k asymptotic solution for the fluid layer thickness h, given by (5.46), that is valid on this "long" timescale was calculated. The leading order small-k asymptotic solution for h given by (5.46) reaches zero in a finite contact time $t_{\mathrm{c}} \propto k^{-2/3}$, given by (5.47), and inherits the spatial structure of the solution that is valid for "short" times. Expressed in terms of dimensional variables, the leading order small-k asymptotic solution for the contact time t_c given by (5.47) is

$$t_c = \frac{4\pi\mu\mathcal{R}}{\sqrt{3}(2G+\lambda)H_p}\left(\frac{H_p^2}{12k}\right)^{2/3}. \tag{5.62}$$

Perhaps surprisingly, this solution for t_c is independent of the prescribed load L_0 that pushes the elastic layer towards the porous bed. The leading order small-k solution for the radial position $r = r_C$ of the corner that forms in the interface $z = h$ between the elastic and fluid layers, which is given by (5.31) and is expressed in terms of dimensional variables as

$$r_C = \left(\frac{4H_p\mathcal{R}L_0}{\pi(2G+\lambda)}\right)^{1/4}, \tag{5.63}$$

does, however, depend on the prescribed load L_0. Increasing L_0 increases the radial position $r = r_C \propto L_0^{1/4}$ of the corner, i.e. the elastic layer deforms in such a way as to distribute the additional stress in the fluid layer required to support the increased load L_0 over a larger area.

Since eventually a fluid layer of uniform thickness h in $r < r_C$ separates the elastic layer and the porous bed, their approach is qualitatively the same as the approach of a flat impermeable disc of radius $\mathcal{R}$ moving under constant load L_0 through a thin layer of fluid towards a flat surface coated with a thin stationary porous bed of permeability k, a problem that was considered in Chapter 3. The leading order small-k solution for the contact time t_c given by (5.62) can be expressed in terms of the leading order small-k solution for r_C given by (5.63) as

$$t_c = \frac{\pi^2\mu r_C^4}{\sqrt{3}L_0(12H_pk)^{2/3}}. \tag{5.64}$$

In fact, comparing (5.64) and the dimensional equivalent of (3.58), namely the leading order small-k solution for the contact time when a flat impermeable disc of radius $\mathcal{R}$ moves under constant load L_0 through a thin layer of fluid towards a flat surface coated with a thin stationary porous bed of uniform thickness H_{p} and permeability k, we see that the solutions are equivalent, the radial position $r = r_{\text{C}}$ of the corner in the interface $z = h$ between the elastic and fluid layers playing the role of the radius $\mathcal{R}$ of the disc in (5.64). As the parabolic bearing approaches the porous bed, the elastic layer that coats it deforms in such a way that it behaves like a flat impermeable disc of radius r_{C}. The "radius" r_{C} can adjust so that the fluid layer can support larger loads for the same amount of time as smaller ones.

Chapter 6

Conclusions and Future Work

6.1 Summary of the Results

In this thesis we have considered the squeeze-film flow of a thin layer of Newtonian fluid filling the gap between an impermeable surface (the bearing) moving under a prescribed load and a thin porous bed of uniform thickness coating a stationary flat impermeable surface. Lubrication approximations were used to describe the flows in both the fluid layer and the porous bed. Three distinct cases were considered in Chapters 3, 4 and 5, respectively, the results of which we now summarise.

6.1.1 Chapter 3

In Chapter 3 the simplest situation was considered in which the bearing was modelled as a *flat* impermeable surface of finite radius $r = \mathcal{R}$. An explicit expression for the fluid pressure $p = p(r, t)$, given by (3.6), and an implicit expression for the fluid layer thickness $h = h(t)$, in the form of an explicit expression for the time $t = t(h)$ taken for the fluid layer thickness to reduce to a value h, given by (3.11), were obtained and analysed. It was shown that as the bearing approaches the

porous bed under a prescribed constant load L_0 all of the fluid is squeezed out of the gap between the bearing and the porous bed in a finite contact time t_c, given by (3.14), which increases as the permeability k decreases. Furthermore, it was shown that the fluid pressure $p = p(r,t)$ is parabolic in r and independent of the permeability k and time t. In addition, the fluid particle paths were calculated, and the penetration depths z_{pen} of fluid particles initially situated in the fluid layer into the porous bed and the relative penetration depths $z_{\mathrm{pen}} - z_0$ of fluid particles initially situated in the porous bed were determined.
In particular, the behaviour in the asymptotic limit of small permeability $k \to 0$ was investigated, and it was shown that in this limit the contact time $t_c = O(k^{-2/3}) \gg 1$ is large but finite. Furthermore, it was shown that the penetration depths z_{pen} (into the porous bed) of fluid particles initially situated in the fluid layer, with initial positions (r_0, z_0) such that $r_0 = O(k^{1/4})$ and $0 < z_0 < d$, satisfy $z_{\mathrm{pen}} = O(k^{1/3})$, and the relative penetration depths $z_{\mathrm{pen}} - z_0$ (further into the porous bed) of fluid particles initially situated in the porous bed satisfy $z_{\mathrm{pen}} - z_0 = O(k^{1/3})$.

6.1.2 Chapter 4

In Chapter 4 the approach presented in Chapter 3 was extended to the case of a *curved* bearing of shape $H \propto r^{2n}$, where n (≥ 1) is an integer. Again, an explicit expression for the fluid pressure $p = p(r,t)$, given by (4.4), was obtained and analysed. In addition, an implicit expression for the minimum fluid layer thickness $h_{\mathrm{min}} = h_{\mathrm{min}}(t)$, in the form of an explicit expression for the time $t = t(h_{\mathrm{min}})$ taken for the minimum fluid layer thickness to reduce to a value h_{min}, given by (4.7), was obtained and analysed. It was shown that as the bearing approaches the porous bed under a prescribed constant load L_0 all of the fluid is, again, squeezed out of the gap between the bearing and the porous bed in a finite contact time t_c, given by (4.10). The contact time t_c was shown to increase as the permeability k decreases (as in the case of a flat bearing) or n increases.

In contrast to the case of a flat bearing treated in Chapter 3, it was shown that the fluid pressure $p = p(r,t)$, given by (4.4), is dependent on both the permeability k and time t. The fluid pressure p was shown to increase and become localised over a smaller area as the permeability k decreases.

For "small" values of the permeability k, increasing n was shown to decrease the fluid pressure p and distribute it over a larger area. Furthermore, it was shown that for small values of k the maximum fluid pressure $p_{\mathrm{max}} = p_{\mathrm{max}}(t)$ does not attain its maximum value at the contact time t_c, but that it increases monotonically to its maximum value $p^{\star}_{\mathrm{max}}$ which it attains at some time $t^{\star} < t_c$ and then decreases to its value at the contact time t_c; this is consistent with observations made by Goren [24].

In particular, the behaviour in the asymptotic limit of small permeability $k \to 0$ was again investigated, and it was shown that in this limit the contact time

$$t_c = \left\{ \begin{array}{ll} O\left(\ln\left(\dfrac{1}{k}\right)\right) & \text{when} \quad n = 1 \\ O(k^{-2(n-1)/3n}) & \text{when} \quad n \geq 2 \end{array} \right\} \gg 1 \tag{6.1}$$

is large but finite. Furthermore, it was shown that the maximum fluid pressure $p_{\mathrm{max}} = O(k^{-1/3n}) \gg 1$ is also large but finite. In Chapter 3 it was shown that in the case of a flat bearing to leading order in the limit of small permeability $k \to 0$ the contact time $t_c = O(k^{-2/3})$ and the maximum fluid pressure $p_{\mathrm{max}} = O(1)$. Hence, since in the case of a curved bearing the contact time t_c, given by (6.1), is such that $t_c = o(k^{-2/3})$ and $p_{\mathrm{max}} \gg 1$ for all n, we deduce that t_c is shorter and p_{max} is larger when the bearing is curved than when it is flat. As n increases, i.e.

as the bearing becomes flatter near its minimum, t_c increases and $p_{\max}$ decreases, with both t_c and $p_{\max}$ becoming the same size as they are in the case of a flat bearing in the limit $n \to \infty$.

Once again, the paths of fluid particles initially situated in the fluid layer and fluid particles initially situated in the porous bed were calculated. It was shown that, as in the case of a flat bearing, as k increases the fluid particles that flow from the fluid layer into the porous bed penetrate deeper and wider. The maximum penetration depth z_{pen} of these fluid particles, given by (4.21), was shown to be independent of n. However, increasing n was shown to widen the region into which these fluid particles penetrate into the porous bed. Furthermore, it was shown that, in contrast to the case of a flat bearing, there are fluid particles, initially situated in the porous bed, that flow from the porous bed into the fluid layer. In fact, it was shown that there are fluid particles, initially situated in the fluid layer, that flow from the fluid layer into the porous bed and then re-emerge into the fluid layer. The region in the fluid layer in which these fluid particles are initially situated was also calculated.

6.1.3 Chapter 5

In Chapter 5 the approach presented in Chapter 4 was extended to the case in which the curved bearing of shape $H \propto r^{2n}$, where n (≥ 1) is an integer, is coated with a thin *elastic* layer of compliance

$$\eta = \frac{L_0}{(2G+\lambda)l^2} = \left(\frac{\mathcal{R}}{2nH_{\text{p}}}\right)^{1/n} \frac{L_0}{(2G+\lambda)\mathcal{R}^2}. \tag{6.2}$$

Numerical solutions for the fluid pressure $p = p(r,t)$ and the fluid layer thickness $h = h(r,t)$ were obtained and analysed. Furthermore, in the special case when the bearing is parabolic, i.e. when $n = 1$, the asymptotic limit of small permeability $k \to 0$ was investigated and asymptotic solutions for p and h were obtained.

Similarly to the inelastic case $\eta = 0$ treated in Chapter 4, it was shown that as the bearing approaches the porous bed under a prescribed load $L_0 > 0$ the fluid is squeezed out of the gap between the bearing and the porous bed in a finite contact time t_c. The contact time t_c was shown to increase as either the permeability k decreases or, at least for the "small" values of k used in the numerical calculations, n increases or the compliance η increases.

In the special case when the bearing is parabolic, i.e. when $n = 1$, it was shown that a region of approximately *uniform* fluid layer thickness h forms in $r < r_C$ as the elastic layer approaches the stationary porous bed under a prescribed load $L_0 > 0$, where $r = r_C$ is the radial position of a corner that forms in the interface $z = h$ between the elastic and fluid layers. Hence their approach is qualitatively the same as the approach of a flat impermeable disc of radius $\mathcal{R}$ moving under a prescribed constant load $L_0 > 0$ through a thin layer of fluid towards a flat surface coated with a thin stationary porous bed, as studied in Chapter 3. In particular, the behaviour in the limit of small permeability $k \to 0$ was, again, investigated and it was shown that in this limit the contact time t_c, given by (5.47), satisfies $t_c = O(k^{-2/3})$, meaning that t_c is of the same order of magnitude as the contact time t_c, given by (3.58), for the approach of a flat impermeable disc of radius $\mathcal{R}$ moving under a prescribed constant load $L_0 > 0$ through a thin layer of fluid towards a flat surface coated with a thin stationary porous bed. Comparing (5.47) with the corresponding solution for t_c in the inelastic case $\eta = 0$, given by (4.75), shows that coating the parabolic bearing with a thin elastic layer increases the contact time t_c by a factor that is $O(k^{-2/3} \ln(1/k)) \gg 1$.

For bearing shapes that are flatter near their minimum, i.e. for $n \geq 2$, qualitatively different behaviour was observed. In these cases it was shown that a region of approximately uniform fluid layer thickness h does not form as the elastic layer approaches the porous bed. Furthermore, it was shown that when $n \geq 2$ the fluid layer thickness h attains its minimum value at $r = r_{\min} > 0$, whereas when $n = 1$ the fluid layer thickness h attains its minimum value at $r = 0$. It was shown that as the minimum fluid layer thickness $h_{\min}$ approaches zero at $r = r_{\min} > 0$ it becomes increasingly difficult for the fluid in $r < r_{\min}$ to flow out through the fluid layer, and if there is an insufficient flow of fluid from $r < r_{\min}$ into the porous bed then this can lead to an increase in the maximum fluid pressure $p_{\max}$ as the fluid "trapped" in $r < r_{\min}$ is squeezed between the elastic layer and the porous bed. This is qualitatively different from the behaviour observed in the inelastic case $\eta = 0$ when $p_{\max}$ was found to decrease as $h_{\min}$ approaches zero.

6.2 Interpreting the Results in the Context of the Human Knee Joint

As outlined in Chapter 1, throughout this thesis our interest in porous squeeze-film flow was motivated by a desire for a better understanding of the lubrication of the human knee joint, and so in the remainder of this Chapter we seek to interpret the results obtained in Chapters 3–5 in this context.

6.2.1 Estimates of the Dimensional Parameters

Estimates of the dimensional parameters appearing in the models considered in Chapters 3–5 that are relevant to the human knee joint are given in Table 6.1. Recall that synovial fluid is a non-Newtonian shear-thinning fluid with a viscosity μ ranging from approximately 15 Pa s for low shear rates $\dot{\gamma} = O(10^{-2})\,\mathrm{s}^{-1}$ to

Parameter	Typical Size	Units	Reference(s)
μ	0.004–0.016	Pa s	Stewart *et al.* [65], Hlaváček [27]
$\mathcal{R}$	1.41–4.16	cm	Nuño and Ahmed [44]
L_0	800–1200	N	Figure 1.5(b), Stewart *et al.* [65]
H_{p}	1–6	mm	Ateshian and Hung [6]
k	0.12–2.20	nm^2	Mow and Guo [37] Ateshian and Hung [6]
ϕ	0.65–0.85		Mow and Guo [37], Ateshian and Hung [6]
G	2	MPa	Carter and Wong [15]
λ	30	MPa	Carter and Wong [15]

Table 6.1: Estimates of the dimensional parameters appearing in the models considered in Chapters 3–5 that are relevant to the human knee joint

0.004 Pa s for high shear rates $\dot{\gamma} = O(10^4)\,\mathrm{s}^{-1}$ (Hlaváček [27]). However, in Table 6.1 we have taken $\mu = 0.016$ Pa s, corresponding to the viscosity of carboxyl methyl cellulose sodium salt solution which has similar rheological properties to healthy synovial fluid (Stewart *et al.* [65]), as an upper bound on the synovial fluid viscosity.

The range for the prescribed constant load L_0 given in Table 6.1 is representative of the maximum vertical force that acts vertically through the knee joint during gait (see, for example, Figure 1.5(b) and Stewart *et al.* [65]). This range is assumed to be representative of the (approximately constant) vertical force that acts through the knee joint when a person stands still.

The range for the permeability k of articular cartilage given in Table 6.1 has been estimated from the range for the hydraulic permeability of articular cartilage (i.e. the ratio of the permeability and the interstitial fluid viscosity) given by Mow and Guo [37] and Ateshian and Hung [6]. It was assumed that the viscosity of the interstitial fluid (which, recall, is water containing sodium and chloride ions) is 10^{-3} Pa s, i.e. the viscosity of water at room temperature (Barnes *et al.* [9]). (Note that the range for the permeability k of articular cartilage given in Table 6.1 is consistent with the order-of-magnitude estimate $k = O(10^{-18})\,\mathrm{m}^2$ given by Skotheim and Mahadevan [59].)

Finally, the estimates for the Lamé parameters λ and G for articular cartilage were obtained from the estimates for the Young's modulus E and Poisson's ratio ν for articular cartilage given by Carter and Wong [15] using the relationships $\lambda = E\nu/(1+\nu)(1-2\nu)$ and $G = E/2(1+\nu)$. Note that the estimates for E and ν given by Carter and Wong [15] are appropriate when modelling articular cartilage as a single-phase deformable solid but not when modelling articular cartilage as a poroelastic material. In the latter case estimates of E and ν for "dry" articular cartilage that has been drained of all its interstitial fluid are more appropriate. Estimates of E and ν for dry articular cartilage are generally smaller than those given by Carter and Wong [15] since the interstitial fluid content of articular cartilage reduces its compressibility (see, for example, Mow and Guo [37]).

6.2.2 Estimates of the Dimensionless Parameters k and η

Using the parameter estimates in Table 6.1 we see that the non-dimensional permeability $k = O(10^{-15})$–$O(10^{-12})$ is typically very small, meaning that the limit of small permeability $k \to 0$ is most relevant to the human knee joint.

In Chapter 5 it was shown that when a parabolic bearing ($n = 1$) coated with a thin elastic layer moves under a prescribed load $L_0 > 0$ through a thin layer of fluid towards a stationary thin porous bed, then to leading order in the limit of small permeability $k \to 0$ the compliance of the elastic layer η, namely

$$\eta = \frac{L_0}{2H_{\mathrm{p}}\mathcal{R}(2G+\lambda)}, \tag{6.3}$$

must satisfy $\eta < \pi/2 \simeq 1.5708$ for a physically consistent solution. Using the parameter estimates in Table 6.1 we see that the compliance of the elastic layer $\eta = O(10^{-2})$–$O(1)$. Therefore, the model considered in Chapter 5, more specifically the case of parabolic bearing ($n = 1$), is a sensible model for the human knee joint since for articular cartilage the compliance of the elastic layer η is within the range required for a physically consistent solution.

6.2.3 Chapter 3

In Chapter 3 the femoral condyles were modelled as a flat bearing. Though this simple mathematical model does not explicitly include the effects of cartilage elasticity, modelling the femoral condyles as a flat surface accounts for an anticipated effect of cartilage elasticity, namely the formation of a fluid layer of approximately uniform thickness.

To leading order in the limit of small permeability $k \to 0$ and in terms of dimensional variables, the contact time t_c, given by (3.58), was found to be

$$t_c = \frac{\pi^2 \mu \mathcal{R}^4}{\sqrt{3} L_0 (12 H_p k)^{2/3}} = O(1)\text{–}O(10^4)\,\text{s}. \tag{6.4}$$

Hence the model considered in Chapter 3 predicts that when a person stands still for a short period of time their knees may be fluid-lubricated, but that when they stand still for a longer period of time contact between the cartilage-coated surfaces may occur. Of course, during physical activity such as walking or running a person repeatedly loads and unloads their knees with a temporally varying load. Since typically each step or stride takes around 1 s, which is somewhat less than the typical size of t_c, given by (6.4), the model considered in Chapter 3 suggests that a person's knees may also remain fluid-lubricated during walking or running.

Moreover, the corresponding size of $h = O((H_\mathrm{p}k)^{1/3}) = O(10^{-8})$–$O(10^{-7})$ m is consistent with the value of 5×10^{-7} m quoted by Stewart *et al.* [65].

We also found that to leading order in the limit of small permeability $k \to 0$ the penetration depth z_pen of fluid particles initially situated in the fluid layer into the porous bed is given by (3.75) and is expressed in terms of dimensional variables as

$$z_\mathrm{pen} = -1.1027 \times \frac{(H_\mathrm{p}k)^{1/3}}{\phi} = O(10^{-8})\text{–}O(10^{-7})\,\mathrm{m}, \tag{6.5}$$

which is much less than H_p. Hence the model considered in Chapter 3 predicts that when a person stands still any nutrients initially in the fluid layer penetrate only a relatively small distance into the cartilage. Moreover, the relative penetration depth $z_\mathrm{pen} - z_0$ of fluid particles initially situated in the porous bed is given by (3.80) and is expressed in dimensional variables as

$$z_\mathrm{pen} - z_0 = -\frac{2\pi(H_\mathrm{p} + z_0)(12H_\mathrm{p}k)^{1/3}}{3\sqrt{3}\phi H_\mathrm{p}} = O(10^{-7})\text{–}O(10^{-6})\,\mathrm{m}, \tag{6.6}$$

which is of approximately the same size as z_pen given by (6.5). Hence the model considered in Chapter 3 also predicts that when a person stands still any nutrients initially in the cartilage penetrate only a relatively small distance further into it. However, the cumulative effect of repeated loading and unloading of the knees may alter this conclusion. Assuming that a reasonably active person takes $O(10^4)$ steps per day (see, for example, Tudor-Locke *et al.* [69]), the size of the relative penetration depth given in (6.6) corresponds to a maximum cumulative vertical displacement of $O(10^{-3})$–$O(10^{-2})$ m, which is comparable with H_p, i.e. the model considered in Chapter 3 also suggests that the cumulative effect of repeated loading and unloading of the knees during physical activity such as walking or running may be sufficient to carry nutrients deep into the cartilage.

6.2.4 Chapter 4

In Chapter 4 the femoral condyles were modelled as a curved bearing of shape $H \propto r^{2n}$, where n (≥ 1) is an integer. At first sight the case $n = 1$, i.e. the case of a parabolic bearing, should apparently be of most relevance to the human knee joint, since the femoral condyles are approximately parabolic. However, though the bearing shapes considered in Chapter 4, and specifically the case of a parabolic bearing $n = 1$, are a more realistic model for the shape of the femoral condyles, no attempt was made to account for the effects of cartilage elasticity. Therefore, the model considered in Chapter 4 is in fact a less realistic model for the human knee joint than the model considered in Chapter 3, where the femoral condyles were modelled as a flat surface to account for an anticipated effect of cartilage elasticity. To leading order in the limit of small permeability $k \to 0$ and in terms of dimensional variables, the contact time t_c, given by (4.75) when $n = 1$ and (4.124) when $n \geq 2$, was found to be

$$t_{\mathrm{c}} = \begin{cases} \dfrac{\pi\mu\mathcal{R}^2}{L_0}\left(2\ln\left(\dfrac{H_{\mathrm{p}}^2}{12k}\right) + 3\left[3 + 2\ln\left(\dfrac{H_{\mathrm{f}}}{H_{\mathrm{p}}}\right)\right]\right) & \text{when} \quad n = 1, \\ \dfrac{\pi^2 \csc[\pi(n+2)/3n]\mu\mathcal{R}^4}{2H_{\mathrm{p}}^2 L_0}\left(\dfrac{2nH_{\mathrm{p}}}{\mathcal{R}}\right)^{2/n}\left(\dfrac{H_{\mathrm{p}}^2}{12k}\right)^{2(n-1)/3n} & \text{when} \quad n \geq 2. \end{cases} \tag{6.7}$$

This result illustrates very clearly the crucial role played by the shape of the femoral condyles if a person's knees are to be fluid-lubricated while standing still for a short period of time. The model considered in Chapter 4, with $n = 1$, predicts that if articular cartilage was inelastic then when standing still a person's knees would be fluid-lubricated for only a very short time $t_c = O(10^{-7})$–$O(10^{-6})$ s. Comparing the contact time t_c given by (6.4), corresponding to the case when the femoral condyles are modelled as a flat surface to account for an anticipated effect of cartilage elasticity, with the contact time t_c given by (6.7) with $n = 1$ we see that the former is seven to ten orders of magnitude greater than the latter. Hence we deduce that the anticipated effect of cartilage elasticity is to increase the contact time t_c by seven to ten orders of magnitude from $t_c = O(10^{-7})$–$O(10^{-6})$ s to $t_c = O(1)$–$O(10^4)$ s, meaning that when a person stands still for a short period of time their knees may be fluid-lubricated.

It is clear from (6.7) that increasing n increases the contact time t_c. Furthermore, it was shown that the maximum penetration depth z_{pen} of a fluid particle flowing from the fluid layer into the porous bed, given by (4.21), is independent of n but increasing n widens the region into which these fluid particles penetrate. The increases in the contact time t_c and the width of the region into which fluid particles penetrate into the porous bed that occur as a result of increasing n are desirable in the human knee joint. It is obvious that an increase in t_c would increase the time for which a person's knees are fluid-lubricated when standing still, whereas an increase in the width of the region into which fluid particles penetrate into the porous bed would increase the fraction of the articular cartilage that receives nutrition via the flow of synovial fluid into the cartilage.

It may, therefore, appear odd that nature has determined that the femoral condyles are approximately parabolic in shape when a flatter shape would have resulted in the desirable consequences described above. However, nature is presumably seeking to optimize many competing effects simultaneously, not just the load-bearing effects treated by these models. For example, the joint also rotates (something not considered in the present analysis) and the parabolic shape of the condyles will help facilitate this motion.

6.2.5 Chapter 5

In Chapter 5 the femoral condyles were modelled as a curved bearing of shape $H \propto r^{2n}$, where n (≥ 1) is an integer, coated with a thin elastic layer. The model considered in Chapter 5, and specifically the case of a parabolic bearing $n = 1$, accounts for more physical features present in the human knee joint than the models considered in Chapters 3 and 4. The thin elastic layer that coats the bearing represents the thin layer of articular cartilage that coats the femoral condyles. Thus the thin layers of articular cartilage that coat both the femoral condyles and the tibial plateau are accounted for; only the thin layer of articular cartilage that coats the tibial plateau was explicitly accounted for in the models considered in Chapters 3 and 4.

Clearly this model still has limitations. For example, in reality articular cartilage is a poroelastic material, yet the thin layer of articular cartilage that coats the tibial plateau is modelled as an inelastic porous bed and the thin layer of articular cartilage that coats the femoral condyles is modelled as an impermeable elastic layer. However, considering this simpler scenario allows us to analyse the physical mechanisms in greater detail, gaining insight into the coupled effects of articular cartilage permeability and elasticity in the human knee joint.

In the case when the femoral condyles were modelled as a parabolic bearing, i.e. in the case $n = 1$, it was shown that, to leading order in the limit of small permeability $k \to 0$, a region of uniform fluid layer thickness h forms in $r < r_{\mathrm{C}}$ as the femoral condyles approach the tibial plateau. Here r_{C}, which is given by (5.31) and is expressed in terms of dimensional variables as

$$r_{\mathrm{C}} = \left(\frac{4H_{\mathrm{p}}\mathcal{R}L_0}{\pi(2G+\lambda)} \right)^{1/4} = O(10^{-3})\text{–}O(10^{-2})\,\mathrm{m}, \tag{6.8}$$

is the radial position of a corner that forms in the interface $z = h$. Hence the approach of the femoral condyles and the tibial plateau is qualitatively the same as the approach of a flat impermeable disc of radius $\mathcal{R}$ moving under a constant load L_0 through a thin layer of fluid towards a flat surface coated with a thin stationary bed, i.e. the scenario considered in Chapter 3 for which the contact time t_c is given by (6.4). In particular, it was shown that the cartilage-coated surfaces of the femoral condyles and the tibial plateau touch in a finite contact time t_c, given by (5.47) and expressed in terms of r_C and dimensional variables as

$$t_c = \frac{\pi^2 \mu r_C^4}{\sqrt{3} L_0 (12 H_p k)^{2/3}} = O(10^{-1})\text{–}O(10)\,\mathrm{s}, \tag{6.9}$$

which is identical to (6.4) if we set $r_C = \mathcal{R}$.

Comparing the contact times t_c given by (6.9) and (6.7) (with $n = 1$) illustrates the crucial role that cartilage elasticity plays in keeping a person's knees fluid lubricated when standing still for a short period of time. If cartilage was inelastic then (6.7) shows that when standing still a person's knees would be fluid lubricated for only $t_c = O(10^{-7})\text{–}O(10^{-6})\,\mathrm{s}$. Furthermore, since $t_c = O(10^{-7})\text{–}O(10^{-6})\,\mathrm{s} \ll 1\,\mathrm{s}$ it is unlikely that a person's knees would remain fluid lubricated during walking or running.

In Chapter 4 it was shown that increasing n increases t_c. The contact time t_c was shown to be shortest when $n = 1$ (parabolic bearing) and longest in the limit $n \to \infty$ (flat bearing). We see, therefore, that the thin layer of articular cartilage that coats the femoral condyles deforms in such a way that it "optimises" the shape of the femoral condyles which essentially behave like a flat disc of radius r_C.

It was shown in Chapter 5 that, similarly to Chapter 4, increasing n increases t_c. It is not, therefore, true that the approximately parabolic ($n = 1$) shape of the femoral condyles produces the optimal contact time t_c. If the femoral condyles were flatter ($n \geq 2$) the contact time t_c would be longer. However, it is possible that undesirable consequences (not considered herein) could result from the femoral condyles being flatter.

6.3 Future Work

Modelling the articular cartilage as a poroelastic material would be a natural extension to the work presented in Chapter 5. Specifically, it would be of interest to consider the squeeze-film flow of a thin layer of Newtonian fluid filling the gap between an impermeable parabolic bearing moving under a prescribed load towards a stationary flat surface coated with a thin poroelastic layer of permeability k. A similar problem has been studied by Skotheim and Mahadevan [59]. Skotheim and Mahadevan [59] considered only the transverse motion of the bearing (at a prescribed constant velocity) and calculated the force exerted on it by the fluid. In particular, it would be of interest to determine the effect of modelling the articular cartilage as a poroelastic material on the contact time t_c between femoral condyles and the tibial plateau. We hypothesise that for "small" values of the permeability k a region of approximately uniform fluid layer thickness h will form about the axis of symmetry, meaning that the approach is qualitatively the same as the approach of a flat impermeable disc moving under a prescribed load through a thin layer of fluid towards a flat surface coated with a thin stationary porous bed, and, in particular, that the contact time t_c satisfies $t_\mathrm{c} = O(k^{-2/3})$.

A further, and again natural, extension to the work presented in this thesis would be to model the synovial fluid as a non-Newtonian shear-thinning fluid. Since healthy synovial fluid behaves like a power-law fluid for shear rates in the range $O(10^{-2})$–$O(10^{4})\,\mathrm{s}^{-1}$ (see, for example, Barnes *et al.* [9], Hlaváček [27] and Fam *et* *al.* [23]), as a first approximation there would be merit in considering the simplest case and modelling the synovial fluid as a power-law fluid of viscosity

$$\mu = K|\dot{\gamma}|^{M-1}, \tag{6.10}$$

where $\dot{\gamma}$ is the shear rate, $M > 0$ is the power-law index and K, which has the units $\mathrm{Pa\,s}^M$, is referred to as the consistency (see, for example, Barnes *et al.* [9]). For shear-thinning fluids (like synovial fluid) $M < 1$. Again, it would be of interest to determine the effect of modelling the synovial fluid as a power-law fluid on the contact time t_c, and, perhaps against our intuition, there is some evidence to suggest that the shear-thinning nature of synovial fluid may actually increase t_c. Specifically, Scott [54] considered the squeeze-film flow of a thin layer of power-law fluid filling the gap between a flat impermeable disc of radius $\mathcal{R}$ moving at a prescribed constant velocity $V_0 > 0$ towards an identical stationary disc and found that the force F exerted on the disc by the fluid is given by

$$F = \left(\frac{2M+1}{M}\right)^M \left(\frac{2\pi K\mathcal{R}^{M+3}}{M+3}\right) \frac{{V_0}^M}{h^{1+2M}}. \tag{6.11}$$

Writing $V_0 = -\mathrm{d}h/\mathrm{d}t$ and setting $F = L_0$, equation (6.11) may be integrated to yield the time $t = t(h)$ taken for the fluid layer thickness to reduce to a value h when the disc moves under a prescribed constant load L_0:

$$t = \frac{2M+1}{M+1}\left(\frac{2\pi K\mathcal{R}^{M+3}}{(M+3)L_0}\right)^{1/M}\left(\frac{1}{h^{(M+1)/M}} - \frac{1}{H_\mathrm{f}^{(M+1)/M}}\right), \tag{6.12}$$

where $h(0) = H_\mathrm{f}$. From (6.12) we deduce that for "large" times, specifically

$$t \gg \frac{2M+1}{M+1}\left(\frac{2\pi K\mathcal{R}^{M+3}}{(M+3)L_0}\right)^{1/M}\frac{1}{H_\mathrm{f}^{(M+1)/M}}, \tag{6.13}$$

the time $t = t(h)$ taken for the fluid layer thickness to reduce to a value h is such that $t \propto h^{-(M+1)/M}$, i.e. for "large" times t satisfying (6.13) the time $t = t(h)$ taken for the fluid layer thickness to reduce to a value h increases as M decreases, and, in particular, $t(h)$ is longer for a shear-thinning fluid ($M < 1$) than it is for a Newtonian fluid ($M = 1$). Using the typical sizes for $\mathcal{R}$ and L_0 given in Table 6.1, assuming that $H_\mathrm{f} = O(10^{-6})$–$O(10^{-3})\,\mathrm{m}$ and taking $M = 0.4$ and $K = 0.5\,\mathrm{Pa\,s}^M$, which are typical power-law parameters for synovial fluid when $\dot{\gamma} = O(10^{-1})$–$O(10^{2})\,\mathrm{s}^{-1}$ (Barnes *et al.* [9]), in (6.13), we hypothesise that after standing still for much less than a second the shear-thinning nature of synovial fluid may mean that a person's knees can be fluid lubricated for a longer time than would be possible if synovial fluid was Newtonian. We hypothesise that modelling the synovial fluid as a shear-thinning power-law fluid will increase the contact time t_c. The validity of the power-law model in the limit of large time and low shear is, of course, a different matter.

While much remains to be done in the mathematical modelling of porous squeeze-film flows and, more specifically, of the human knee joint, we believe that the results presented in this thesis represent a useful advance in both of these directions.

Bibliography

[1] D. J. Acheson. *Elementary Fluid Dynamics*. Oxford University Press, 1990.

[2] N. Alleborn and H. Raszillier. Spreading and sorption of a droplet on a porous substrate. *Chem. Eng. Sci.*, 59(10):2071–2088, 2004.

[3] I. I. Argatov and G. S. Mishuris. Contact problem for thin biphasic cartilage layers: perturbation solution. *Q. J. Mech. Appl. Math.*, 64(3):297–318, 2011.

[4] C. G. Armstrong, W. M. Lai, and V. C. Mow. An analysis of the unconfined compression of articular cartilage. *J. Biomech. Eng.*, 106(2):165–173, 1984.

[5] G. A. Ateshian. The role of interstitial fluid pressurization in articular cartilage lubrication. *J. Biomech.*, 42(9):1163–1176, 2009.

[6] G. A. Ateshian and C. T. Hung. The natural synovial joint: properties of cartilage. *Proc. Inst. Mech. Eng. J: J. Eng. Tribol.*, 220(8):657–670, 2006.

[7] E. A. Balazs. The role of hyaluronan in the structure and function of the biomatrix of connective tissues. *Struct. Chem.*, 20(2):233–243, 2009.

[8] N. J. Balmforth, C. J. Cawthorn, and R. V. Craster. Contact in a viscous fluid. Part 2. A compressible fluid and an elastic solid. *J. Fluid Mech.*, 646(1):339–361, 2010.

[9] H. A. Barnes, J. F. Hutton, and K. Walters. *An Introduction to Rheology.* Elsevier, 1989.

[10] S. I. Barry and M. Holmes. Asymptotic behaviour of thin porous layers. *IMA J. Appl. Math.*, 66(2):175–194, 2001.

[11] G. S. Beavers and D. D. Joseph. Boundary conditions at a naturally permeable wall. *J. Fluid Mech.*, 30(1):197–207, 1967.

[12] M. A. Biot. General theory of three-dimensional consolidation. *J. Appl. Phys.*, 12(2):155–164, 1941.

[13] A. F. Bower. *Applied Mechanics of Solids.* CRC Press, 2011.

[14] H. Brenner. The slow motion of a sphere through a viscous fluid towards a plane surface. *Chem. Eng. Sci.*, 16(3):242–251, 1961.

[15] D. R. Carter and M. Wong. Modelling cartilage mechanobiology. *Philos. Trans. R. Soc. London, Ser. B*, 358(1437):1461–1471, 2003.

[16] C. J. Cawthorn and N. J. Balmforth. Contact in a viscous fluid. Part 1. A falling wedge. *J. Fluid Mech.*, 646:327–338, 2010.

[17] M.-H. Chang, F. Chen, and B. Straughan. Instability of Poiseuille flow in a fluid overlying a porous layer. *J. Fluid Mech.*, 564:287–303, 2006.

[18] R. G. Cox and H. Brenner. The slow motion of a sphere through a viscous fluid towards a plane surface–II Small gap widths, including inertial effects. *Chem. Eng. Sci.*, 22(12):1753–1777, 1967.

[19] H. Darcy. *Les fontaines publiques de la ville de Dijon.* V. Dalmont, 1856.

[20] A. M. J. Davis. Axisymmetric flow due to a porous sphere sedimenting towards a solid sphere or a solid wall: applications to scavenging of small particles. *Phys. Fluids*, 13(11):3126–3133, 2001.

[21] R. H. Davis, J.-M. Serayssol, and E. J. Hinch. The elastohydrodynamic collision of two spheres. *J. Fluid Mech.*, 163:479–497, 1986.

[22] S. H. Davis and L. M. Hocking. Spreading and imbibition of viscous liquid on a porous base. *Phys. Fluids*, 11(1):48–57, 1999.

[23] H. Fam, J. T. Bryant, and M. Kontopoulou. Rheological properties of synovial fluids. *Biorheology*, 44(2):59–74, 2007.

[24] S. L. Goren. The hydrodynamic force resisting the approach of a sphere to a plane permeable wall. *J. Colloid Interface Sci.*, 69(1):78–85, 1979.

[25] A. J. Grodzinsky, M. E. Levenston, M. Jin, and E. H. Frank. Cartilage tissue remodeling in response to mechanical forces. *Annu. Rev. Biomed. Eng.*, 2(1):691–713, 2000.

[26] W. Hardy and I. Bircumshaw. Bakerian lecture. Boundary lubrication. Plane surfaces and the limitations of Amontons' law. *Proc. R. Soc. London, Ser. A*, 108(745):1–27, 1925.

[27] M. Hlaváček. The thixotropic effect of the synovial fluid in squeeze-film lubrication of the human hip joint. *Biorheology*, 38(4):319–334, 2001.

[28] J. S. Hou, V. C. Mow, W. M. Lai, and M. H. Holmes. An analysis of the squeeze-film lubrication mechanism for articular cartilage. *J. Biomech.*, 25(3):247–259, 1992.

[29] M. B. Jones, G. R. Fulford, C. P. Please, D. L. S. McElwain, and M. J. Collins. Elastohydrodynamics of the eyelid wiper. *Bull. Math. Biol.*, 70(2):323–343, 2008.

[30] D. J. Knox, S. K. Wilson, B. R. Duffy, and S. McKee. Porous squeeze-film flow. *IMA J. Appl. Math.* (published online 2013).

[31] D. J. Knox, S. K. Wilson, B. R. Duffy, and S. McKee. A mathematical model for the lubrication of the human knee. In *ECS 11 Proceedings*, 2011.

[32] G. Lian, Y. Xu, W. Huang, and M. J. Adams. On the squeeze flow of a power-law fluid between rigid spheres. *J. Non-Newtonian Fluid Mech.*, 100(1):151–164, 2001.

[33] J.-R. Lin, R.-F. Lu, and C.-B. Yang. Derivation of porous squeeze-film Reynolds equations using the Brinkman model and its application. *J. Phys. D: Appl. Phys.*, 34(22):3217–3223, 2001.

[34] M. Lutianov, S. Naire, S. Roberts, and J.-H. Kuiper. A mathematical model of cartilage regeneration after cell therapy. *J. Theor. Biol.*, 289:136–150, 2011.

[35] G. H. Meeten. Squeeze flow between plane and spherical surfaces. *Rheol. Acta*, 40(3):279–288, 2001.

[36] D. F. Moore. A review of squeeze films. *Wear*, 8(4):245–263, 1965.

[37] V. C. Mow and X. E. Guo. Mechano-electrochemical properties of articular cartilage: their inhomogeneities and anisotropies. *Annu. Rev. Biomed. Eng.*, 4(1):175–209, 2002.

[38] V. C. Mow, S. C. Kuei, W. M. Lai, and C. G. Armstrong. Biphasic creep and stress relaxation of articular cartilage in compression: Theory and experiments. *J. Biomech. Eng.*, 102(1):73–84, 1980.

[39] D. A. Nield. The Beavers-Joseph boundary condition and related matters: A historical and critical note. *Transp. Porous Media*, 78(3):537–540, 2009.

[40] D. A. Nield and A. Bejan. *Convection in Porous Media.* Springer, 2006.

[41] D. A. Nield and A. V. Kuznetsov. The effect of a transition layer between a fluid and a porous medium: shear flow in a channel. *Transp. Porous Media*, 78(3):477–487, 2009.

[42] A. Nir. On the departure of a sphere from contact with a permeable membrane. *J. Eng. Math.*, 15(1):65–75, 1981.

[43] K. Nong and D. M. Anderson. Thin film evolution over a thin porous layer: Modeling a tear film on a contact lens. *SIAM J. Appl. Math.*, 70(7):2771–2795, 2010.

[44] N. Nuño and A. M. Ahmed. Three-dimensional morphometry of the femoral condyles. *Clin. Biomech.*, 18(10):924–932, 2003.

[45] B. P. O'Hara, J. P. G. Urban, and A. Maroudas. Influence of cyclic loading on the nutrition of articular cartilage. *Ann. Rheum. Dis.*, 49(7):536–539, 1990.

[46] S. Park, R. Krishnan, S. B. Nicoll, and G. A. Ateshian. Cartilage interstitial fluid load support in unconfined compression. *J. Biomech.*, 36(12):1785–1796, 2003.

[47] J. Prakash and S. K. Vij. Load capacity and time-height relations for squeeze films between porous plates. *Wear*, 24(3):309–322, 1973.

[48] J. Prakash and S. K. Vij. Effect of velocity slip on porous-walled squeeze films. *Wear*, 29(3):363–372, 1974.

[49] G. Z. Ramon, H. E. Huppert, J. R. Lister, and H. A. Stone. On the hydrodynamic interaction between a particle and a permeable surface. *Phys. Fluids*, 25(7):073103, 2013.

[50] O. Reynolds. On the theory of lubrication and its application to Mr. Beauchamp Tower's experiments, including an experimental determination of the viscosity of olive oil. *Philos. Trans. R. Soc. London*, 177:157–234, 1886.

[51] G. J. Rodin. Squeeze film between two spheres in a power-law fluid. *J. Non-Newtonian Fluid Mech.*, 63(2):141–152, 1996.

[52] P. G. Saffman. Boundary condition at surface of a porous medium. *Stud. Appl. Math*, 50(2):93–101, 1971.

[53] J. Schurz and V. Ribitsch. Rheology of synovial fluid. *Biorheology*, 24(4):385–399, 1987.

[54] J. R. Scott. Theory and application of the parallel-plate plastimeter. *Trans. Inst. Rubber Ind.*, 7:169–186, 1931.

[55] J. D. Sherwood. The hydrodynamic forces on a cylinder touching a permeable wellbore. *Phys. Fluids A*, 2(10):1754–1759, 1990.

[56] J. D. Sherwood. Squeeze flow of a power-law fluid between non-parallel plates. *J. Non-Newtonian Fluid Mech.*, 166(5):289–296, 2011.

[57] J. M. Skotheim and L. Mahadevan. Dynamics of poroelastic filaments. *Proc. R. Soc. London, Ser. A*, 460(2047):1995–2020, 2004.

[58] J. M. Skotheim and L. Mahadevan. Soft lubrication. *Phys. Rev. Lett.*, 92(24):245509, 2004.

[59] J. M. Skotheim and L. Mahadevan. Soft lubrication: the elastohydrodynamics of nonconforming and conforming contacts. *Phys. Fluids*, 17(9):092101, 2005.

[60] M. A. Soltz and G. A. Ateshian. Experimental verification and theoretical prediction of cartilage interstitial fluid pressurization at an impermeable contact interface in confined compression. *J. Biomech.*, 31(10):927–934, 1998.

[61] M. A. Soltz and G. A. Ateshian. A conewise linear elasticity mixture model for the analysis of tension-compression nonlinearity in articular cartilage. *J. Biomech. Eng.*, 122(6):576–586, 2000.

[62] S. Standring. *Gray's Anatomy.* Churchill Livingstone, Elsevier, Fortieth edition, 2008.

[63] J. Stefan. Versuche über die scheinbare Adhäsion. *Sitzber. Math.-Naturw. Kl. Bayer. Akad. Wiss. München*, 69, 1874.

[64] A. J. Steward, Y. Liu, and D. R. Wagner. Engineering cell attachments to scaffolds in cartilage tissue engineering. *JOM*, 63(4):74–82, 2011.

[65] T. Stewart, Z. M. Jin, and J. Fisher. Friction of composite cushion bearings for total knee joint replacements under adverse lubrication conditions. *Proc. Inst. Mech. Eng. H: J. Eng. Med.*, 211(6):451–465, 1997.

[66] H. A. Stone. On lubrication flows in geometries with zero local curvature. *Chem. Eng. Sci.*, 60(17):4838–4845, 2005.

[67] A. Z. Szeri. *Fluid Film Lubrication.* Cambridge University Press, 1998.

[68] S. J. G. Taylor, P. S. Walker, J. S. Perry, S. R. Cannon, and R. Woledge. The forces in the distal femur and the knee during walking and other activities measured by telemetry. *J. Arthroplasty*, 13(4):428–437, 1998.

[69] C. Tudor-Locke, C. L. Craig, W. J. Brown, S. A. Clemes, K. De Cocker, B. Giles-Corti, Y. Hatano, S. Inoue, S. M. Matsudo, N. Mutrie, J.-M. Oppert, D. A. Rowe, M. D. Schmidt, G. M. Schofield, J. C. Spence, P. J. Teixeira, M. A. Tully, and S. N. Blair. How many steps/day are enough? For adults. *Int. J. Behav. Nutr. Phy.*, 8(1):79, 2011.

[70] S. J. Weekley. *Particle Dynamics in Liquid-Lined Lung Airways*. PhD thesis, University of Nottingham, 2004.

[71] S. J. Weekley, S. L. Waters, and O. E. Jensen. Transient elastohydrodynamic drag on a particle moving near a deformable wall. *Q. J. Mech. Appl. Math.*, 59(2):277–300, 2006.

[72] E. W. Weisstein. Lambert W-Function. `http://mathworld.wolfram.com/LambertW-Function.html`.

[73] S. Whitaker. Flow in porous media I: A theoretical derivation of Darcy's law. *Transp. Porous Media*, 1(1):3–25, 1986.

[74] W. Wilson, C. C. van Donkelaar, and J. M. Huyghe. A comparison between mechano-electrochemical and biphasic swelling theories for soft hydrated tissues. *J. Biomech. Eng.*, 127(1):158–165, 2005.

[75] D. A. Winter. *Biomechanics of human movement*. Wiley, 1979.

[76] H. Wu. Squeeze-film behaviour for porous annular disks. *J. Lubr. Technol.*, 92(4):593–596, 1970.

[77] H. Wu. Effect of velocity-slip on the squeeze film between porous rectangular plates. *Wear*, 20(1):67–71, 1972.

Appendix A

Two-Dimensional Problem

In Chapter 3 we considered the axisymmetric squeeze-film flow of a thin layer of Newtonian fluid filling the cylindrical gap between a flat bearing of radius $\mathcal{R}$ moving under a prescribed load $L = L(t)$ and a thin stationary porous bed of uniform thickness H_p bonded to an impermeable surface (see Figure 3.1), and calculated the contact time t_c and the fluid particle paths (r, z). The corresponding results for a two-dimensional bearing of semi-width $\mathcal{L}$, as shown in Figure A.1, are also of interest and may be obtained in a similar manner to those for the axisymmetric problem. In this Appendix the main results for the two-dimensional problem are described and the key similarities to and differences from the corresponding results for the axisymmetric problem are highlighted.

Consider, with reference to the two-dimensional Cartesian coordinate system (x, z) shown in Figure A.1, the two-dimensional problem with (dimensional) load $L = L(t)$ per unit width. This problem is non-dimensionalised in the same way as the axisymmetric problem (2.25) with $\mathcal{L}$ in place of $\mathcal{R}$ and $V = L_0 H_\mathrm{p}^2/(\mu\mathcal{L}^2)$ in place of $V = L_0 H_\mathrm{p}^2/(\mu\mathcal{R}^3)$ as the characteristic scales for horizontal distance and horizontal fluid velocity, respectively. The horizontal and vertical components of

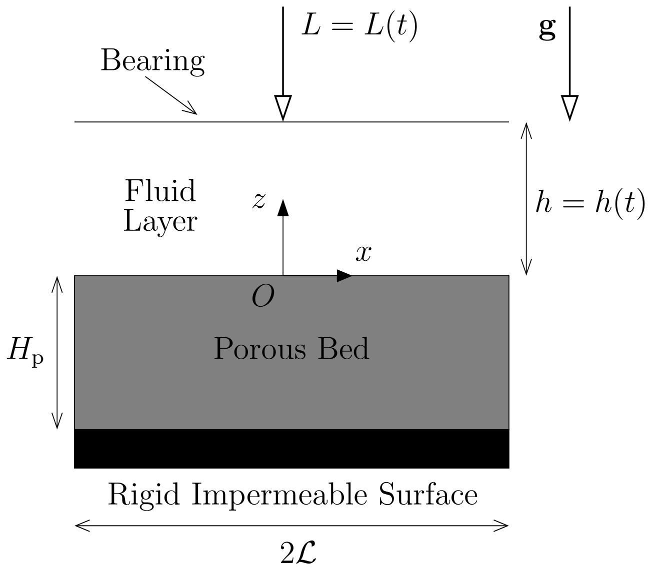

Figure A.1: The geometry of the two-dimensional problem

the fluid velocity, $v_x = v_x(x, z, t)$ and $v_z = v_z(x, z, t)$, are given by

$$v_x = -\frac{(h-z)\left[(\alpha h + k^{1/2})z + k^{1/2}(h + 2\delta\alpha k^{1/2})\right]}{2(\alpha h + k^{1/2})}\frac{\partial p}{\partial x}, \tag{A.1}$$

$$v_z = \frac{\mathcal{F}(h, z)}{12(\alpha h + k^{1/2})}\frac{\partial^2 p}{\partial x^2}, \tag{A.2}$$

respectively, where $\mathcal{F}(h, z)$ is given by (2.62), the horizontal and vertical components of the Darcy velocity, $u_x = u_x(x, z, t)$ and $u_z = u_z(x, z, t)$, are given by

$$u_x = -k\frac{\partial p}{\partial x}, \quad u_z = k(1+z)\frac{\partial^2 p}{\partial x^2}, \tag{A.3}$$

respectively, and the unsteady Reynolds equation governing the pressure $p = p(x, t)$ is

$$\frac{\mathrm{d}h}{\mathrm{d}t} = \frac{h^2(\alpha h^2 + 4k^{1/2}h + 6\delta\alpha k) + 12k(\alpha h + k^{1/2})}{12(\alpha h + k^{1/2})}\frac{\partial^2 p}{\partial x^2}. \tag{A.4}$$

Integrating (A.4) twice with respect to x, applying the boundary conditions $p = 0$

at $x = \pm 1$, and imposing the load condition

$$L(t) = 2\int_0^1 p\,\mathrm{d}x \tag{A.5}$$

yields the pressure

$$p = \frac{3L(t)(1-x^2)}{4}, \tag{A.6}$$

and the differential equation governing the fluid layer thickness $h = h(t)$:

$$L(t) = -\frac{8(\alpha h + k^{1/2})}{h^2(\alpha h^2 + 4k^{1/2}h + 6\delta\alpha k) + 12k(\alpha h + k^{1/2})}\frac{\mathrm{d}h}{\mathrm{d}t}. \tag{A.7}$$

Equation (A.7) is very similar to the corresponding equation (3.5) in the axisymmetric case. In particular, in the special case of constant load $L = L_0 > 0$ equation (3.5) can be recovered from (A.7) simply by rescaling t with $3\pi t/16$, and hence the solutions for the fluid layer thickness $h = h(t)$ and the contact time t_c in the two-dimensional case may be readily obtained from the corresponding results in the axisymmetric case.

The path (x, z) taken by a fluid particle is governed by

$$\frac{1}{x}\frac{\mathrm{d}x}{\mathrm{d}h} = -\frac{6(h-z)\left[(\alpha h + k^{1/2})z + k^{1/2}(h + 2\delta\alpha k^{1/2})\right]}{h^2(\alpha h^2 + 4k^{1/2}h + 6\delta\alpha k) + 12k(\alpha h + k^{1/2})}, \tag{A.8}$$

$$\frac{\mathrm{d}z}{\mathrm{d}h} = \frac{\mathcal{F}(h,z)}{h^2(\alpha h^2 + 4k^{1/2}h + 6\delta\alpha k) + 12k(\alpha h + k^{1/2})} \tag{A.9}$$

in the fluid layer $0 \le z \le h$, where $\mathcal{F}(h, z)$ is again given by (2.62), and

$$\frac{1}{x}\frac{\mathrm{d}x}{\mathrm{d}h} = -\frac{12k(\alpha h + k^{1/2})}{\phi\left[h^2(\alpha h^2 + 4k^{1/2}h + 6\delta\alpha k) + 12k(\alpha h + k^{1/2})\right]}, \tag{A.10}$$

$$\frac{1}{1+z}\frac{\mathrm{d}z}{\mathrm{d}h} = \frac{12k(\alpha h + k^{1/2})}{\phi\left[h^2(\alpha h^2 + 4k^{1/2}h + 6\delta\alpha k) + 12k(\alpha h + k^{1/2})\right]} \tag{A.11}$$

in the porous bed $-1 \leq z \leq 0$. Hence the particle paths in the porous bed are given by

$$\frac{x}{x_0} = \frac{1+z_0}{1+z} = \exp\left[-\frac{12k}{\phi}\int_d^h \frac{\alpha s + k^{1/2}}{s^2(\alpha s^2 + 4k^{1/2}s + 6\delta\alpha k) + 12k(\alpha s + k^{1/2})}\,\mathrm{d}s\right], \tag{A.12}$$

and so, in particular, always satisfy $x(1+z) = x_0(1+z_0) = \text{constant}$. Equations (A.9) and (A.11), which govern the vertical position $z = z(t)$ of a fluid particle, are identical to the corresponding equations (3.20) and (3.22) in the axisymmetric case, and hence the solutions for $z = z(t)$ and z_{pen} in the two-dimensional case may be immediately obtained from the corresponding solutions in the axisymmetric case. Moreover, the right-hand sides of equations (A.8) and (A.10), which govern the horizontal position $x = x(t)$ of a fluid particle, differ from the right-hand sides of the corresponding equations (3.19) and (3.21) for $r = r(t)$ in the axisymmetric case by only a factor of 2, and so the solution for $x = x(t)$ in the two-dimensional case may be readily obtained from the solution for $r = r(t)$ in the axisymmetric case by using the simple relationship $x/x_0 = (r/r_0)^2$.

Appendix B

Limit of Large Permeability $k \to \infty$ in the Special Case of Zero Slip Length, $l_{\mathrm{S}} = 0$

As described in §3.3, in the limit of large permeability $k \to \infty$, the asymptotic expansion for the contact time t_{c} given by (3.88) is not uniformly valid in the limit $\alpha \to \infty$ (i.e. in the special case of zero slip length, $l_{\mathrm{s}} = 0$) corresponding to the boundary condition (2.18), and so this case must be considered separately from the general analysis for finite α (i.e. for $l_{\mathrm{s}} \neq 0$) described in the main body of the present work. Accordingly, in this Appendix asymptotic solutions for the fluid layer thickness $h = h(t)$ (§B.1) and the fluid particle paths (r, z) (§B.2) in the limit of large permeability $k \to \infty$ when $l_{\mathrm{s}} = 0$ are obtained.

When $l_{\mathrm{s}} = 0$ the equation governing the fluid layer thickness $h = h(t)$ given by (3.5) with $L = L_0$ becomes

$$L_0 = -\frac{3\pi}{2\left[h^3 + 6k(h+2)\right]}\frac{\mathrm{d}h}{\mathrm{d}t}, \tag{B.1}$$

and the equations governing the fluid particle paths (r, z) given by (3.19)–(3.22) become

$$\frac{1}{r}\frac{\mathrm{d}r}{\mathrm{d}h} = -\frac{3(h-z)(hz+2k)}{h\left[h^3+6k(h+2)\right]}, \tag{B.2}$$

$$\frac{\mathrm{d}z}{\mathrm{d}h} = \frac{2h(6k-z^3)+3(h^2-2k)z^2+12khz}{h\left[h^3+6k(h+2)\right]} \tag{B.3}$$

in the fluid layer $0 \leq z \leq h$, and

$$\frac{1}{r}\frac{\mathrm{d}r}{\mathrm{d}h} = -\frac{6k}{\phi\left[h^3+6k(h+2)\right]}, \tag{B.4}$$

$$\frac{1}{1+z}\frac{\mathrm{d}z}{\mathrm{d}h} = \frac{12k}{\phi\left[h^3+6k(h+2)\right]} \tag{B.5}$$

in the porous bed $-1 \leq z \leq 0$, respectively.

B.1 Asymptotic Solution for the Fluid Layer Thickness and Contact Time

At leading order in the limit of large permeability $k \to \infty$ equation (B.1) becomes

$$L_0 = -\frac{\pi}{4k(2+h)}\frac{\mathrm{d}h}{\mathrm{d}t}. \tag{B.6}$$

Solving (B.6) subject to the initial condition (2.51) yields

$$t = \frac{\pi}{4L_0k}\ln\left(\frac{2+d}{2+h}\right), \tag{B.7}$$

which may be readily solved for h to obtain

$$h = -2 + (2+d)\exp\left(-\frac{4L_0kt}{\pi}\right). \tag{B.8}$$

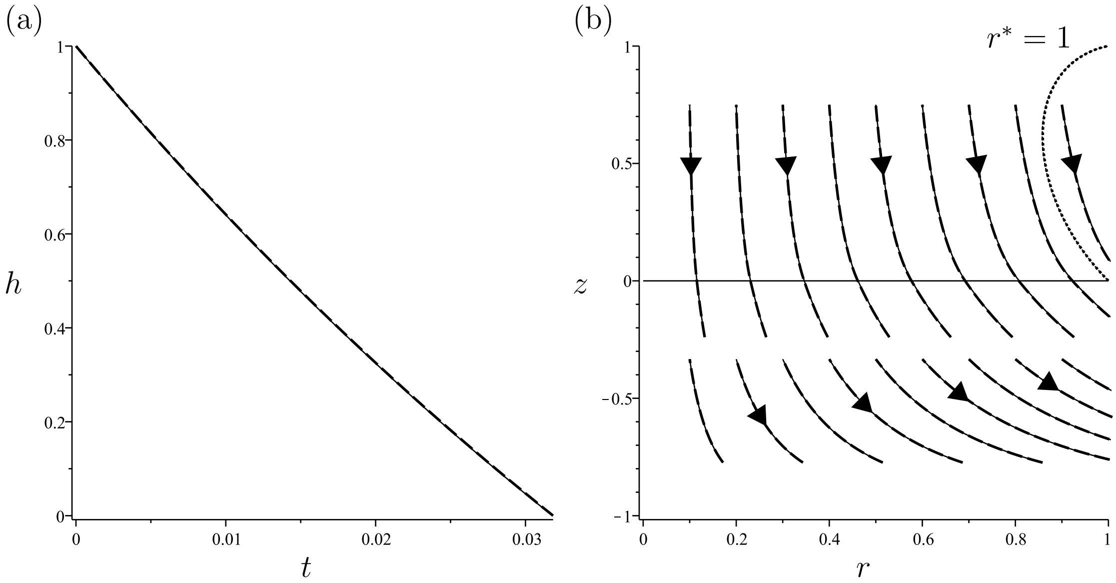

Figure B.1: (a) Plots of the fluid layer thickness h as a function of t in the case $l_s = 0$ given by (3.11) and the leading order large-k asymptotic solution (B.8) (dashed line) for $k = 10$. (b) Plots of fluid particle paths (r, z) in the case $l_s = 0$ where r and z are given by (B.2)–(B.5) subject to $(r_0, z_0) = (0.1, 0.75)$, $(0.2, 0.75)$, $\ldots$, $(0.9, 0.75)$ and $(r_0, z_0) = (0.1, -1/3)$, $(0.2, -1/3)$, $\ldots$, $(0.9, -1/3)$ (solid lines) and the leading order large-k asymptotic solutions (B.12), (B.13), (B.18), (B.19), (B.21) and (B.22) (dashed lines) for $k = 10$ and $\phi = 3/4$. Part (b) also includes a plot of the curve $r^* = 1$ (dotted line)

Figure B.1(a) compares the leading order large-k asymptotic solution for $h = h(t)$ given by (B.8) with the exact solution for $t = t(h)$ given by (3.11) for $k = 10$. Setting $h = 0$ in (B.7) shows that the leading order large-k asymptotic solution for the contact time t_c is

$$t_c = \frac{\pi}{4L_0 k} \ln\left(\frac{2+d}{2}\right). \tag{B.9}$$

Comparing (B.9) with the corresponding expression for the contact time t_c for a non-zero slip length $l_s \neq 0$ given by (3.89) shows that the latter is larger than the former by a factor of $d/2\ln(1 + d/2) > 1$, meaning that, as expected, the effect of a non-zero slip length is to decrease Q_{out} and hence to increase the contact time t_c.

B.2 Asymptotic Solution for the Fluid Particle Paths and Penetration Depths

B.2.1 Fluid Particles Initially Situated in the Fluid Layer $z_0 > 0$

At leading order equations (B.2) and (B.3) governing the path of a fluid particle through the fluid layer become

$$\frac{1}{r}\frac{\mathrm{d}r}{\mathrm{d}h} = -\frac{h-z}{h(2+h)}, \tag{B.10}$$

$$\frac{\mathrm{d}z}{\mathrm{d}h} = \frac{2h(1+z)-z^2}{h(2+h)}. \tag{B.11}$$

Solving (B.10) and (B.11) subject to (3.23) yields

$$r = r_0\left[1-\frac{d-z_0}{2}\ln\left(\frac{(2+d)h}{d(2+h)}\right)\right], \tag{B.12}$$

$$z = h-\frac{d-z_0}{\left[1-\frac{d-z_0}{2}\ln\left(\frac{(2+d)h}{d(2+h)}\right)\right]}, \tag{B.13}$$

which, in contrast to the corresponding results in the case of a non-zero slip length $l_\mathrm{s} \neq 0$, show that (since both v_r and v_z are $O(k) \gg 1$) at leading order the particle moves both radially and vertically through the fluid layer. In particular, setting $z = 0$ in (B.13) shows that a fluid particle reaches the interface $z = 0$ when

$$h = h^* = -2\left[1+W_{-1}\left(-\frac{2+d}{d}\exp\left(-\frac{2+d-z_0}{d-z_0}\right)\right)\right]^{-1}, \tag{B.14}$$

where W_{-1} denotes the lower real branch of the Lambert W function (see, for example, [72]), which, from (B.7), corresponds to the time

$$t = t^* = \frac{\pi}{4L_0 k} \ln\left(\frac{2+d}{2+h^*}\right), \tag{B.15}$$

and, from (B.12), occurs at the radial position $r = r^*$, where $r^* = r_0(d - z_0)/h^*$. Hence at leading order the critical curve $r^* = 1$ is given by $r_0 = h^*/(d - z_0)$.

At leading order equations (B.4) and (B.5) governing the path of a fluid particle after it has entered the porous bed are

$$\frac{1}{r}\frac{\mathrm{d}r}{\mathrm{d}h} = -\frac{1}{\phi(2+h)}, \tag{B.16}$$

$$\frac{1}{1+z}\frac{\mathrm{d}z}{\mathrm{d}h} = \frac{2}{\phi(2+h)}. \tag{B.17}$$

Solving (B.16) and (B.17) subject to the initial conditions $r = r^*$ and $z = 0$ when $h = h^*$ yields

$$r = r^*\left(\frac{2+h^*}{2+h}\right)^{1/\phi}, \tag{B.18}$$

$$z = -1 + \left(\frac{2+h}{2+h^*}\right)^{2/\phi} \tag{B.19}$$

for $0 \le h < h^*$. In particular, setting $h = 0$ in (B.19) shows that the leading order asymptotic solution for z_{pen} is

$$z_{\mathrm{pen}} = -1 + \left(\frac{2}{2+h^*}\right)^{2/\phi}, \tag{B.20}$$

which, like the corresponding result in the case of a non-zero slip length $l_{\mathrm{s}} \neq 0$ given by (3.98), depends on z_0 (via h^*) but is independent of k. Figure B.1(b) compares the fluid particle paths (r, z) with the leading order large-k asymptotic solution given by (B.12), (B.13), (B.18) and (B.19).

B.2.2 Fluid Particles Initially Situated in the Porous Bed $z_0 < 0$

A similar analysis for fluid particles initially situated in the porous bed (i.e. with $z_0 < 0$) yields

$$r = r_0 \left(\frac{2+d}{2+h} \right)^{1/\phi}, \tag{B.21}$$

$$z = -1 + (1+z_0) \left(\frac{2+h}{2+d} \right)^{2/\phi}, \tag{B.22}$$

$$z_{\text{pen}} = -1 + (1+z_0) \left(\frac{2}{2+d} \right)^{2/\phi}. \tag{B.23}$$

Figure B.1(b) also compares the fluid particle paths (r, z) with the leading order large-k asymptotic solution given by (B.21) and (B.22).

Appendix C

Limit of Large Permeability $k \to \infty$ in the Special Case of Zero Slip Length $l_{\mathrm{S}} = 0$, corresponding to the Boundary Condition (2.18)

In §4.4 it was shown that the leading order large-k asymptotic solutions for the contact time t_{c} given by (4.147) when $n = 1$ and (4.155) when $n \geq 2$ are not uniformly valid in the limit $\alpha \to \infty$, i.e. in the special case of zero slip length $l_{\mathrm{s}} = 0$ corresponding to the boundary condition (2.18). This case must, therefore, be treated separately from the analysis for $\alpha = O(1)$ (i.e. for large slip length $l_{\mathrm{s}} = O(k^{1/2}) \gg 1$) described in §4.4. Accordingly, in this Appendix the leading order large-k solutions for the fluid pressure $p = p(r,t)$ and the minimum fluid layer thickness $h_{\mathrm{min}} = h_{\mathrm{min}}(t)$ that are valid in the limit $\alpha \to \infty$ are obtained.
When the slip length $l_{\mathrm{s}} = 0$ the Reynolds equation (4.3) that governs the fluid

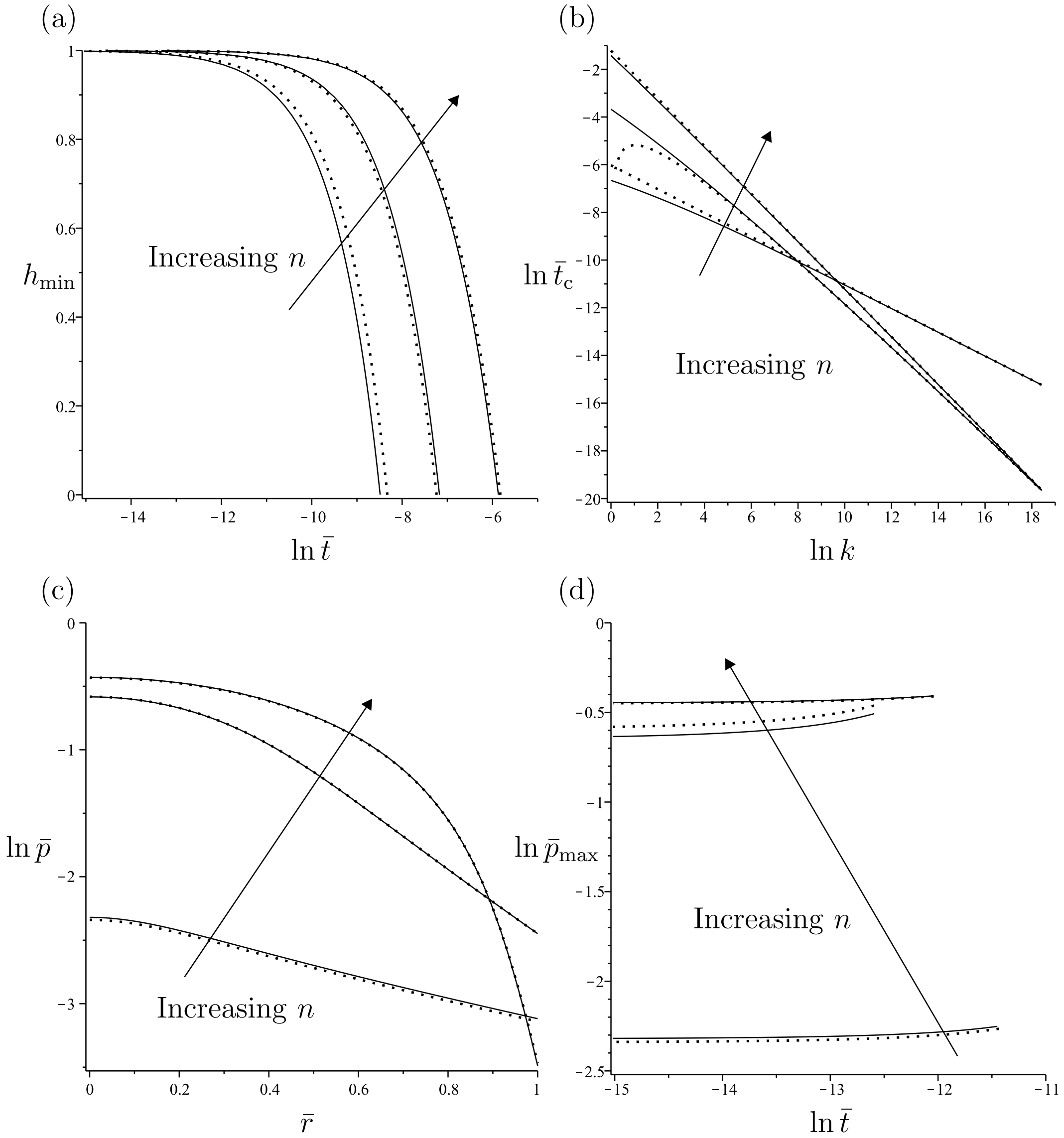

Figure C.1: (a) Plots of $h_{\min}$ as a function of $\ln \bar{t}$ given by (4.7) (solid lines) and the leading order large-k solutions (C.13), (C.27) and (C.34) (dotted lines) for $k = 10^2$ and $n = 1, 2$ and 10, respectively. (b) Plots of $\ln \bar{t}_c$ as a function of $\ln k$ given by (4.10) (solid lines) and the leading order large-k solutions (C.15), (C.28) and (C.35) (dotted lines) for $n = 1, 2$ and 10, respectively. (c) Plots of $\ln \bar{p}$ as a function of $\bar{r}$, at the time when $h_{\min} = d/2$, given by (4.4) (solid lines) and the leading order large-k solutions (C.10), (C.24) and (C.31) (dotted lines) for $k = 5 \times 10^4$ and $n = 1, 2$ and 10, respectively. (d) Plots of $\ln \bar{p}_{\max}$ as a function of $\ln \bar{t}$ given by (4.4) and (4.7) (solid lines) and the leading order large-k solutions (C.12) and (C.13), (C.26) and (C.27), and (C.33) and (C.34) (dotted lines) for $k = 5 \times 10^4$ and $n = 1, 2$ and 10, respectively. In all plots the slip-length $l_s = 0$, i.e. $\alpha \to \infty$

pressure $p = p(r,t)$ becomes

$$\frac{\partial p}{\partial r} = \frac{6r}{h\left(h^2+6k\right)+12k}\frac{\mathrm{d}h_{\min}}{\mathrm{d}t}. \tag{C.1}$$

Similarly to the case when $\alpha = O(1)$ treated in §4.4, there are inner and outer regions in which different large-k solutions for the fluid pressure $p = p(r,t)$ are valid. The cases of a parabolic bearing ($n = 1$), a quartic bearing ($n = 2$) and more general bearing shapes ($n \geq 3$) are treated separately in §C.1, §C.2 and §C.3, respectively.

C.1 Parabolic Bearing $n = 1$

Since the contact time $t_{\mathrm{c}} = O\left(k^{-1/2}\right)$ we re-scale time t according to

$$t = k^{-1/2}T, \tag{C.2}$$

where T is $O(1)$ in the limit $k \to \infty$.

C.1.1 Inner Solution for $p(r,t)$ valid when $r = O(1)$

In the inner region $r = O(1)$ we re-scale p according to

$$p = k^{-1/2}(\ln k)\hat{p}, \tag{C.3}$$

where $\hat{p}$ is $O(1)$ in the limit $k \to \infty$. In terms of the re-scaled variables (C.2) and (C.3) and to leading order in the limit $k \to \infty$ equation (C.1) is

$$\frac{\partial \hat{p}}{\partial r} = \frac{r}{\ln k\left(2+h_{\min}+r^2\right)}\frac{\mathrm{d}h_{\min}}{\mathrm{d}T}. \tag{C.4}$$

Solving (C.4) yields, in terms of the original variables, the solution

$$p = \frac{\ln\left(2 + h_{\min} + r^2\right)}{2k} \frac{\mathrm{d}h_{\min}}{\mathrm{d}t} + f(t) \sim \frac{\ln r}{k} \frac{\mathrm{d}h_{\min}}{\mathrm{d}t} + f(t) \quad \text{as} \quad r \to \infty, \tag{C.5}$$

where $f = f(t)$ is an arbitrary constant of integration which shall be determined by matching the solutions for $p = p(r,t)$ that are valid in the inner and outer regions. Note that if the solution for $p = p(r,t)$ given by (C.5) is used in the load condition (2.59) then the integral diverges in the limit $r \to \infty$, meaning that (C.5) is not valid in the limit $r \to \infty$. There is in fact an outer region $r = O(k^{1/4})$ in which a different large-k solution for the fluid pressure $p = p(r,t)$ is valid.

C.1.2 Outer Solution for $p(r,t)$ valid when $r = O(k^{1/4})$

In the outer region $r = O(k^{1/4})$ we re-scale r and p according to

$$r = k^{1/4} R, \quad p = k^{-1/2} P, \tag{C.6}$$

where R and P are $O(1)$ in the limit $k \to \infty$. In terms of the re-scaled variables (C.2) and (C.6) and to leading order in the limit $k \to \infty$ equation (C.1) is

$$\frac{\partial P}{\partial R} = \frac{6}{R\left(6 + R^4\right)} \frac{\mathrm{d}h_{\min}}{\mathrm{d}T}. \tag{C.7}$$

Solving (C.7) subject to the boundary condition $P \to 0$ as $R \to \infty$ yields, in terms of the original variables, the solution

$$p = \frac{1}{4k} \ln\left(\frac{r^4}{6k + r^4}\right) \frac{\mathrm{d}h_{\min}}{\mathrm{d}t} \sim \frac{1}{4k} \ln\left(\frac{r^4}{6k}\right) \frac{\mathrm{d}h_{\min}}{\mathrm{d}t} \quad \text{as} \quad r \to 0. \tag{C.8}$$

Note that the solution for $p = p(r,t)$ given by (C.8) has a logarithmic singularity at leading order in the limit $r \to 0$. The outer limit, i.e. the limit $r \to \infty$, of the inner solution for $p = p(r,t)$ given by (C.5) matches (at leading order) with the inner limit, i.e. the limit $r \to 0$, of the outer solution for $p = p(r,t)$ given by (C.8) provided that

$$f(t) = -\frac{\ln 6k}{4k}\frac{\mathrm{d}h_{\min}}{\mathrm{d}t}. \tag{C.9}$$

C.1.3 A Uniformly Valid Leading Order Composite Solution for $p(r,t)$

A uniformly valid leading order composite solution for $p = p(r,t)$ is

$$p = -\frac{1}{4k}\ln\left(\frac{6k + r^4}{(2 + h_{\min} + r^2)^2}\right)\frac{\mathrm{d}h_{\min}}{\mathrm{d}t}. \tag{C.10}$$

Figure C.1(c) compares the uniformly valid leading order large-k solution for the fluid pressure $p = p(r,t)$ given by (C.10) with the exact solution given by (4.4). Note that the uniformly valid leading order composite solution for $p = p(r,t)$ given by (C.10) is such that $p = O(r^{-2})$ as $r \to \infty$ and, therefore, the normal force F_z exerted on the bearing by the fluid is infinite. This is a consequence of the fact that the leading order inner solution for $p = p(r,t)$ given by (C.5) is $O(r^{-2})$ at first order in the limit $r \to \infty$ and can, in principle, be resolved by calculating a higher order composite solution for $p = p(r,t)$.

Since the largest contribution to the normal force F_z exerted on the bearing by the fluid is from the outer region, applying the load condition (2.59) to the outer solution for $p = p(r,t)$ given by (C.8) yields the equation governing the leading order large-k solution for the minimum fluid layer thickness $h_{\min} = h_{\min}(t)$:

$$L_0 = -\frac{\sqrt{6}\pi^2}{4k^{1/2}}\frac{\mathrm{d}h_{\min}}{\mathrm{d}t}. \tag{C.11}$$

Re-arranging (C.11) for $\mathrm{d}h_{\min}/\mathrm{d}t$, substituting into equation (C.10) and setting $r = 0$ yields the leading order large-k solution for the maximum fluid pressure $p_{\max}$:

$$p_{\max} = \frac{L_0}{\sqrt{6}\pi^2 k^{1/2}} \ln\left(\frac{6k}{(2 + h_{\min})^2}\right). \tag{C.12}$$

Figure C.1(d) compares the leading order large-k solution for $p_{\max}$ given by (C.12) with the exact solution given by setting $r = 0$ in (4.4).

C.1.4 Asymptotic Solution for the Minimum Fluid Layer Thickness and Contact Time

Solving (C.11) subject to the initial condition (2.51) yields the solution

$$t = \frac{\sqrt{6}\pi^2}{4L_0 k^{1/2}}\left(d - h_{\min}\right), \tag{C.13}$$

i.e.

$$h_{\min} = d - \frac{4L_0 k^{1/2}}{\sqrt{6}\pi^2}t. \tag{C.14}$$

Figure C.1(a) compares the leading order large-k solution for $t = t(h_{\min})$ given by (C.13) with the exact solution given by (4.7). Setting $h_{\min} = 0$ in (C.13) we obtain the leading order large-k solution for the contact time t_{c}:

$$t_{\mathrm{c}} = \frac{\sqrt{6}\pi^2 d}{4L_0 k^{1/2}}. \tag{C.15}$$

Figure C.1(b) compares the leading order large-k solution for $t_{\rm c}$ given by (C.15) with the exact solution given by (4.10).

C.2 Quartic Bearing $n = 2$

Since the contact time $t = O(k^{-1} \ln k)$ we re-scale time t according to

$$t = k^{-1} \ln k T, \tag{C.16}$$

where T is $O(1)$ in the limit $k \to \infty$.

C.2.1 Inner Solution for $p(r, t)$ valid when $r = O(1)$

In the inner region $r = O(1)$ we re-scale p according to

$$p = (\ln k)^{-1} \hat{p}, \tag{C.17}$$

where $\hat{p}$ is $O(1)$ in the limit $k \to \infty$. In terms of the re-scaled variables (C.16) and (C.17) and to leading order in the limit $k \to \infty$ equation (C.1) is

$$\frac{\partial \hat{p}}{\partial r} = \frac{r}{2 + h_{\rm min} + r^4} \frac{{\rm d}h_{\rm min}}{{\rm d}T}. \tag{C.18}$$

Solving (C.18) subject to the boundary condition $\hat{p} \to 0$ as $r \to \infty$ yields, in terms of the original variables, the solution

$$\begin{aligned} p &= -\frac{1}{2k\,(2 + h_{\rm min})^{1/2}} \left[\frac{\pi}{2} - \tan^{-1} \left(\frac{r^2}{(2 + h_{\rm min})^{1/2}} \right) \right] \frac{{\rm d}h_{\rm min}}{{\rm d}t} \qquad \text{(C.19)} \\ &\sim -\frac{1}{2kr^2} \frac{{\rm d}h_{\rm min}}{{\rm d}t} \quad \text{as} \quad r \to \infty. \end{aligned}$$

Note that if the solution for $p = p(r,t)$ given by (C.19) is used in the load condition (2.59) then the integral diverges logarithmically in the limit $r \to \infty$, meaning that (C.19) is not valid in the limit $r \to \infty$. There is in fact an outer region $r = O(k^{1/8})$ in which a different large-k solution for the fluid pressure $p = p(r,t)$ is valid.

C.2.2 Outer Solution for $p(r,t)$ valid when $r = O(k^{1/8})$

In the outer region $r = O(k^{1/4})$ we re-scale r and p according to

$$r = k^{1/8}R, \quad p = k^{-1/4}(\ln k)^{-1}P, \tag{C.20}$$

where R and P are $O(1)$ in the limit $k \to \infty$. In terms of re-scaled the variables (C.16) and (C.20) and to leading order in the limit $k \to \infty$ equation (C.1) is

$$\frac{\partial P}{\partial R} = \frac{6}{R^3\left(6+R^8\right)}\frac{\mathrm{d}h_{\min}}{\mathrm{d}T}. \tag{C.21}$$

Solving (C.21) subject to the boundary condition $P \to 0$ as $R \to \infty$ yields, in terms of the original variables, the solution

$$p = -\frac{g\left(r/k^{1/8}\right)}{96k^{5/4}}\frac{\mathrm{d}h_{\min}}{\mathrm{d}t} \sim -\frac{1}{2kr^2}\frac{\mathrm{d}h_{\min}}{\mathrm{d}t} \quad \text{as} \quad r \to 0, \tag{C.22}$$

where

$$\begin{aligned} g(R) &= \frac{48}{R^2} + 6^{3/4}\sqrt{2}\left[\ln\left(\frac{R^4 - 6^{1/4}\sqrt{2}R^2 + \sqrt{6}}{R^4 + 6^{1/4}\sqrt{2}R^2 + \sqrt{6}}\right)\right. \\ &+ \left. 2\left(\tan^{-1}\left(\frac{6^{3/4}\sqrt{2}R^2 + 6}{6}\right) + \tan^{-1}\left(\frac{6^{3/4}\sqrt{2}R^2 - 6}{6}\right) - \pi\right)\right]. \end{aligned} \tag{C.23}$$

The solution for $p = p(r,t)$ given by (C.22) is singular at leading order in the limit $r \to 0$ and if it is used in the load condition (2.59) then the integral diverges logarithmically in the limit $r \to 0$, meaning that (C.22) is not valid in the limit $r \to 0$. Note that the outer limit, i.e. the limit $r \to \infty$, of the inner solution for $p = p(r,t)$ given by (C.19) automatically matches (at leading order) with the inner limit, i.e. the limit $r \to 0$, of the outer solution for $p = p(r,t)$ given by (C.22).

C.2.3 Uniformly Valid Leading Order Composite Solution for $p = p(r,t)$

A uniformly valid leading order composite solution for $p = p(r,t)$ is

$$\begin{aligned} p &= -\frac{1}{96k^{5/4}}\left(\frac{48k^{1/4}}{(2+h_{\min})^{1/2}}\left[\frac{\pi}{2} - \tan^{-1}\left(\frac{r^2}{(2+h_{\min})^{1/2}}\right)\right]\right. \\ &+ \left. g\left(\frac{r}{k^{1/8}}\right) - \frac{48k^{1/4}}{r^2}\right)\frac{\mathrm{d}h_{\min}}{\mathrm{d}t}. \end{aligned} \tag{C.24}$$

Figure C.1(c) compares the uniformly valid leading order large-k solution for $p = p(r,t)$ given by (C.24) with the exact solution for $p = p(r,t)$ given by (4.4). Unlike the case of a parabolic bearing ($n = 1$) treated in §C.1, there are $O(1)$ contributions to the normal force F_z exerted on the bearing by the fluid from both the inner $r = o(k^{1/8})$ and outer $r = O(k^{1/8})$ regions. The equation governing the leading order large-k solution for $h_{\min} = h_{\min}(t)$ is, therefore, obtained by applying the load condition (2.59) to the uniformly valid leading order large-k solution for $p = p(r,t)$ given by (C.24), which yields

$$L_0 = -\frac{\pi}{8k}\ln\left(\frac{6k}{(2+h_{\min})^2}\right)\frac{\mathrm{d}h_{\min}}{\mathrm{d}t}. \tag{C.25}$$

Re-arranging (C.25) for $\mathrm{d}h_{\min}/\mathrm{d}t$, substituting into equation (C.24) and letting $r \to 0$ yields the leading order large-k solution for the maximum fluid pressure

$p_{\max}$:

$$p_{\max} = \frac{2L_0}{(2+h_{\min})^{1/2}\ln\left(6k/(2+h_{\min})^2\right)}. \tag{C.26}$$

Figure C.1(d) compares the leading order large-k solution for $p_{\max}$ given by (C.26) with the exact solution given by setting $r = 0$ in (4.4).

C.2.4 Asymptotic Solution for the Minimum Fluid Layer Thickness and Contact Time

Solving (C.25) subject to the initial condition (2.51) yields the solution

$$\begin{aligned} t &= \frac{\pi}{8L_0k}\left[2\left(d-h_{\min}\right)+d\ln\left(\frac{6k}{(2+d)^2}\right)-h_{\min}\ln\left(\frac{6k}{(2+h_{\min})^2}\right)\right. \\ &+ \left. 4\ln\left(\frac{2+h_{\min}}{2+d}\right)\right]. \end{aligned} \tag{C.27}$$

Figure C.1(a) compares the leading order large-k asymptotic solution for $t = t(h_{\min})$ given by (C.27) with the exact solution given by (4.7). Setting $h_{\min} = 0$ in (C.27) yields the leading order large-k solution for the contact time t_c:

$$t_c = \frac{\pi}{8L_0k}\left[d\ln k + d\left(2+\ln\left(\frac{6}{(2+d)^2}\right)\right)+4\ln\left(\frac{2}{2+d}\right)\right]. \tag{C.28}$$

Figure C.1(b) compares the leading order large-k solution for the contact time t_c given by (C.28) with the exact solution given by (4.10).

C.3 General Bearing Shapes $n \geq 3$

Since the contact time $t_c = O\left(k^{-1}\right)$ we re-scale time t according to

$$t = k^{-1}T, \tag{C.29}$$

where T is $O(1)$ in the limit $k \to \infty$.

C.3.1 Inner Solution for $p(r,t)$ valid when $r = O(1)$

In terms of the re-scaled time T given by (C.29) and to leading order in the limit $k \to \infty$ equation (C.1) is

$$\frac{\partial p}{\partial r} = \frac{r}{2 + h_{\min} + r^{2n}} \frac{\mathrm{d}h_{\min}}{\mathrm{d}T}. \tag{C.30}$$

Solving (C.30) subject to the boundary condition (2.48) yields, in terms of the original variables, the solution

$$p = -\frac{1}{k}\left(\int_r^\infty \frac{\tilde{r}}{2 + h_{\min} + \tilde{r}^{2n}}\,\mathrm{d}\tilde{r}\right)\frac{\mathrm{d}h_{\min}}{\mathrm{d}t}. \tag{C.31}$$

Figure C.1(c) compares the leading order large-k solution for $p = p(r,t)$ given by (C.31) with the exact solution given by (4.4). The solution for $p = p(r,t)$ given by (C.31) is valid when $r = O(1)$. There is an outer region $r = O(k^{1/4n})$ in which a different leading order large-k solution for $p = p(r,t)$ is valid. However, since the largest contribution to the normal force F_z exerted on the bearing by the fluid is from the inner region $r = o(k^{1/4n})$, in order to obtain the equation governing the leading order large-k solution for $h_{\min} = h_{\min}(t)$ it is not necessary to determine the outer solution for $p = p(r,t)$ and we do not, therefore, pursue this any further. Applying the load condition (2.59) to (C.31) yields the equation governing the leading order large-k solution for $h_{\min} = h_{\min}(t)$:

$$L_0 = -\frac{\pi^2 \csc(2\pi/n)}{2nk(2 + h_{\min})^{(n-2)/n}} \frac{\mathrm{d}h_{\min}}{\mathrm{d}t}. \tag{C.32}$$

Setting $r = 0$ in (C.31) yields the leading order large-k solution for the maximum fluid pressure $p_{\max}$:

$$p_{\max} = \frac{2\cos(\pi/n)\, L_0}{\pi\,(2+h_{\min})^{1/n}}. \tag{C.33}$$

Figure C.1(d) compares the leading order large-k solution for $p_{\max} = p(0,t)$ given by (C.33) with the exact solution given by setting $r = 0$ in (4.4).

C.3.2 Asymptotic Solution for the Minimum Fluid Layer Thickness and Contact Time

Solving (C.32) subject to the initial condition (2.51) yields the solution

$$t = \frac{\pi^2 \csc(2\pi/n)}{4L_0 k}\left((2+d)^{2/n} - (2+h_{\min})^{2/n}\right). \tag{C.34}$$

Figure C.1(a) compares the leading order large-k solution for $t = t(h_{\min})$ given by (C.34) with the exact solution given by (4.7). Setting $h_{\min} = 0$ in (C.34) yields the leading order large-k solution for the contact time t_{c}:

$$t_{\mathrm{c}} = \frac{\pi^2 \csc(2\pi/n)}{4L_0 k}\left((2+d)^{2/n} - 2^{2/n}\right). \tag{C.35}$$

Figure C.1(b) compares the leading order large-k solution for t_{c} given by (C.35) with the exact solution given by (4.10).

Note that letting $n \to \infty$ in (C.35) we recover the result for a flat bearing obtained in Appendix B and given by equation (B.9).

Appendix D

Limit of Large Permeability $k \to \infty$ in the Special Case of Zero Slip Length $l_{\mathrm{S}} = 0$, corresponding to the Boundary Condition (2.19)

In §4.4 it was shown that the leading order large-k asymptotic solutions for the contact time t_c given by (4.147) when $n = 1$ and (4.155) when $n \geq 2$ are not uniformly valid in the limit $\alpha \to \infty$, i.e. in the special case of zero slip length $l_s = 0$. In the particular case when $\delta = 0$ this limit corresponds to the boundary condition (2.19), and this case must be treated separately from the analysis for $\alpha = O(1)$ described in §4.4. Accordingly, in this Appendix the leading order large-k solutions for the fluid pressure $p = p(r, t)$ and the minimum fluid layer thickness $h_{\min} = h_{\min}(t)$ that are valid in the limit $\alpha \to \infty$ when $\delta = 0$ are obtained.

When the slip length $l_s = 0$ and $\delta = 0$ the Reynolds equation (4.3) that governs

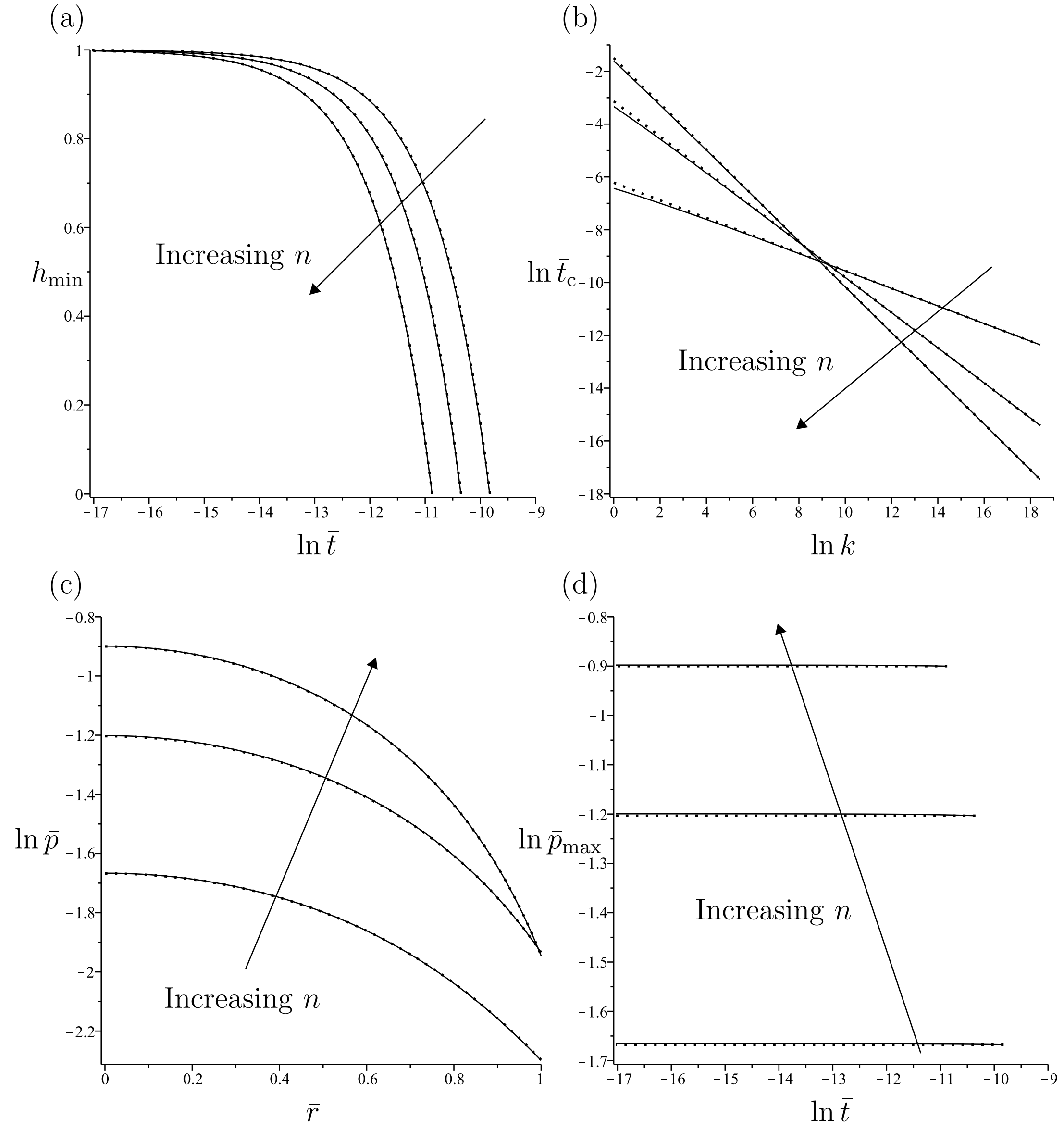

Figure D.1: (a) Plots of $h_{\min}$ as a function of $\ln \bar{t}$ given by (4.7) (solid lines) and the leading order large-k solution (D.7) (dotted lines) for $k = 10^2$ and $n = 1, 2$ and 5, respectively. (b) Plots of $\ln \bar{t}_c$ as a function of $\ln k$ given by (4.10) (solid lines) and the leading order large-k solution (D.9) (dotted lines) for $n = 1, 2$ and 5, respectively. (c) Plots of $\ln \bar{p}$ as a function of $\bar{r}$ when $h_{\min} = d/2$ given by (4.4) (solid lines) and the leading order large-k solution (D.4) (dotted lines) for $k = 5 \times 10^4$ and $n = 1, 2$ and 5, respectively. (d) Plots of $\ln \bar{p}_{\max}$ as a function of $\ln \bar{t}$ given (4.4) and (4.7) (solid lines) and the leading order large-k solutions (D.6) and (D.7) (dotted lines) for $k = 5 \times 10^4$ and $n = 1, 2$ and 5, respectively. In all plots the slip-length $l_s = 0$, i.e. $\alpha \to \infty$, and $\delta = 0$

the fluid pressure $p = p(r,t)$ becomes

$$\frac{\partial p}{\partial r} = \frac{6r}{h^3 + 12k}\frac{\mathrm{d}h_{\min}}{\mathrm{d}t}. \tag{D.1}$$

In contrast to the case when $\delta = 1$, corresponding to the boundary condition (2.18) and treated in Appendix C, it is found that for each bearing shape $n = 1, 2, 3, \ldots$ there is a single large-k solution for the fluid pressure $p = p(r,t)$ that is uniformly valid for all r.

D.1 Asymptotic Solution for the Fluid Pressure

Since the contact time $t_c = O(k^{-(3n-2)/3n})$ and the maximum fluid pressure $p_{\max} = O(k^{-1/3n})$ we re-scale the variables r, t and p according to

$$r = (12k)^{1/6n}R, \quad t = (12k)^{-(3n-2)/3n}T, \quad p = (12k)^{-1/3n}P, \tag{D.2}$$

where R, T and P are $O(1)$ in the limit $k \to \infty$. In terms of re-scaled variables (D.2) and to leading order in the limit $k \to \infty$ equation (4.3) is

$$\frac{\partial P}{\partial R} = \frac{6R}{1 + R^{6n}}\frac{\mathrm{d}h_{\min}}{\mathrm{d}T}. \tag{D.3}$$

Solving (D.3) subject to the boundary condition $P \to 0$ as $R \to \infty$ yields, in terms of the original variables, the solution

$$p = -\frac{6}{(12k)^{(3n-1)/3n}}\left(\int_{(12k)^{-1/6n}r}^{\infty} \frac{\tilde{r}}{1 + \tilde{r}^{6n}}\,\mathrm{d}\tilde{r}\right)\frac{\mathrm{d}h_{\min}}{\mathrm{d}t}. \tag{D.4}$$

Figure D.1(c) compares the leading order large-k solution for $p = p(r,t)$ given by (D.4) with the exact solution given by (4.4). Applying the load condition

(2.59) to (D.4) yields the equation governing the leading order large-k solution for $h_{\min} = h_{\min}(t)$:

$$L_0 = -\frac{\pi^2 \csc(2\pi/3n)}{n(12k)^{(3n-2)/3n}} \frac{\mathrm{d}h_{\min}}{\mathrm{d}t}. \tag{D.5}$$

Setting $r = 0$ in (D.4) yields the leading order large-k solution for the maximum fluid pressure $p_{\max}$:

$$p_{\max} = \frac{2\cos(\pi/3n)\, L_0}{\pi(12k)^{1/3n}}. \tag{D.6}$$

Figure D.1(d) compares the leading order large-k solution for $p_{\max}$ given by (D.6) with the exact solution given by setting $r = 0$ in (4.4).

D.2 Asymptotic Solution for the Minimum Fluid Layer Thickness and Contact Time

Solving (D.5) subject to the initial condition (2.51) yields the solution

$$t = \frac{\pi^2 \csc(2\pi/3n)}{nL_0(12k)^{(3n-2)/3n}}(d - h_{\min}), \tag{D.7}$$

i.e.

$$h_{\min} = d - \frac{nL_0(12k)^{(3n-2)/3n}}{\pi^2 \csc(2\pi/3n)} t. \tag{D.8}$$

Figure D.1(a) compares the leading order large-k solution for $t = t(h_{\min})$ given by (D.7) with the exact solution given by (4.7). Setting $h_{\min} = 0$ in (D.7) yields the leading order large-k solution for the contact time t_c:

$$t_c = \frac{\pi^2 \csc(2\pi/3n) d}{nL_0(12k)^{(3n-2)/3n}}. \tag{D.9}$$

Figure D.1(b) compares the leading order large-k solution for $t_{\rm c}$ given by (D.9) with the exact solution given by (4.10).

Note that letting $n \to \infty$ in (D.9) we recover the result for a flat bearing obtained in Chapter 3 and given by equation (3.89).

Appendix E

Integration along a Ray Emanating from the Origin in the Complex Plane

In the analysis of the limit of small permeability $k \to 0$ for general bearing shapes $n \geq 2$ given in §4.3.2, in order to obtain an explicit expression for the leading order solution for $t(h_{\min})$ that is valid for "long" times $t = O(k^{-2(n-1)/3n})$ it is necessary to evaluate an integral of the form

$$I = \int_C \frac{z^a}{1+z^2}\,\mathrm{d}z, \quad a \in \mathbb{R}, \tag{E.1}$$

where C is a ray that emanates from the origin in the complex plane and makes an angle ϕ with the positive real axis that satisfies $-\pi/2 < \phi < \pi/2$. In this Appendix we will show that the value of this integral is independent of the direction of the ray provided that $-1 < a < 1$, and in particular

$$I = \int_C \frac{z^a}{1+z^2}\,\mathrm{d}z = \int_0^\infty \frac{z^a}{1+z^2}\,\mathrm{d}z \quad \text{when} \quad -1 < a < 1, \tag{E.2}$$

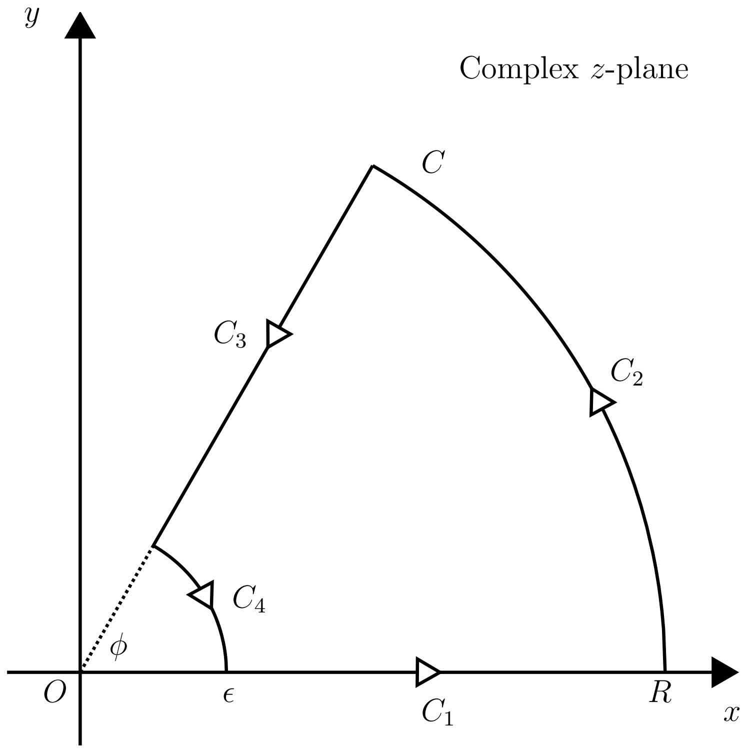

Figure E.1: The contour of integration C in (E.3)

i.e. the integral can be evaluated by integrating along the positive real line.

Consider the integral

$$I = \int_C f(z)\,\mathrm{d}z, \tag{E.3}$$

where the function $f = f(z)$ is defined by

$$f(z) = \frac{z^a}{1+z^2}, \tag{E.4}$$

where a is a real number and C is the contour illustrated in Figure E.1 with $-\pi/2 < \phi < \pi/2$. We choose the specific branch of z^a so that, with polar representation, $z = r\exp(\mathrm{i}\theta)$, $z^a = r^a \exp(a\mathrm{i}\theta)$, $-\pi \le \theta < \pi$. By Cauchy's theorem, since $f(z)$ is analytic inside C we have that

$$I = \int_C f(z)\,\mathrm{d}z = \int_{C_1} f(z)\,\mathrm{d}z + \int_{C_2} f(z)\,\mathrm{d}z + \int_{C_3} f(z)\,\mathrm{d}z + \int_{C_4} f(z)\,\mathrm{d}z = 0, \quad \text{(E.5)}$$

where C_1, C_2, C_3 and C_4 are as shown in Figure E.1. Now

$$\int_{C_1} f(z)\,\mathrm{d}z = \int_{\epsilon}^{R} \frac{z^a}{1+z^2}\,\mathrm{d}z, \quad \text{(E.6)}$$

$$\int_{C_2} f(z)\,\mathrm{d}z = \mathrm{i}\phi R^{1+a} \int_0^1 \frac{\exp[\mathrm{i}(1+a)\phi s]}{1+R^2\exp(2\mathrm{i}\phi s)}\,\mathrm{d}s, \quad \text{(E.7)}$$

$$\int_{C_3} f(z)\,\mathrm{d}z = -\int_{\epsilon\exp(\mathrm{i}\phi)}^{R\exp(\mathrm{i}\phi)} \frac{z^a}{1+z^2}\,\mathrm{d}z, \quad \text{(E.8)}$$

$$\int_{C_4} f(z)\,\mathrm{d}z = -\mathrm{i}\phi\epsilon^{1+a} \int_0^1 \frac{\exp[\mathrm{i}(1+a)\phi s]}{1+\epsilon^2\exp(2\mathrm{i}\phi s)}\,\mathrm{d}s. \quad \text{(E.9)}$$

Using the ML inequality we have that

$$\left|\int_{C_2} f(z)\,\mathrm{d}z\right| \le \frac{\pi R^{1+a}}{2|1-R^2|} \sim \frac{\pi}{2R^{1-a}} \to 0 \quad \text{as} \quad R \to \infty, \quad \text{(E.10)}$$

when $a < 1$, and

$$\left|\int_{C_4} f(z)\,\mathrm{d}z\right| \le \frac{\pi\epsilon^{1+a}}{2|1-\epsilon^2|} \sim \frac{\pi\epsilon^{1+a}}{2} \to 0 \quad \text{as} \quad \epsilon \to 0, \quad \text{(E.11)}$$

when $a > -1$. So assuming that $-1 < a < 1$ and letting $\epsilon \to 0$ and $R \to \infty$ in (E.5) we have that

$$\lim_{R\to\infty} \int_0^{R\exp(\mathrm{i}\phi)} f(z)\,\mathrm{d}z = \int_0^{\infty} f(z)\,\mathrm{d}z, \quad \text{(E.12)}$$

i.e. provided that $-1 < a < 1$ the integral of $f(z)$ along a ray emanating from the origin that makes an angle ϕ, satisfying $-\pi/2 < \phi < \pi/2$, with the positive real axis is independent of the direction of the ray and, in particular, is equal to the integral of $f(z)$ along the positive real line.